UNIVERSITÀ
DEGLI STUDI
DI TRIESTE

UNIVERSITÀ DEGLI STUDI DI TRIESTE

XXXIV CICLO DEL DOTTORATO DI RICERCA IN FISICA

Study of cosmic-ray proton and deuteron solar modulation and its relevence for indirect dark-matter searches with the PAMELA and GAPS experiments

Settore scientifico-disciplinare: FISICA SPERIMENTALE

Dottorando:
Alex Lenni

Coordinatore:
Prof. Francesco Longo

Supervisore di tesi:
Dott. Mirko Boezio

Cosupervisore di tesi:
Dott. Riccardo Munini

ANNO ACCADEMICO 2020–2021

Summary

Cosmic rays are electrically charged particles of high energy, accelerated by astrophysical powerful sources. This cosmic radiation consists mainly of protons and helium nuclei and in minimal part of other nuclei and electrons. Among these, there are the deuterons, i.e. the deuterium nuclei, which, unlike protons, are produced as a secondary component by interactions of cosmic rays with the atoms of the interstellar medium. Indeed, along their journey through the Galaxy, cosmic rays experience energy losses, fragmentations in secondary products, deflections in their travelling direction as an effect of the galactic magnetic fields and generally a change of the spectral features with respect to their initial injection spectrum. Before reaching the Earth, cosmic rays propagate through the Heliosphere, the space region permeated by the solar magnetic field embedded in the turbulent solar wind flowing from the Sun to beyond the boundaries of the solar system. The interaction with the heliospheric magnetic field and the solar wind makes cosmic-ray flux decrease with respect to the intensity of their energy spectra outside the Heliosphere. Moreover, a time dependence of the cosmic-ray fluxes is induced by the different phases of the 11-year cycle of solar activity and of the 22-year cycle of the heliospheric magnetic field. The latter also induces polarity-dependent drift motions, which are followed by cosmic rays of opposite charges in the opposite direction. All these effects, commonly named solar modulation of cosmic rays, are significant up to about 50 GeV, beyond this energy they are too small to be observed with the current cosmic-ray detectors.
The charge-sign dependence introduced by the drift motions in the Heliosphere is relevant for the studies of the galactic antinuclei. These are a rare component of cosmic rays and are considered promising probes for indirect searches for dark matter. Especially the antideuteron is extremely rare in cosmic rays and it has not been detected. However, according to a variety of dark-matter models, antideuterons could be produced by dark-matter annihilation or decay processes with a flux of orders of magnitude above the astrophysical background of secondary antideuterons in the energy range below a few GeV/n. This signal should also be inside the sensitivities of the

current AMS-02 and future GAPS experiments. However, at the considered low energies, the uncertainty related to the modelling of the solar modulation is significant. This can be reduced by studying the solar modulation of the corresponding particles, the deuterons, with advanced numerical models accounting for the charge sign effect induced by the drift.
In this work, a new measurement of the time-dependent galactic cosmic-ray proton and deuteron fluxes between 50 and 800 MeV/n is presented. This analysis was conducted on the data collected by the PAMELA experiment from July 2006 to September 2014. This period is particularly relevant for solar-modulation studies because it covers almost a whole solar cycle and includes a change of solar magnetic polarity in 2013 as well. A set of selections was developed to extract clean samples of galactic protons and deuterons from the data maintaining a high selection efficiency. As a result, nine yearly rigidity spectra from 2006 to 2014 have been measured between 0.6 and 2.6 GV for both galactic protons and deuterons. The obtained deuteron fluxes were compared with those obtained from a numerical 3D model of cosmic-ray propagation in the Heliosphere. Such comparison can be useful to constrain the modulation parameters of the model for the different heliospheric conditions observed in the analysed period. The deuteron-to-proton flux ratios were also calculated and can be used to study the solar modulation effects depending on the different local-interstellar-spectrum shapes as well as on the charge-to-mass ratio dependence of the principal propagation mechanisms in the Heliosphere. All these results can help to improve the accuracy of the solar modulation modelling of the cosmic-ray deuteron fluxes, which is paramount to properly model the solar-modulation effects on the expected energy spectra of antideuterons, reducing the current related uncertainty.
A preliminary study of the deuteron acceptance achievable with the GAPS experiment was also performed using simulated data. Although the GAPS apparatus has been designed to perform a novel exotic-atom capture and decay technique to detect cosmic-ray antinuclei, particle detection is possible at low energy. An analysis technique was developed to identify the deuteron Bragg peaks occurring in the GAPS detectors and separate in this way deuterons from the larger background of protons. The values of acceptance for the deuteron selection and the proton power rejection obtained for the GAPS experiment are provided in the thesis.

Contents

1 Hydrogen isotopes in Cosmic Rays and their propagation to the Earth **1**

1.1 Cosmic Rays: an overview 2
1.2 Isotopic abundances in Cosmic Rays 7
1.2.1 Protons and Deuterons in Cosmic Rays 8
1.3 Origin and acceleration of Cosmic Rays 10
1.4 Propagation in the Galaxy 12
1.5 Motion of cosmic rays in a magnetic field 13
1.5.1 Drift motion induced by magnetic gradients and curvatures 14
1.5.2 The magnetic mirror effect 16
1.5.3 Diffusion by magnetic field irregularities 17
1.6 Measurements for modelling of the CR propagation 19
1.7 Transport equation 20
1.8 Galprop 21
1.9 Solar propagation of Cosmic Rays in Heliosphere 23
1.10 The Sun and the solar activity 23
1.11 Solar wind and heliospheric magnetic field 25
1.12 Cosmic Ray modulation in Heliosphere 27
1.13 Charge-sign dependent modulation 29
1.14 The transport equation of cosmic rays in the Heliosphere . . . 29
1.15 The Force Field approximation 31
1.16 Numerical solution of Parker's transport equation 32
1.17 CR interaction with the Earth's magnetic field and the geomagnetic cut-off 33

2 Search for dark matter with cosmic-ray antiprotons and antideuterons **35**

2.1 Introduction 35
2.2 Astrophysical evidence for dark matter 36
2.3 The dark matter searches 39

2.4 Indirect search for dark matter with astroparticles 40
2.5 DM search through cosmic ray antinuclei 43
2.6 Dark matter searches in cosmic ray antiprotons 44
2.7 Dark matter searches in cosmic ray antideuterons 47
2.8 Antideuteron production from Dark Matter 49
2.9 Antideuteron propagation in the Galaxy 50
2.10 Solar modulation effects for antinuclei 52

3 PAMELA and GAPS experiments 56
3.1 PAMELA experiment 56
3.1.1 The Resurs-DK1 satellite and its orbit 57
3.1.2 The PAMELA apparatus 58
3.1.3 The Time-of-Flight system 59
3.1.4 Anticoincidence system 62
3.1.5 Magnetic spectrometer 63
3.1.6 Electromagnetic calorimeter 65
3.1.7 Shower tail catcher scintillator (S4) 66
3.1.8 Neutron detector 66
3.1.9 Data acquisition 66
3.1.10 Trigger system 68
3.2 The GAPS experiment 70
3.2.1 The GAPS instrument design 70
3.2.2 The Time-of-Flight system 71
3.2.3 Si(Li) tracker 72
3.2.4 GAPS antinucleus identification 73
3.2.5 GAPS trigger configurations 73
3.2.6 GAPS current status 74

4 The proton and deuteron selections on the PAMELA data 77
4.1 Measured quantities for the event selections 78
4.2 Selection of well-reconstructed tracks 78
4.3 Selection of particles with $Z = 1$ 83
4.4 Proton and deuteron identification 84
4.5 Proton and deuteron selections in the Tracker and ToF dE/dX distributions 86
4.6 Additional selections for efficiency and contamination studies . 89
4.7 Division in geomagnetic cut-off slices 91
4.8 The fit procedure for deuterons $1/\beta$ distributions 94
4.8.1 Mean and Sigma determination for the fitting Gaussian functions 95
4.8.2 The double Gaussian fit 103

5 The flux calculation **109**
5.1 Efficiency calculation 110
5.2 Tracking efficiency 110
5.3 Estimation of the selection efficiency in simulation 113
5.3.1 Efficiency of the AC selection (criterion 8) 113
5.3.2 Efficiency of the charge-one selection (criterion 9) . . . 115
5.3.3 Efficiency of the tracker dE/dX selection (criteria 10d, 10p) 117
5.3.4 Efficiency of the ToF dE/dX selection (criterion 11d) . 122
5.4 Unfolding method 123
5.5 Galactic particle selection 129
5.6 Contamination from fragmentation products 130
5.7 Geometrical factor 135
5.8 Live time 138

6 Proton and Deuteron fluxes **141**
6.1 Yearly Fluxes proton and deuteron fluxes 142
6.2 Systematic uncertainties 143
6.3 The deuteron-to-proton flux ratio 145
6.4 Comparison of the deuteron fluxes with numerically modulated spectra 145
6.5 Test on time evolution of the deuteron fluxes 147

7 Identification of cosmic-ray deuterons with the GAPS experiment **152**
7.1 Selection criteria for the incoming particles 153
7.2 Deuteron identification with Bragg peaks in the tracker layers 155
7.3 Selection efficiency 156
7.4 Estimation of the residual proton contamination 160
7.5 The acceptance 161

8 Conclusions **164**

Chapter 1

Hydrogen isotopes in Cosmic Rays and their propagation to the Earth

This first chapter discusses the cosmic-ray propagation through the Galaxy and especially through the Heliosphere, which is the space region surrounding the solar system and permeated by the solar wind and the embedded solar magnetic field. Particular attention is given to the propagation mechanisms and their effects on the two hydrogen isotopic components in cosmic rays, the galactic protons and deuterons, whose low energy (<1 GeV/n) fluxes are studied in this work. In this energy range, the effects of the propagation in the Heliosphere are more significant and therefore a good comprehension of them is needed to interpret correctly the experimental fluxes measured in this work.
After a short initial overview of cosmic ray physics, the propagation issue is approached by studying initially the effect that slow-varying magnetic fields have on the charged particles' trajectories. This insight allows to figure out the mechanisms, that affect cosmic ray propagation in the spatial environments permeated by magnetic fields, such as the Galaxy and the Heliosphere. Later, the modelling of the cosmic ray propagation through the galaxy is treated by looking at the differential equation known as the cosmic ray transport equation. State-of-the-art computational tools are needed to solve numerically this equation, the one used in this work is the GALPROP [1] code. This software allows obtaining the expected energy spectra of any cosmic ray species, in this case, protons and deuterons, just beyond the outer boundaries of the Heliosphere. Then, applying the effects of the propagation through the Heliosphere on these spectra, it is possible to obtain the expected fluxes at the Earth, which can be compared with the measured experimen-

tal fluxes, in order to get information on the cosmic ray solar modulation. Transport in the Heliosphere is discussed starting from the description of the spatial features of the heliospheric environment, to be able to describe the effects that these features have on the cosmic ray fluxes measured at the Earth. A transport equation of cosmic rays in the Heliosphere is studied and a description of a numerical three-dimensional state-of-the-art model is also provided. This model is the one used later in the analysis to reproduce the experimental results for the galactic proton and deuteron fluxes at low energies obtained in this PhD thesis work.
Most of the information in this chapter was obtained by the following sources: [2], [3], [4], [5], [6], [7] and [8] for the cosmic ray physics, propagation in the Galaxy and detection at the Earth, [9], [10], [11] specifically for solar modulation of cosmic rays.

1.1 Cosmic Rays: an overview

Cosmic rays (CRs) are highly energetic charged particles, they are accelerated by powerful astrophysical sources in the universe and propagate isotropically through space at approximately the speed of light. Being electrically charged, cosmic rays interact with stellar and interstellar magnetic fields, which curve their trajectory in a complex way along their paths. This implies that the information about their original direction is lost when they are detected around the Earth, except for very few of them with extreme-high energy ($E > 10^{18}$ eV).
The first evidence of the presence of this charged cosmic radiation was found at the start of the last century with the observations of a spontaneous discharge of the shielded electroscopes. Paramount measurements of the electroscope discharge were performed by Theodor Wulf at the top of the Eiffel tower in 1910, by Domenico Pacini at sea level and underwater from 1910 to 1912 and by Victor Hess and Werner Kolhörster on balloon flights as a function of the atmosphere altitude, respectively in 1912 and from 1913 to 1914. All these measurements were fundamental to demonstrate the cosmic origin of the ionization radiation detected in the electroscopes. In the following years, the use of Geiger-Müller counters in coincidence separated by an absorber before and the introduction of the cloud chambers able to detect the tracks of charged particles after, confirmed the electrical nature of this cosmic radiation. Then in 1932, Carl Anderson detected for the first time in cosmic rays in the atmosphere a positively charged particle with the same physical properties of an electron, today it is known as positron. Later, several other experiments using atmospheric cosmic rays discovered new particles

like the muons (Anderson and Neddermeyer in 1936), the pions (Occhialini and Powell in 1947), the kaons (Rochester and Butler in 1947). However, from 1953 new larger and improved accelerating machines allowed to accelerate particles in a laboratory to a chosen energy at values comparable with the mean energy of cosmic rays at the ground (about 4 GeV); this made the focus of cosmic ray physics move towards new subjects such as the sources and the acceleration mechanisms, the propagation through the Galaxy and the Heliosphere and the search for indirect signals of new physics like dark matter.

Over the years, new more performing charged particle detectors have been developed, allowing to design new precise experiments able to measure CRs with different detecting strategies. Among the latter, two major categories can be identified: direct detection and indirect detection.

The direct measurements allow detecting the cosmic radiation and its properties before any interaction with the Earth's atmosphere. This type of detection employs detectors placed on board aerostatic balloons or spacecrafts at an altitude from tens to hundreds of kilometers. Some of the major recent experiments of direct detection have been ATIC [12], BESS [13], HEAT [14], CAPRICE [15] (on a balloon), PAMELA [16], FERMI [17], DAMPE [18](on satellite), and AMS-02 [19] and CALET [20](on the International Space Station). With direct detection, it is feasible to perform measurements of the abundance and composition of CRs, but the limited size of the in-flight detectors reduces the reachable energy range and the collectible statistics. Nowadays, experiments based on a spectrometer can reach the TeV energy limit, whereas detectors based on calorimeters can reach energies of O(100) TeV.

The cosmic ray detection at energies of the order of 10^{14} eV and more adopts indirect detection techniques, which exploit the Earth's atmosphere as a big calorimeter and measure the properties of the particle showers generated by the interactions of CRs with atoms and molecules of the atmosphere. The studied shower features are generally the shower shape and the particle multiplicity, which can be used to estimate the energy and the direction of the primary particle at the top of the atmosphere. Experiments of indirect detection can be composed by arrays of particle detectors at the ground (AGASA [22], TA [23], Auger [24]), big telescopes at ground measuring the fluorescence light in the sky (HiRes [25] and Auger), emitted by air molecules excited by the charged particles, Imaging Cherenkov Telescopes (MAGIC [26], VERITAS [27] and HESS [28]) looking for Cherenkov ultraviolet light emitted by the relativistic particles of the generated shower in the atmosphere in a small cone along their direction.

Figure 1.1 shows the CR differential energy spectrum measured at Earth,

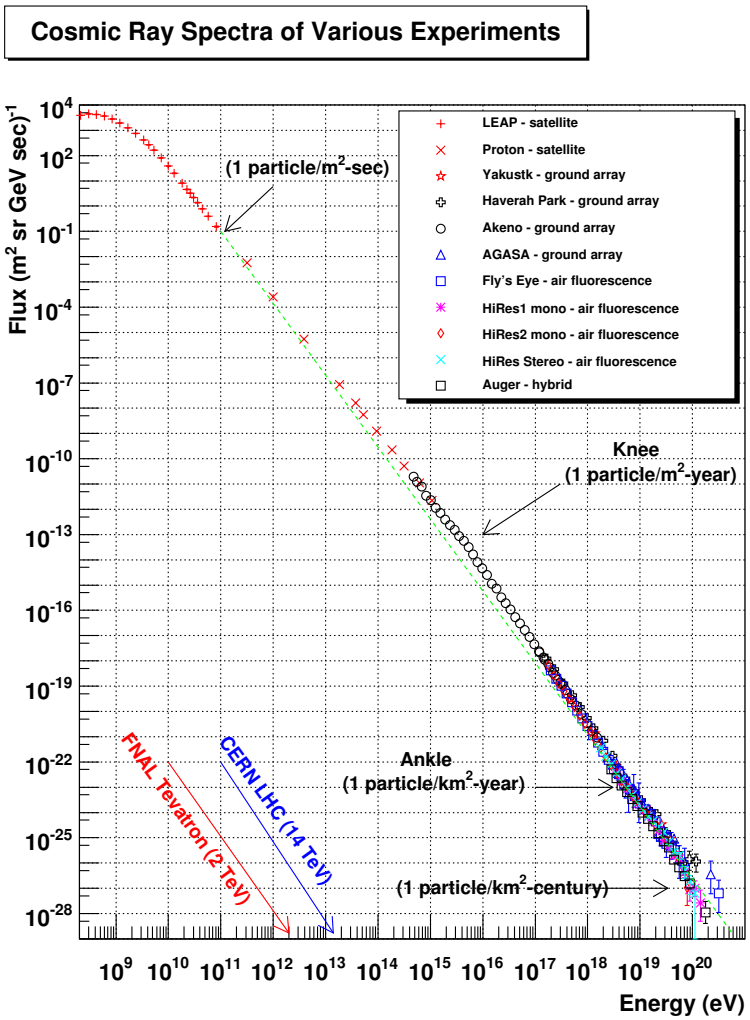

Figure 1.1: Differential energy spectrum of cosmic rays. Data from different kind of experiments are shown in the plots. Credit to [21].

which is the number of detected particles over units of area, solid angle, energy and time. It spans more than 20 orders of magnitude in flux and 10 in energy. Its shape is approximately described by a power law:

$$\frac{dN}{dE} \propto E^{-\gamma} \tag{1.1}$$

where dN is the number of particles per energy interval dE, and γ is a spectral index which varies slightly value for different energy ranges:

- $\gamma \simeq 2.7$ in the first part of the spectrum, approximatively from 1 GeV to 3 PeV;
- $\gamma \simeq 3$ above 3 PeV, from here the spectrum gets steeper, this energy region of slope change is commonly known as the knee;
- γ returns equal to 2.7 again above 3 Ee, this other region is known as the ankle.

This spectrum is supposed to be the result of a combination of several processes of acceleration and propagation within the Galaxy, which affect the cosmic radiation before reaching our planet. According to their energy, cosmic rays are classified in galactic for $E < 10^{15}$ and extragalactic beyond. Indeed, the knee region is believed to be the highest energy achievable by charged particles accelerated by galactic sources and the observed spectrum steepening is explained as a convolution of the cut-offs in the spectra of the individual nuclear components, until an extragalactic component takes over above the ankle. At the highest energies, above about $5 \cdot 10^{19}$ eV, extragalactic cosmic rays are expected to be suppressed by the interaction with the cosmic microwave background radiation. This theoretical upper limit called GZK cutoff seems to have been observed in the measurements of Auger and HiRes experiments, but still uncertainties remain in their interpretation of the experimental results and further work is needed. Besides, since the acceleration limit of the known celestial objects is or the order of 10^{20} eV, the spectral suppression can be also due to an acceleration limit of the sources.
On the other side, at low energies below a few tens of GeV, the CR spectrum in Figure 1.1 is characterized by a downturn, which is a lower limit relative to the power-law observed to the higher energies. This feature is generated by the effect of the solar activity, which causes in this energy region a measurable decrease of the cosmic ray intensity with respect to outside the Heliosphere, but also a time dependence of the measured fluxes. This phenomenon is called solar modulation.
A useful quantity in cosmic ray studies is the magnetic rigidity R. This quantity is defined in the following way:

$$R = \frac{pc}{Ze} = rBc \tag{1.2}$$

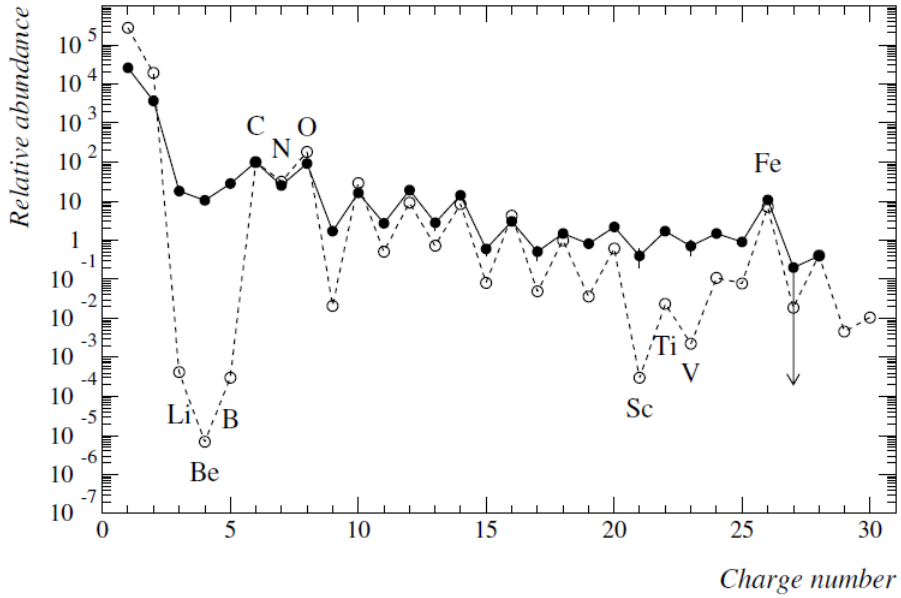

Figure 1.2: Elements abundance in cosmic rays and in the solar system. Credit to [2]

It is particularly useful in CR propagation analyses, because it links the curvature radius r of the followed trajectory through a magnetic field B, with its linear momentum p and the electrical charge Ze. Generally, the natural units are adopted to discard both the speed of light in vacuum c and the elementary charge e, in this way $c = 1$, $e = 1$. Cosmic radiation is mainly composed of protons (85%), helium nuclei (12%), electrons (2%) and other light nuclei. According to the mechanisms at the base of their production, the cosmic rays components are generally classified as primary and secondary particles. Primary cosmic rays are accelerated by astrophysical sources, whereas the secondary cosmic rays are the particles produced by collisions or interactions of the primary particles with the Interstellar Medium (ISM) during the propagation through the Galaxy. Figure 1.2 shows the element abundance in cosmic radiation compared with the chemical composition of the Solar System, obtained from the study of the absorption lines in the Sun photosphere and from the composition of meteorites. Both distributions peak for the three groups of elements, H and He, C, N and O, Fe. Moreover, the nuclei with even atomic number Z are more abundant than those with odd Z, because of the larger binding energy, which favours them during the production mechanisms. The two distributions differ for the abundance of the following distributions: Li, Be, B and Sc, Ti, V, Cr, M. The nuclei of these

elements are less abundant in the stellar nucleosynthesis than in cosmic rays, they are produced in nuclear processes such as spallation of primary CRs on nuclei of atoms and molecules composing the ISM:

$$A + p \rightarrow X + Y \tag{1.3}$$

where a nucleus A collides with a proton forming the two nuclei X and Y. Antiparticles can also be generated as a product of these interactions, in particular antiprotons and positrons. Until now the experimental data have shown that the antiparticle component in CRs has a secondary nature, however, a primary nature from exotic physics can not be excluded.
With regards to the isotopic abundances instead, they have also become available for some species present in CRs, thanks to the improved instrumentations employed in recent years.

1.2 Isotopic abundances in Cosmic Rays

The most common isotopes found in cosmic radiation correspond to those in the Solar System and the interstellar medium, but in some cases, a significantly greater abundance of rare isotopes have been found in the CRs.
The lightest stable isotopes, which are ^1H, ^2H, ^3He, ^4He, are a privileged study sample because their isotopic abundances are much greater than those of all the other elements. Comparing abundances of these light isotopes in CRs with the corresponding ones in ISM, it was found that the ^2H and ^3He are significantly more abundant in the cosmic radiation, suggesting that they mostly result from the interaction of proton and ^4He with ISM. Indeed, since their abundances are too much greater than the heavier elements, the spallation products of carbon, oxygen and nitrogen can contribute very little to the isotopic abundances of hydrogen and helium. The advantage of the light isotopes ^2H and ^3He in this context compared to the more heavy secondary particles lies in the fact that they do not have so many progenitors compared to the sub-iron particles or to lithium, beryllium and boron, it is predominantly ^4He [29]. In the next section the hydrogen isotopes, the focus of this thesis, are examined in depth. Regarding the heavier isotopes instead, some of these created in spallation reactions are radioactive, if the production rate of the isotopes for a given element is known, information can be obtained about the time needed for these particles to reach the Earth from their sources. The most common of these "cosmic radioactive clocks" is the ^{10}Be, which has a radioactive half-life time of around $1.5 \cdot 10^6$ year, which is similar to the escape time of the CRs from the Galaxy. For this reason,

the ^{10}Be turns out to be a useful discriminant for the study of the typical lifetime of spallation products in the Earth vicinity.

1.2.1 Protons and Deuterons in Cosmic Rays

Protons and deuterons are the main hydrogen isotopes present in cosmic radiation. Since tritons, which are the unstable nuclei of tritium (^3H), have a half time of around 12 years, which is much shorter than the confinement time of CRs in the Galaxy.
Protons are the major component in cosmic radiation and have a mainly primary origin. The deuterons are instead much less abundant in cosmic rays, they account for only a few percent (around 3%) of the overall hydrogen signal, and they are of secondary origin. In fact, deuterium nuclei are destroyed rather than created during the stellar nucleosynthesis, thus no significant amount of primary deuterons can be ejected by astrophysical sources in the Galaxy. Instead, deuterons are produced by spallation reactions of primary cosmic rays with the interstellar medium (ISM), so that their fluxes are the result of the combination of the production cross section and measured fluxes of primary CRs. In principle, all nuclei must be considered but ISM and CRs are mainly made up of ^1H and ^4He nuclei, making reactions involving these species dominant. The main production channel is the spallation process of ^4He nuclei on a proton: $^4He + p \rightarrow {}^2H + {}^3He$. Actually, two different production mechanisms in this reaction can be considered, the break-up and the stripping [29]. In the former case, the helium nucleus breaks up leading to the coalescence of free nucleons into a deuteron, while in the latter case the incident proton tears a neutron off the helium nucleus. The cross sections of both the reactions and the sum of these two are shown along with experimental in Figure 1.3 left.
Similar reactions occur with the ^3He nuclei as well, with values of deuteron production cross section similar to that involving ^4He (see Figure 1.3 right). However, ^3He is less abundant in CRs, its flux is about 20% of the ^4He one up to 1 GeV/nucleon and then decreases at higher energies, therefore it is expected to contribute the same fraction at GeV/nucleon to the deuteron production and then to become negligible above 10 GeV/nucleon.
Another significant contribution to the deuteron production comes from the proton fusion process: $p + p \rightarrow {}^2H + \pi$. This makes the deuteron to be one of the few particles together with antiprotons, positrons and electrons that can be produced by proton propagation in the ISM. As shown in Figure 1.3 right, the cross section of this reaction is non-vanishing for only a very narrow energy range and has its maximum for incident protons with a kinetic energy of 0.6 GeV. Even though its values are 10 times smaller than those involving

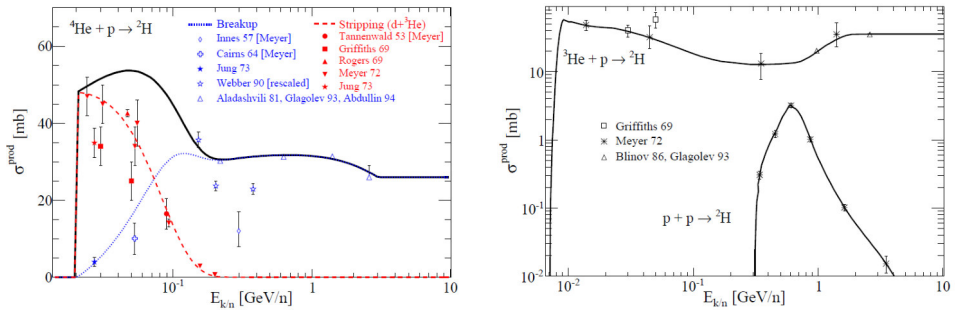

Figure 1.3: Left: inclusive production cross section of ^2H in the $^4He + H$ reaction, The data are from Tannenwald (1953); Innes (1957); Cairns et al. (1964); Rogers et al. (1969); Griffiths & Harbison (1969); Meyer (1972); Jung et al. (1973a); Aladashvill et al. (1981); Webber (1990b); Glagolev et al. (1993); Abdullin et al. (1994). Credit to [29]. Right: ^2H other production channels from the less abundant ^3He and the peaked fusion pp reaction. The data are from Griffiths & Harbison (1969); Meyer (1972); Blinov et al. (1986); Glagolev et al.(1993). Credit to [29].

He nuclei, protons are more abundant than ^4He with about a factor of 10 in the cosmic radiation, for this reason, the proton fusion reaction provides a significant contribution slightly below 1 GeV/nucleon.

For the contribution of heavier species to the deuteron production, their decreasing abundance in CR is balanced by higher cross sections. Several studies found that C, N and O nuclei in CRs (CNO_{CR}) interacting with hydrogen nuclei of the interstellar medium (H_{ISM}) can contribute up to 30% of the ^2H flux above a few GeV/nucleon. On the other side, the reverse reaction $H_{CR} + CNO_{ISM}$ produces mostly fragments at lower energies, making them irrelevant for CR studies for energies $>$ 100 MeV/nucleon.

A proper contribution of the fractional contribution to the ^2H production was calculate in [29]. Until only now a few experimental data exist because of the difficulties to implement a precise isotopic separation from the large background of protons.

From the 1970s to the 1990s several measurements of hydrogen isotopes in cosmic rays were carried out by balloon experiments with a magnetic spectrometer. However, these experiments flew under a few g/cm^2 of residual atmosphere, which was the source of a non-negligible source of secondary deuterons produced by the interaction of CR with air nuclei. Then, the atmospheric background had to be estimated and subtracted from the measured deuteron flux. However, this correction suffered by large uncertainties, because of the limited knowledge of the deuteron production cross section.

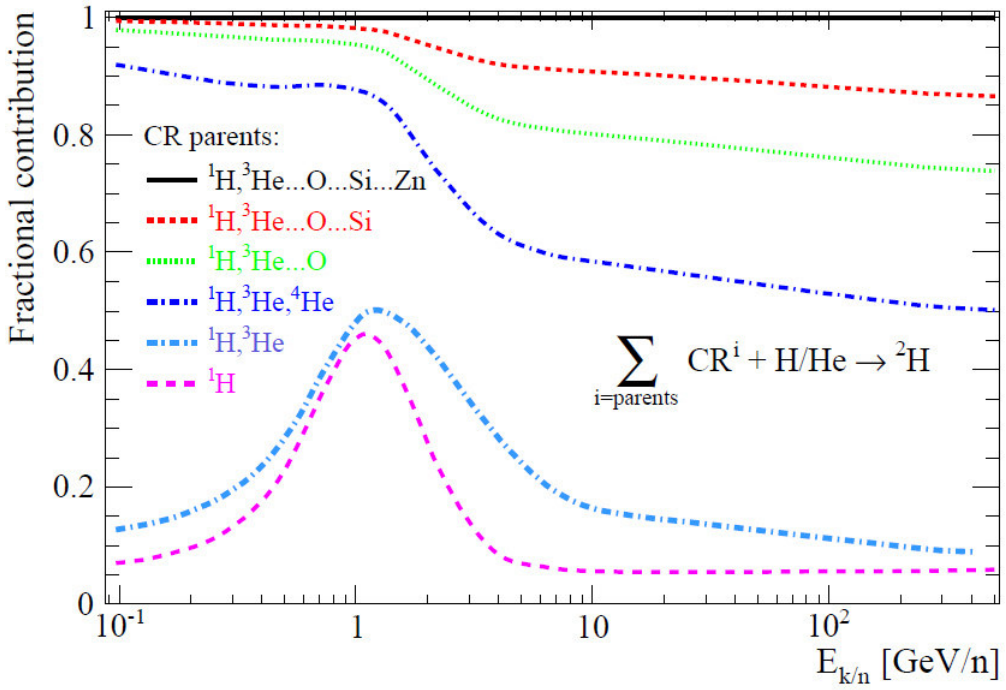

Figure 1.4: Fractional contributions to the propagated ^2H fluxes as a function of the kinetic energy over nucleon. Credit to [29].

The results obtained by the PAMELA collaboration for the time between July 2006 and December 2007 (see Figure 1.5), were free of this systematic error because taken outside of the Earth's atmosphere [30]. In this work a further step was performed, CR proton and deuteron annual fluxes have been measured over a period of nine years using the PAMELA data.

1.3 Origin and acceleration of Cosmic Rays

The nature of the accelerating sources of cosmic rays is still a matter of study. Being CRs electrically charged particles, their trajectory is bent by the interstellar magnetic fields during their voyage through the galaxy, therefore when they are detected at Earth, it is not possible to trace them back to their sources. Besides, the cosmic-ray energy spectrum is approximately described by a power law up to 10^{15} eV, the knee region. This suggests that cosmic ray acceleration is governed by the same mechanism over orders of magnitudes energy inside our Galaxy, while the same or another should work at higher energies outside the Galaxy. The Sun and the other stars are known to eject

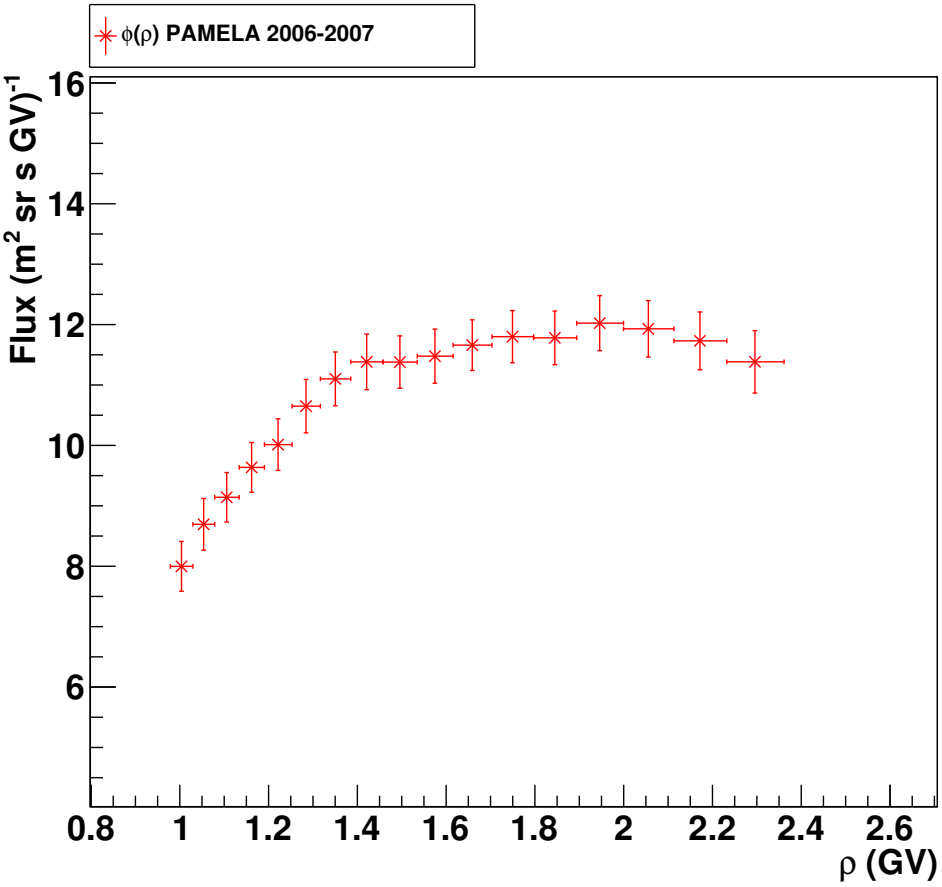

Figure 1.5: Deuteron flux measured by PAMELA in the time period 2006-2007 as a function of rigidity ρ and published in [30].

low-energy charged particles up to a few GeVs, but their production rate is too low to account for the observed cosmic ray fluxes. The most accredited sources of cosmic-ray acceleration are believed to be SuperNovae explosions and subsequent remnants (SNRs) together with other powerful astrophysical sources like pulsars, AGNs. Observations of the electromagnetic emissions in the X-ray and γ-ray bands from these objects point to the presence of energetic particles, indicating efficient acceleration processes near these objects. Besides, the rate and the released energy of SuperNovae are capable to account for the energy density of cosmic rays measured at Earth. After the SN explosions, the formed clouds of gas and magnetic fields expand for thousands of years and can entrap and accelerate in a multiple collision mechanism charged particles. Two efficient acceleration mechanisms were proposed to account for the cosmic ray energies up to 10^15 eV and are still in

use, they are called the Fermi-acceleration mechanisms. Two types of Fermi acceleration are formulated:

- The first-order Fermi acceleration takes place at the source when a particle collides with strong shock waves, like those of SN and AGN. These shock waves reach supersonic velocities and move magnetic turbulent inhomogeneities both behind and in front of it. The charged particle encountering these shock waves are bounced back and forward repeatedly, increasing their energy at every collision with the shock. It is possible to demonstrate that the average energy gain is given by $\left\langle \frac{\Delta E}{E} \right\rangle = \frac{4}{3}\beta$, that makes the acceleration process very efficient. Particles undergoing this acceleration mechanism follow an energy spectrum with spectral index $\gamma \sim 2$, which is close to 2.7 which is the spectral index of cosmic rays after the propagation. The SNR is the ideal place where cosmic rays bouncing back and forth can gain energy in the magnetic field of the SNR. When these particles earned enough high energy in this stochastic process, they are too fast to be still entrapped in the magnetic fields of the SNR and they can escape into outer space becoming cosmic rays.

- The second-order Fermi acceleration takes place during the cosmic ray propagation and is also called reacceleration. This mechanism describes the energy gain of charged particles during their motion in presence of randomly moving magnetic mirrors. However, this mechanism is less efficient than the one before, because the particle earns energy only when the magnetic mirror is moving towards it, whereas it loses energy when the magnetic mirror is receding. Since in a random motion the probability of head-on collision is greater than head-tail one, on average the particle is accelerated, with ana average energy gain following $\left\langle \frac{\Delta E}{E} \right\rangle = \frac{4}{3}\beta^2$. This mechanism can take place in SNRs and in other space regions with the presence of magnetic clouds.

1.4 Propagation in the Galaxy

After the acceleration at the source, cosmic rays escape into outer space and voyage for tens of millions of years through the Galaxy, here they undergo continuous interactions with the interstellar medium and magnetic fields. Consequently, cosmic rays do not travel linearly but follow spiral trajectories along the galactic magnetic field lines with a gyroradius proportional to their rigidity. Besides, the irregularities in the interstellar magnetic fields scatter

the charged astroparticles over random directions in a diffusive process similar to a random walk. The interaction with ISM along their path makes cosmic rays lose energy through ionization and Coulomb interactions or fragmented in inelastic scattering processes. In the latter, the primary particles are destroyed via interactions giving rise to secondary particles, which are usually unstable (anti)nuclei or (anti)leptons generating often decay chains and γ-ray emissions. As a result of all these interactions, the shape and composition of the starting spectrum change.

1.5 Motion of cosmic rays in a magnetic field

Along their paths through the Galaxy, cosmic rays interact with stellar and interstellar magnetic fields. From this encounter, the charged particles undergo a Lorentz Force $\vec{F}$, orthogonal to the direction of their velocity and of the magnetic field:

$$\vec{F} = q\vec{v} \times \vec{B}. \tag{1.4}$$

Since this force is always perpendicular to the motion direction, the kinetic energy of the particle remains constant.
In the following, the dynamics of charged particles in presence of magnetic fields will be described to review the main mechanisms that affect the propagation of cosmic rays in magnetic environments, such as the Milky Way Galaxy and the Heliosphere.
Considering the simple case of a uniform static magnetic field, the particle velocity vector can be decomposed into two components, one parallel and one perpendicular to the magnetic field direction:

$$\vec{v} = v_{\parallel}\vec{b} + \vec{v}_{\perp} \quad , \tag{1.5}$$

with $\vec{b} = \frac{\vec{B}}{B}$ the versor in the magnetic field direction. The angle θ between the vectors $\vec{v}$ and $\vec{B}$ is called pitch angle and can be worked out simply as $\theta = \tan\left(\frac{v_{\parallel}}{v_{\perp}}\right)$. Comparing 1.4 and 1.5, it is easy to note that $v_{\parallel}$ does not play a role in the Lorentz force calculation and remains constant, whereas $\vec{v}_{\perp}$ interacts with $\vec{B}$ to lead to a circular motion:

$$Zev_{\perp}B = \frac{\gamma m v_{\perp}^2}{r} \tag{1.6}$$

from wich, remembering the definition of magnetic rigidity (Equation 1.2), one can simply derive

$$r = \frac{p_{\perp}c}{Ze}\frac{1}{Bc} = \frac{\rho}{Bc} \quad , \tag{1.7}$$

In these equations, Ze, m, $p_\perp$ and ρ are respectively the electric charge, the mass, the orthogonal momentum and the rigidity of the particle, whereas the position r is commonly called gyration radius or Larmor radius. From 1.6 it is also possible to calculate the angular frequency of this gyration, called cyclotron frequency ω_c:

$$\omega_c = \frac{v_\perp}{r} = \frac{ZeB}{\gamma m}, \tag{1.8}$$

From Equation 1.7 it can be noticed that particle motion is ruled by the rigidity variable: particles with different mass and electric charge, but same rigidity and pitch angle into the same magnetic field configuration have the same dynamical behaviour.
At this point, for convenience, the particle position is described in terms of a guiding centre position $\vec{R}$ that moves with velocity $v_\parallel \vec{b}$ along a magnetic field line and a gyrorotating radius $\vec{r}$:

$$\vec{x} = \vec{R} + \vec{r}, \tag{1.9}$$

The resulting particle trajectory is a helix, which is the sum of a guiding centre motion with constant velocity and a circular motion with radius $\vec{r}$ from the magnetic field line. In this configuration of uniform static magnetic field, during the spiral motion the pitch angle θ remains constant. This is no longer true in presence of magnetic instabilities and irregularities.

1.5.1 Drift motion induced by magnetic gradients and curvatures

Now a more complex situation is considered: a constant force $\vec{F}$ acting on the particle is added. The motion Equation 1.4 becomes:

$$m\vec{a} = q\vec{v} \times \vec{B} + \vec{F}, \tag{1.10}$$

Using the guiding center reference frame, one can calculate the velocity of the guiding centre $\vec{v}_g = \dot{\vec{R}}$ and obtain:

$$\vec{v}_g = v_\parallel \vec{b} + \frac{\vec{F} \times \vec{B}}{qB^2}. \tag{1.11}$$

It follows that any force with a component perpendicular to $\vec{B}$ provokes a drift motion of the particle orthogonal to both $\vec{F}$ and $\vec{B}$. This drift turns out to be a periodic variation of the gyroradius: when a particle accelerates in a force field, the gyroradius increases, when the particle slows down its

gyroradius decreases.
On the other hand, the $\vec{F}$ component parallel to $\vec{B}$ induces a parallel acceleration according to Equation 1.10:

$$\frac{dv_{g\|}}{dt} = \frac{F_\|}{m} \tag{1.12}$$

A more realistic configuration includes a spatially varying magnetic fields. Equations 1.10, 1.11 and 1.12 obtained for a force can still be applied if the variation of $\vec{B}$ along one gyroration of the particle is small. First, the case of a curved magnetic field is considered. The field curvature is defined as $\nabla_\|\vec{b} = -\frac{\vec{R}_c}{R_c^2}$ and it is a vector perpendicular to $\vec{B}$. $\vec{R}_c$ is the curvature radius of the magnetic field and $\nabla_\| \equiv \vec{b}\cdot\vec{\nabla}$ the gradient along the $\vec{B}$ direction. A particle moving along a curved magnetic field line, experiences a centrifugal force with velocity:

$$\vec{F_c} = m v_\|^2 \, \frac{\vec{R}_c}{R_c^2} \tag{1.13}$$

which induces a drift motion:

$$\vec{v_c} = \frac{m v_\|^2}{qB^2} \, \vec{B} \times \nabla_\|\vec{b}, \tag{1.14}$$

Also in the case of a magnetic field with a transverse gradient, a drift motion is induced. The particle orbit must have a smaller radius of curvature on the orbit part where the magnetic field is stronger, a larger radius of curvature where B is weaker. This leads to a drift motion orthogonal to both the magnetic field and its gradient directions. However, the force induced by the magnetic field gradient is not constant, therefore we can not use Equation 1.10. Instead of it, the average effect of $\vec{\nabla}B$ on the gyro-orbit of the charged particle can be calculated by considering its current $I = \frac{q\omega_c}{2\pi}$ associated. The magnetic moment is defined as the product of the current I and the area A surrounded by it, $\mu = I \cdot A$, where the area is simply $A = \pi r^2$. Thus, redefining μ as the magnetic moment per unit of particle mass, one obtains

$$\mu = \frac{(\pi r^2)}{m}\frac{q\omega}{2\pi} = \frac{r^2}{m}\frac{q^2 B}{2m} = \frac{v_\perp^2}{2B} \quad , \tag{1.15}$$

The gyro-averaged force equals the force on a magnetic dipole in a magnetic field gradient:

$$\vec{F}_{\nabla B} = -m\mu\vec{\nabla}B, \tag{1.16}$$

now applying Equation 1.11 to this force it follows that:

$$v_{\nabla B} = \frac{m v_\perp^2}{2qB^3}\vec{B}\times\vec{\nabla}B \tag{1.17}$$

Curvature and gradient drifts are often comparable. In a plasma in equilibrium $\vec{\nabla} \times \vec{B} \parallel \vec{B}$ is approximately true. This implies a relation between the curvature vector and the gradient $\vec{\nabla} B$:

$$\nabla_{\parallel} \vec{b} = \frac{\vec{\nabla} B}{B} \tag{1.18}$$

At this point we can sum the two drift motions from magnetic curvature and gradient and obtain:

$$v_c + v_{\nabla B} = \frac{m}{qB^3} \left(v_{\parallel}^2 + \frac{1}{2} v_{\perp}^2 \right) \vec{B} \times \vec{\nabla} B, \tag{1.19}$$

These concepts of drift motions induced by magnetic curvature and gradients will be useful to understand later the drift effects on cosmic rays propagation in the Heliosphere induced by the solar magnetic field.

1.5.2 The magnetic mirror effect

The invariance of μ can also be used to explain the magnetic mirror effect as well. This phenomenon occurs when the charged particle moves towards a space region with a stronger magnetic field. This is the case when the magnetic field lines met by a gyro-rotating particle are converging and the resulting Lorentz force has an averaged component opposite to ∇B. This mirror force is parallel to $\vec{B}$ and is precisely the force on a magnetic dipole μ in a gradient $\nabla_{\parallel} B$. Using Equation 1.12 this force provokes a parallel deceleration

$$\dot{v_{\parallel}} = -\mu \nabla_{\parallel} B \tag{1.20}$$

The particle experiences a magnetic field change $\dot{B} = v_{\parallel} \nabla_{\parallel} B$. Now we can use the conservation of energy $E = 1/2 v_{\perp}^2 + \frac{1}{2} v_{\parallel}^2$ and the conservation of the magnetic moment. The change of the parallel velocity of the particle in a (spatially or temporary) varying magnetic field can be easily derived from the invariance of μ and E:

$$v_{\parallel} B = \pm \sqrt{2(E - \mu B)} \tag{1.21}$$

The reflection of the particle on a magnetic mirror occurs for $v_{\parallel} = 0$ in the space region with higher magnetic field intensity, so that:

$$E = \frac{1}{2} v_{\parallel,0}^2 + \mu B_{min} \leq \mu B_{max} \tag{1.22}$$

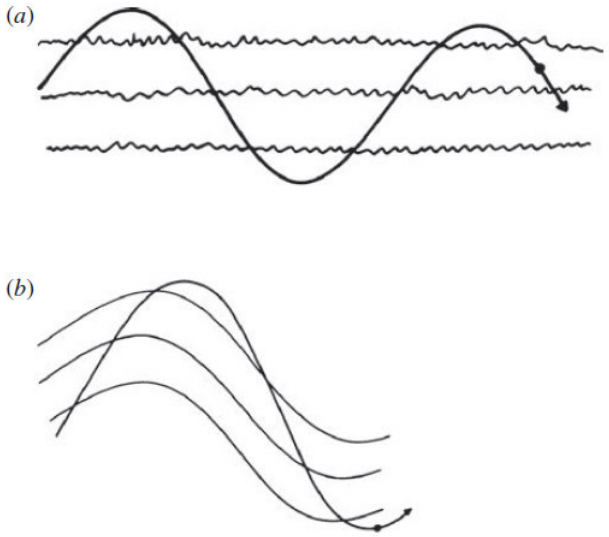

Figure 1.6: Dynamics of a charged particle in a magnetic field, (a) when the irregularities in the magnetic field are on a scale much smaller than the gyroradius of the particle's orbit; (b) when they are of the same order of magnitude. Credit to [2].

Where $v_{\parallel,0}$ is the parallel velocity in the low field region. Dividing by $\mu B_{min} = \frac{1}{2}v_{\perp,0}^2$, we get

$$\frac{v_{\parallel,0}}{v_{\perp,0}} \leq \sqrt{\frac{B_{max}}{B_{min}} - 1}, \tag{1.23}$$

This is the basis of the Fermi acceleration principle of cosmic radiation.

1.5.3 Diffusion by magnetic field irregularities

The interstellar magnetic fields are characterised by irregularities, which can induce the pitch angle scattering in cosmic rays travelling in the Galaxy. This phenomenon takes place when the gyroradius of the propagating charged particle is smaller or at the same order of the scale of fluctuations in the magnetic field as in Figure 1.6(b), whereas if the particle has got a gyroradius much greater than the scale of the fluctuations, as in Figure 1.6(a), it keeps propagating unperturbed along the mean magnetic field direction.

The magnitude of the magnetic irregularities as a function of a physical scale can be described applying the Parseval's theorem to find the power

spectrum of the fluctuations in the magnetic field:

$$\int_{-\infty}^{+\infty} B^2(t)dt = \int_{-\infty}^{+\infty} B^2(\omega)d\omega \tag{1.24}$$

where $B(\omega)$ is the Fourier transform of the measured magnetic flux density as a function of time, $B(t)$. The power spectrum $B^2(\omega)$ of the fluctuations in the magnetic field provides information about how much energy there is in each Fourier transform. Direct measurements of interplanetary magnetic fluctuations were made by the Mariner 4 space probe which went on to take the first pictures of the Martian surface, finding that most of the power is in fluctuations on the scale of about 10^9 m.
The model of the diffusion process is based on the assumptions that the magnetic irregularities are random and that the charged particle feels the effect of a particular component of the power spectrum for about a wavelength, before meeting another wave with a random phase to the previous one. In a singular wavelength λ, the average inclination of the magnetic line with the respect to the mean-field direction is

$$\phi \sim \frac{B_1}{B_0} \quad , \tag{1.25}$$

where B_1 is the amplitude of the random component and B_0 is the mean magnetic field density. Therefore, particles with a gyroradius $r \approx \lambda$, have a change in pitch angle of about ϕ, whereas the guiding center is displaced by a distance $d \approx \phi \cdot r$. In the next wavelength, the particle is affected by another fluctuation of roughly the same energy density which changes the particle pitch angle randomly with respect to the previous wave. Thus, the random superposition of all the fluctuations in the interstellar magnetic fields leads to stochastic pitch angle changes according to a uniform distribution and a diffusion process for cosmic-ray propagation across the magnetic field lines.
To be scattered randomly through 1 rad, the particle has to be scattered N times, where $N^{1/2}\phi = 1$. Thus, the distance to be scattered through 1 rad is

$$\lambda_{sc} \approx N \cdot \lambda \approx N \cdot r \approx r \cdot \phi^{-2} \quad , \tag{1.26}$$

which is effectively the mean free path for pitch angle scattering of a particle diffusing along the magnetic field. At this distance, the pitch angle has been changed by a large factor and the particle has lost all memory of its initial pitch angle. This mechanism converts streaming motion into a random distribution of pitch angles over a distance λ_{sc}. This concept was successfully included in the modelling of the cosmic ray propagation in the Heliosphere, thanks to measurements of magnetic field irregularities inside

the Heliosphere. Similar considerations can be applied to the diffusion of particles in the interstellar medium, although information about the spectrum of fluctuations on the relevant scales is not available.

1.6 Measurements for modelling of the CR propagation

The study of the spectra of the large variety of species and isotopes in cosmic radiation has provided important information about the propagation of cosmic rays in the Milky Way Galaxy. Secondary stable particles, long-lived radioactive nuclei, K-capture isotopes and the lepton component in the CR are analysed for this purpose because each of them can deliver different information about the several propagation mechanisms through the Galaxy. In particular, the secondary stable nuclei bring information about the diffusion process, the convection induced by galactic winds and the re-acceleration in the interstellar medium through a 2nd Fermi-like acceleration mechanism. On the other hand, the long-lived radioactive nuclei are extremely useful to constrain the global size of the galactic halo, while the abundance of the K-capture isotopes, which are nuclei decaying via electron capture from the ISM, allows probing the gas density and the acceleration time scale. The lepton component, mainly electrons and positrons, undergo instead heavy energy losses along its path, thus they provide information about the vicinity of the solar system.
However, all this information comes from CR measurements taken only at a particular point on the outskirts of the Galaxy, the solar system, and the assumption that galactic particle spectra and composition are almost the same over the whole Galaxy is not necessarily correct. To overcome this issue, the study of the diffuse γ -ray continuum emission can help as well, indeed it delivers information directly from distant regions integrated over the line of view, resulting to be complementary to the information coming from nearby cosmic ray measurements. The diffuse γ-ray continuum emission is produced by three different mechanisms linked to interactions of CR: the inverse Compton scattering of energetic CR leptons on the photons of the interstellar radiation field (ISRF), Bremsstrahlung of highly energetic charged particles within the interstellar medium, decay of neutral pions produced in the interactions of the energetic nuclei with the interstellar gas. These three processes are dominant in different parts of the γ-rays spectrum, therefore deciphering them can provide information about the large-scale spectra of nucleonic and leptonic components of cosmic rays. The combined information

coming from the current precise measurement of cosmic rays and diffusive γ-ray continuum emissions have allowed developing sophisticated models of astroparticle production and propagation in the Milky Way Galaxy.

1.7 Transport equation

Taking into account the several mechanisms of cosmic ray propagation in the galactic environment, a general diffusive transport equation for the different intensity N_i of a single cosmic ray species (labelled i) can be written as:

$$\frac{\partial N_i}{\partial t} = Q_i + \nabla\cdot(D_{xx}\nabla N_i - \vec{u}N_i) + \frac{\partial}{\partial p}\left[p^2 D_{pp}\frac{\partial}{\partial p}\frac{N_i}{P^2} + \frac{p}{3}(\nabla\cdot\vec{u})N_i - \dot{p}N_i\right] - \frac{N_i}{\tau_c}, \tag{1.27}$$

where on the left there is the time derivative of the N_i is the i-type particle density per unit of total momentum p, at position x and time t. On the right various term take into account the different processes, which are spatial diffusion, convection, reacceleration and adiabatic losses:

- source term $Q_i\,(x,p,t)$ describes the acceleration of i-type particles per cm^3, time t and momentum included in $[p, p+\delta p]$ in a given x position in the Galaxy. It can be made explicit in the following from:

$$Q_i = S_i + \sum_{j\geq i}[N_j v_j n_{gas}\sigma_{j\to i}] + \sum_{k\geq i}\frac{1}{\tau_{k\to i}}N_k, \tag{1.28}$$

  with S_i accounting for sources of primary CRs, such as SNRs. The second term includes the secondary CR sources with the spallation phaenomena in the ISM, where N_j is the j-type particle density with velocity v_j and n_gas the gas density in space and $\sigma_{j\to i}$ the partial cross section for j-type particles becoming i-type particles. The third term conveys the the contribution to i-type particles from radioactive decay of particles of k species.

- The term $\nabla\cdot(D_{xx}\nabla N_i)$ describes the spatial diffusion of cosmic rays scattering on the galactic magnetic field, which leads to a random walk in space. D_{xx} is a spatial diffusion coefficient, whose value and rigidity dependence are determined by the mean value of the galactic magnetic field.

- $\nabla\cdot\vec{u}N_i$ represents the convection term, where $\vec{u}$ is the velocity of galactic or stellar winds which act the spatial convection phaenomena on travelling charged particles,

- $\frac{\partial}{\partial p}\left[p^2 D_{pp}\frac{\partial}{\partial p}\frac{N_i}{p^2}\right]$ represents the reacceleration term, which accounts for scattering of CRs on randomly moving plasma waves (2nd order Fermi acceleration). It leads to stochastic acceleration, which is described in the transport equation as a diffusion process in momentum space with diffusion coefficient D_{pp}.

- $\frac{\partial}{\partial p}\frac{p}{3(}\left(\nabla\cdot\vec{u}\right)N_i$ is the term which accounts for the adiabatic energy loss, due do the expansion of the volume including the travelling CRs,

- $-\frac{\partial}{\partial p}\left(\dot{p}N_i\right)$ term describes the energy loss of the particles involved in ionization processes of atoms in the ISM, or for the leptons by processes of Bremsstrahlung, inverse Compton effect or synchrotron radiation,

- $\frac{N_i}{\tau_c}$ term accounts of the particle losses due to the fragmentation or decay events. The coefficient $\frac{1}{\tau_c}=\frac{1}{\tau_f}+\frac{1}{\tau_r}$ describes both the characteristic time for loss by fragmentation τ_f and the time scale for nuclear decay τ_r .

This transport equation can be solved numerically to get the cosmic ray fluxes of the various nuclear species of CRs in a specific place in the Milky Way. However, this equation does not take into account the effects of the solar modulation inside the Heliosphere, therefore this equation is useful to obtain the so-called Local Interstellar Spectrum, which is the CR energy spectrum just outside the heliospheric boundaries. The obtained fluxes have associated theoretical uncertainties. These uncertainties come from the propagation parameters, which are not directly measured, but extrapolated by comparing the numerically calculated results with secondary-to-primary nuclei ratios, which are very sensitive to their variations.

1.8 Galprop

In this research work, a CR deuteron LIS was obtained by running the GALPROP code [1]. This software can be considered the current state-of-the-art numerical code for the calculation of the CR propagation and the related galactic diffuse γ-ray continuous emission. The first version of the Galprop code was written in Fortran in the mid-1990s by a collaboration financed by NASA led by Andrew Strong and Igor Moskalenko and then rewritten in C++. The Galprop code tries to incorporate as many realistic astrophysical inputs as possible together with the latest theoretical developments, it is still in continuous development and currently available to the scientific community via a suitable website.

Given a source distribution and boundary conditions for all CR species, the GALPROP computes the transport equation for CR nuclei, antiprotons, electron and positron as well as the diffusive γ-ray and synchrotron emissions in the same framework [31]. The distribution of CR sources is chosen to reproduce the CR source distribution determined by the analysis of EGRET γ-ray data. The injection spectrum of nucleons is assumed to be a power law in momentum. Each run of the code is governed by a configuration file allowing the user to define and control many details of the calculation so that each run of the code corresponds to a potentially different model. Astronomical data required by GALPROP are provided as separate datasets including interstellar hydrogen surveys, interstellar radiation field distributions.
Many parameters are present in the Galprop code to describe the different mechanisms ruling the CR propagation in the Galaxy. The injection density q for CR species i is assumed to follow a rigidity power law according to the formula:

$$q_i = N_i f(R,z)\rho^{-\nu} \tag{1.29}$$

Where $f(R,z)$ is the spatial distribution of sources and N_i is the normalization abundances for CR species i. A broken power law of the spectrum can be employed different injection indices ν_1 and ν_2 above and below a reference rigidity ρ_{br}. In Galprop the source abundance of protons N_p is normalized based on the propagation proton spectrum at 100 GeV, and N_i for other species are scaled by their abundances relative to that of protons.
The diffusion coefficient and the reacceleration or convection parameters are determined by the Boron-to-Carbon ratio data. The diffusion coefficient is expressed as a function of the velocity

$$D_{xx} = \beta D_0 \left(\rho/\rho_0\right)^{\delta} \tag{1.30}$$

where D_0 is the normalization of the diffusion coefficient at a reference rigidity ρ_0, β is the particle velocity and δ is the diffusion spectral index, if necessary with a break at $\delta = \delta_{1,2}$ below/above the rigidity ρ_0. The diffusion momentum space D_{pp} is related to the the value of D_{xx} according the following formula:

$$D_{pp} = \frac{4v_a^2 p^2}{3\delta(4-\delta^2)(4-\delta)D_{xx}}, \tag{1.31}$$

where v_A is the velocity of fluctuations in the hydrodynamical plasma, called Alfven velocity. The convection velocity $V(z)$ is assumed to have a z-direction and increase linearly with the distance from the galactic plane: $dV/dx > 0$ for every z consistently with models of Cosmic Rays driven by magnetohydrodynamic wind. $V(0) = 0$ because the wind can not blow in both directions. A more general case was implemented with wind starting from $|z| \leq z_0$ and

$dV/dz = 0$ which imply a constant wind velocity equal to the value at z_0. The numerical solution of the transport equation is based on a Crank-Nicholson implicit 2nd order scheme. The reaction network is solved starting from the heaviest nucleus ${}^{64}_{28}Ni$, so that the propagation equation is solved computing all the diffusion processes and the interactions resulting in secondary source functions before proceeding to the nucleus $A - 1$, keep working in this way until it gets down to $A = 1$. The loop is repeated twice to account for special β-decay cases such as $Be^{10} \rightarrow B^{10}$. The final step is the normalization of the absolute proton and electron spectra to experimental fluxes. All the other primary and secondary nuclei spectra follow the same normalization factor as for protons.

1.9 Solar propagation of Cosmic Rays in Heliosphere

During their propagation from the interstellar space towards the Earth, cosmic rays traverse the Heliosphere, the spatial region permeated by the solar magnetic field. This latter is frozen in the turbulent plasma continuously flowing out from the Sun into the outer space, called the solar wind. Crossing the Heliosphere boundaries, cosmic rays undergo interactions with the turbulent solar wind and the heliospheric magnetic field, which scatter and obstruct the propagation of the galactic particles. The result is a significant global and time variation in intensity and energy of cosmic ray fluxes measured inside the Heliosphere with respect to the corresponding LIS in a low energy range, below a few tens of GeVs. For this reason, it is essential to understand the features of the heliospheric environment, the mechanisms of CR propagation inside it and the effects that these have on the CR fluxes.

1.10 The Sun and the solar activity

The Sun constitutes the 99.86% of the mass budget of the solar system and it is composed of 70% hydrogen, 28% helium and 2% heavier nuclei. The Sun is classified as a yellow dwarf in the main sequence of the Hertzsprung-Russel star diagram, with an effective surface temperature measured at a value of $5.778 \cdot 10^3$ K. Its age is assessed about $4.6 \cdot 10^9$ years and it is believed to be originated from interstellar material formerly reprocessed by a previous generation of massive star formations. Its position is estimated at about 8.3 kpc from the center of the Milky Way Galaxy, just near the inner rim of the Orion Arm, and it takes $250 \cdot 10^6$ years to perform the whole orbit around

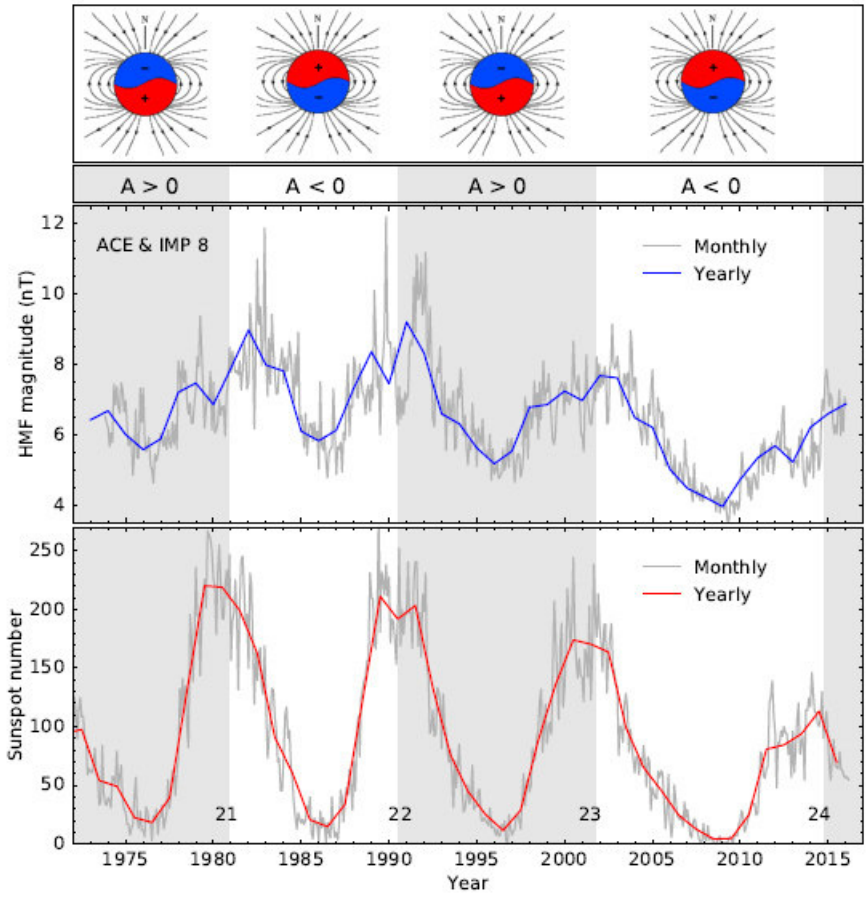

Figure 1.7: Top panel: Sun magnetic configuration for different polarity epochs. Middle panel: the solar magnetic field as measured by IMP8 and ACE in the period from 1970 to 2017. Magnetic field data from ACE and IMP8 were obtained from http://nssdc.gsfc.nasa.gov/. Bottom panel: data of the solar sunspots numbers (SNN) obtained from http://sidc.oma.be/ for the same period. The grey lines represent monthly averages, while the blue and red lines represent yearly averages.

the galactic center.
The Sun also generates its own magnetic field, which in first approximation can be described as a magnetic dipole with opposite polarities in the Northern and Southern hemispheres. This magnetic field is produced within the thin layer between the radioactive and the convective regions and it flows through the photosphere. Besides, the differential rotation of the solar gaseous surface is believed to generate the so-called solar dynamo, which inverts the solar magnetic polarity every 11 years, following a 22-year cycle. When the solar

magnetic field (SMF) points outward in the Northern hemisphere and inward in the Southern hemisphere, it is considered to have a positive polarity ($A > 0$), while in the opposite polarity configuration ($A < 0$) the magnetic field lines go out from the Southern- and enter the Northern hemisphere. Another solar cycle of an 11-year periodicity affects the intensity of the solar emission. One of its more extensively studied indicators is the number of sunspots, a temporary phenomenon in the solar photosphere appearing like dark regions. These phenomena are provoked by intense magnetic activities, that inhibit the convection and form colder areas on the Sun surface. The period between two consecutive solar minima in the sunspots numbers (SSN) defines a cycle. According to Waldmeier's numeration [32], the first cycle started at the solar minimum in the year 1755, preceded by a zero cycle with the maximum in 1750, when an extensive recording of the SNN began. In Figure 1.7 one can note a correlation between the solar magnetic field magnitude and the 11-year cycle of sunspot numbers. The solar magnetic field magnitude is significantly lower during the phase of solar minimum (SSN low), with an average value of 5 nT, than in solar maximum conditions (SNN high), with a magnitude between 8 nT and 12 nT. The period analyzed in this research work starts in July 2006 and ends in September 2014, including the last part of the 23rd cycle and the first part of the 24th one. The observations about the 23rd cycle revealed anomalous behavior with respect to the previous one, indeed the solar minimum activity was expected in 2008, while the number of sunspots kept decreasing in 2009. From 2010 the SNN start raising again and the solar magnetic field reversed its polarity between 2013 and 2014 in the middle of the maximum of the 24th solar cycle. In Figure 1.7 one can see that the magnetic field magnitude had an average value in the minimum of the 23rd cycle lower than the previous cycle. In the next section, it will be explained how the SMF affects the propagation of cosmic rays through the Heliosphere.

1.11 Solar wind and heliospheric magnetic field

The solar wind (SW) is a stream of supersonic plasma ejected from the solar corona at a speed ranging between 400 km/s and 800 km/s. This flow of plasma consists mainly of protons, helium nuclei and electrons, and its ejection is due to the difference in pressure and temperature between the ionized gas of the solar corona and the outer space. As the Sun and the solar system with it move through space, the solar wind interacts with the interstellar medium, the result of this interaction is a space structure like a bubble permeated by the solar wind, the Heliosphere. A schematic model of

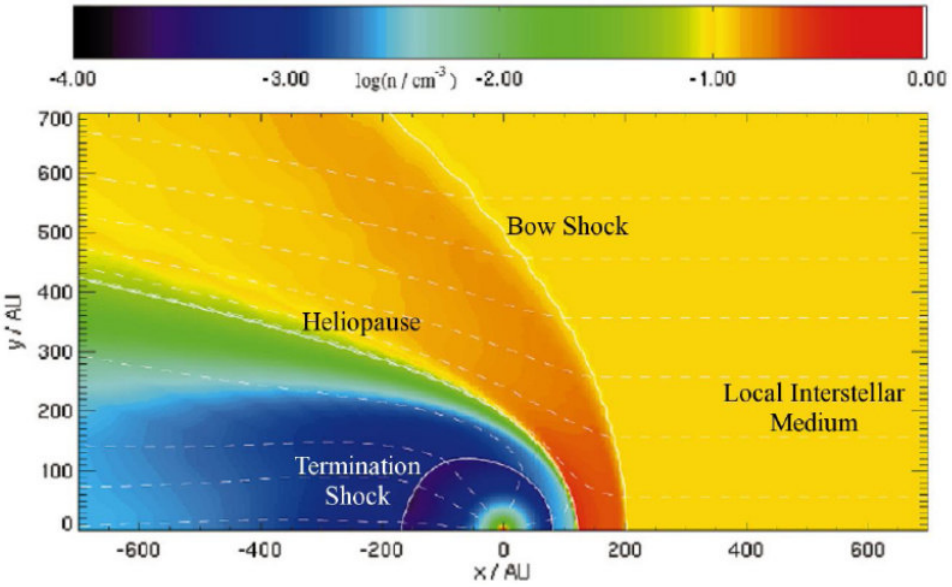

Figure 1.8: Hydrodynamical model of the Heliosphere, where the solar wind number density is shown as a function of the distance from the Sun. The solid lines indicate the different regions of the Heliosphere, corresponding to Bow Shock, Heliopause and Termination Shock [9].

the Heliosphere is shown in Figure 1.8. The relative motion of the Sun with respect to the ISM makes the heliospheric structure asymmetric, with an extension of almost 120 AU in the forward direction and several hundreds of AU in the backward. Several substructures have been identified in the Heliosphere: when the density of the solar wind is too low to compensate the ISM pressure, suddenly its velocity falls to subsonic values creating a shock, this space area is called Termination Shock. The SM continues to move forward until its decreasing pressure reaches values comparable to those of the ISM. Here the trajectory of the SM is expected to be deviated around a surface, called Heliopause, forming a new shock area, called Bow Shock. The solar wind is an excellent electric and thermal conductor, able to freeze the solar magnetic field and transport it away from the solar surface towards the interplanetary space, generating the so-called heliospheric magnetic field (HMF), which affects the propagation of cosmic rays in the Heliosphere. An important parameter that defines the shape and magnitude of the heliospheric magnetic field, is the tilt angle, which is the inclination angle between the solar magnetic dipole and its rotation axis. This angle assumes values very close to zero during the solar minimum and then rises to higher values up

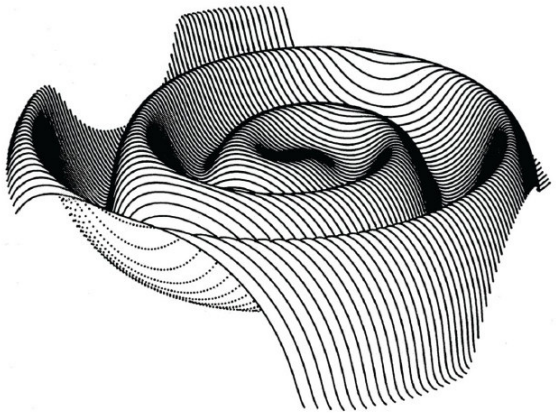

Figure 1.9: Drawing of the Neutral Currrent Sheet.

to 70° during the maximum phase. This feature generates a wavy sheet between two heliospheric hemispheres with opposite magnetic polarity (see Figure 1.9). This wavy structure is known as Heliospheric Current Sheet (HCS) and will be explained in the following sections since it significantly affects the propagation of cosmic rays through the Heliosphere.

1.12 Cosmic Ray modulation in Heliosphere

Crossing the Heliosphere boundaries, galactic cosmic rays encounter the turbulent solar wind and the heliospheric magnetic field frozen in it and they interact with them. The primary result of this interaction is a measurable decrease of the cosmic ray intensity at energies below s few tens of GeV, with respect to the LIS intensity. An additional effect of the interaction of CRs with SW and HMF is a time dependence of Cosmic Ray fluxes at low energies as a function of the solar activity cycle. To study the solar modulation of cosmic rays over a large period, ground base neutron monitors (NM) are employed, these instruments measure CR fluxes at Earth detecting the secondary neutrons produced in the atmosphere by the interaction of CRs with atoms and molecules in the air. Figure 1.10 shows a graph of neutron monitor counts measured by the Hermanos NM in South Africa, as a function of time from 1960 until today. The data show that the 11-year solar cycle generates an 11-year modulation cycle of cosmic rays. This is identified by the increase of cosmic ray fluxes that occurred around 1965, 1976, 1987, 1997 and recently 2009. A comparison between Figure 1.10 and Figure 1.7 reveals an anticorrelation between solar activity and observed CR fluxes, this means higher

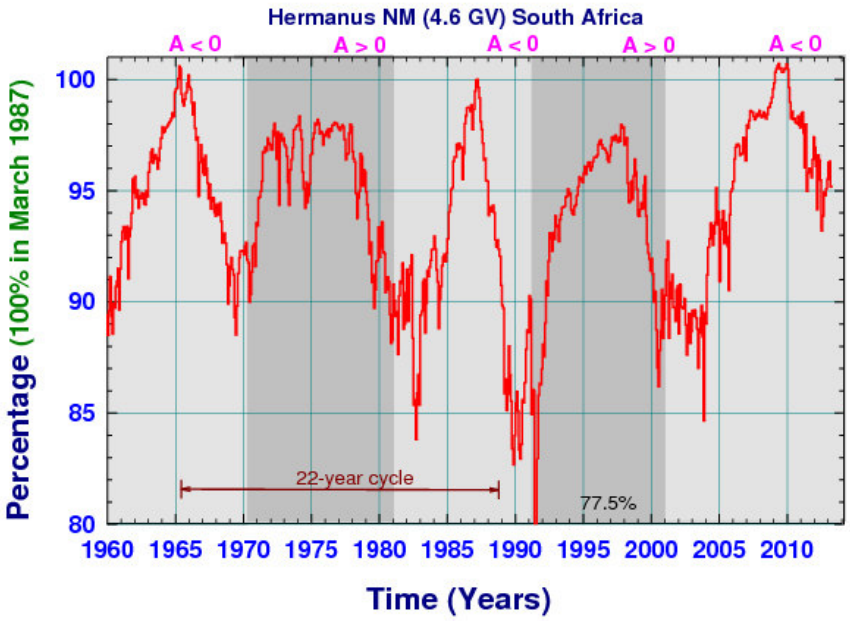

Figure 1.10: The cosmic ray intensity measured by the Hermanus neutron monitor located in South Africa. Data are normalized to March 1987. The cosmic ray intensity variation illustrates the 11 years and 22 years solar cycles. The data were obtained from http://www.nwu.ac.za/neutron-monitor-data.

cosmic ray intensities measured in correspondence of solar minimum phases. In fact, the CR propagation through the Heliosphere is more favourite during the minimum solar activity phase when the heliospheric magnetic field is characterized by a more ordered structure, than in maximum periods, when the magnetic field lines are more chaotic and the heliospheric magnetic field reverses its polarity. Additionally, a 22-year cosmic ray modulation cycle can be also identified from Figure 1.10, related to the HMF polarity changes and the resulting drift motion. The trend in the graphic shows a sharper profile in the $A < 0$ period and a flatter shape in the $A > 0$ period. This suggests a different propagation of cosmic rays depending on the heliospheric magnetic field orientation.

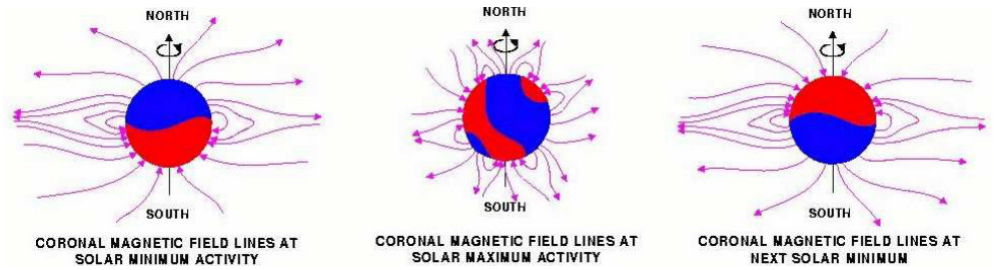

Figure 1.11: Display of the magnetic field lines during different activity times between two consecutive solar minima [33].

1.13 Charge-sign dependent modulation

It was already exposed in Section 1.5 how the presence of gradients and curvatures of the magnetic field induces a drift motion in the charged particles. The direction of the drift motion depends on both the particle charge sign and the magnetic field polarity: particles of opposite charge affected by the same magnetic field follow the same trajectory but in the opposite direction, similarly a particle reverses the direction of its spiral motion when the magnetic polarity changes. Charge particles propagating through the HCS, undergo a magnetic field of opposite polarity so that particles with opposite electric charge drift towards Earth through different directions in the Heliosphere. During the positive polarity period ($A > 0$), positive charge particles, like protons and deuterons, drift towards the Earth through the heliospheric polar regions, while during the negative polarity period ($A < 0$) they drift inward through the heliospheric equatorial regions, where the waviness of the HCS make the propagation more difficult resulting in a decrement of the intensity of cosmic rays measured at Earth. For negative charge particles, the drift motions occur oppositely. Simultaneous measurements of electrons and positrons, protons and antiprotons in cosmic radiation are fundamental to study how large is the effect of the charge-sign modulation in the Heliosphere, as a function of energy and position inside the Heliosphere. Simultaneous observations of particles and respective antiparticles over a multi-year period were performed extensively by the PAMELA collaboration [34] [35].

1.14 The transport equation of cosmic rays in the Heliosphere

In 1965 the physicist E. N. Parker derived a transport equation of CRs through the Heliosphere, studying the motion equation of a particle in a

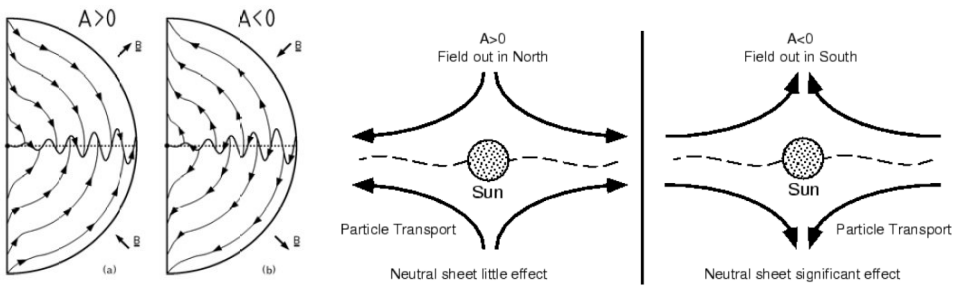

Figure 1.12: Left: ideal structure of the global drift motion of positively charged particles inside the Heliosphere in $A > 0$ and $A < 0$ cycles [9]. Right: direction of the drift motion for opposite solar polarity.

variable magnetic field and from the reasonable assumption of cosmic ray isotropy. This equation takes into account the four major modulation mechanisms in the Heliosphere: outward convection by the SW, adiabatic deceleration due to the expanding SW, diffusion along and across the HMF and drift motion due to magnetic field gradients and curvature and the NCS. The Parker transport equation is described by the following equation:

$$\frac{\partial f}{\partial t} = -\left(\vec{V} + \langle \vec{v_d} \rangle\right) \cdot \nabla f + \nabla \cdot \left(\vec{K_s} \cdot \nabla f\right) + \frac{1}{3}\left(\nabla \cdot \vec{V}\right) \frac{\partial f}{\partial \ln \rho} + Q\left(\vec{r}, p, t\right), \tag{1.32}$$

Where on the left $f(\vec{r}, \rho, t)$ is the cosmic ray distribution function depending on the rigidity ρ, the space position $\vec{r}$ and the time coordinate t. On the right:

- $\nabla \cdot \left(\vec{K_s} \cdot \nabla f\right)$ represents the spatial diffusion parallel and perpendicular to the average magnetic field, which are ruled by the diffusion tensor $\overleftrightarrow{K}$. In this expression $\overleftrightarrow{K_s}$ is the so-called symmetric diffusion tensor.
- $\vec{V} \cdot \nabla f$ describes the outward particle convection caused by the solar wind, that blows radially outwards from the Sun with velocity $\vec{V}$. From experimental observations, the $\vec{V}$ is not uniform over all the latitudes, but fast and slow regions are present during the solar minimum phase.
- $\langle \vec{v_d} \rangle \cdot \nabla f$ describes the drift motion with average drift velocity $\langle \vec{v_d} \rangle$. As it was explained in the previous section, this motion is caused by gradients and curvatures of the heliospheric magnetic field. The charge-sign effect discussed in the previous section is included in this equation component.

- $\frac{1}{3}\left(\nabla\cdot\vec{V}\right)\frac{\partial f}{\partial \ln p}$ is the term describing the adiabatic energy exchange. In the case of $\left(\nabla\cdot\vec{V}\right)>0$ there is an adiabatic energy loss, if $\left(\nabla\cdot\vec{V}\right)<0$ one has a diffusion energy gain, which corresponds to the case of the so-called anomalous cosmic rays in the Heliosheath, in the last case of $\left(\nabla\cdot\vec{V}\right)=0$ no energy change occurs, which may be the case when CRs are outside of the Termination Shock.

- $Q\left(\vec{x},p,t\right)$ takes into account possible CR sources inside the Heliosphere, e.g. the Jovian electrons.

This transport equation can be solved numerically, this allows the evaluation of the CR fluxes for a specific CR species at a certain time and position inside the Heliosphere starting from the corresponding LIS.

1.15 The Force Field approximation

In 1968 an approximate analytical solution of Parker's transport equation of cosmic rays in the Heliosphere was proposed in [36]. This model, commonly known as force field approximation, starts from several assumptions: a spherically symmetric Heliosphere with no internal sources of cosmic rays, a negligible adiabatic energy loss rate, a steady-state of the TPE. Under these assumptions, the TPE is approximated as follows:

$$\frac{\partial f}{\partial r}+\frac{VR}{3\kappa}\frac{\partial f}{\partial R}=0 \tag{1.33}$$

where f is the CR distribution function, r the heliospheric radial distance, V the solar wind velocity, R the particle rigidity, κ a diffusion coefficient, which is separable into radially and rigidity dependent parts

$$\kappa\left(r,R\right)=\beta\kappa_1\left(r\right)\kappa_2\left(R\right) \tag{1.34}$$

for relativistic particles ($\beta=\frac{v}{c}\sim 1$). The final solution depends on just one parameter Φ, called force field parameter:

$$\Phi=\frac{1}{3}\int_{r_E}^{r_b}\frac{V}{\kappa_1}dr \tag{1.35}$$

where r_E is the radial distance of the Earth from the Sun, 1 AU, and r_b is the boundary of the Heliosphere. With $\kappa_2\propto R$ and $\beta\approx 1$ [37], the solution reduces to the widely used form

$$\Phi=R_b-R_E \quad , \tag{1.36}$$

where R_E and R_b are the rigidity of a galactic particle at the Earth and at the boundaries of the Heliosphere respectively. This entails that the force field parameter becomes the rigidity loss experienced by cosmic rays in the Heliosphere approaching the Earth. Working in terms of kinetic energy E_{kin}, cosmic rays with E_{kin}^{LIS} at the Heliosphere boundaries, arrive at the Earth with

$$E_{kin} = E_{kin}^{LIS} - |Z|\, e\Phi \quad , \tag{1.37}$$

where Φ is multiplied by the absolute charge $|Z|\, e$ of the considered particle species. The flux at the top of the Earth's atmosphere $\frac{dN}{dE}(r_E, E_{kin}, t)$ is related to the local interstellar one $\frac{dN^{LIS}}{dE}(r_b, E_{kin} + |Z|\, e\Phi(t))$ according to the following relation:

$$\frac{dN}{dE}(E_{kin}, r, t) = \frac{\left(E_{kin}^2 + m\right)^2 - m^2}{\left(E_{kin} + m + |Z|\, e\Phi\right)^2 - m^2} \frac{dN^{LIS}}{dE_{kin}}(r_b, E_{kin} + |Z|\, e\Phi(t)) \quad , \tag{1.38}$$

with m the mass of the galactic particle and t the time. It follows that the time dependence of the CR fluxes is reproduced by the time dependence of the force field parameter Φ. Typically, Φ varies from 300 MV to 1000 MV from solar minimum to solar maximum conditions.
Equation 1.38 is commonly used to assess approximately the effects of the solar modulation on the cosmic-ray fluxes because of its simple calculation. However, this approximate solution does not include the charge-sign dependence of the solar modulation and the assumption on the separability of the diffusion coefficient is a valid approximation only for rigidities above ~ 1 GV.

1.16 Numerical solution of Parker's transport equation

Due to the increasing computing power available throughout the years, it has been possible to numerically solve the transport equation with high precision. In this thesis, the state-of-the-art 3D numerical model for the modulation of CR energy spectrum in the Heliosphere developed in [38] [39] [40] was considered for precise solar modulation studies.
This model rewrites Parker's transport equation in a parabolic differential equation in terms of rigidity within a spherical coordinate system that rotates together with the Sun. This parabolic equation is then solved in terms of their spatial coordinates and time. A full discussion of this procedure can be found in [38]. A LIS is used as an input spectrum at the Heliosphere boundaries at 120 AU, for all the values of the angular coordinates, while

the inner boundary is taken for $r > R_{sun}$. Symmetry for rotation around the polar axis in correspondence of the poles is assumed:

$$\frac{\partial f}{\partial \theta} = 0, \tag{1.39}$$

At the poles $\theta = 0$ and $\theta = \pi$. 3D grid is built across which the TPE is solved. A first solution is achieved at one-third of a rigidity step forward solving the TPE in spherical coordinates in the direction of the radial distance r. A second solution is then obtained at one-third of the rigidity step forward, using the first solution, by solving the differential equation in the direction of the polar angle θ. The solution for the final third of the rigidity step is retrieved applying again the mechanism for the azimuthal angle ϕ, using the previous two solutions. The result is a system of linear equations, that is possible to solve. This process is repeated for all rigidity values to get a solution of the final distribution f. See [40] for a full discussion about the solving numerical method of the TPE in 3D.
In this work, a deuteron LIS calculated by the GALPROP was used as input of this 3D numerical model to obtain the deuteron modulated spectra during the solar minimum phase at 1 AU. These numerical rigidity spectra will be then compared with the experimental fluxes, measured with the PAMELA data.

1.17 CR interaction with the Earth's magnetic field and the geomagnetic cut-off

A geomagnetic cut-off is usually introduced to describe in a simply the effect of the geomagnetic field on the charged particle travelling towards the Earth. This geomagnetic cut-off is defined for each orbital position and angular direction around the Earth and it is the minimum rigidity value necessary for a charged particle to be measured by a cosmic ray detector in that orbit position and angular orientation. The geomagnetic cut-off is higher at the equator and decreases towards the poles, because of the dipole nature of the Earth's magnetic field. An analytical solution of the equation of motion of a charged particle in Earth's magnetic field was found by Störmer, expressing the cut-off rigidity as:

$$R_s = \frac{\mu_0}{4\pi} \frac{M \cos^4 \delta}{r^2 \left(1 - cos^3 \delta \cos \epsilon \cos \zeta\right)}, \tag{1.40}$$

where r is the distance from the dipole center, M the magnetic dipole of the dipolar term, δ the magnetic latitude, ϵ and ζ are the angles that specify

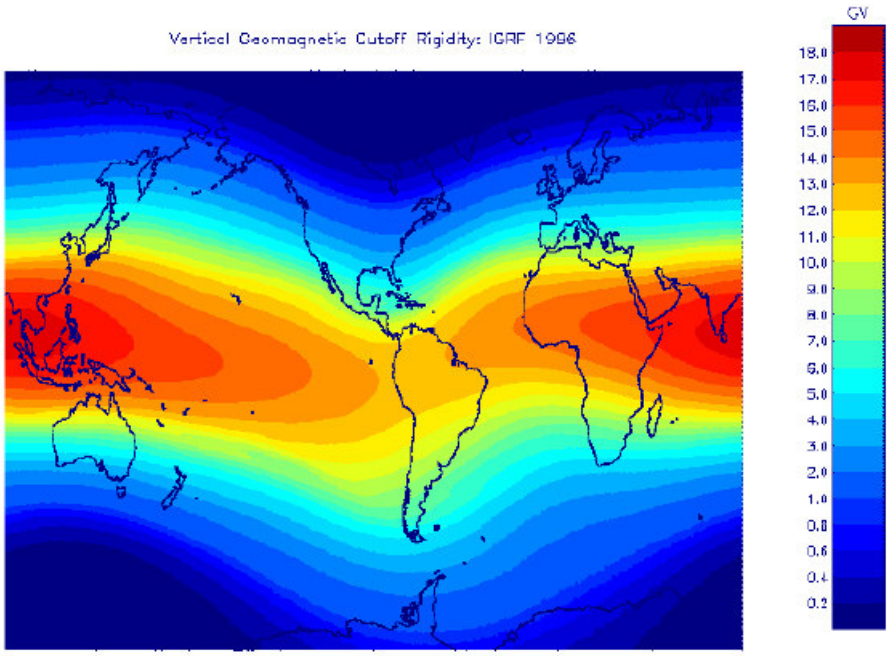

Figure 1.13: Global grid of calculated vertical geomagnetic cut-off rigidities (GV), obtained from [41].

the incoming direction of the particle. For vertically incident particles this equation simplifies and becomes

$$R_{svl} = 14.9\ GV \cos^4 \frac{\delta}{4}, \tag{1.41}$$

where R_{svl} is called Störmer vertical cut-off, whose values are shown in Figure 1.13. The Störmer vertical cut-off can be considered as the minimal rigidity for a galactic charged particle to be detected by an instrument placed in that position.

Chapter 2

Search for dark matter with cosmic-ray antiprotons and antideuterons

2.1 Introduction

This chapter is dedicated to the indirect search for dark matter (DM) by means of precise measurements of galactic antiprotons and antideuterons, which are rare components of cosmic radiation.
Generally, the search for potential dark matter signals in cosmic rays is challenging, because of large uncertainties coming from the astrophysical background and the effects induced by CR acceleration and propagation mechanisms, which are still a matter of study. Therefore, a deep understanding and precise modelling of the measured cosmic ray spectra are needed to reduce their related uncertainty and improve the capacity to identify a possible dark matter signal.
In particular at low energies, below a few tens of GeVs, the uncertainty introduced by the modelling of the solar modulation of the CR antinucleus components is significant. This is due to the lack of precise measurements of time-dependent fluxes in the case of antiprotons. However, state-of-the-art models of solar modulation calibrated to reproduce the fluxes of the cosmic-ray nuclei and accounting for the charge-sign dependent effect induced by the drift motions can predict solar modulation effects for the corresponding antinuclei. Precise modelling of the solar modulation is essential to study the low energy part of the antiproton and antideuteron spectra, which is a region of big interest for the DM search.
In the first part of the chapter, an introduction to dark matter and its detec-

tion technique, in particular with CR antinuclei, is discussed. General information about these topics were obtained mainly from the following sources: [2], [42], [43] and [44]. The end of the chapter focuses on how the solar modulation effects on these antinuclei are evaluated. For this last part concerning DM-induced antiprotons and antideuterons, [43], [45] and [46] were used as main sources of information.

2.2 Astrophysical evidence for dark matter

Relying on Newton's law of gravity and the general relativity, evidence for excess gravitational acceleration not explained by observable matter has been found on both galactic and cosmological scales over years of space observations. These measurements have testified that the universe must contain a large amount of invisible matter of unidentified nature, whose presence has been able to be detected only through gravitation. This unknown matter, called dark matter (DM), accounts for about 25% of the mass-energy content of the whole universe.
The first hint of the presence of DM was observed by Jan Ort in 1932 studying the motion of the nearby stars, indeed he discovered that the mass of the galactic plane had to be higher than that evaluated from the bright star population. However, at that time Ort interpreted this result in terms of dim stars.
In the same years, Fritz Zwicky was studying the motion of the galaxies inside the COMA galaxy cluster and applied the virial theorem to the galaxies in motion. He achieved the conclusion that on average the galaxies were moving too fast and that the COMA cluster was not possible to be held together only by the mass of the visible matter. However, Zwicky's estimation suffered from limited statistics of the observed galaxies and from the uncertainty of the COMA radius.
In the 1970s strong evidence for dark matter presence was found in precise measurements of the galaxy rotation curves. From the equality of the attractive gravitational force and the centrifugal force

$$\frac{G_N M(<r)m}{r^2} = \frac{mv^2}{r} \quad , \tag{2.1}$$

where G_N is Newton's gravitational constant and $M(<r)$ is the mass enclosed in the radius r, one obtains that the revolution velocity v for stars outside the central luminous galactic disk is proportional to the distance from the galactic center according to the relation:

$$v \propto \frac{1}{\sqrt{r}} \quad , \tag{2.2}$$

from which one expects a so-called Keplerian fall-off of the circular velocity for celestial objects outside the central luminous disk. However, it was found that most of the stars and atomic hydrogen gas clouds rotate along their orbit at the same velocity independently from the distance from the galaxy center, and this is worth also for the stars beyond the boundaries of the galactic visible halo. This result implied that the galaxy mass must rise even in the outer regions, where only a few stars and little gas are localized. The gravitational lenses also allow us to assess the mass distribution of the galaxy clusters. A gravitational lens is large mass distribution in space, like a galaxy, a galaxy cluster or a black hole, which produces a curvature of space-time according to the theory of general relativity. Similar to a lens, this space-time curvature can generate a distortion or even multiple pictures of the image of a luminous source in space, whose electromagnetic emissions cross this curvature. The analysis of effects leads to determine the characteristics of the luminous source as well as the properties of the massive object acting as a gravitational lens. In agreement with other types of measurements, the gravitational lensing observations provide convincing evidence that galaxy clusters must include a DM mass of about a factor five higher than the mass amount coming from the visible baryonic matter.
The strongest astrophysical evidence for dark matter finally came from the observation of the so-called Bullet Cluster: a collision of two galaxy clusters. According to the observation through gravitational lenses, most of the mass remained concentrated in the two individual clusters, whereas the thermal X-ray emission measurements pointed to a baryon gas distributed in the collision region.
On cosmological scales, evidence for dark matter can be found on its impact on the density fluctuations of the universe, which are observed through surveys of cosmic microwave background radiation (CMBR). In agreement with the Big Bang model, the CMBR is the residual electromagnetic radiation coming from the first phases of the primordial universe. In the early cosmological history, before photons and baryonic matter decoupled, radiation provided most of the pressure, but interacted only with ordinary baryonic matter. Dark matter could only act gravitationally on the density fluctuations of the baryonic matter, arised from the interplay of gravity and pressure. These density fluctuations are measured as acoustic fluctuations in the CMBR, whose temperature anisotropies have been measured with higher and higher precision with the Wilkinson Microwave Anisotropy Probe (WMAP) [47] and later by the Planck mission. The analysis of the peaks in the angular power spectrum of CMBR temperature fluctuations indicates evidence of a

flat universe dominated by cold dark matter [1] (CDM) with a density five times larger than that of the ordinary baryonic matter. This deduction was also supported by the Sloan Digital Sky Survey (SDSS) measurements of the so-called baryonic acoustic oscillations (BAO) [48], the density fluctuations detected from the uneven distribution of galaxies and clusters in the observed universe.

DM particle candidates

Very massive cold objects, like planets, brown dwarfs or primordial black holes, which are commonly named Massive Compact Halo Objects (MACHOs), have been extensively looked for with microlensing experiments and they have been found too few in number to account for dark matter [49] [50] [51]. Besides, the mass range for which primordial black holes can contribute to dark matter is also quite restricted to roughly the mass range between 10^{17} and 10^{25} solar masses [52]. This makes it very likely that dark matter has to be made up of a new type of particles.
Dark matter can not be baryonic, because this would conflict with the yield of the big-bang nucleosynthesis [53] and results of a CMBR fluctuation analysis. The non-baryonicity implies the color-neutrality for a dark matter candidate, that can not engage in strong interactions. In its lightest form, it must be electrically neutral, otherwise it would be visible instead of being dark. But this does not exclude the existence of heavier charged siblings that may have existed in the early universe.
Coupling with the electroweak gauge bosons $W^{\pm}$ and Z^0 is not excluded, but it must be weaker than that of other Standard Model particles, otherwise direct-detection experiments would have already seen these interactions. The stability of at least the lightest dark matter particles must be high and consequently the self-interactions rather weak. The lack of impact on the dark-matter distribution of cosmic events that do not affect the baryonic-matter distribution, such as the merger of the Bullet Cluster, implies that the dark-matter particles must be highly collisionless. The Standard Model of particle physics does not include any particle with all these requirements, consequently several theories beyond the Standard Model have been proposed over the years to include new particles with the requirements to be dark matter candidates. Three of the most popular DM candidates are reported hereinafter:

[1] dark matter composed of individual particles with a rest mass higher than the energy scale of the universe shortly before the recombination, they are massive enough to allow the growth of small-scale density fluctuations.

- In supersymmetric extensions of the Standard Model, the lightest supersymmetric particle (LSP) is stable on account of a specific symmetry. Such particles typically have a mass above a few GeV and therefore they are candidates for CDM. Among these so-called weakly interacting massive particles (WIMPs), there are the supersymmetric partners of the gauge bosons and the Higgs boson, i.e. a neutralino, of a neutrino, i.e. a sneutrino, or even of the graviton, i.e. the gravitino.

- The Kaluza-Klein excitations of the quantum fields describing elementary particles found in higher dimensional extensions. The lightest particle of this type is stable and long-lived, which makes it a dark-matter WIMP candidate.

- Pseudo scalar axions and axion-like particles (ALPs) are generally very light DM candidates, with masses below the MeV scale, even much less down to 10^{-9} eV and can couple to the photon field. In contrast to WIMPs, these weakly interacting slim particles (WISPs) were not produced through thermal freeze-out in the early universe, but they formed a Bose-Einstein condensate with very high occupation numbers.

A strong advantage of the WIMP with respect to all the other dark matter candidates is given by the theoretical expectation known as the WIMP miracle. In fact, a very plausible hypothesis is that dark matter consists of thermal relics of the Big Bang, this would connect the DM ability to interact via annihilation or decay processes regulating the Standard Model particle abundance in the Universe and the cosmologically relevant properties and observables. In particular, a thermal relic abundance calculated accurately starting from assumptions on interaction strength and mass for the WIMPs was achieved with a value very close to that measured very accurately by cosmological observations. This coincidence is commonly named the WIMP miracle and makes the WIMP currently the most accredited and searched dark matter candidate.

2.3 The dark matter searches

The proposed dark matter particle candidates span more than 60 orders of magnitude in cross-section for annihilation in SM particles, and about 45 orders of magnitude in mass. From these numbers, it is clear that a non-single experimental technique can cover such a large parameter range. Also focusing only on the search for WIMP candidates, different detecting techniques are used, these can be classified into three main search methods:

- The direct detection: it looks for the scattering of DM particles in a detector on Earth through the detection of the recoil of the target nuclei. Currently, there are about twenty operating or planned experiments (e.g. LUX [54], CDMS [55], DAMA/LIBRA [56], CoGeNT [57]). They are usually located deep underground, to shield them from cosmic rays, which together with natural radioactivity in the rocks and the detector materials are the most important source of background.

- The indirect detection: this detection probes the annihilation cross section or decay lifetime of DM particles measuring their Standard Model products. DM annihilation and decay processes may contribute to flux of γ-rays, cosmic neutrinos or charged particles and antiparticles. The energy of these products can reach up to the mass of the dark matter particle. For this reason detectors for cosmic rays and γ-rays, neutrino and radio telescopes are employed in the indirect search for dark matter in a multi-messenger approach. Accurate modelling of the acceleration and propagation of cosmic rays as well as their production of secondary γ-rays and neutrinos are required to be able to distinguish a possible signal from dark matter from the ordinary astrophysical background.

- Escape detection probes the presence of DM particles produced in the collisions in colliders looking for a characteristic signal of missing transverse energy similarly as neutrino but not predicted by the Standard Model. In hadron colliders such as the Large Hadron Collider (LHC) at CERN [58], only the missing transverse energy can be measured, since the longitudinal momentum fractions of the incoming partons are unknown.

In general, all dark matter detection techniques try to estimate the DM annihilation cross-section/decay half lifetime and the mass of the DM particles, assuming known its velocity and its density distribution. In the absence of a clear signal, constraints on these quantities can still be obtained.

2.4 Indirect search for dark matter with astroparticles

The DM indirect search aims to detect a distinctive DM signature in the measured spectra of the astroparticle components, i.e. gamma-rays, galactic neutrinos and cosmic-rays, through the different kinematics between the astroparticle production by dark matter and standard astrophysical processes. Such a search requires a deep understanding of the astrophysical background

and an accurate uncertainty estimation introduced from models describing the dark-matter spatial distribution and dark-matter annihilation or decay into Standard Model products. Besides, any possible DM signal must be also consistent with the constraints provided by observations in all the other astroparticle spectra and must retain their significance after considering all the systematic uncertainties.
For all the reasons listed above, a multi-messenger approach is essential in the DM indirect search. The contributions to the fluxes of the different astroparticles coming from DM annihilation or decay events are described in the following formula introduced in [61]:

$$\frac{d\Phi_{astrop-DM}}{dE} = \eta \cdot \sum_{a=1}^{2} \sum_{i}^{SMch} \frac{\zeta_i^{(a)}}{a} \frac{dN_i^{(astrop)}}{dE} \frac{\kappa^{(a)}}{4\pi M^a}, \tag{2.3}$$

where a is an index differentiating the two cases of products from decayed DM ($a = 1$) and annihilated DM ($a = 2$) and i is an index running on the different Standard Model particles produced from DM. The various parameters and physical mechanisms identified in the Equation 2.3 are listed here:

- η is a factor depending on the nature of the produced particle and its propagation in the space. In particular, η can assume the following values for the different astroparticle messengers:
  - $\eta = 1$ for gamma-rays, since they allow directional observations along the line-of-sight,
  - $\eta = \sum_{p=1}^{3} P_{fp}$ for neutrinos, where P_{fp} is the element of the symmetric 3×3 matrix accounting for the neutrino oscillation from a flavour f produced at the source to a flavour p observed at the telescope along the line-of-sight.
  - $\eta = \frac{v}{4\pi}$ for cosmic rays propagating with velocity v through the Galaxy. Clearly, cosmic rays does not allow directional observations as already largely explained.
- Depending on a and i indexes, the factor $\zeta_i^{(a)}$ represents the inverse decay half time $\zeta_i^{(1)} = \frac{1}{\tau_i^{decay}}$ of a WIMP into an i-th Standard Model product or the average annihilation cross section times velocity $\zeta_i^{(2)} = \langle \sigma_i \cdot v \rangle$, of WIMP into SM particles.
- $\frac{dN_i^{(astrop)}}{dE}$ is the differential number (yield) of astroparticles produced at the source by subsequent events of DM annihilation or decay of into i-th SM particles. This yield is assessed in simulations by means

of Monte Carlo event generator softwares such as Pyhtia or Herwig. These calculations introduced uncertainties in the evaluation of both $\zeta_i^{(a)}$ and $\kappa^{(a)}$ factors.

- $\kappa^{(a)}$ is a factor depending on the astrophysics of the DM distributions as well as on the astroparticle propagation. For the γ-ray and neutrinos, which propagated almost un-perturbated along the observed line-of-sight, this $\kappa^{(a)}$ takes the name of astrophysical J-factor and it is defined as:

$$\kappa^{(a)} = \langle J \rangle_{\Delta\Omega} = \frac{1}{\Delta\Omega} \int_{\Delta\Omega} d\Omega \int_{l_{min}}^{l_{max}} \rho^a \left[r(l) \right] dl \left(\alpha \right), \tag{2.4}$$

where $\rho(r)$ is the DM density, l the line-of-sight, defined as the distance of the observer to any observed source, while r is defined from the relation

$$r^2 = l^2 + d^2 - 2dlcos\alpha \tag{2.5}$$

where r is the radial distance from the center of the target (commonly our galactic center) to a given point inside it, d is the distance of the Earth from the center of the target. In this way $l\left(r, d, \alpha\right) = dcos\alpha + \sqrt{r^2 - d^2 sin\alpha}$ is therefore equal to the distance from the Earth to the DM target in the direction α.
The flux must be averaged over the solid angle of the detector, typically $\Delta\Omega = 2\pi(1 - cos\theta)$ where θ is the angular resolution of the telescope.
For cosmic rays the directional observations are not feasible and $\kappa^{(a)}$ is proportional to a diffusion term according to the formula:

$$\kappa^{(a)} = \left(\frac{\rho_\odot}{M^a} \right)^{(a)} R_{CR} \left(r_\odot, E \right) \tag{2.6}$$

where $R_{CR}(r_\odot, E)$ is a diffusion factor at the position of the Sun for charged particles, obtained from the solution of the cosmic ray diffusion equation. It accounts for the diffusion effects and production of secondary particles along the path.

Equation 2.3 can therefore be used to predict the signals expected from DM annihilation or decay processes in the astroparticle spectra. In recent years, cosmic-ray and γ-ray observations have provided several intriguing hints of dark matter signals, but most of them disappeared subsequently due to systematic uncertainties, a difficult characterization of the backgrounds or a possible source confusion. Currently, there are three detected ambiguous anomalies, which can be explained through a DM contribution: the rising fraction of positrons measured by PAMELA [65] and confirmed by AMS-02 [66], the hardening of the antiproton fraction reported by AMS-02 [75] and

the excess in the γ-ray emission in the GeV range from the Galactic Center measured by Fermi-LAT [64]. However, none of these anomalies lack a plausible conventional explanation and ample literature is present discussing these ambiguous signals.
About the constraints on the averaged cross section (times velocity) and the WIMP mass, the best upper limits have been obtained from the analysis of the γ-ray emission detected by Fermi-LAT from dwarf galaxies [67]. In particular, these results excluded DM candidates lighter than 100 GeV with an average annihilation cross section larger than the benchmark of the thermal cross section. These results are also in agreement with them obtained by AMS-02 from the antiproton measurements [59]. At higher energies, the best limits are provided by the γ-ray observations of the inner Galactic Halo performed by the Cherenkov Telescope HESS [68].

2.5 DM search through cosmic ray antinuclei

The indirect search for DM in cosmic rays focuses on the galactic antiparticles, because these are produced as a small secondary component from interactions of primary CRs with the interstellar medium. A potential dark matter signal in these antiparticle components is still challenging to find, but it is not buried by the CR standard-scenario background. In particular, the antinuclei, i.e. galactic antiprotons, antideuterons and antihelium nuclei, are currently a promising channel for the indirect search for dark matter. Indeed, they are expected to have a high sensitivity to DM annihilation or decay processes, allowing to test the expectations of a variety of dark matter models.
Nowadays, with the PAMELA and AMS-02 experiments, the cosmic-ray antiprotons measurements have achieved high statistics accuracy, which has consequently increased the sensitivity to a possible dark matter signal. and they have provided strict constraints on the WIMP across a wide mass range. The antiproton formation from both DM processes and interaction of primary CRs with the ISM implies a smaller component of Standard Model products able to hadronize in heavier antinuclei as well. These antinuclei are much less abundant cosmic-ray components and their detection has not been possible so far with the current experimental sensitivities. Many dark matter models predict antideuteron and antihelium signals from DM annihilations or decays at low energies a few orders of magnitude higher than those from secondary production. This makes these channels particularly interesting for the dark matter search. In particular, the antideuteron is the most studied, because the expected fluxes from dark matter processes are included in the sensitivi-

ties of the current AMS-02 experiment and of the future GAPS experiment. Regarding the antihelium nuclei, these have a signal-to-background ratio at low energies similar to that for antideuterons ($10^2 - 10^3$), but, according to the DM models, their formation from dark matter is more suppressed compared with the antideuteron channel. Despite this unfavourable expectation, surprisingly the AMS-02 collaboration announced a few years ago the observation of some potential antihelium-3 and antihelium-4 candidates. Such a confirmation would have significant implications for both DM indirect search and the predicted antiproton and antideuteron fluxes, but further data taking, analyses and interpretation as well as verification with a different detection technique, e.g. with the GAPS experiment, are needed to be able to confirm an antihelium detection.
The next sections will expose the current status and the prospects of the indirect search for dark matter in the antiproton and antideuteron channels.

2.6 Dark matter searches in cosmic ray antiprotons

According to the standard cosmic-ray scenario, antiprotons are produced in the Galaxy by spallation of primary protons and heavy nuclei interacting with the nuclei of the ISM. The first detections of the antiprotons in CRs date back to the 1970s and the early 1980s. Later, antiproton measurements performed by the BESS [69] [70] and CAPRICE [71] collaborations provided early constraints on the antiproton astrophysical production and propagation scenarios as well as on its production from dark-matter processes. A relevant improvement in the accuracy of the antiproton fluxes was achieved with the PAMELA results published in 2009 [72] and refined in [73]. These measurements were in good agreement with conventional models of only secondary production of antiprotons, but they were also used to define upper constraints on the WIMP annihilation cross section [74]. Later, in 2015 even more accurate antiproton fluxes were published by the AMS-02 collaboration [75]. The antiproton measurements taken by PAMELA and AMS-02 are displayed in Figure 2.1 together with the error bands from the modelling of cross section, production, CR galactic transport and solar modulation for the antiproton fluxes.
The first discrepancy in the AMS antiproton fluxes with the standard scenario expectations was claimed due to excess at high energies above 100 GeV. A subsequent analysis of this excess [76] revealed only a mild overshooting of the expected background explainable reasonably employing con-

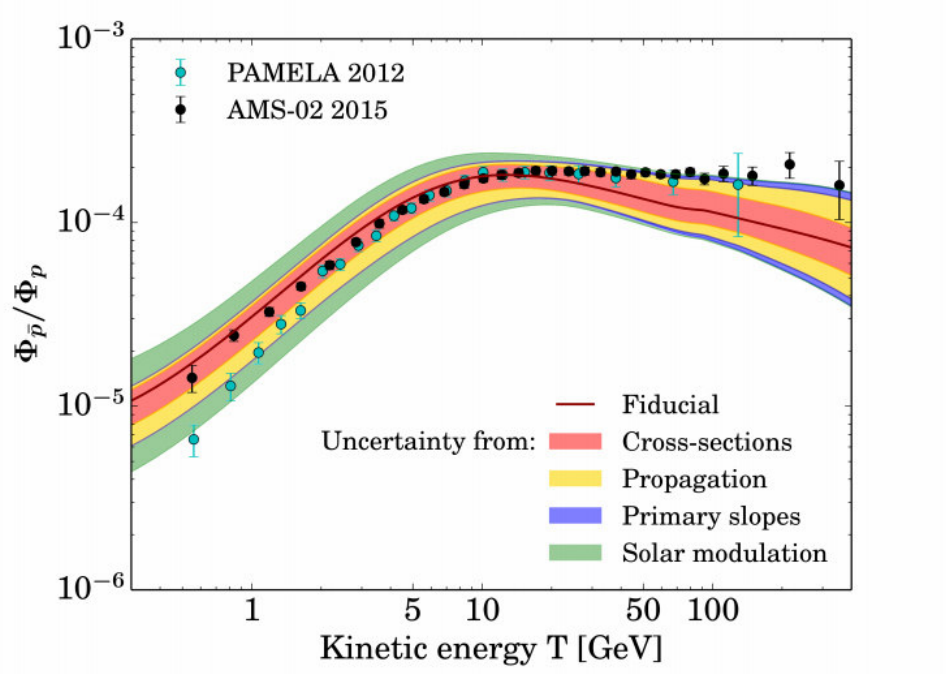

Figure 2.1: Uncertainties from cross section, CR galactic transport and solar modulation for the conventional antiproton predictions compared to the antiproton fluxes measured by the PAMELA and the AMS-02 collaborations. Credit to [59]

ventional mechanisms, although a DM interpretation for this discrepancy has still been possible by introducing a heavy massive DM [77]. In particular, an acceleration of the secondary cosmic rays, like antiprotons, was proposed to explain the AMS-02 and introduced before to explain the positron ratio anomaly. This mechanism is also supported by a mild discrepancy found between the region of parameter space pointed by the boron-to-carbon and antiproton data measured by AMS-02. Other models solved the discrepancy with spatial-dependent diffusion setups.

More recently, on the low energy side, a possible indication of excess at the level of about 10% was found in the AMS antiproton fluxes between 10 and 20 GeV as shown in Figure 2.2, right panels. This is consistent with an antiproton signal from a dark matter particle with a mass between 20 and 80 GeV and an average annihilation cross section close to the thermal value. This is shown in the left panels of Figure 2.2. This excess is compatible with DM models interpreting the gamma-ray excess at the galactic center. A deeper investigation of the uncertainties related to galactic and heliospheric propagation and a detailed study of this signal together with

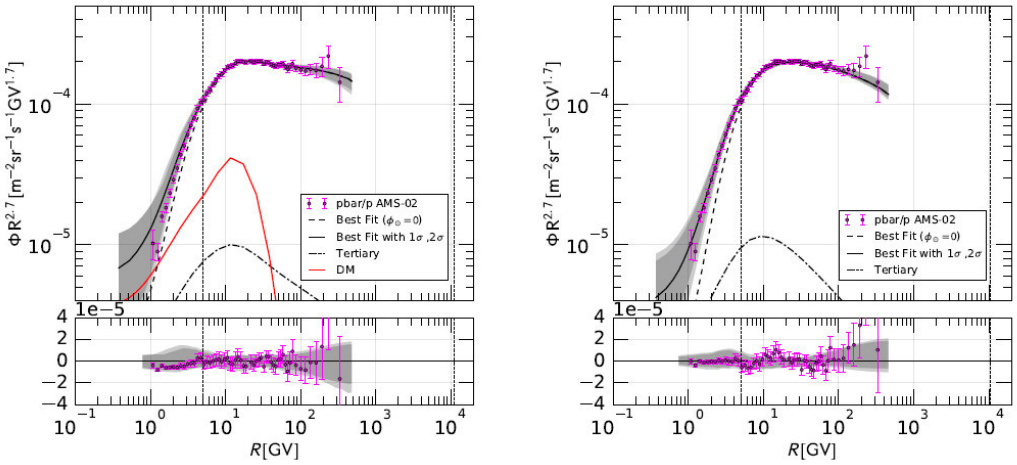

Figure 2.2: Comparison of the best fit to the $\bar{p}/p$ ratio to the AMS-02 data, with a DM component (left panel) and without DM (right panel). The lower panels display the corresponding residuals. The fit is carried out between the dotted vertical lines, i.e. for rigidities R satisfying 5 GV $< R <$ 10 TV. The grey bands around the best fit represent the 1 and 2σ uncertainty. The dashed black line shows the best fit without solar modulation effects. The solid red line represents the best fit DM contribution, whereas the dot-dashed line the contribution from astrophysical tertiary antiprotons. Credit to [60], Fig 1.

constraints from other probes is crucial to confirm the significance of this anomaly. A dominant uncertainty comes from the modelling of the cosmic-ray propagation into the interstellar and heliospheric environments, but even the cross section of antiproton production in interactions of cosmic-ray protons and helium with ISM remains a significant source of uncertainty.
Whereas AMS-02 keeps collecting data in orbit around the Earth, in the next years, balloon flights of the GAPS experiment will perform precise measurements of the antiproton spectrum in a low-energy region ($E < 0.25$ GeV) with unprecedented statistics, probing an unexplored phase space zone of the DM models. At the same time, these will also be valuable for more accurate studies of CR antinucleus propagation through the Galaxy and the Heliosphere.

2.7 Dark matter searches in cosmic ray antideuterons

A very promising cosmic-ray component for the DM indirect search is the antideuteron. This antinucleus, composed of an antiproton and antineutron strongly bonded together, was discovered for the first time in the early 1960s among the secondary particles generated from the collisions of proton beams to nuclear targets at the CERN Proton Synchrotron and the Brookhaven Alternating Gradient Synchrotron. In these processes, the produced particles were found to hadronize in a couple of antiproton and antineutron, which can coalesce on some occasions to form an antideuteron.
In cosmic rays, the antideuteron has not been detected so far, but according to the standard CR scenario, it should be produced as products of the interaction of cosmic ray protons, helium or even antiproton with hydrogen and helium atoms of the interstellar medium. The current best flux upper limits are provided by the BESS experiment [78]. More sensitive limits could be achieved in the next years by AMS-02 and GAPS (coloured areas Figure 2.3). According to some DM models, during DM annihilation or decay processes, the SM products could hadronize and coalesce in an antideuteron with a rate, that at low energies is predicted to be at least two orders of magnitude higher than the rate expected from secondary production. The high threshold energy for the antideuteron production and the steep energy spectrum of cosmic rays make that only a few particles can produce secondary antideuterons, and the produced ones have typically relatively high kinetic energy. Besides, the low binding energy of the antideuteron makes energy losses through collisions difficult. All this entails that the search for a DM signal in the antideuteron channel has an ultra-low astrophysical background at the low energies below 1 GeV/n.

This large signal-to-background ratio at low energy reveals the potentiality of such a measurement, indeed for other astroparticles like the cosmic-ray positrons and antiprotons or the γ-rays the predicted DM signals constitute only a small component on top of a large astrophysical background. Many dark matter models predict antideuteron fluxes within the sensitivities of the current operating or planned experiments, as shown in Figure 2.3, but even a missing antideuteron detection would be important to constrain these models. A measurement of cosmic-ray antideuterons is sensitive to a wide range of theoretical models, probing dark matter with a mass from O(1 GeV) to O(1 TeV). In Figure 2.3 antideuteron fluxes are reported according to three different DM candidates: a lightest supersymmetric particle (LSP) neutralino from the minimal supersymmetric model, a 5D warped GUT Dirac neutralino

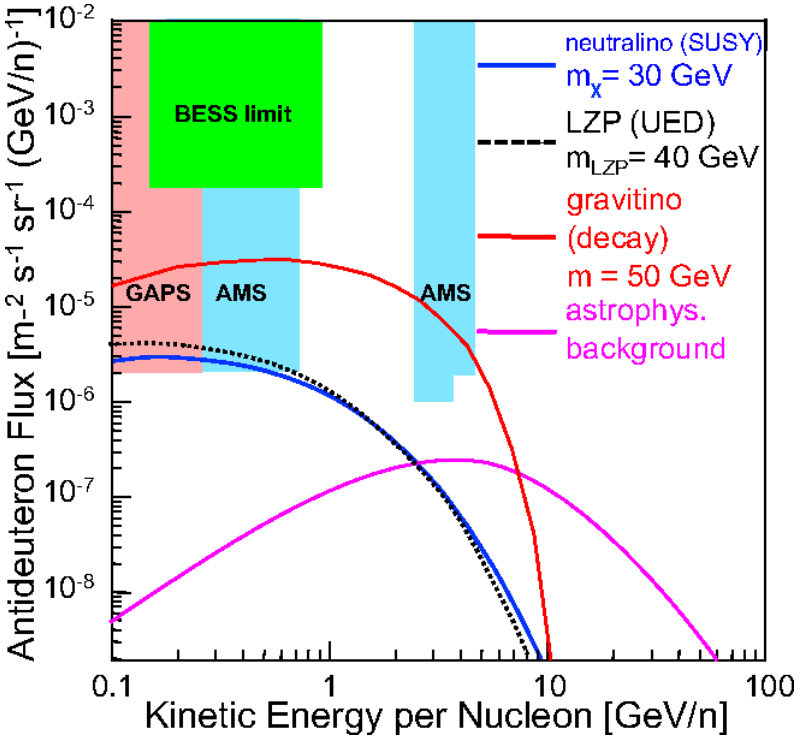

Figure 2.3: Antideuteron fluxes as a function of the kinetic energy per nucleon predicted for a 30 GeV neutralino, a 40 GeV GeV extra-dimensional Kaluza-Klein neutrino and a 50 GeV gravitino [79] [80] [81] [82]. The antideuteron limits from BESS are displayed [78], together with the projected sensitivities of AMS-02 for the superconducting-magnet configuration [83] after 5 years of operation and GAPS after three 35-day flights [84] [85]. A MED Galactic propagation scenario is assumed. The predictions use a coalescence momentum that is set to 195 MeV and the Einasto dark matter density profile. Credit to [45]

(LZP), and an LSP gravitino. The antideuteron fluxes from secondary and tertiary production are also shown. The antideuteron fluxes predicted by the three DM models exceed the background flux by more than two orders of magnitude in the energy below 0.25 GeV/n and by more an order of magnitude up to 1 GeV/n.
The predicted cosmic-ray antideuteron flux predictions rely on the modelling of the mechanisms of its production and propagation to the Earth and each of these issues are an uncertainty source. Especially the modelling of the cosmic-ray transport in the Milky Way Galaxy represents the dominant uncertainty, while the solar modulation is relevant to shape the low-energy

tail of the predicted spectrum. The hadronization and coalescence models employed to describe the antideuteron formation in both DM processes and interactions of primary CRs with the ISM are a significant uncertainty source as well. Indeed, the antideuteron production mechanism remains not well understood and needs further studies. All these issues will be treated more in detail in the next sections.
Finally, it is also paramount to note that all the DM processes capable to produce antideuterons generate at the same time a much larger antiproton flux. This makes these two DM search channels tightly linked, any prospective antideuteron signature is constrained by the observations of the CR antiproton spectrum, but at the same time, it can act as a probe to confirm or rule out potential deviations in the antiproton spectrum due to processes of DM annihilation or decay.

2.8 Antideuteron production from Dark Matter

The understanding of the antideuteron formation is essential to correctly interpret possible signatures from DM processes in this specific channel.
The coalescence model is at the base of the process of the antideuteron formation from an antiproton and an antineutron. This model was first proposed by Schwarzschild and Zupancic to describe the production of light nuclei like deuterons, tritons, helions and alpha particles in fixed target scattering experiments, but it was then extended also for the formation of the corresponding antinuclei in the products of colliders and in cosmic rays. It is based on the simplifying assumption that the (anti)nucleons within a sphere of radius p_0 in momentum space may coalesce to produce an (anti)nucleus. Therefore, any $\bar{p}\bar{n}$-pair with a $\Delta p < p_0$ condition may coalesce to produce an antideuteron. The coalesce momentum p_0 is a phenomenological quantity and has to be determined through fits to experimental data, whereas Δp is defined as $\Delta p = k_p^\mu - k_n^\mu$, where k^μ is the quadri-momentum of a(n) (anti)nucleon.
The strength of this simple model is that under the assumption of isotropic and uncorrelated (anti)proton and (anti)neutron momentum distributions, an analytic expression can be found for the spectra of different (anti)nuclei in terms of the (anti)nucleon spectra and the coalescence parameter p_0. For the case of the antideuteron one can obtain:

$$\frac{dN_{\bar{d}}}{dK_{\bar{d}}} = \frac{p_0^3}{6}\frac{m_{\bar{d}}}{m_{\bar{n}}m_{\bar{p}}}\frac{1}{\sqrt{K_{\bar{d}} + 2m_{\bar{d}}K_{\bar{d}}}}\frac{dN_{\bar{n}}}{dK_{\bar{n}}}\frac{dN_{\bar{p}}}{dK_{\bar{p}}}, \tag{2.7}$$

where m_i, K_i, and dN_i/dK_i are respectively the mass, the kinetic energy and the differential yield per event of a particle i.
It must be noticed that the assumptions of isotropic and uncorrelated nucleon spectra are good approximations only for low-energy or minimum bias nuclear interactions, i.d. the physical cases for which this model was thought. They are no longer worth in elementary particle interactions such as dark matter annihilation or decay and $p - p$ collisions at low center-of-mass energies. In fact, in these cases the (anti)nucleons are typically produced in geometrically restricted QCD jets and this leads to a strong correlation between (anti)nucleons on a per-event basis.
To take into account these correlations, it is possible to apply the coalescence condition to $\bar{p}\bar{n}$-pairs on a per-event basis in Monte Carlo events. However, this procedure has the disadvantage of needing four orders of magnitude more events than the isotropic approximation to achieve the same level of statistical errors on the predictions.
Currently, the coalescence momentum p_0 can not be calculated from first principles and therefore it must be determined from fits to the experimental results on antideuteron production. However, it was found that different event generators provide different p_0 values when compared to a particular experiment and even the same event generator gives inconsistent values of p_0 for different experiments differing in energy and interaction type. This entails a significant systematic uncertainty for p_0. This uncertainty is particularly significant for the cosmic-ray antideuteron search, because of the strong dependence of the antideuteron yield on the coalescence momentum $N_{\bar{d}} \propto p_0^3$. According to the current Monte Carlo simulations, the mechanisms of antideuteron production carries an uncertainty of around an order of magnitude on the predicted fluxes.
Another quantity to be taken into account in the antideuteron formation is the spatial separation, since the nuclear interactions occur typically on scales of a few femtometers. For the case of weakly decaying particles with long lifetimes, these could travel for macroscopic decay lengths and antinucleons could be produced too far from the primary interaction vertex to be able to interact with antinucleons in the primary collision. To take into account also this aspect, weakly decaying particles can be considered stable in this context.

2.9 Antideuteron propagation in the Galaxy

After their formation, the cosmic-ray antinuclei propagate from the galactic halo to the Galactic disk, here they continue to travel up to arrive at the

Heliosphere boundaries. Along their path, they are deflected by the galactic magnetic field, they lose energy through the interaction with the interstellar medium or in some cases they are destroyed by fission or annihilation events. The mechanisms of cosmic-ray propagation in the Galaxy are the main source of uncertainty in the predictions of the cosmic-ray antinucleus fluxes at Earth. Different choices for the parameters of the propagation models can predict antideuteron fluxes differing up to an order of magnitude. The parameter values are typically constrained by cosmic-ray measurements of primary fluxes and secondary-to-primary flux ratios, however the fits of these measurements still leave a strong degeneracy between the parameters. Especially the degeneracy between the diffusion coefficient D_{xx} and the galactic halo size L is highly relevant for the predictions of a DM signal in the antideuterons. This is proportional to the amount of cosmic rays generated by dark matter processes taking place within the Galactic halo, therefore a larger Galactic halo produces more dark-matter-induced antideuterons. Whereas antideuterons from secondary production are produced in the Galactic disk and different choices of the Galactic halo size keep almost unchanged their predicted LIS, this is not worth for the antideuterons generated from DM processes, for which models with different halo sizes can predict at low energies antideuteron fluxes differing of an order of magnitude, as shown in Figure 2.4.
To break the D_{xx}/L degeneracy a radioactive-secondary-to-stable-secondary flux ratios such as $^{10}Be/^{9}Be$ have been used. In fact, radioactive secondaries decay before reaching the Galaxy edge and therefore they can not escape, this makes their modelling independent of the Galactic halo size L. However, according to several studies, this method is very sensitive to the local ISM modelling and strongly affected by the presence of a local under-density, known as local bubble. In addition, the lack of precise measurements over sufficient large energy does not allow a precise estimation of the halo. Indirect constraints on the halo size can anyway be obtained from the analysis of diffusive γ-rays or radio emissions, which disfavor both very small ($L \leq 2$ kpc) and very large ($L \geq 10$ kpc) halo size. Unfortunately, the predictions of these observables rely on additional model parameters with non-negligible systematics and correlations.
Besides, a proper determination of the effects induced by changing the profile of the galactic DM distribution can not be separated from the properties and size of the galactic disk and halo, because the measured antinuclei can not be traced back to the place where the dark matter process occurred. Therefore the uncertainty about the DM profile in the Galaxy must be added as an additional source of systematic error for the predicted LIS of DM-induced antinuclei.

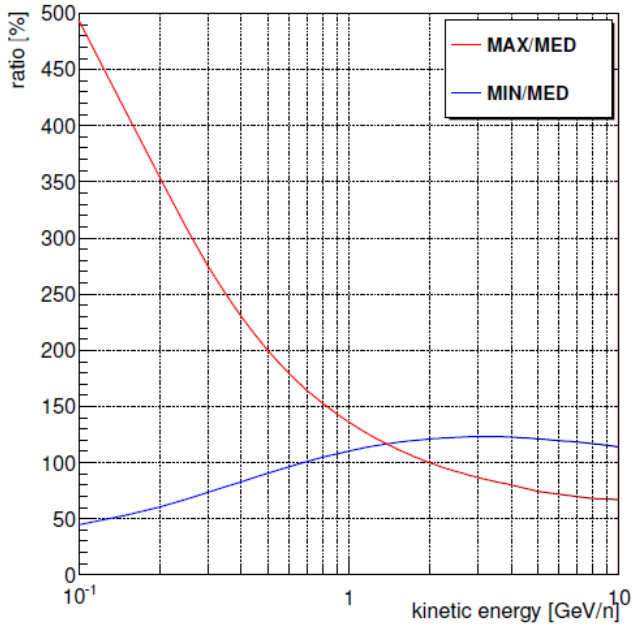

Figure 2.4: Ratios of the antideuteron fluxes from dark matter annihilation (m_{DM} = 100 GeV, $b\bar{b}$ channel) in MAX and MIN propagation models with respect to the a MED propagation model. Credit to [45]

2.10 Solar modulation effects for antinuclei

Crossed the Heliosphere boundaries, the cosmic-ray antinuclei experience along their path the interaction with the turbulent solar wind and the embedded heliospheric magnetic field. As a consequence, at low energy, the CR antinucleus spectrum measured at the Earth is affected in its shape and intensity by the solar modulation, as discussed in chapter 1.
Below a few tens of GeV, an accurate prediction of the antiproton and antideuteron signals from both dark matter and secondary production requires proper modelling of the solar modulation mechanisms. Antiproton and antideuteron measurements as a function of time would allow studying and modelling very well the solar modulation effects on their fluxes for different solar activity phases and heliospheric magnetic polarity. Unfortunately, such a time dependence study has not been possible so far.
Usually, the solar modulation models are calibrated with proton measurements. These differ from the corresponding antiparticles for their higher abundance in CRs and the different drift patterns they follow because of the opposite electric charge. Approximated estimations of the solar modulation

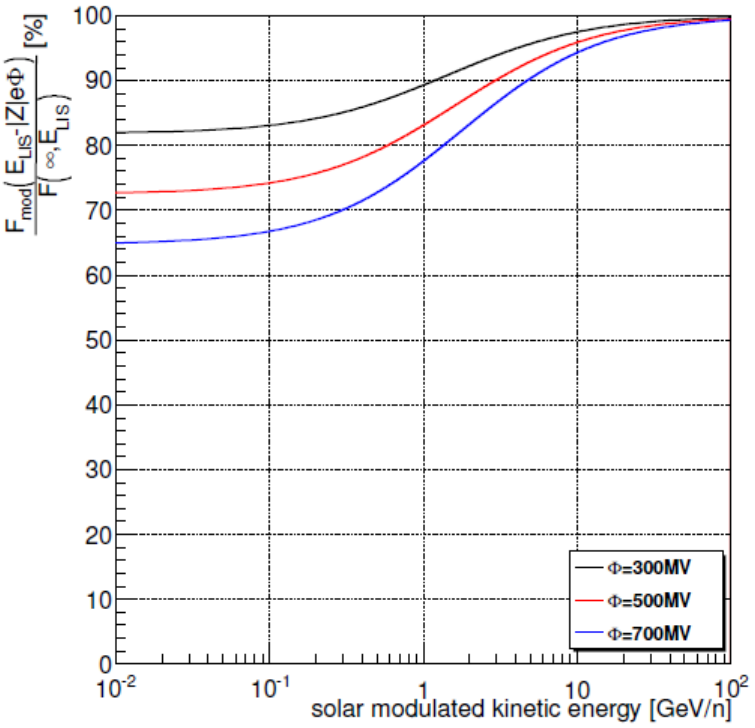

Figure 2.5: Solar modulation effect for antideuterons as a function of the kinetic energy calculated using the force-field approximation. Credit to [45]

effects were already obtained for antideuterons using the force-field approximation, for different choices of its modulation parameter Φ representing different solar activity phases, the results show at 100 MeV/n a modulation effect at the level of 25%, as it can be seen in Figure 2.5. However, the force-field approximation has some criticalities, even more if applied on extremely rare cosmic-ray antiparticle components like the antideuterons. First of all, the force field treats the solar modulation with only one modulation parameter assumed equal for every CR species. Furthermore, the force-field approximation does not take into account the charge-sign of the considered CR species and consequently neither the related charge-sign effect introduced by the drift motion as well. A more precise solar modulation model, like that described in chapter 1, has to be used.

For an accurate study of the charge-sign dependence of the solar modulation effects, measurements of particle and antiparticle fluxes in CRs over an extended period are crucial. Such measurements are currently available only for the cosmic-ray electrons and positrons, provided by PAMELA and

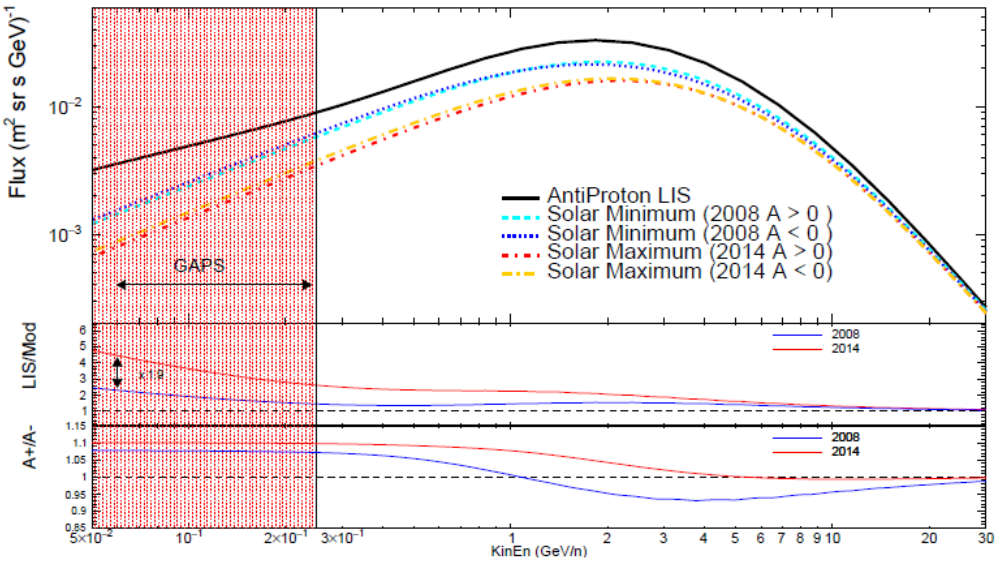

Figure 2.6: Top panel: antiproton flux for solar minimum and maximum from a 3D numerical model for solar modulation. Both the solar minimum and maximum spectra were evaluated for positive and negative polarity of the HMF ($A > 0$ and $A < 0$) to probe the charge-sign effect introduced by the drift motion. Middle panel: the ratio between the LIS and the modulated spectra for the period maximum of the minimum and maximum solar activity assuming with $A < 0$ polarity. Bottom panel: ratio between the modulated spectra for opposite polarity of the HMF for the minimum and maximum solar activity phases. Credit to [46]

AMS-02. These results studied with the 3D model of solar modulation have demonstrated in [86] that the drift mechanism, which introduces the charge-sign dependence, is relevant but not dominant during a solar minimum phase like that recorded between 2006 and 2009, while it is almost negligible during a period of higher solar activity and HMF polarity reversal, like that observed between November 2012 and March 2014. In [86] it is also shown that the 3D model of solar modulation has reproduced well the electron and positron fluxes and related ratios using the same modulation parameters for both electrons and positrons, which differed in this way only for the introduced LIS as input and the experienced drift motions. There is no physical evidence that this could not be worth for the other CR species as well.

Some preliminary modelling studies for antiprotons and proton-to-antiproton ratios have already been performed [87]. These results, displayed in Figure 2.6, show that the antiproton flux for solar period minimum as in 2008

a factor 2 higher than in a period of solar maximum as in 2014. Besides, the antiproton results from the model for a same period of solar activity but opposite HMF polarity (equivalent to flip the charge sign of the particle) show a difference of around 10%, clearly not included in a force field approach.
For the antideuteron case, the issue is more complicated because precise and continuous measurements of CR deuteron fluxes below a few GeVs over different solar acidity phases are still missing. Such deuteron measurements are needed to calibrate the modulation parameters of the 3D model of solar modulation as well as their rigidity and time dependence. The deuteron fluxes as well as deuteron-to-proton ratios obtained in this thesis work have exactly the purpose to provide such measurements. After being calibrated to reproduce the obtained deuteron results over time with different heliospheric conditions, this solar-modulation model with a theoretical antideuteron LIS as input and changing the charge sign will be able to predict the solar modulated antideuteron spectra expected at Earth after transport effects in the Heliosphere. Such a modelling development will reduce the current uncertainty induced by solar modulation modelling for the antideuteron component, allowing getting more sensitivity to possible DM signals.

Chapter 3

PAMELA and GAPS experiments

This chapter provides a general description of the PAMELA and GAPS experiments. First, the PAMELA mission and its goals are briefly discussed, followed by an overview of the detectors composing the PAMELA apparatus. A deeper description is provided for the Time-of-Flight system and the magnetic spectrometer, which were the most used detectors in the analysis work performed on the PAMELA data. Later, the GAPS mission as well as its scientific goals are also discussed. The GAPS detecting design and the detection technique studied to measure the galactic antinuclei rejecting the huge background of cosmic-ray particles are described in detail.

3.1 PAMELA experiment

PAMELA (Payload for Antimatter Matter Exploration and Light-nuclei Astrophysics) was an earth-orbiting experiment designed to detect cosmic rays, with a particular focus on the antiparticle component, mainly antiprotons and positrons [88]. PAMELA was installed on board the Russian Resurs-DK1 satellite inside a pressurized container of cylindrical shape and made of a 2 mm thick aluminium alloy. The satellite was launched into orbit on 15^{th} June 2006 by a Soyuz-U rocket from the Baikonur cosmodrome in Kazakhstan. From that moment, PAMELA had been almost continuously taking data until the end of January 2016.
The goals of the PAMELA mission were the investigation of the dark matter, the baryon asymmetry in the Universe, cosmic ray generation and propagation in our galaxy and in the solar system, the antimatter component of cosmic radiation, studies of solar modulation, and the interaction of cosmic

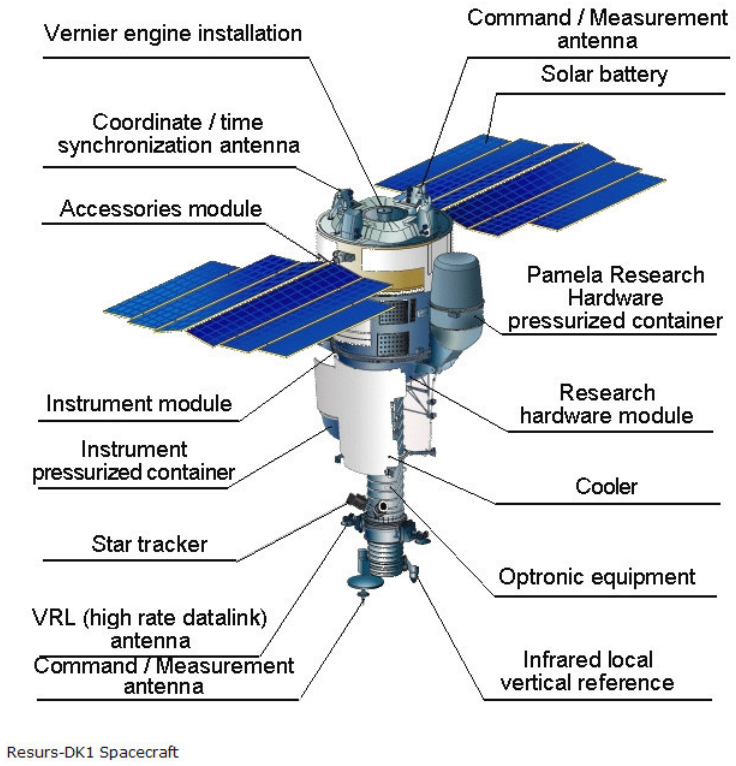

Figure 3.1: A sketch of the Resurs-DK1 satellite hosting the PAMELA experiment in a Pressurized Container [89].

rays with the earth's magnetosphere.

3.1.1 The Resurs-DK1 satellite and its orbit

Resurs-DK1, shown in Figure 3.1, was designed in Russia to perform multispectral remote sensing of the earth's surface and acquire high-quality images in near real-time [90]. It had a mass of ~ 7.7 tonnes and a height of 7.4 m. The length of the solar array was about 14 m.

Resurs-DK1 followed a Low Earth Orbit, which was initially elliptical and semipolar with an altitude between 350 km and 610 km and an inclination of 70°. In 2010 it was modified and got circular at a height of about 600 km, maintaining the same inclination.

All data recorded by Resurs-DK1, including those recorded by PAMELA, were sent to the ground with a high-speed radio connection. The ground segment of the Resurs-DK1 system was located at the Research Center of Earth Operating Monitoring (NTs OMZ) of the Roscomos in Moscow, Russia.

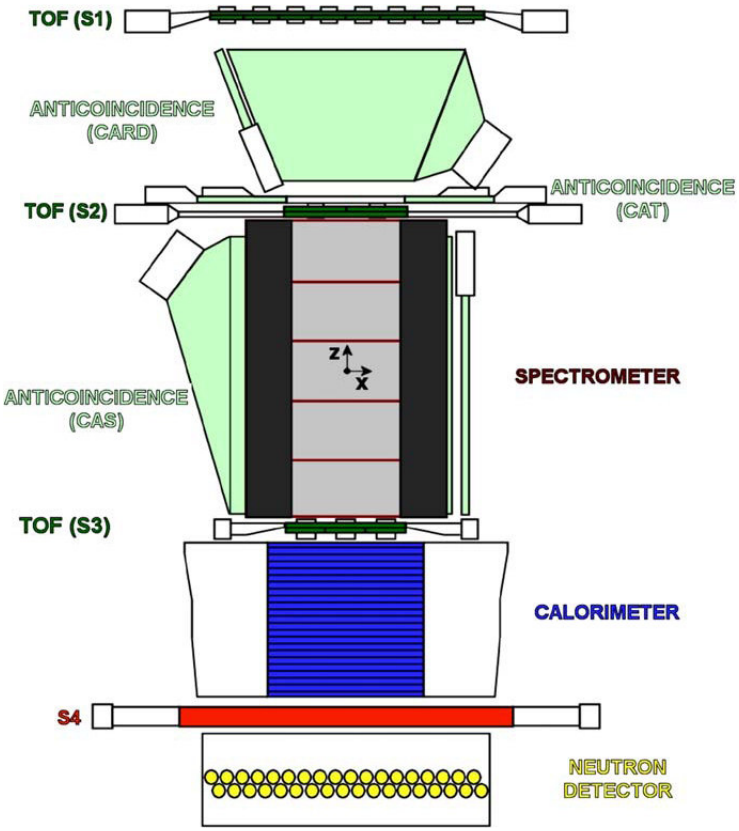

Figure 3.2: A schematic overview of the PAMELA apparatus with its subdetectors [89]. The magnetic field lines in the spectrometer are oriented along the y-direction.

Later, PAMELA raw and preliminarily processed data were moved through an internet line to the storage center located at MePHI in Moscow. From there, GRID infrastructure was used to move raw and first-level processed data to the main storage and analysis center of the PAMELA collaboration, located at CNAF (Bologna, Italy), a specialized computing center of INFN. From this hub, data were accessible to all various institutes within the PAMELA collaboration.

3.1.2 The PAMELA apparatus

PAMELA was about 1.3 m high, it had a mass of 470 kg and average power consumption of 355 W [88, 91]. As shown in Figure 3.2, PAMELA was composed of several detectors: a Time-of-Flight system, a magnetic spectrometer, an anticoincidence system, an electromagnetic calorimeter, a shower

tail catcher scintillator and a neutron detector. Their combined use allows identifying several cosmic-ray species with a high rejection power in a wide energy range.
The magnetic spectrometer was the core of the PAMELA apparatus, it was equipped with 6 planes of doubled-sided silicon detectors located inside a magnetic cavity with a permanent magnetic field of 0.43 T. Planes of plastic scintillators mounted above and below the spectrometer formed a Time-of-Flight (ToF) system, which also provided the primary experimental trigger. The combined use of the information about the track curvature measured in the magnetic spectrometer and of the incoming direction provided by the ToF system enables the separation of positively and negatively charged particles. Moreover, measurements of the ionising energy losses in the scintillators of the ToF system and in the silicon detectors of the magnetic spectrometer allow determining the absolute charge and the momentum of the traversing particle.
The spectrometer was also surrounded by plastic scintillator shields forming the anticoincidence system. Below the spectrometer, there was an electromagnetic calorimeter, that measured the energy of incident electrons and it enables to distinguish electromagnetic- and hadronic showers and non-interacting particles. A plastic scintillator was located below the calorimeter and aids in the identification of high-energy electrons. This scintillator was followed by a neutron detector, which improves the calorimeter capacity to discriminate between hadronic and electromagnetic showers.
In the next sections, all these detectors are described more in detail.

3.1.3 The Time-of-Flight system

The ToF system was composed of six layers of fast plastic scintillators (Bicron BC-404) [92] arranged in three double planes called S1, S2 and S3, shown in Figure 3.3.
The distance between S1 and S3 was 77.3 cm. S1 and S3 were 7 mm thick while S2 was 5 mm thick. The sensitive area of each S1 layer was (33×40.8) cm^2, with the first layer (S11) divided into 8 paddles and the second layer (S12) divided into 6 paddles. Each layer of S2 and S3 planes (named S21, S22, S31, S32) had a sensitive area of (15×18) cm^2 and it was divided into 2 (for S2) or 3 (for S3) paddles. For each plane, the paddles of the upper layer were orthogonal to those of the lower layer to obtain a bidimensional geometrical measurement of the impact point of a charged particle. The position of the hit point along the main dimension of a scintillator paddle (for example x) is proportional to the difference of the time measurements

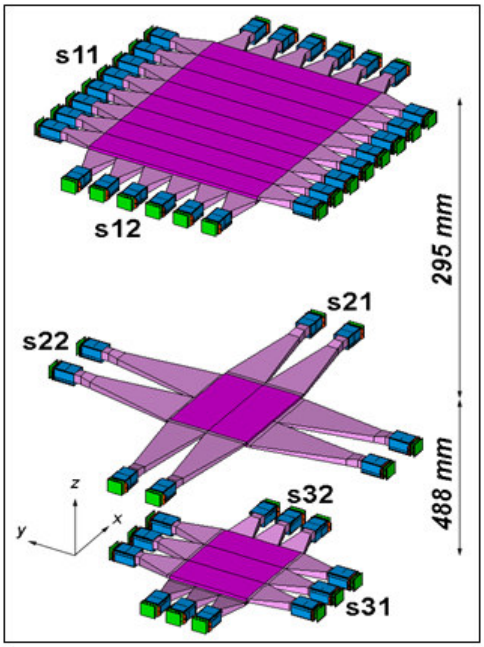

Figure 3.3: A schematic overview of the six scintillator layers (S11, S12, S21, S22, S31 and S32) of the PAMELA ToF system [89].

t_1 and t_2 at the two sides of the paddle:

$$x = \frac{v_{eff}(t_1 - t_2)}{2} + k \qquad , \tag{3.1}$$

where v_{eff} is the signal velocity inside the scintillator and k a parameter coming from the calibration.
The ends of each of the 24 scintillator paddles were glued to adiabatic UV-transmitting Plexiglas light guides, which were coupled to Hamamatsu R5900U photomultipliers (PMTs) through silicone pads with thickness 3 mm for S1 and S2 and 6 mm for S3. The scintillators and light guides were wrapped in 2 layers of 25 μm thick Mylar foil. A high-voltage circuit was mounted directly behind each PMT. The high-voltage and discrimination threshold of each PMT were chosen to optimize the performance of a given ToF paddle.
The ToF electronics system converted the 48 PMTs pulses into (TDC) time- and (ADC) charge-based measurements. In the TDCs a capacitor was linearly charged during a time interval defined by the passage of a particle through the ToF system. In ADC a capacitor was charged with the PMT pulse charge. In both cases, during the read-out, the capacitor was linearly

Intrinsic time resolution of a ToF paddle	
Z	Δt
1	117.3±0.7
2	122±4
3	114±4
5	50±2
6	46.5±0.3

Table 3.1: Time resolution of a ToF paddle for different samples of nuclei.

discharged into an analogical to digital converter.
The combined TDC information of the whole ToF system was used to measure the flight time of the incoming particle and to generate the main PAMELA trigger. The trigger conditions are described in detail in Section 3.1.10.
Test with particle beams [93] were performed at the ground before the PAMELA launch to evaluate the time resolution of a single paddle of the ToF system for each nucleus family from hydrogen to carbon. The values for the time resolution are summarized in Table 3.1. The improvement in time resolution for higher charges seen in Table 3.1 is due to the higher number of photons produced by particles in the scintillator with respect to that measured for a proton of equal energy per nucleon.
The time-of-flight resolution measured for the full ToF system was equal to $\sim$ 250 ps. The time-of-flight information combined with the track length information provided by the magnetic spectrometer was used to determine the velocity of any crossing particle. This gives useful information to reject albedo particles or secondary particles produced in the mechanical structure of the apparatus.
The ADC information provides independent measurements of ionisation energy loss over path length (dE/dx) in each ToF plane. The energy released inside any scintillator by a charged particle is proportional to the mean charge deposited, Q. This feature is clear by looking at the number of photoelectrons (PEs) produced in each PMT, which is related to Q through the formula

$$PE = \frac{Q}{e \cdot G} \quad , \tag{3.2}$$

where Q is the released charge, e is the elementary charge and G is the gain of the PMT. The mean number of PEs produced in S3 is greater than that in S1 and S2 paddles, because S3 is thicker than S2 (more photons produced) and shorter than S1 (less attenuation) [93]. The charge Q can be measured by converting the ADC signal (in units of ADC channels) into charge (in units of pC) and correcting this value for the attenuation of light in the scin-

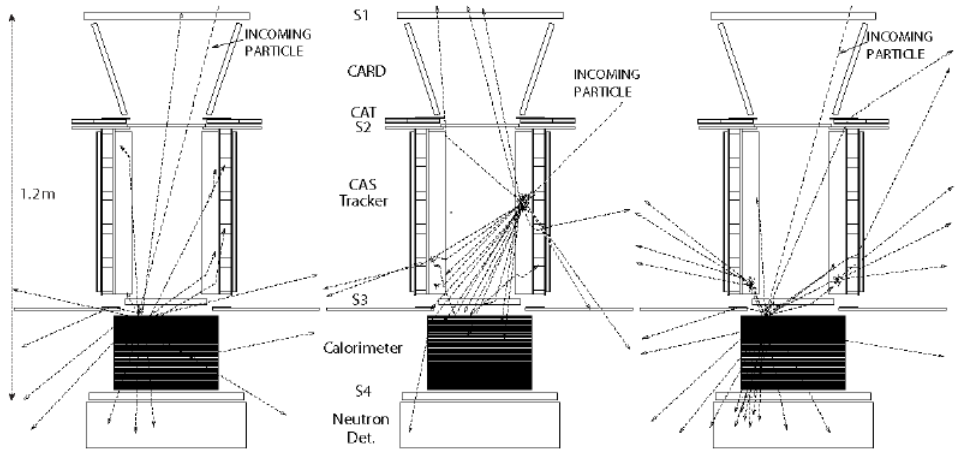

Figure 3.4: Schematic representation of simulated proton interaction in the PAMELA apparatus [88]. Left: a good trigger event without anticoincidence (AC) activity. At middle: a false trigger created by a particle entering the apparatus from the side generating a shower and AC activity. Right: particles backscattered from the calorimeter, which can also give rise to AC activity for good trigger.

tillator.
Measurements of the ionisation energy loss over path length (dE/dx) combined with measurements of velocity enable the identification of the particle absolute charge at least up Z=8 with a satisfactory resolution.

3.1.4 Anticoincidence system

The anticoincidence system was used to identify, during offline data analysis, the false triggers generated by energy deposits in the ToF scintillators caused by interactions of cosmic rays with the satellite or near the apparatus (see Figure 3.4). PAMELA contained two anticoincidence (AC) systems [94]. The primary AC system consisted of four plastic scintillators (CAS) surrounding the sides and one covering the top (CAT) of the magnetic spectrometer. A secondary AC system consisted of four plastic scintillators (CARD) that surrounded the volume between the first two ToF planes. The CARD detectors were scaled-down versions of CAS. Each CARD and CAS detector was read out by two identical PMTs to decrease the probability of single-point failure. For this reason and because of the irregularly shaped area, the CAT detector was read out by eight PMTs. The scintillators and PMTs of the AC system were located in aluminium containers, fixed to the PAMELA apparatus.

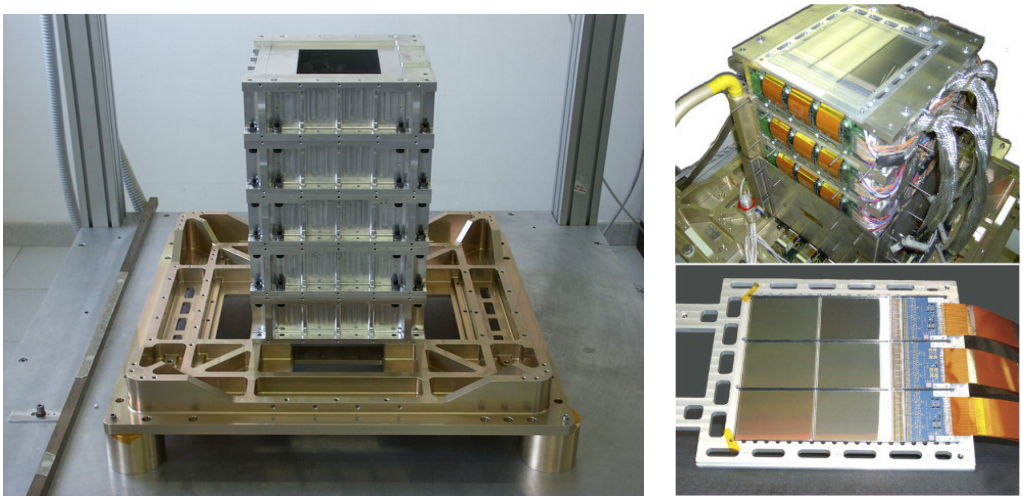

Figure 3.5: Left: the permanent magnet on a platform at ground [89]. Right: at the top an overview of the magnetic spectrometer showing the top silicon plane, on the bottom a silicon plane comprising three silicon strip detectors and front-end electronics [91].

3.1.5 Magnetic spectrometer

The magnetic spectrometer consisted of a permanent magnet and a silicon tracker [95], shown in Figure 3.5.

The magnet was composed of five modules forming a tower 44.5 cm high. Each module comprised twelve blocks in a Nd-Fe-B alloy configured to provide an almost uniform magnetic field oriented along the y-direction inside a cavity of dimensions (13.1×16.1) cm^2. Figure 3.6 shows the y-component of the magnetic field measured in the $z = 0$ plane as a function of x and y and the y-component as measured along the z-axis. The mean magnetic field inside the cavity of the spectrometer was 0.43 T with a value of 0.48 T measured at the centre. To attenuate the stray magnetic field outside the cavity, the magnet was enclosed by a ferromagnetic shield. Accurate knowledge of the magnetic field inside the cavity allowed to perform precise rigidity measurements from the reconstructed particle trajectory.

Six equidistant 300 μm thick detecting planes were inserted inside the magnetic cavity. Each plane was built from three ladders, the basic detecting units, inserted in a carbon fiber frame. Each ladder comprised two double-sided orthogonal silicon sensors, (5.33×7.00) cm^2, assembled with a front-end hybrid circuit to provide two independent impact coordinates on each plane. The front-end electronics system was a circuit based on the VA1 chips containing 128 charge-sensitive preamplifiers. The signal from the chips was sent

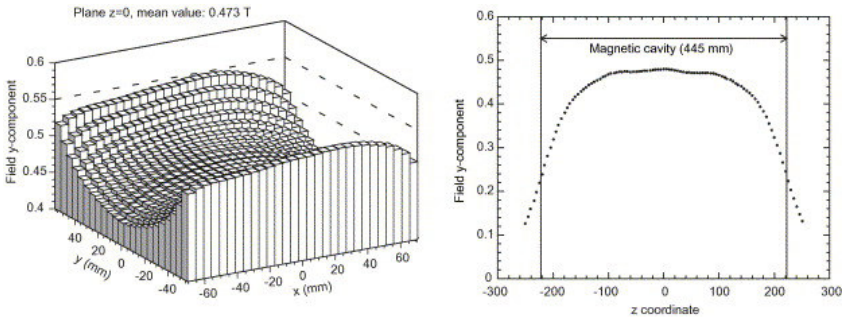

Figure 3.6: Left: plot of the y-component of the spectrometer magnetic field measured in T at z=0. Right: the variation of the y-component of the spectrometer magnetic field (T) evaluated along the z-axis (mm) [88].

through 5 cm long Kapton cables to ADC boards mounted on the magnet.
The main task of the spectrometer was to measure the deflection η of a particle due to its inner magnetic field, in order to determine the rigidity as $\rho = \frac{1}{\eta}$ for particles up to $\sim$ 1 TV/c.
Measurements of the ionisation energy loss were also made in the silicon planes, allowing the identification of the particle absolute charge up to at least Z=6
Using the combined information about rigidity and the absolute value of the electric charge, the linear momentum p and the electric charge Ze of the particle can be derived from the relation $\rho = \frac{pc}{Ze}$.
For this purpose, an algorithm, based on the numerical integration of the equation of motion was developed and checked through tests with particle beams at the ground [96]. This algorithm identifies for each tracker plane the so-called *cluster*, that is the group of strips that collected charges created at the passage of a charged particle in the detector. In fact, under the effect of the electric field inside the reverse polarized junction material, the produced charges could migrate towards one or more strips, where they were collected and converted in a signal.
To determine the hit coordinates in every tracker plane, a technique, named the non-linear η algorithm, was used. It was based on a mean of the coordinates of the cluster strips, weighted with the measured signals. However, further features were introduced in the calculation to account for the real non-linearity of the charge division between the strips. Then, for each event with at least a hit point reconstructed in each tracker plane, a group of trace candidates, considering all possibilities of 5 clusters, were evaluated with the use of a tracking algorithm. An iterative procedure of minimization of the sum of the squared gaps between the measured coordinates belonging to the

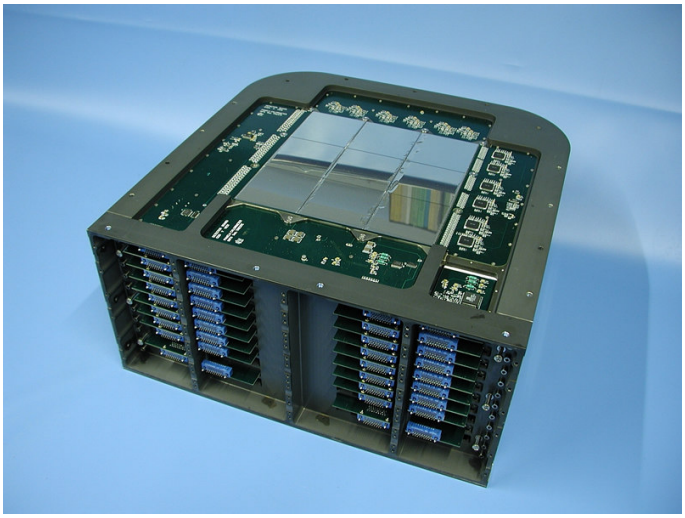

Figure 3.7: The PAMELA electromagnetic calorimeter with the top silicon plane visible [89].

traces and the coordinates evaluated by the algorithm was used to select the tracks and from these the deflection.
The resolution in the deflection measurement depends on the geometrical configuration of the spectrometer, on the intensity of the magnetic field and on the spatial resolution of the silicon sensors. The spatial resolution depends on the particle incident angle. For normal incident tracks tests with particle beams showed a spatial resolution of (3.0±0.1) μm and (11.5±0.6) μm in the bending and non-bending view respectively.

3.1.6 Electromagnetic calorimeter

The main task of the calorimeter was to provide a high rejection power to separate hadrons from leptons. The sampling electromagnetic calorimeter, displayed in Figure 3.7, comprised 44 single-sided silicon sensor planes interleaved by 22 plates of tungsten absorber [97]. Each tungsten layer had a thickness of 0.26 cm, which corresponds to 0.74 X_0 (radiation lengths), giving a total depth of 16.3 X_0 ($\sim$ 0.6 nuclear interaction lengths). The silicon detectors are large area devices (8×8) cm^2, 38 μm thick and segmented in 32 strips. The orientation of the strips of two consecutive layers was orthogonal to provide two-dimensional spatial information. The longitudinal and transverse segmentation of the calorimeter, combined with the measurement of the particle energy loss in each silicon strip, allowed a high identification power of the electromagnetic shower. Electromagnetic and hadronic showers

differ in their spatial development and energy distribution, these features are used by the calorimeter to distinguish them. The calorimeter was also used to reconstruct the energy of the electromagnetic showers, measuring the energy of the incident electrons independently from the spectrometer. This allowed cross-calibration of the two-energy determinations.

3.1.7 Shower tail catcher scintillator (S4)

The shower tail catcher scintillator (S4) in Figure 3.8 improved the PAMELA electron-hadron separation performance by measuring shower leakage from the calorimeter [88]. The scintillator was placed below the calorimeter and consisted of a single square scintillator of 1 cm thick of dimensions 48×48 cm^2, read out by six PMTs. It also provided a high-energy trigger for the neutron detector.

3.1.8 Neutron detector

The neutron detector was sensitive to evaporated neutrons, which were thermalized in the calorimeter [98]. The number of neutrons generated in a hadronic shower is 10-20 times larger than that expected in an electromagnetic one, this allowed the neutron detector to complement the electron-proton discrimination capabilities of the calorimeter.
The neutron detector $(60 \times 55 \times 15)$ cm^3 was located below the S4 scintillator and it was composed of 36 ^3He proportional counters, shown in Figure 3.8. These counters were surrounded by a polyethylene moderator enveloped in a thin cadmium layer to prevent thermal neutrons from entering the detector from the sides and from below. The counters were stacked in two planes of 18 counters, oriented along the y-axis of the instrument. The moderator was used to slow down the neutrons coming from the calorimeter at such a speed that the probability of interaction with ^3He increased because the cross section of the process depends on $1/v$, where v is the neutron velocity.

3.1.9 Data acquisition

A schematic overview of the PAMELA data acquisition (DAQ) system is shown in Figure 3.9. The PSCU (PAMELA Storage and Control Unit) handled all slow controls, communication with the satellite, data acquisition, storage and downlink tasks.
The PSCU was composed of 4 subsystems [88]:

- a processor module built around a CPU, running the RTEMS real-time operating system at 24 MHz;

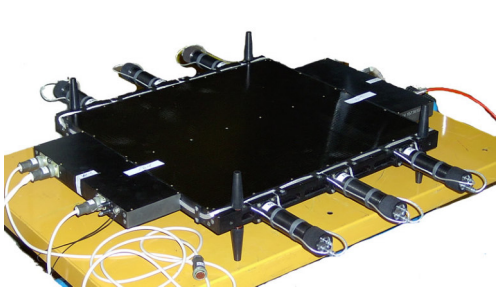

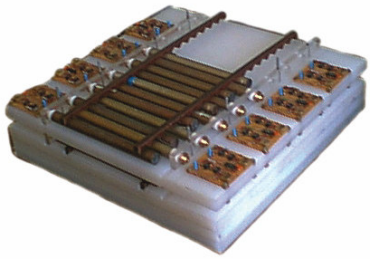

Figure 3.8: Left: The PAMELA shower tail catcher scintillator, S4, with the six PMTs used for read-out [89]. Right: The PAMELA neutron detector partially equipped with ^3He proportional counters [89].

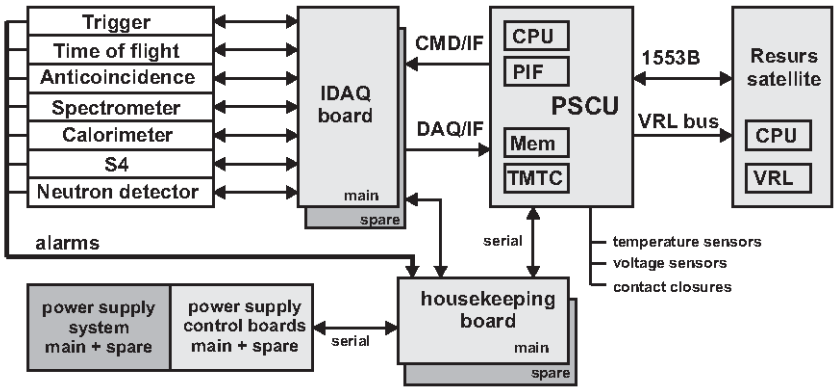

Figure 3.9: Schematic view of the PAMELA DAQ system [89].

- two redundant 2 GByte mass memory modules;
- a PIF (PAMELA interface board) that performed the communication with the IDAQ system;
- a TMTC (Telemetry and Control) board that handled the housekeeping operations of PAMELA, like alarm, temperature and voltage monitoring.

Data acquisition from the detectors was managed by the IDAQ system at a rate of 2 MByte/s. For each trigger, the PSCU initiated the IDAQ procedure to read out data from the detectors and the resulting data were stored in the PSCu mass memory. Several times a day, the data were transferred to the

satellite on board memory via a 12 MByte/s VRL bus, where they were stored before the downlinking to the ground.

3.1.10 Trigger system

The PAMELA trigger condition was defined by coincident energy deposits in the scintillator ToF layers. The standard trigger configuration required the coincidence of at least one TDC signal from each of the three ToF double planes. The default conditions [88] requested were:

- ($S11$ or $S12$) and ($S21$ or $S22$) and ($S31$ or $S32$) outside radiation belts and South Atlantic Anomaly (SAA);
- ($S21$ or $S22$) and ($S31$ or $S32$) inside radiation belts and SAA.

According to the PAMELA simulation, the radiation environment saturated the S1 counting rate but it did not affect the S2 and S3 scintillators, because these were more shielded.
A total of 29 trigger configurations were implemented using combinations of *and* and *or* of the scintillator layers with or without the calorimeter self-trigger and the S4 trigger. These trigger configurations could be changed from the ground with dedicated commands to the PSCU.
The self-trigger of the calorimeter was activated by a signal generated when a specific energy distribution was detected in predetermined planes within the lower half of the calorimeter. These trigger configurations allowed PAMELA to enlarge its default acceptance and measure rare events, like very high-energy (from 300 GeV to > 1 TeV) electrons in the cosmic radiation.

The trigger rate observed during typical orbits is shown in Figure 3.10. The maxima at 2200 events per minute (35 Hz) correspond to passages over the polar regions (North Pole, NP and South Pole, SP), while the minima (15 Hz) correspond to equatorial regions (E). The contribution from the South Atlantic Anomaly (70 Hz) was recorded using the second default trigger configuration. The missing acquisition time after the peaks of the SAA corresponds to the detector calibrations upon crossing the equator (about 1 minute in duration).
Dead and live times were monitored by two clocks that counted the time during which the data acquisition system was busy or waiting for a trigger respectively. The dead time varied significantly over an orbit, due to the large changes in trigger rate shown in Figure 3.10. The dead time also depended on the trigger configuration. For an orbit not crossing the SAA the fraction of dead time was approximately 26% and the fraction of live time was the remaining $\sim 74\%$.

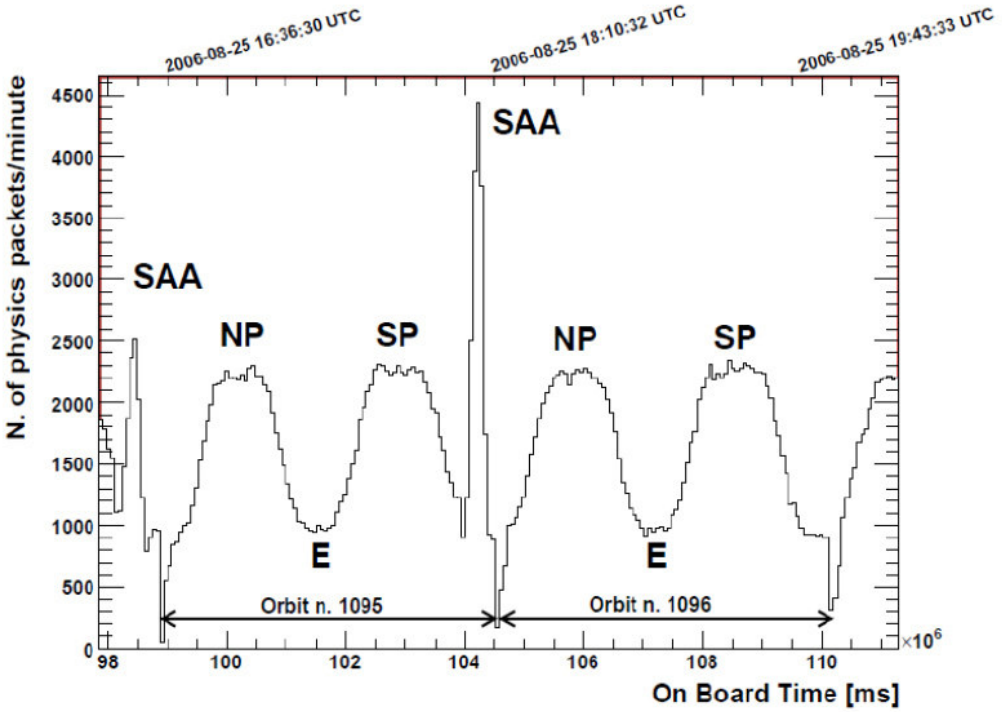

Figure 3.10: The PAMELA trigger rate shown in events per minute evaluated during two consecutive orbits (period $\sim$ 94 min) [88]. The trigger rate was strongly dependent on the orbital position: NP the North Pole, SP the South Pole, E Equator, SAA South Atlantic Anomaly (SAA).

Large solar particle events (SPE) occurring during the solar minimum could lead to a high rate of particles hitting the S1 scintillators. However, for a large number of events, the automatic trigger selection procedure switched to the configuration without the S1 detector, as during SAA passages.

3.2 The GAPS experiment

GAPS (General AntiParticle Spectrometer) is a balloon-borne experiment designed to measure low-energy (< 0.25 GeV/n) cosmic-ray antinuclei during a series of long-duration flights in Antarctica [99]. The first GAPS flight is scheduled for the austral summer of 2022-2023.
Its design has been optimized to perform a novel antiparticle identification technique based on an exotic atom formation and decay [100], allowing more active target material and a larger overall geometrical acceptance since no magnet is required. In particular, the GAPS apparatus, currently under construction, consists of ten planes of large-area Si(Li) detectors surrounded by a large-acceptance Time-of-Flight (ToF) system made of plastic scintillators. All these features will enable GAPS to achieve unprecedented sensitivity to cosmic-ray antideuterons, allowing to probe the predictions of a variety of dark-matter models [101], as well as a high statistics galactic antiproton spectrum in an unexplored low-energy range [102], and leading sensitivity to cosmic-ray antihelium [103].

3.2.1 The GAPS instrument design

The full payload of the GAPS experiment is illustrated in Figure 3.11. It weighs about 2.5 t and has a total power consumption of about 1.3 kW. It is composed of two main detectors [105]: a two-layer ToF system of thin plastic scintillators and a $1.6 \times 1.6 \times 1.0$ m^3 multiple-layer tracker including 1440 lithium-drifted silicon (Si(Li)) detectors. Since Si(Li) must work at cold temperatures [-45; -35]°C, an Oscillating Heat Pipe (OHP), faced away from the Sun, is used to maintain this temperature range in the instrument. The heat produced by the tracker is transferred into space via a radiator. On the Sun-facing side, there is a solar array to supply power. At the bottom of the apparatus, the electronics bay houses the electronics and other mechanical supports.
The GAPS mission has been planned for at least three Antarctic long-duration balloon flights, each lasting around 35 days, at an altitude of about 35 km (5 g cm^{-2} of overhead atmosphere). The polar location is ideal for studies of low-energy cosmic rays because of the very low geomagnetic cut-off. Moreover, the instrument provides a geometrical acceptance of about 18 m^2 sr in the $0.05 - 0.25$ GeV/nucleon energy range, which is very large if compared to that of experiments with a magnetic spectrometer. This will allow GAPS to collect large statistics to improve the sensitivities to antiprotons and especially to the heavier antinuclei. [104].

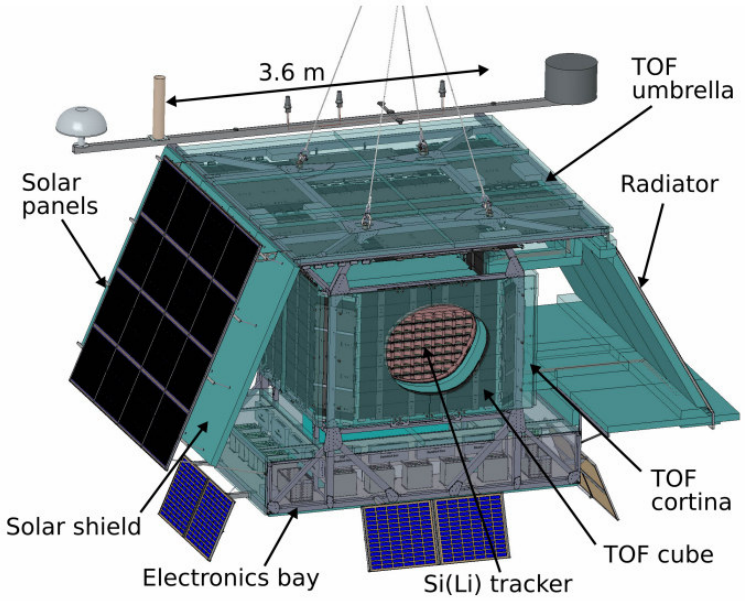

Figure 3.11: Pictorial representation of the GAPS instrument design. The front panel of the cortina was removed to show the inner detector and that of the inner ToF was cut open to show the tracker.

3.2.2 The Time-of-Flight system

The ToF system provides the time information needed to reconstruct the particle velocity, to trigger the readout of the whole apparatus as well as a measurement of the ionisation energy losses.
It is composed of about 160 plastic scintillator paddles (EJ-200) arranged in a two-layer structure [106]. The outer ToF includes a top horizontal plane, named "umbrella" and four lateral walls, named "cortina", whereas the inner ToF includes a hermetic "cube" encapsulating the tracker and separated by a distance of $\sim$ 0.95 m and $\sim$ 0.3 m from the umbrella and the cortina respectively.
All scintillator paddles are 6.35 mm thick and 16 cm wide, whereas their length is variable: 1.8 m in the umbrella, 1.72 m in the cortina, 1.8 m, 1.56 m and 1.082 m in the cube. Since adjacent paddles overlap approximately one centimeter, the ToF faces will have close to 100% hermeticity. Each paddle is wrapped to be light-tight and held in place with a carbon-fiber structure. Six silicon photomultipliers (SiPMs) are coupled to each end of each paddle and connected to custom preamplifiers and readout boards, which allow sample rates of several GHz. Each paddle system provides the measurement of the energy deposit, time and longitudinal position along its largest dimension.

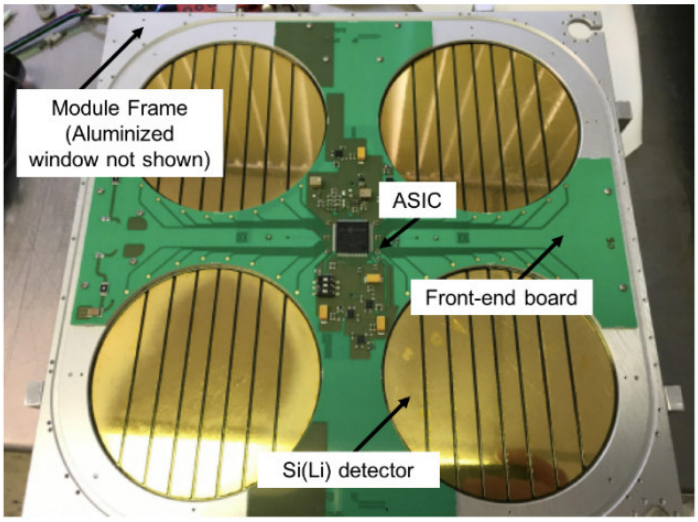

Figure 3.12: Tracker module containing four large-area Si(Li) detectors, each of which is divided into eight equal-area strips for readout performed by the integrated ASIC [106].

3.2.3 Si(Li) tracker

Surrounded by the ToF cube, the $1.6 \times 1.6 \times 1.0$ m^3 Si(Li) tracker is the core of the whole apparatus [106]. It measures the dE/dX of the incoming particles, tracks the annihilation products (X-rays and charged particles) and reconstructs the annihilation vertex (combined with ToF).
It is made of 1440 large-area Si(Li) detectors arranged in 10 evenly spaced layers supported and insulated by a light-weight foam. Every layer is composed of an aluminium structure supporting 6×6 arrays of modules, each of which contains four Si(Li) detectors of cylindrical shape (see Figure 3.12). Each Si(Li) detector has a diameter of 10 cm, is thick 2.5 mm and segmented in eight strips of equal area for readout. These Si(Li) wafers provide a timing of 50 ns and a $\sim$ 4 keV energy resolution (FWHM) for the X-ray channel sufficient to resolve the different X-rays from antideuterons and antiprotons at the operational temperature of -40°C. The operational temperature range $[-45, -35]$ °C required for the Si(Li) detectors is maintained by the OHP cooling system, which makes the thermal working fluid circulate through a latticework of capillary tubing perpendicular to the detector planes.
In each module, the four Si(Li) detectors are connected to a fully integrated ASIC using custom wire bonds. This includes a low-noise custom analog front end and readout core working in a large dynamical range (20 keV to MeV) needed to detect both X-rays and heavy annihilation products. The

ASIC digital outputs are routed into a back-end system that manages data acquisition and slow control processes.

3.2.4 GAPS antinucleus identification

The detection technique is based on the observation of the annihilation products of the incoming antinucleus (referred to as "the primary").
Coming from the overhead atmosphere, the primary crosses the ToF system and gets slowed down and finally stopped by dE/dx losses in the Si(Li) tracker. After stopping, the antinucleus can substitute an atomic electron (mostly in a silicon detector or in the aluminium frame) and form an exotic atom in an excited state with near-unity probability [100]. The exotic atom then decays through a series of atomic transitions emitting characteristic X-rays and finally the antinucleus annihilates with the target nucleus producing a nuclear star of several secondary particles, mainly pions and protons, originated from a common vertex. The multiplicity of the pion and proton stars depends on the incoming particle mass, for an antiproton the multiplicity is expected to be in a range between 3 and 6 while for an antideuteron between 8 and 12 (see Figure 3.13).
Each X-ray line energy uniquely identifies the antinucleus mass and charge. The simultaneous detection in a narrow time of X-rays of measured energy and a nuclear star with measured multiplicity provides discrimination between antiprotons and antideuterons and suppresses the huge non-antiparticle background. Moreover, as the dE/dx energy loss depends on kinetic energy, antideuterons of the same velocity of antiprotons penetrate about twice as deep into the Si(Li) tracker. Penetration depth together with velocity and change of dE/dx from layer to layer provides additional rejection power.
To discriminate antiprotons from the background of cosmic-ray particles, a rejection power of at least 10^6 is required and an additional 10^5 rejection factor is needed to identify a possible antideuteron component from the antiprotons. To achieve these discrimination performances, a custom reconstruction algorithm was designed to precisely reconstruct the event typology. For more information on this reconstruction algorithm see [110].

3.2.5 GAPS trigger configurations

The GAPS trigger condition is defined by energy deposits detected in the scintillator paddles of outer and inner ToF in a narrow time. Two trigger configurations have been developed so far [110]. A minimum-biased trigger

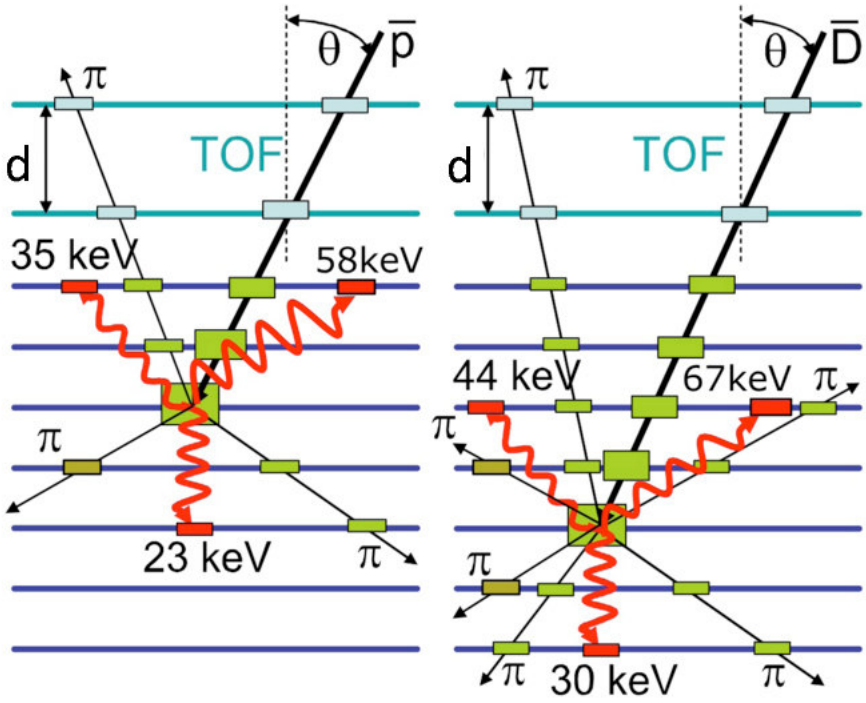

Figure 3.13: For the same angle measured by GAPS ToF, an antideuteron (right) will penetrate deeper, typically emit twice as many annihilation pions and protons and emit X-rays of different well-defined energies than an antiproton (left) [109].

condition, referred to as trigger level 1, requires the coincidence of a hit in the outer- and a hit in the inner ToF. Another trigger configuration, referred to as trigger level 2, was conceived to select the annihilating events: eight hits are required in the ToF system, with at least three hits both in the outer and in the inner ToF. This second trigger configuration reduces the trigger rate from the expected MHz rate with trigger level 1 down to less than 1 kHz.

3.2.6 GAPS current status

The GAPS novel detection technique was successfully tested in an accelerator environment at KEK in 2004 and 2005 [108]. To validate the GAPS instrument concept, a balloon-borne prototype GAPS (pGAPS) payload [111] was

constructed and successfully flown in June 2012 for about 5 hours from the Taiki balloon base of the Japan Aerospace Exploration Agency JAXA (see Figure 3.14). pGAPS consisted of three layers of crossed scintillator paddles (16 paddles in total) with a PMT readout on both the ends of each paddle and six Si(Li) detectors with active cooling. Because of the limited geometrical acceptance, stopping power and flight duration, pGAPS did not have sensitivity to cosmic-ray antiparticles. Its goals were to verify the operation of the Si(Li) detectors in a balloon environment, measure the velocity of cosmic rays using the prototype ToF, verify X-ray and cosmic-ray backgrounds at flight altitude and validate the model of the thermal system using a prototype OHP system. Over 600000 cosmic-ray triggers were recorded and all engineering and scientific goals of the flight were satisfied.
Currently, the GAPS apparatus is under construction: hundreds of Si(Li) detectors have been procured and calibrated as well as a few dozen full assembled ToF scintillator paddles. A new scaled functional prototype (GFP) [106] is under construction at MIT's Bates lab to validate the performance of the integrated, flight model, system components. It will be composed of two ToF layers currently being tested, three layers of Si(Li) tracker in 6×2 array of modules and a scaled thermal system to reach the optimal operational temperatures. The GFP will primarily study muons and other minimum ionizing particles (MIPs). Degraders will also be added to explore non-MIP particles with kinematics and dE/dX similar to those of the low-energy antiprotons and antideuterons expected to detect in flight and potentially muonic X-rays. The GFP will provide an excellent test for preliminary data analysis and reconstruction tools and understanding the limitations of the current hardware.
The first balloon flight of the completed GAPS instrument is scheduled for the austral summer of 2022-2023 in Antarctica.

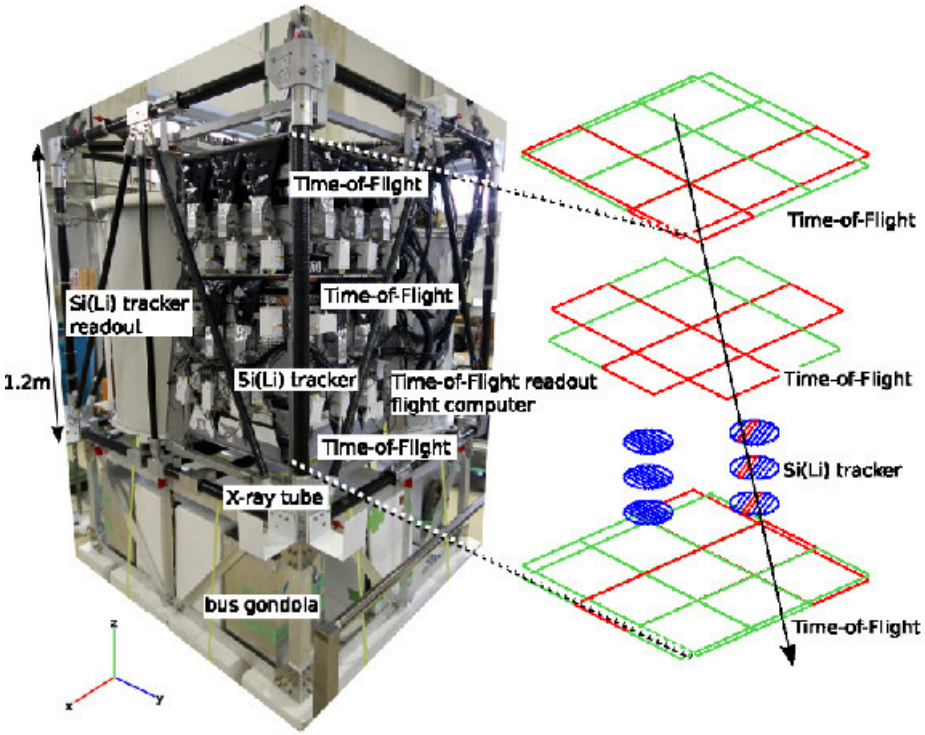

Figure 3.14: Left: Flight ready pGAPS payload without insulation foam. Right: Event display showing the position of the ToF and Si(Li) tracker systems and a typical cosmic ray track reconstructed from flight data [101].

Chapter 4

The proton and deuteron selections on the PAMELA data

This chapter describes the analysis work performed on the PAMELA data to obtain yearly proton and deuteron fluxes over a period of nine years. In particular, the data collected by PAMELA from July 2006 up to the end of September 2014 were analysed for this purpose.
Protons and deuterons are the nuclei of two different hydrogen isotopes and thus they have the same electrical charge Z but different mass m. They have also different origins and abundance in cosmic rays: protons are primary galactic particles accounting for more than 97% of the total amount of hydrogen in cosmic radiation, while deuterons are galactic particles of secondary origin.
Protons have no significant background and can be selected with high efficiency and negligible contamination. Deuterons are affected by a huge background of protons and tight data selections are needed to get a clean sample. However, because of the limited instrumental resolution of the PAMELA detectors, an accurate isotopic separation between protons and deuterons is possible in a limited rigidity range, approximately up to 2.6 GV.
The first part of the chapter is dedicated to the description of the selection criteria adopted in the analysis: after some standard criteria to select events with well-reconstructed tracks, selection cuts designed to extract samples of protons and deuterons are described. Then, a double-Gaussian fit procedure aimed to remove the residual proton contamination in the selected deuteron sample is described in detail. Later, the residual contaminations surviving the selected samples are also discussed. Finally, the number of events as a function of the rigidity is discussed.

4.1 Measured quantities for the event selections

For each triggered event, a set of measured quantities are provided to identify different CR species. In this analysis, three different quantities were studied:

- The ionisation energy loss dE divided by the crossed mass thickness dX [1], $\frac{dE}{dX}$, measured by tracker, ToF system and calorimeter.
- The velocity v normalized for the speed of light in vacuum c, i.e. $\beta = \frac{v}{c}$. It is calculated from the time of flight and the track length information.
- The rigidity ρ measured from the track deflection in the magnetic spectrometer.

These quantities allowed to define a procedure for the identification of protons and deuterons. As a start, the dE/dX information was studied as a function of the β to select particles with a unitary charge. Among these particles, there were hydrogen atoms but also positrons and positively charged pions, which can be removed using dE/dX information as a function of the rigidity because of their much smaller mass. Then, for the isotopic separation between protons and deuterons, the difference of the masses of the two isotopes was used. The dE/dX and the β distributions were analysed as a function of the rigidity, which according to its definition accounts for the charge-to-mass ratio allowing to separate the two isotopes up to 2.6 GV. Beyond this, the β and dE/dX values of the selected particles reach those of a relativistic particle and the instrumental resolution of the PAMELA detectors is not sufficient to distinguish the two isotopes.
In the following sections, all these event selections are discussed.

4.2 Selection of well-reconstructed tracks

A set of criteria were required to obtain positively charged events with a single downward-going track well reconstructed inside the spectrometer. These criteria are listed hereinafter:

- 1) A set of checks was performed to reject events, whose data got corrupted during the transmission from the satellite memory to the ground station.

[1] $dX = \rho_{mat} \cdot dx$ where ρ_{mat} and dx are the density and the crossed path in the detector respectively

- 2) Events collected during the flight over the South Atlantic Anomaly were excluded requiring an absolute value of the geomagnetic field $|B| < 0.26$ G. This was done to avoid any problem of trigger saturation due to the increased density of the trapped particles.

- 3) Only events with a single track reconstructed inside the magnetic spectrometer were selected. In this way, secondary multi-track events created typically by the interaction of a primary particle with the 2 mm thick aluminium layer of the PAMELA container were excluded.

- 4) The tracks of the selected events were required to have a minimum number of 3 hits in the tracker both on the x-view ($n_x \geq 3$) and the y-view ($n_y \geq 3$) and a level arm L (the distance measured in terms of the number of tracker planes between the first and the last hit in the x-view) greater or equal than four ($L \geq 4$). These requirements are related to the quality of the reconstructed track since the number of hits and the level arm are linked to the uncertainty of the measured deflection $\delta\eta$ according to the following formula:

$$\delta\eta = \frac{\sigma_x}{BL^2\sqrt{n_x}} \quad , \tag{4.1}$$

  where σ_x is the spatial resolution of the silicon detectors on the x-view, i.e. the bending view, and B is the magnetic field intensity inside the spectrometer cavity. The magnetic field has also a small component on the y-view, which must be considered in the reconstruction-fit procedure of the track inside the spectrometer. For this reason, a minimum number of 3 hits was required on the y-view as well.

- 5) Events were required to be inside a defined fiducial acceptance. This means that the reconstructed tracks had to be 0.15 mm away from the magnet walls. This request reduced the nominal instrumental acceptance, but it also rejects events, whose trajectory was deflected interacting with the walls.

- 6) A selection was applied on the χ^2 given by the track reconstruction fit:

$$0 < \chi^2 < p_0 + p_1\eta + p_2\eta^2 + p_3\eta^3 + p_4\eta^4, \tag{4.2}$$

  where η is the deflection of the event. The values of the parameters are reported in Table 4.1 The χ^2 value gives quantitative information about the goodness of the track reconstructed by the fit procedure. It

Parameters of the χ^2 upper cut				
p_0	p_1	p_2	p_3	p_4
1.8095	0.952066	2.498	-1.21729	0.22343

Table 4.1: The values of the parameters applied in the upper limit on χ^2 of the track fit.

is calculated as follows:

$$\chi^2 = \frac{1}{n_x + n_y - 5} \left[\sum_{i=1}^{n_x} \frac{(x - x_i^{meas})^2}{\sigma_x^2} + \sum_{i=1}^{n_y} \frac{(y - y_i^{meas})^2}{\sigma_y^2} \right], \qquad (4.3)$$

where x_i^{meas} and y_i^{meas} are the x- and y hit coordinates measured inside the tracker, whereas the x and y are the corresponding coordinates given by the track-reconstruction fit algorithm. The $\frac{1}{n_x+n_y-5}$ normalization accounts for the 5 parameters estimated by the fit, which reduce the number of degrees of freedom from $n_x + n_y$ to $n_x + n_y - 5$. This means that at least 5 hits, three on the x-view and two on the y-view are needed to fit a track in the spectrometer.
For high deflection values, that correspond to low rigidity values, effects of multiple scattering and δ-emission grow significantly, making harder a good track reconstruction from the fit algorithm. This results in χ^2 values tending to rise at low rigidities. To remove this drawback, the χ^2 was required to satisfy the selection criterion parameterized in equation 4.3 to get an almost constant efficiency over the whole rigidity range. The values of the 5 parameters in the equation were calibrated in [114] making the χ^2 upper limit have an efficiency of about 95%.

- 7) Events were required to have positive values of β and rigidity. With these requirements, particles crossing the PAMELA apparatus from the top to the bottom and with a positive value of the electric charge were selected. Especially, the request of $\beta > 0$ was used to reject albedo particles from the bottom.

- 8) Events with no associated signal on the CARD and CAT detectors were selected. This criterion rejects multi-particle events, which typically activate these AC detectors. No request was done for the CAS detector, because of possible signals induced by secondary particles produced in the spectrometer or backscattered from the calorimeter.

Figure 4.1 shows an event satisfying the criteria1-8 through the PAMELA apparatus. The β distribution for the events surviving the selections 1-8 is

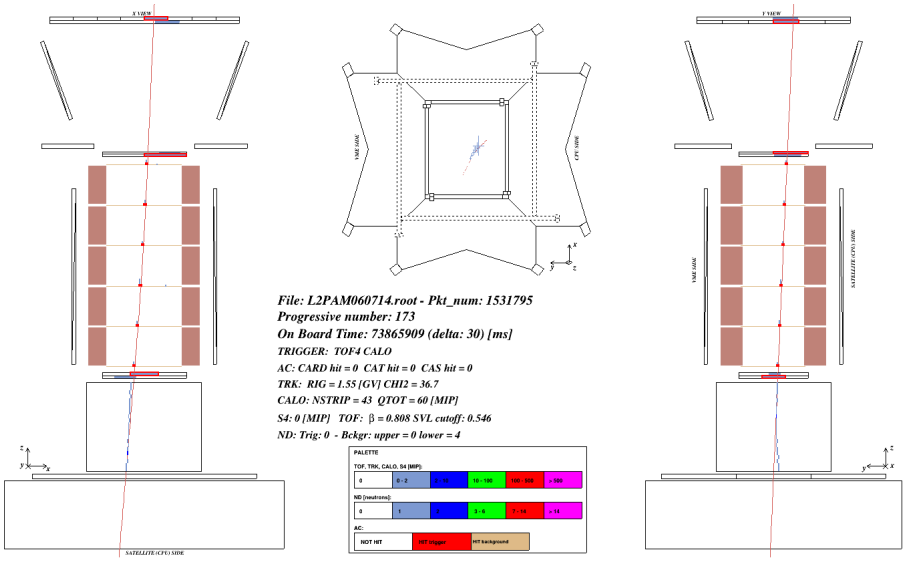

Figure 4.1: View of a proton crossing the PAMELA apparatus and satisfying the selection criteria 1-8 in the flight data.

displayed as a function of the rigidity in Figure 4.2 . It is possible to note that there are β-values greater than 1, which would correspond to particles with a measured velocity higher than the light speed in vacuum c. These exceeding values are due to the instrumental resolution of the speed measurement $\beta c = \frac{l}{t}$, where l is the length of the reconstructed track and t is the time employed by the particle to cross the apparatus provided by the ToF. Both l and t measurements have an associated resolution, which affects the β measurement and gives it in some cases values greater than 1. In Figure the selected events distribute around the theoretical β curves as a function of rigidity defined as follows:

$$\beta = \frac{Ze\rho}{\sqrt{(Ze\rho)^2 + (mc^2)^2}}, \tag{4.4}$$

with m and Z respectively the mass and the electric charge number of the particle, e and c respectively the elementary electric charge and the speed of light in a vacuum. In the picture, the theoretical β curves for protons and deuterons were highlighted respectively in magenta and red colours to be easily distinguished from the others. It can be noted that the deuteron curve overlies that of helium-4 because they have an almost equal charge-to-mass ratio.

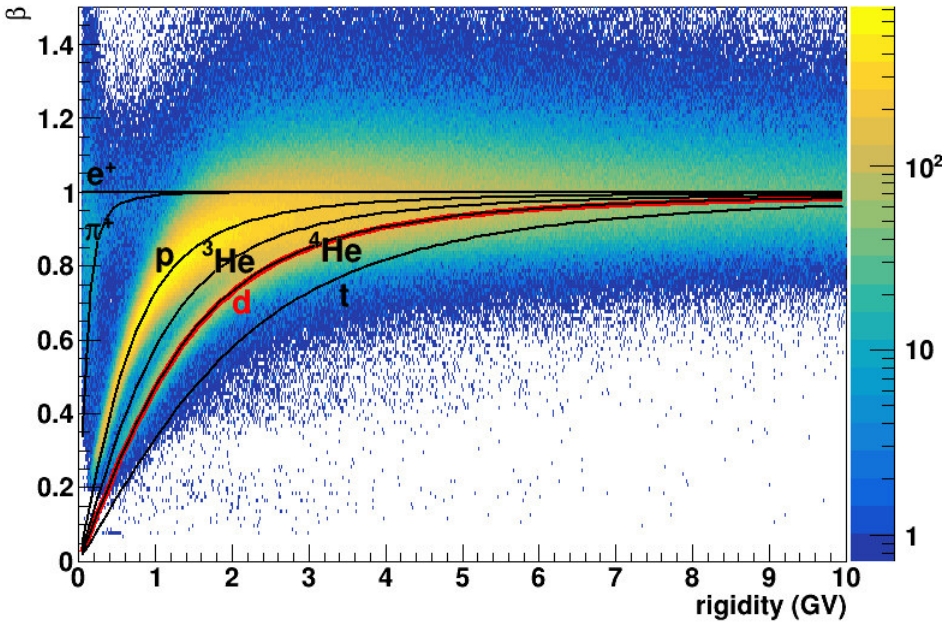

Figure 4.2: β distributions versus rigidity for downward particles with positive electric charge, selected from flight data surviving selection criteria 1-8. The black lines are the theoretical curves predicted by the Equation 4.4 for different particle species. The red line presents the predicted β values for deuterons.

4.3 Selection of particles with $Z = 1$

Among the events selected with the criteria 1-8, particles with different charge Z were present. The next step was to reduce the sample to the only events with $Z = 1$. To do this, the ionisation stopping power dE/dX as a function of the β was employed. The dE/dX is well approximated by the Bethe-Bloch formula [113]:

$$dE/dX = 2\pi N_a r_e^2 m_e c^2 \rho_m \frac{z}{A}\frac{Z^2}{\beta^2}\left[\ln\left(\frac{2m_e\gamma^2 v^2 W_{max}}{I^2}\right) - 2\beta^2 - \delta - \frac{2C}{z}\right] \quad , \tag{4.5}$$

where Z, β, γ are respectively the charge, the beta and the Lorentz factor $\gamma = 1/\sqrt{1-\beta^2}$ of the traversing particle, ρ_m, z and A are respectively the density, the charge value and the atomic number of the absorbing material, N_a is the Avogadro number, r_e is the classical electron radius, W_{max} is the maximum energy releasable in a single interaction, I is the mean excitation potential of the absorbing material, C and δ are corrections depending on the material properties contributing respectively at very low and very high energies.
Since the logarithmic factor in Equation 4.5 starts to have a relevant contribution in the relativistic regime of a particle, in the energy range of interest $dE/dX \propto \frac{Z^2}{\beta^2}$ is a good approximation. This entails that particles with the same velocity but with a different charge value release dE/dX values assembling into separate distributions as a function of β. This feature was used to select particles with $Z = 1$:

- 9) Selection cuts were calibrated on the dE/dX distributions of the first four ToF layers S11, S12, S21, S22. This ensures to reject particles with $Z > 1$ which fragment above the tracker. Figure 4.3 shows the dE/dX distributions for each ToF plane above the tracker as a function of β for a sample of events satisfying the criteria 1-8 in the year 2006. The lower band of events in the distributions consists of particles with $Z = 1$, which are mainly protons but also in smaller amounts deuterons, tritons, positron and positively charged pions. The upper band corresponds to particles with $Z = 2$, which are helium nuclei. The black curves between the two bands are the four cut curves defined to select the particles with $Z = 1$ in each ToF layer. These cut curves were parameterized according to the following formula:

$$f(x) = \frac{a}{b \cdot x + c} + d + e \cdot x \quad , \tag{4.6}$$

  where $f(x)$ and x correspond to the dE/dX and β quantities, whereas a, b, c, d, e are five parameters calibrated for each ToF layer to achieve

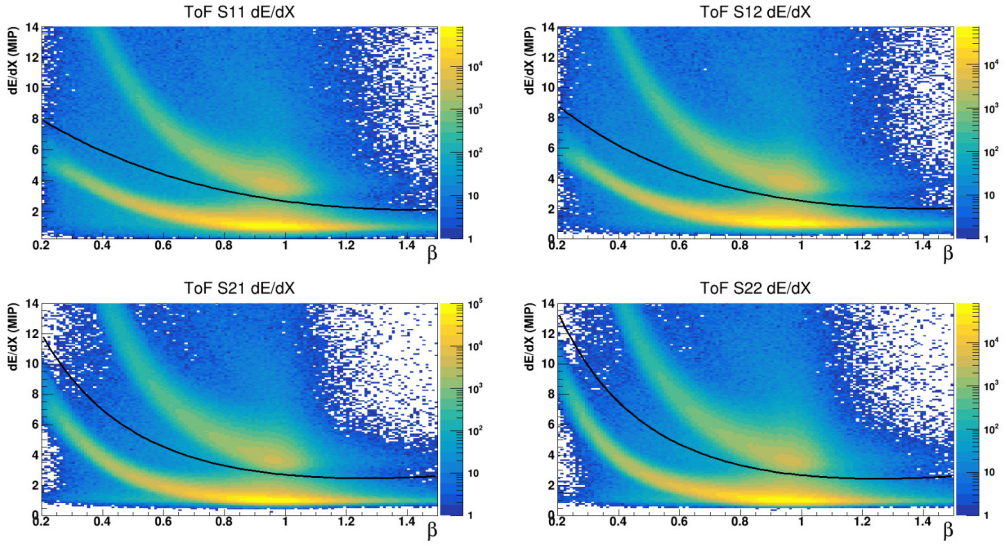

Figure 4.3: dE/dX distributions measured for each of the first four ToF layers: S11 at the top left, S12 at the top right, S21 at the bottom left and S22 at the bottom right. The black curves correspond to the upper cut selecting events with Z=1.

a selection efficiency higher than 99%. These calibrations were performed on the four dE/dX distributions of a flight sample of hydrogen events obtained with a selection on the average dE/dX measured in the tracker already described in [112].

These four selections allowed to obtain a sample of downward particles with unitary charges. Based on these events, the isotopic separation between protons and deuterons was then performed, as detailed in the next section.

4.4 Proton and deuteron identification

To separate the different components present in the events selected with criteria 1-9, the dE/dX deposits recorded in the various PAMELA detectors and the β measurement were analysed as a function of the rigidity. When the dE/dX is analysed as a function of the kinetic energy, particles enter their non-relativistic regime around energy comparable to their rest mass value. Based on the dE/dX measurements provided by the PAMELA detectors, the hydrogen nuclides into separate distributions can be observed in a restricted low-rigidity range, from a few tenths of GVs to around 3 GV. Beyond this value, all they have become quite relativistic and minimum ionizing and the

limited instrumental resolution of the detector responses does not allow to distinguish the separate bands any longer.
In the event samples selected with criteria 1-9 small positron and positively charged pion components were present. Their small mass with respect to those of the hydrogen nuclides makes them relativistic in the considered energy range $[0.1, 1.1]$ GeV/n. This could allow rejecting positrons and pions easily based on the dE/dX as a function of the rigidity up to about 1 GV.
In the remaining hydrogen component, the different isotopes can be separated in the considered non-relativistic regime exploiting their different masses. In addition to protons and deuterons, a very small component of tritons, i.e. the tritium nuclei, is present in the selected samples as well. The triton has a decay half-time of about 12 years, which is much shorter than the confinement time of CRs in the Galaxy ($\approx 10^7$ years). This entails that the triton component found in the selected samples must be originated from fragmentations of heavier nuclei interacting with the PAMELA apparatus.
When the dE/dX is analysed as a function of the kinetic energy, particles enter their non-relativistic regime around energy comparable to their rest mass value. Based on the dE/dX measurements provided by the PAMELA detectors, the hydrogen nuclides into separate distributions can be observed in a restricted low-rigidity range, from a few tenths of GVs to around 3 GV. Beyond this value, all they have become quite relativistic and minimum ionizing and the limited instrumental resolution of the detector responses does not allow to distinguish the separate bands any longer.
This isotopic separation can be observed in the distributions of the mean values of the dE/dX measurements in the tracker (Figure 4.4) and in ToF (Figure 4.5) as a function of the rigidity for events satisfying the criteria 1-9 in 2006. In both these pictures, protons and deuterons are distributed into two well separate bands from the lowest rigidities up to a value of about 1.5 GV. From this rigidity value, the deuteron dE/dX distribution starts to overlap the lower one of protons making difficult the isotopic separation beyond. As already explained, this is because deuterons are becoming relativistic and minimum ionising as well as the protons, for which this occurred at lower rigidities around 0.8 GV. Triton events can be also noted above the deuteron distribution but in a very small number.
To extend the separation between protons and deuterons achieved with the dE/dX, the β information was also used. The β quantity looked as a function of the rigidity also allows separating the hydrogen nuclides, in fact, according to Equation 4.4 particles with the same rigidity but different charge-to-mass ratios distribute along different theoretical β curves. In Figure 4.8 the β distribution for a sample of particles of $Z = 1$ selected with criteria 1-9 in 2006 are drawn as a function of the rigidity together with the theoretical β

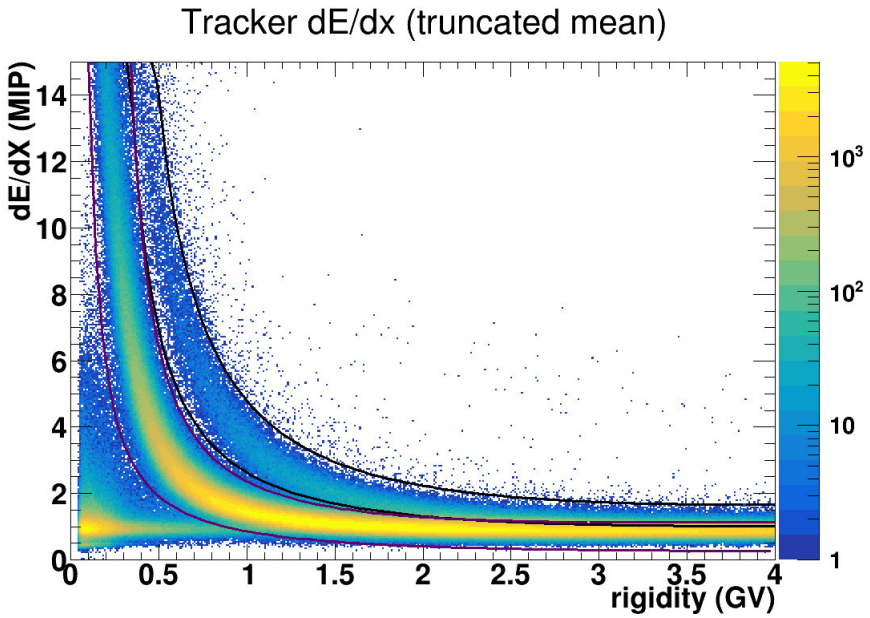

Figure 4.4: The truncated mean distribution of the dE/dX measured in the tracker as a function of rigidity for Z=1 particles surviving selection criteria 1-9. The black lines represent the deuteron cuts (selection criterium 10), whereas the purple lines depict the proton cuts.

curves for proton, deuteron, tritons, positron and positively charged pions. It can be noted that the proton and deuteron distributions can be well distinguished up to a rigidity value of about 2.0 GV, beyond this value they start to overlap because of the limited instrumental resolution.
As it will be described in Section 4.8 the β information was used in a smarter way to select deuterons selection: an elaborate fit procedure was developed to identify in the $1/\beta$ histograms for a set of rigidity bins separate distributions for proton and deuteron and obtain the related counts up to a higher rigidity value of 2.6 GV.
All these techniques for the isotopic separation are described in detail in the next sections.

4.5 Proton and deuteron selections in the Tracker and ToF dE/dX distributions

Measurements of the dE/dX provided by the tracker and ToF were used to separate protons and deuterons. The x and y detecting layer of the tracker

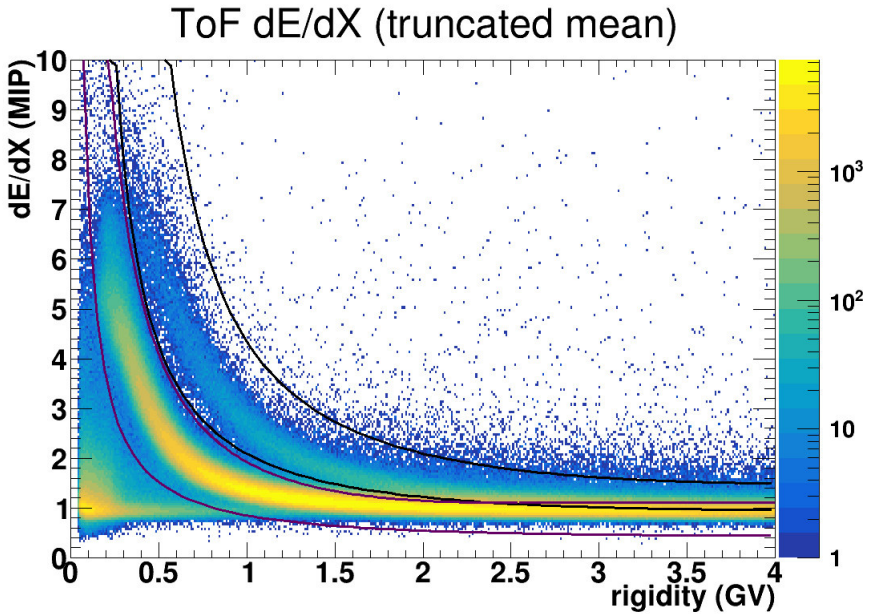

Figure 4.5: The truncated mean distribution of the dE/dX measured in the ToF system as a function of the rigidity for Z=1 particles surviving selection criteria 1-9. The black lines represent the deuteron cut (selection criterium 11).

planes provide up to twelve dE/dX measurements, whereas the ToF provides six dE/dX measurements. Different combinations of these quantities were studied to define the best solution for the isotopic separation.
First, the arithmetic mean of all the dE/dX measurements in the tracker and the average dE/dX measured in ToF were considered. A second approach was a mean dE/dX value calculated with the n lowest dE/dX measurements among the N collected ones. This approach is referred to as truncated mean in the following. dE/dX distributions calculated with these approaches are compared in Figure 4.6 for the events selected with criteria 1-9 in 2006 for four different rigidity intervals. The blue distributions represent the average dE/dX measured in the tracker layers, while the red distributions represent the lowest measured dE/dX. The distributions have two peaks, the highest one is populated by protons and the lowest one, at higher $1/\beta$ value, by deuterons. The two peaks are better separated in the red distribution. This occurred because the truncated mean at the lowest value reduces the probability to take high energy deposits, which generate the typical long tail of the Landau dE/dX distribution.
However, the red distributions in Figure 4.6 also have a long tail extending

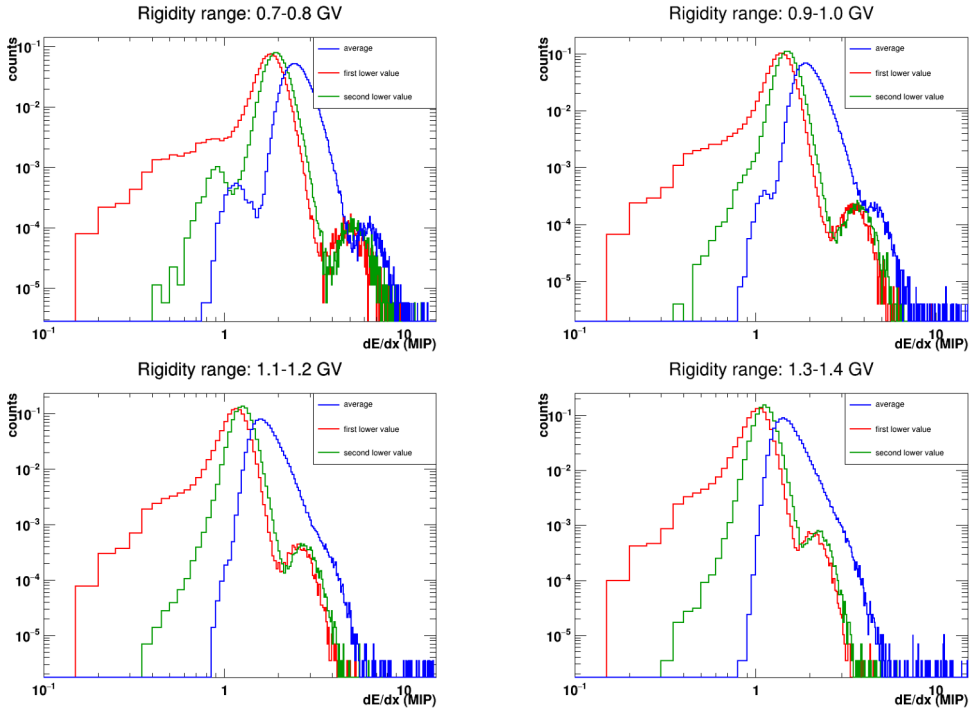

Figure 4.6: Tracker dE/dX distributions measured for charge one particles calculated as the average in blue, the truncated mean to the first lower value in red and to the second lower value in green for four different rigidity ranges. For a better comparison, the dE/dX distributions were normalized to one.

down to a few percent of MIP. This is due to an inefficiency of some tracker and ToF planes. In a non-negligible fraction of cases, the inefficient planes recorded a noise signal higher than the threshold. These "fake" signals were usually a small fraction of a MIP. To solve this problem a truncated mean to the second-lowest value was considered. The corresponding dE/dX distributions are drawn in Figure 4.6 with the green colour. It can be noticed that the long tail at low dE/dX was significantly reduced, allowing the identification of the positron and pion peak at low rigidities. For these reasons, also the ToF dE/dX truncated mean to the second-lowest value was employed for the isotope identification. From now on, the term "truncated mean" will be referred to this last approach.
Figure 4.4 and Figure 4.5 show the distributions of the truncated means of the dE/dX measurements collected respectively in tracker and ToF for the events selected with the criteria 1-9 in 2006. The proton and deuteron distributions are well separate up to about 1.5 GV. On these distributions, selection cuts for protons and deuterons were defined according to the Equa-

tion 4.6 and are shown in Figure 4.4 and Figure 4.5 for protons in purple and for deuterons in black. The upper selection cuts for deuterons remove the tritons.

- 10p) - 11p) For protons, the large dominant component among the events selected with criteria 1-9, it was enough to use only the selection on the Tracker to obtain the final clean sample for the flux calculation. From now on, this selection will be referred to as criterion 10p. The proton selection on the ToF dE/dX distribution, named criterion 11p, was used later to obtain uncorrelated proton samples for the efficiency calculation for criterion 10p.

- 11d) - 11d) For the case of deuterons, both the selection cuts on the tracker and ToF dE/dX, referred to as criterion 10d and 11d respectively, were needed to reject the large proton background up to high rigidities, around 2.0 GV. Beyond this value, the beta information was exploited with a fit procedure to reject the residual proton contamination in the deuteron samples, as reported later.

4.6 Additional selections for efficiency and contamination studies

Since both the criteria 10d and 11d were needed for the selection of deuterons, further selections were needed to obtain uncorrelated deuteron samples to study the efficiency and the surviving contaminations on the flight data. In particular, two additional criteria were defined on the distributions of the mean dE/dX measured in the calorimeter and of the velocity β.

- 12d) An algorithm developed in [30] for the calculation of a truncated mean of the dE/dX measurements in the PAMELA calorimeter was adopted. First, non-interacting events at least in the first five of the 44 silicon planes in the calorimeter were selected. This selection was performed measuring for each silicon plane the ratio between the total detected energy q_{tot} and the sum of the energy deposited in the strip closest to the track and in the two neighbouring strips q_{track}. This ratio is close to one if all the energy was released along the track, i.e. for non-interacting events. Starting from the top layer of the calorimeter, this ratio was calculated progressively moving to the deepest planes as

follows:

$$\frac{\sum_{i=0}^{j} q_{track}}{\sum_{i=0}^{j} q_{tot}} \tag{4.7}$$

where j is the iterator on the 44 layers. The events for which this ratio was greater than 0.9 at least for the first five layers were selected as non-interacting. The 0.9 value was arbitrarily chosen to achieve a good compromise between high efficiency and high rejection of interactions. This criterion selected slow particles stopping early or interacting more in depth inside the calorimeter or even particles traversing the whole detector without any interaction. For convenience, all these three records will be unproperly referred to as non-interacting events.
For these events, a truncated mean of the dE/dX measurements collected in the calorimeter layers was calculated. Among all the dE/dX values, the half with the highest values were excluded and an average of the remaining ones was calculated. This improves the resolution of the dE/dX by rejecting the events which populated higher tails of the Landau distribution. Figure 4.7 depicts the truncated mean dE/dX distribution for the non-interacting events in calorimeter satisfying criteria 1-9 as a function of the rigidity. Here the proton and deuteron bands are well separated up to about 2.5 GV. The black curves are the cuts calibrated according to the parameterization of Equation 4.6 to select deuterons. These selection cuts will be referred to as criterion 12d.
This selection criterion can select a clean sample of deuterons up to around 2.5 GV extending the range with respect to the criteria 10d and 11d. However, it had two disadvantages: the requirement of non-interacting events in the calorimeter reduced the deuteron statistics of about a factor 2 and selects deuterons only from about 0.8 GV since particles with lower rigidity stopped before reaching the first calorimeter layers.

- 13d) An additional selection criterion for deuterons was developed based on the β information as a function of the rigidity. This cut is shown in Figure 4.8 for the events satisfying criteria 1-9 in 2006. The black lines represent the theoretical curves predicted for deuterons and protons, while the magenta line was the cut curve parameterized as:

$$f(x) = \frac{x}{\sqrt{a + x^2}} + b \quad , \tag{4.8}$$

The two parameters a and b were optimized to select a clean deuteron sample up to about 1.5 GV, beyond this rigidity the proton and deuteron

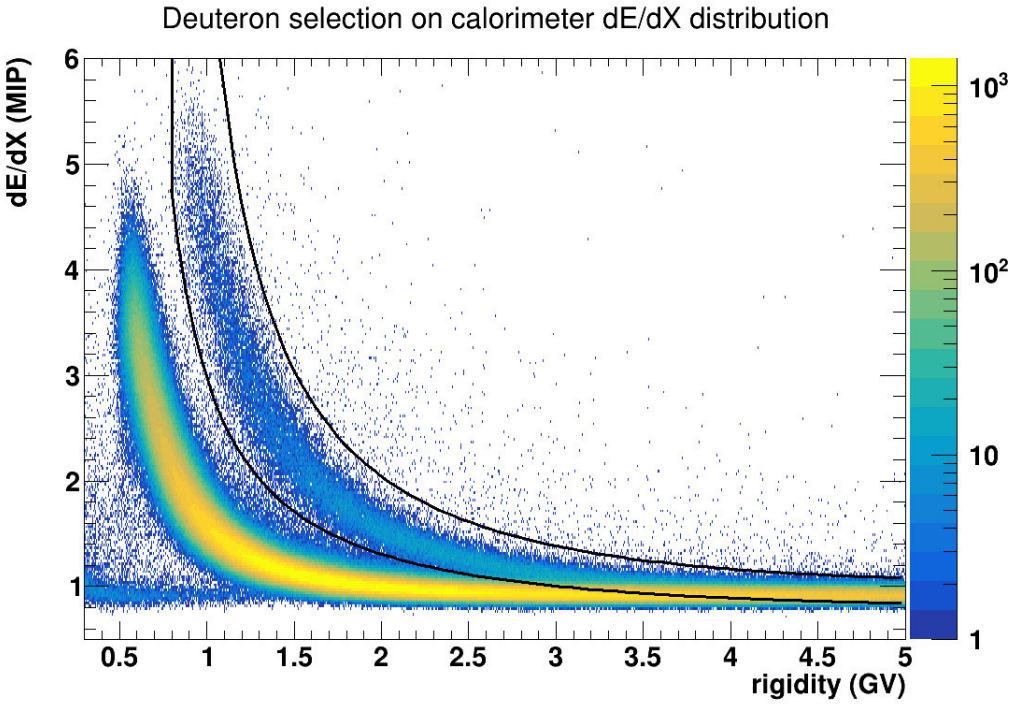

Figure 4.7: The truncated mean distribution of the dE/dX measured in the calorimeter for the non-interacting events satisfying criteria 1-9 as a function of the rigidity. The black lines represent the deuteron cuts (selection criterium 12d).

distributions overlap and the selected deuteron sample has a proton component. This selection cut will be referred to as criterion 13d.

4.7 Division in geomagnetic cut-off slices

At this point of the analysis, samples for protons and deuterons were obtained with the selection criteria 1-9, 10p and 1-9, 10d, 11d respectively. The events were then selected according to their geomagnetic cut-off. In particular, the satellite orbit was divided into 8 geomagnetic cut-off slices, listed in Table 4.2, where the first two geomagnetic cut-off slices used for protons were merged into one for deuterons. This merge was done because of the different lowest rigidity values at which protons and deuterons can be detected by PAMELA, respectively around 0.35 GV and about 0.5 GV. This is due to the higher ionisation energy losses experienced by deuterons with respect to protons at the same rigidity.

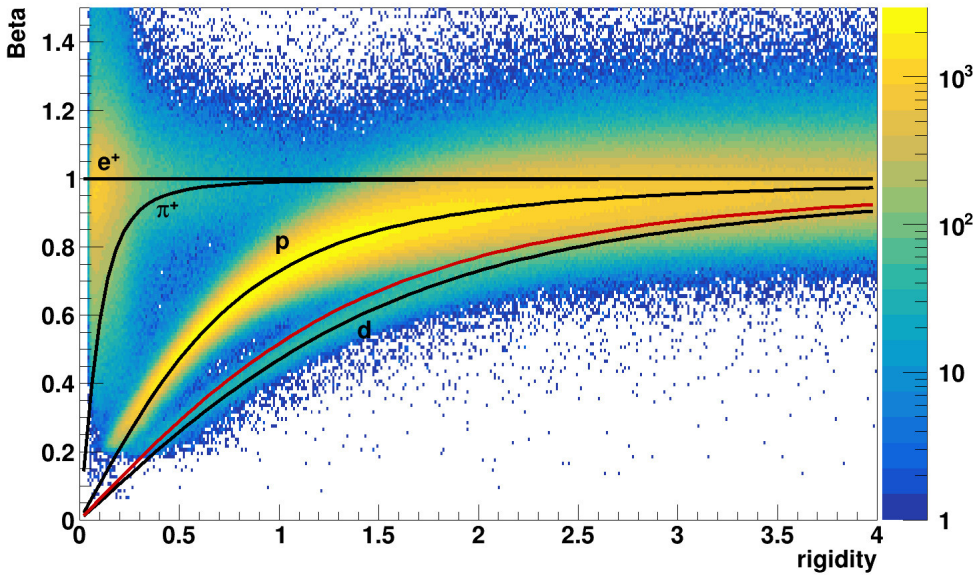

Figure 4.8: β distribution measured as a function of the rigidity for Z=1 events satisfying criteria 1-9. The black curves depict the theoretical curves defined as 4.4 for protons, deuterons, positrons and charged pions, whereas the red curve represents the deuteron cut.

This division into geomagnetic cut-off slices was adopted to reject the re-entrant albedo particles present among the selected events after having applied the unfolding procedure detailed in Section 5.4. In each geomagnetic cut-off slice, the events were distributed into rigidity bins, whose edges are defined in Table 4.3. It can be noted that the first three rigidity bins, defined between 0.35 GV and 0.5 GV, were used only for protons, since the deuteron rigidity threshold is above 0.5 GV. The widths of the rigidity bins were chosen tight enough in the rigidity region of interest to obtain the right balance between high statistics especially for deuterons in each bin and a detailed reconstruction of the final spectral shapes.
For protons, no further selection to clean the samples was needed because of the already low residual contamination, and for each rigidity bin, the corresponding number of events n_p was taken with a Poissonian standard deviation $\sigma_p = \sqrt{n_p}$ for the flux calculation. In Figure 4.9 the proton counts are shown for the year 2006 for each geomagnetic cut-off slice after having divided the number of events for the rigidity bin widths. From these distributions, the component of re-entrant albedo particles can be noticed, especially for the last three slices. Later in the analysis, only protons with rigidities higher

Geomagnetic cut-off slices

slice	protons	deuterons
1°	0 - 0.26 GV	0 - 0.38 GV
2°	0.26 - 0.38 GV	0.38 - 0.535 GV
3°	0.38 - 0.535 GV	0.535 - 0.69 GV
4°	0.535 - 0.69 GV	0.69 - 1.153 GV
5°	0.69 - 1.153 GV	1.153 - 1.46 GV
6°	1.153 - 1.46 GV	1.46 - 1.84 GV
7°	1.46 - 1.84 GV	1.84 - 2.3 GV
8°	1.84 - 2.3 GV	

Table 4.2: Division in geomagnetic cut-off slices for protons and deuterons.

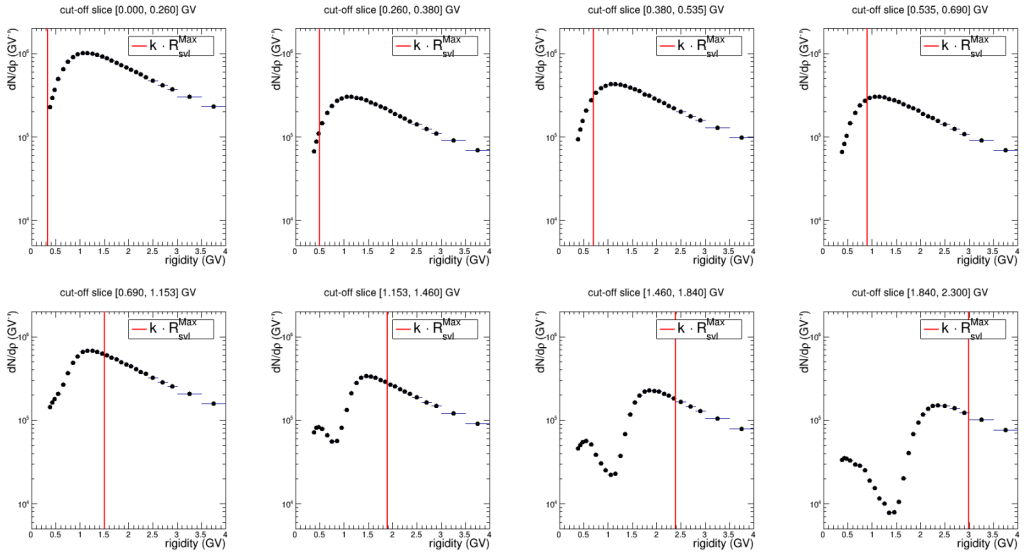

Figure 4.9: Counts of proton events divided by the rigidity bin widths are depicted as a function of the rigidity for each of the eight geomagnetic cut-off slices.

than the maximum geomagnetic cut-off rigidity of the corresponding slice times a factor k (red lines in Figure 4.9) were selected as galactic protons.

At this stage, a clean sample of deuterons was obtained from 0.5 GV up to a rigidity value of 2.0 GV. To extend this range at higher rigidities, the β of the particles was used to define a fit procedure to remove the residual proton contamination. This procedure is described in detail in the next section.

Partition into rigidity bins

rigidity bin edges	protons	deuterons
0.35 GV - 0.40 GV	✓	×
0.40 GV - 0.45 GV	✓	×
0.45 GV - 0.50 GV	✓	×
0.50 GV - 0.60 GV	✓	✓
0.70 GV - 0.80 GV	✓	✓
0.80 GV - 0.90 GV	✓	✓
1.00 GV - 1.10 GV	✓	✓
1.10 GV - 1.20 GV	✓	✓
1.20 GV - 1.30 GV	✓	✓
1.30 GV - 1.40 GV	✓	✓
1.40 GV - 1.50 GV	✓	✓
1.50 GV - 1.60 GV	✓	✓
1.60 GV - 1.70 GV	✓	✓
1.70 GV - 1.80 GV	✓	✓
1.80 GV - 1.90 GV	✓	✓
1.90 GV - 2.00 GV	✓	✓
2.10 GV - 2.20 GV	✓	✓
2.20 GV - 2.30 GV	✓	✓
2.30 GV - 2.40 GV	✓	✓
2.40 GV - 2.60 GV	✓	✓
2.60 GV - 2.80 GV	✓	✓
3.00 GV - 3.50 GV	✓	✓
3.50 GV - 4.00 GV	✓	✓

Table 4.3: Division in rigidity bins defined for protons and deuterions.

4.8 The fit procedure for deuterons $1/\beta$ distributions

The residual proton contamination in the deuteron samples from around 2.0 GV was removed by means of a fit procedure performed on the $1/\beta$ distributions for the events satisfying criteria 1-9, 10d, 11d.
Since the β is obtained from the ratio between the path length of the particle inside the apparatus and the time of the particle passage measured by the ToF system, the quantity $1/\beta$ is directly proportional to the particle time of flight, whose resolution can be approximated by a Gaussian. Since the accuracy of the path length is much higher with respect to that of the time-of-flight, it can be neglected and the $1/\beta$ distributions of a specific particle

are expected to be well described by a Gaussian distribution.
The $1/\beta$ distributions of the deuteron samples were then fitted with two Gaussian functions peaked at different $1/\beta$ values according to the values predicted by Equation 4.4 for protons and deuterons respectively (see Figure 4.22). However, as the rigidity grows and the relativistic regime is approached, the peaks of the two Gaussians tend to converge and the isotopic separation becomes inefficient when the two peaks are closer than the sigma of the $1/\beta$ distributions. This occurred for rigidities higher than about 3.0 GV.
To reduce the number of free parameters of the fit, the mean and the sigma values were determined with independent samples of protons and deuterons. In this way, just two parameters, the amplitudes, must be determined to reproduce the $1/\beta$ distributions.

4.8.1 Mean and Sigma determination for the fitting Gaussian functions

To determine the mean and sigma values for the double Gaussian fit, clean samples of protons and deuterons were selected to fit their $1/\beta$ distributions with a single Gaussian. These samples were selected for each year considered in the analysis to study a possible temporal evolution of the mean and sigma values. In these samples, the events were not divided into geomagnetic cut-off slices and were required to have a measured rigidity ρ higher than a factor k times the cut-off rigidity R_{svl} corresponding to the geomagnetic orbital position at the moment of its acquisition:

$$\rho > k \cdot R_{svl} \quad . \tag{4.9}$$

The factor k was chosen equal 1.3, the origin of this value will be explained in Section 5.5. This allowed to remove the re-entrant albedo particles from the selected samples to avoid possible bias in the shape of the $1/\beta$ distributions. For the deuterons, two sets of samples diversely selected and useful for two different rigidity intervals were selected for each year.
First, yearly samples were selected with the standard criteria 1-9, 10d, 11d, for simplicity referred to as samples A. The $1/\beta$ distributions for each rigidity bin were fitted with a Gaussian function as shown in Figure 4.10 (Left). Since above 2.0 GV the proton contamination among the deuterons grew to not negligible values, an additional Gaussian function was added to fit the protons. This allowed to proceed up to 2.3 GV, after this value the protons were considered high enough to potentially affect the determination of the Gaussian fitting the deuterons.

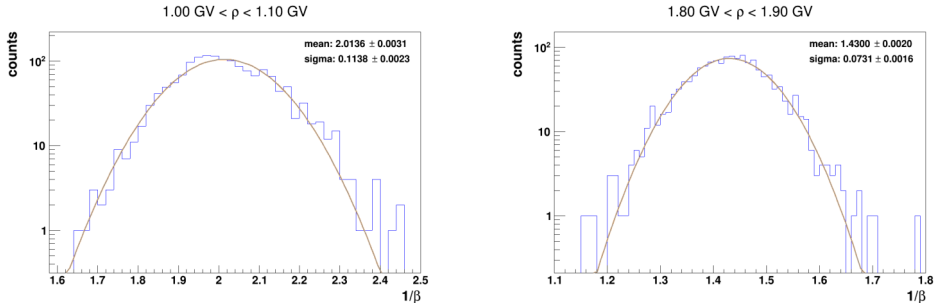

Figure 4.10: Left: Gaussian fit of a $1/\beta$ distribution in the rigidity bin $[1.0, 1.1]$ GV for the sample A collected in 2006. Right: Gaussian fit of a $1/\beta$ distribution in the rigidity bin $[1.8, 1.9]$ GV for the sample B collected in 2006.

To determine the Gaussian mean and sigma values for deuterons at higher rigidities, other yearly samples (named samples B) were selected with criteria 1-9, 10d, 11d, 12d to obtain negligible proton contamination up to 3.0 GV. Since criterion 12d requires non-interacting events in the calorimeter, the statistics at the low rigidities were much lower than in samples A and even null below 0.8 GV, forcing to start to fit the $1/\beta$ distributions from 1.1 GV. In figure Figure 4.10 Right an example of Gaussian fit of a $1/\beta$ distribution is reported for the sample B.
The mean and sigma values obtained from samples A and B were then compared for each year to check their compatibility between 1.1 GV and 2.3 GV and a good agreement was found. After this check, single sets of mean and sigma values were created for each year taking the values from samples A in the rigidity range $[0.5, 1.5]$ and those from samples B beyond 1.5 GV up to 3.0 GV. This choice was based on the observation of higher fluctuations in the sigma trends of samples A with respect to those of samples B in the rigidity range [1.5, 2.3] GV.
The yearly sets of mean and sigma values are depicted as black points in Figure 4.11 and Figure 4.12 respectively . These values were then fitted to obtain smooth values and the corresponding confidence intervals. The distribution in Figure 4.11 were fitted with:

$$f(x) = \frac{\sqrt{x^2 + a^2}}{x} + b + d \cdot x \quad , \tag{4.10}$$

was used, where x corresponds to the rigidity. The red curves in Figure 4.11 are the results of the fit. These curves will be used to determine the values of the deuteron means for the double Gaussian fit. The confidence intervals evaluated by these fits are not visible in the pictures because of the extremely

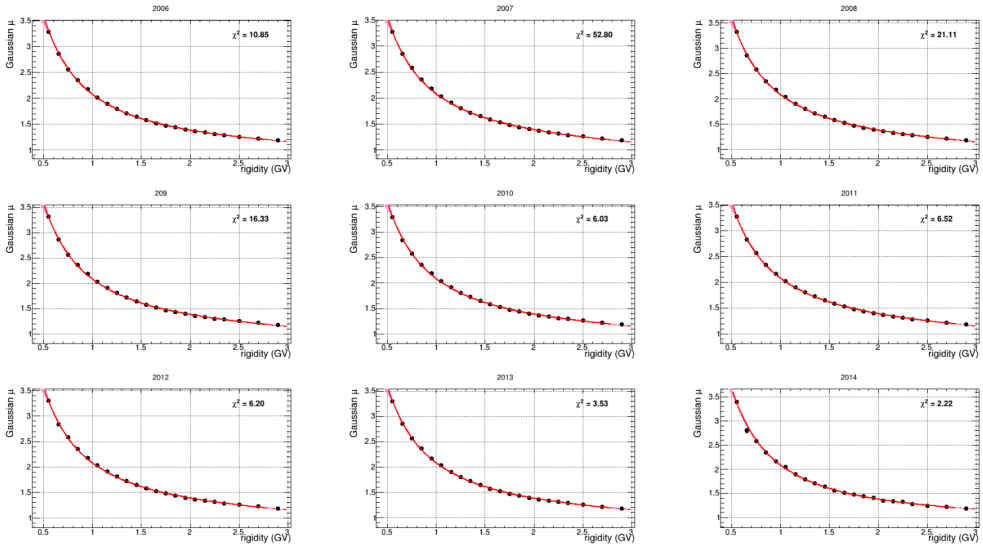

Figure 4.11: Yearly trends of the Gaussian mean values obtained for deuterons are depicted as black points in the nine pictures, one for each year. The red curves and the pink shaded area are respectively the functions fitting the mean values and confidence intervals evaluated by the fit.

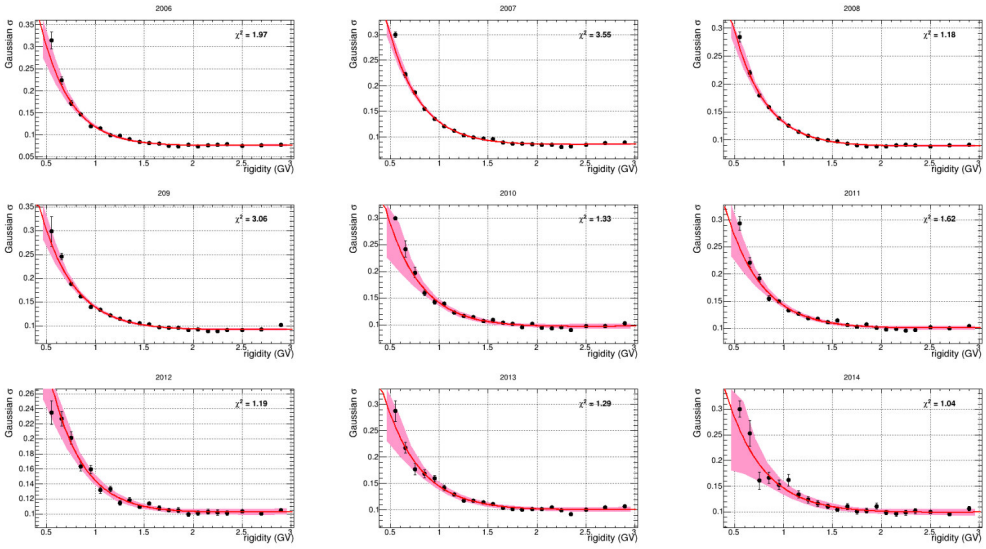

Figure 4.12: Yearly trends of the Gaussian sigma values obtained for deuterons are depicted as black points in the nine pictures, one for each year of the analysis. The red curves and the pink shaded area are respectively the functions fitting the sigma values and confidence intervals evaluated by the fit.

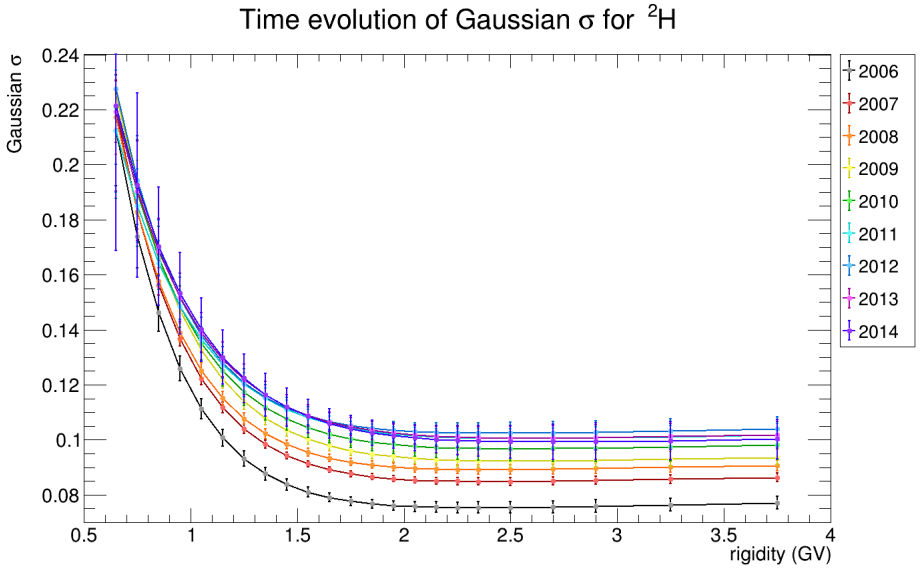

Figure 4.13: The sigma trends for deuterons are depicted in the picture with different colours. Time evolution is evident, lower values were obtained for 2006 and an increasing trend is observed over the years.

small uncertainty, at the level of 0.1%. Comparing the results obtained for each year, the mean parameter does not show any time dependence.
For the sigma parameter, the fitting function was:

$$f\left(x\right) = e^{a\cdot(-x+b)} + c + d\cdot x + e\cdot x^2 \quad , \tag{4.11}$$

where the exponential part was employed to follow the slope at the lower rigidities, whereas the quadratic polynomial was introduced to account for the slight rise starting around 2.5 GV. In Figure 4.12 the red curves represent the results of the fit, whereas the pink shaded areas represent the estimated confidence intervals. Because of the larger uncertainties on the sigma values and the residual fluctuations in their trend, the confidence intervals obtained for the sigma parameter are larger than those obtained for the mean parameter. Moreover, time evolution is observed for the sigma values which increase over the years starting from 2006 up to 2014 as shown in Figure 4.13. This increase is due to a worsening of the track length determination caused by some read-out chips failure in the tracker over the years. This effect will be described in Section 5.2.

The same procedure was followed for protons. First, yearly proton samples were selected with criteria 1-9,10p (named samples C) and the $1/\beta$ distributions within the range $[0.5, 4.0]$ GV were fitted with a Gaussian function as in

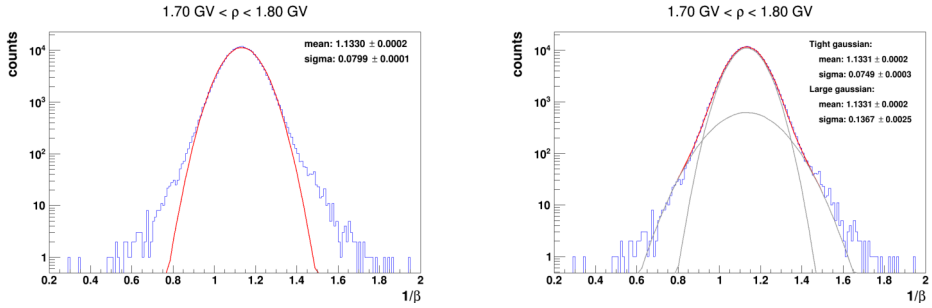

Figure 4.14: Fit of a $1/\beta$ distribution in the rigidity bin $[1.7, 1.8]$ GV for the sample C collected in 2006 with a Gaussian function at left and a double Gaussian model at right.

Figure 4.14, left panel. In the picture, it can be observed that there are tails of events which are not fitted by a single Gaussian. Since this occurred at all the rigidities, it was decided to repeat the fit with two Gaussians with the same mean but different widths. An example of this is shown in Figure 4.14, right panel. The results for the mean and sigma parameters obtained for the tighter Gaussian were analysed to study the effects that the distribution tails can have on the parameter estimation. In particular, the sigma values, referred to as C2 sigmas, were compared with the corresponding results obtained with a single Gaussian fit on the same $1/\beta$ distributions, referred to as C1 sigmas. This comparison is illustrated in Figure 4.15 for the year 2006. It can be observed that the C1 sigmas (black points) are larger than C2 sigmas (black stars) along all the rigidity range, showing that the single Gaussian functions broadened trying to fit the events in the tails.
Since the β is reconstructed based on the information collected by the ToF system, the criterion 11d, selecting deuterons on the truncated mean ToF dE/dX, can affect the shape of the $1/\beta$ distributions of the residual protons in the deuteron samples. To study this effect, an additional sample was selected with criteria 1-9,11d,$\overline{12\text{d}}$ (called samples D) for each year. The criterion $\overline{12\text{d}}$ is defined in the following way: it selects all the non-interacting events with a truncated mean dE/dX in the calorimeter under the lower cut defined in criterion 12d, which are protons. For each rigidity bin, the $1/\beta$ distribution was fitted with a Gaussian function as shown in the example of Figure 4.16. In this case, a single Gaussian was sufficient to fit the distributions. Since criterion 11d removed all the protons up to 1.5 GV, only above about 2.3 GV enough proton statistics allowed to perform a fit. For this reason, results for mean and sigma parameters from the fits were considered reliable only in the range $[2.3, 3.0]$ GV. The mean and sigma values were then

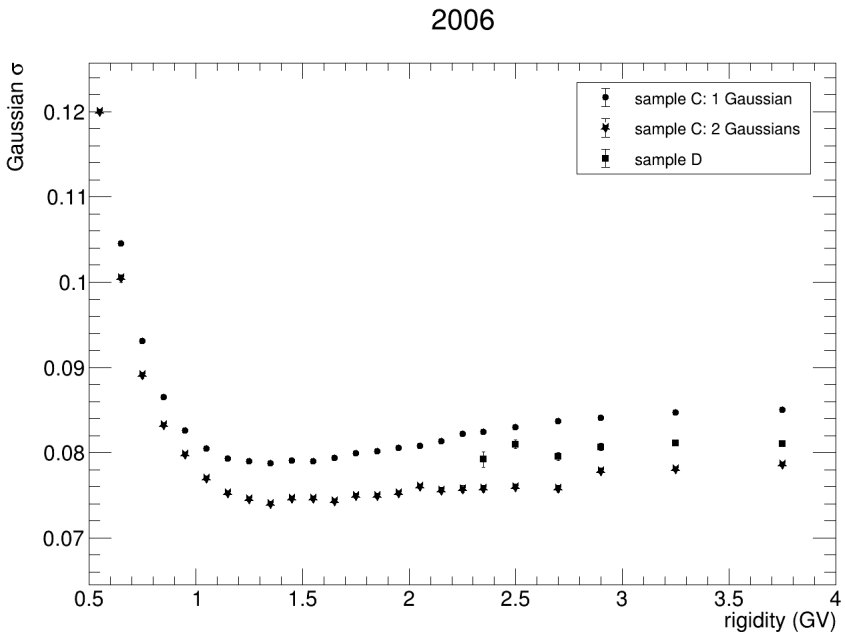

Figure 4.15: Sigma values as a function of rigidity obtained for year 2006 from fits of $1/\beta$ distributions of samples C with one Gaussian (black points), two Gaussians (black stars) and of sample D (black squares).

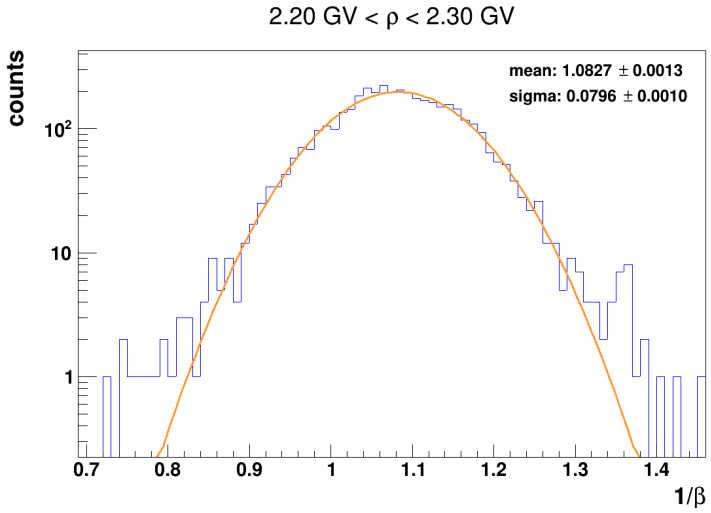

Figure 4.16: Fit of a $1/\beta$ distribution in the rigidity bin $[2.2, 2.3]$ GV for the sample D collected in 2006 with a Gaussian function.

compared to those obtained for samples C with one and two fitting Gaus-

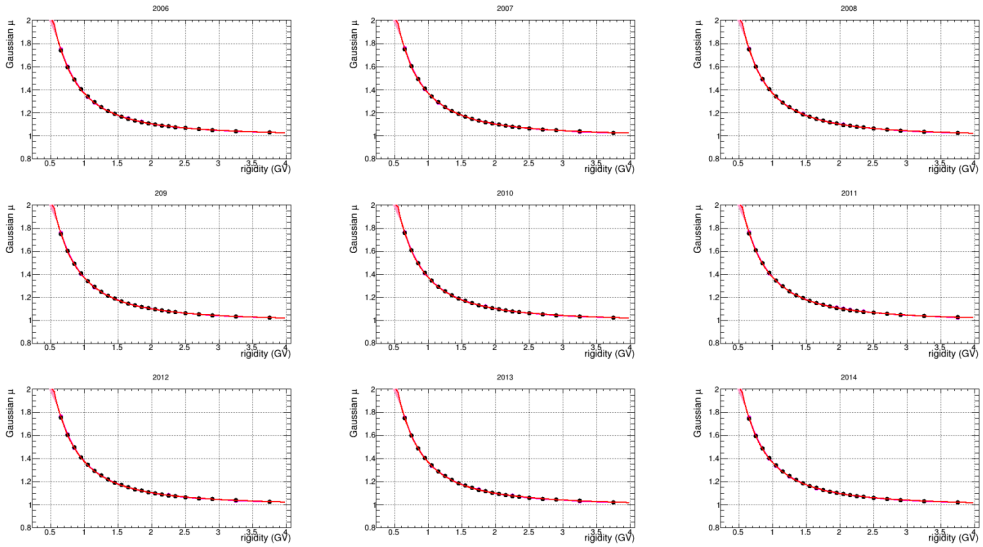

Figure 4.17: Yearly trends of the Gaussian mean values obtained for protons are depicted as black points in the nine pictures, one for each year of the analysis. The red curves and the pink shaded area are respectively the functions fitting the mean values and confidence intervals evaluated by the fit.

sians, as shown in Figure 4.15 for the sigma values in 2006, where the results obtained for sample D are depicted as black squared. The values of the mean obtained for sample D were found in good agreement with those obtained from samples C, for this reason, it was decided to fit the mean values obtained for samples C with a function parameterized as in Equation 4.10 to obtain smooth fitting curves and the confidence intervals. No time variation was found for protons as well. About the sigma parameter, in Figure 4.15 the sigmas obtained for samples D positioned themselves at intermediate values between the C1 and C2 sigmas. This indicates that the effect of criterion 11d on the width of the proton $1/\beta$ distributions can not be described directly by the C1 or C2 sigmas. To obtain sigma values affected by criterion 11d for all the rigidity range, it was chosen to calculate the ratios of the sigma values of samples D over the C1 ones, since in both cases a single Gaussian fit was used. These ratios were then fitted with a constant value for each year as shown in Figure 4.18. The resulting factors were then applied on the C1 sigma values, obtaining the sigma values depicted in Figure 4.19 for all the rigidity range $[0.5, 4.0]$ GV, which were then fitted with the Equation 4.11 to obtain the smooth fitting curves and the associated confidence intervals illustrated as pinked shaded areas.

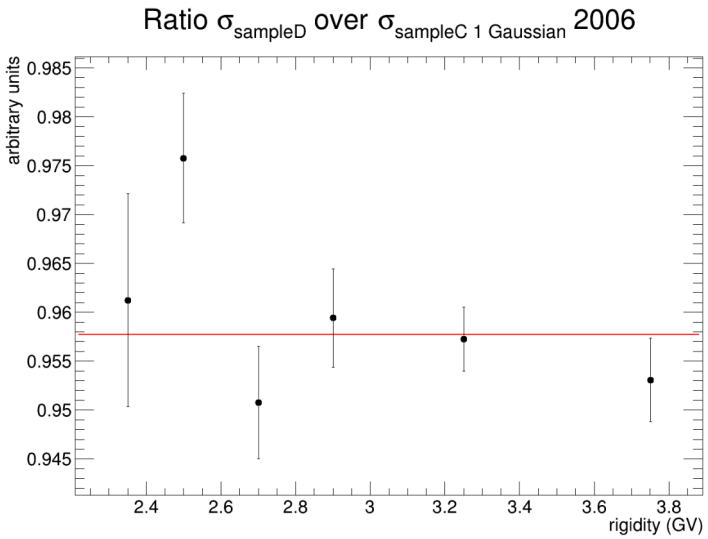

Figure 4.18: Ratio of sigma values obtained for sample D over sigma values obtained from sample C with single Gaussian fits for year 2006 as a function of the rigidity. These ratio values were fitted with a constant value (red horizontal line).

Also for protons, time variation was found for the sigma parameter, this is clearly visible in Figure 4.20, where a gradual broadening over time is observed for the sigma values of protons similar to what observed for deuterons.

At this point, initial values and confidence intervals for the Gaussian mean and sigma parameters were obtained for both protons and deuterons for each year. It can be noted that for the last two rigidity bins, which are $[3.0, 3.5]$ GV and $[3.5; 4.0]$ GV, mean and sigma values were retrieved directly only for protons, for deuterons this was not possible and mean and sigma values were extrapolated from the smooth fitting curves.

For a direct comparison between the sigma trends obtained for protons and deuterons, these were converted as a function of the β. This check is shown in Figure 4.21 for the year 2006. The two sigma trends show a similar shape, although the proton sigma values are lightly higher, probably due to a rigidity dependence. It can also be noticed that the confidence intervals evaluated for deuterons are larger than the protons ones. This is because the proton statistics in samples C are significantly higher than the deuteron statistics in samples A and B. This is not a relevant issue, because, in the $1/\beta$ distributions of the selected deuterons, the residual protons are the minor component needed to be fitted with more accuracy.

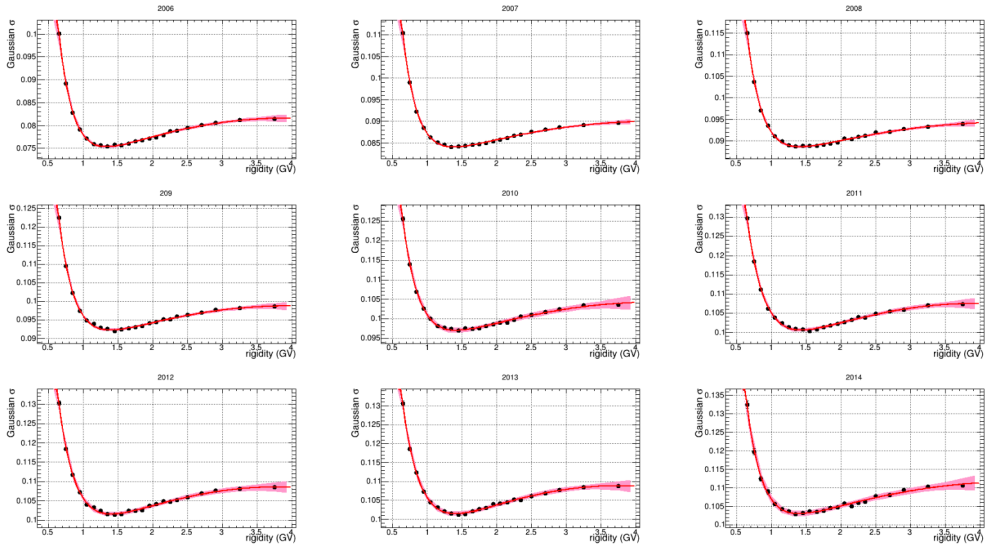

Figure 4.19: Yearly trends of the Gaussian sigma values obtained for protons are depicted as black points in the nine pictures, one for each year of the analysis. The red curves and the pink shaded area are respectively the functions fitting the sigma values and confidence intervals evaluated by the fit.

4.8.2 The double Gaussian fit

In the next stage of this fit procedure, the division in geomagnetic cut-off slices was temporarily not employed and the $1/\beta$ histograms for each rigidity bin were filled with the events selected with criteria 1-9,10d,11d from all the slices. This enabled to collect higher statistics and thus better defined $1/\beta$ distributions to be then fitted. The events collected in these $1/\beta$ distributions were also required to be of galactic origin according to the criterion based on the cut-off rigidity formulated in Equation 4.9. This was done to avoid any possible bias on the event distributions introduced by the re-entrant albedo particles.
At this point, the $1/\beta$ distributions were fitted with the Maximum Likelihood method with two Gaussians with the mean and the sigma parameters of each Gaussian initialized with the values evaluated with the procedure described in the previous subsection. The mean and the sigma parameters were allowed to move inside the confidence interval, while the amplitude parameters were left free to vary. Figure 4.22 shows the double Gaussian fit for the $1/\beta$ distributions for some of the rigidity bins in logarithmic scales. The fit gave back the estimated parameter values with the corresponding uncertainty together with the covariance matrix expressing the covariance values between the dif-

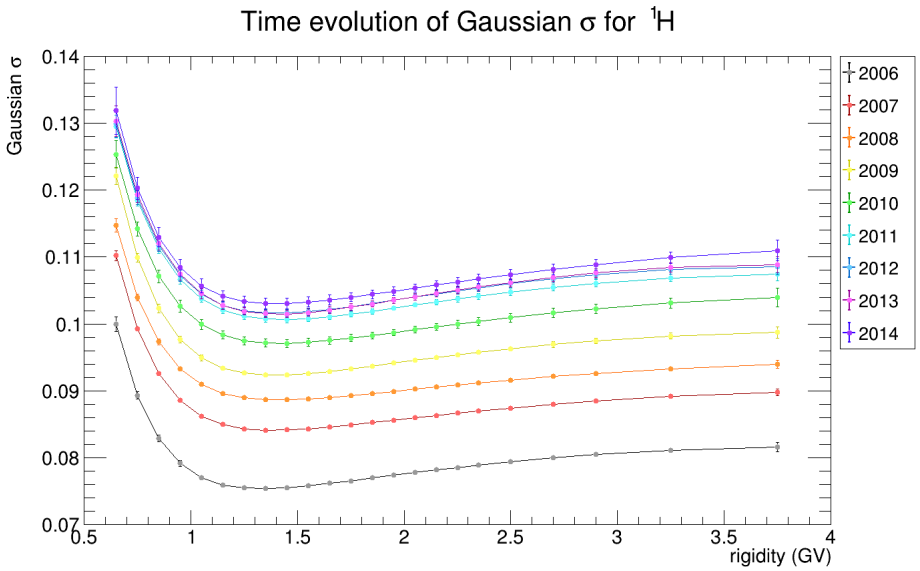

Figure 4.20: The sigma trends for protons are depicted in the picture with different colours. A time evolution is evident, lower values were obtained for 2006 and an increasing trend is observed over the years.

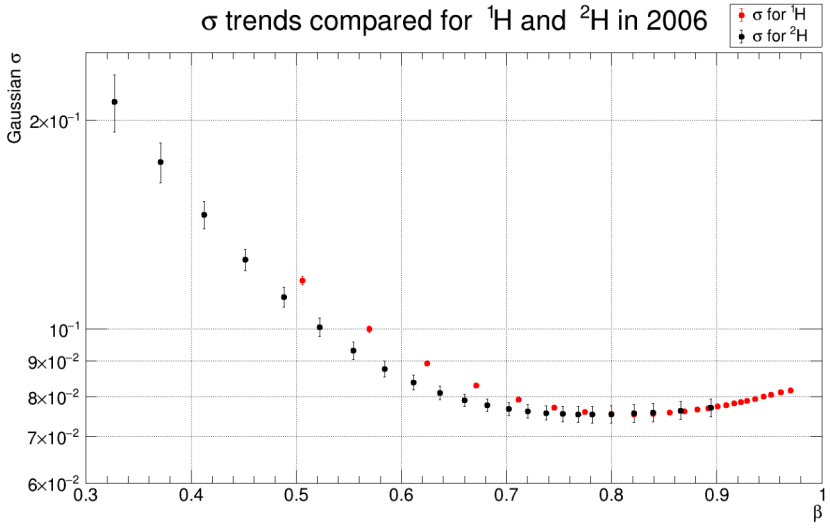

Figure 4.21: Trends of the Gaussian sigma values obtained for the year 2006 for protons (red points) and for deuterons (black points) are depicted in the picture as a function of the β.

ferent parameters. The proton and deuteron counts were then calculated in

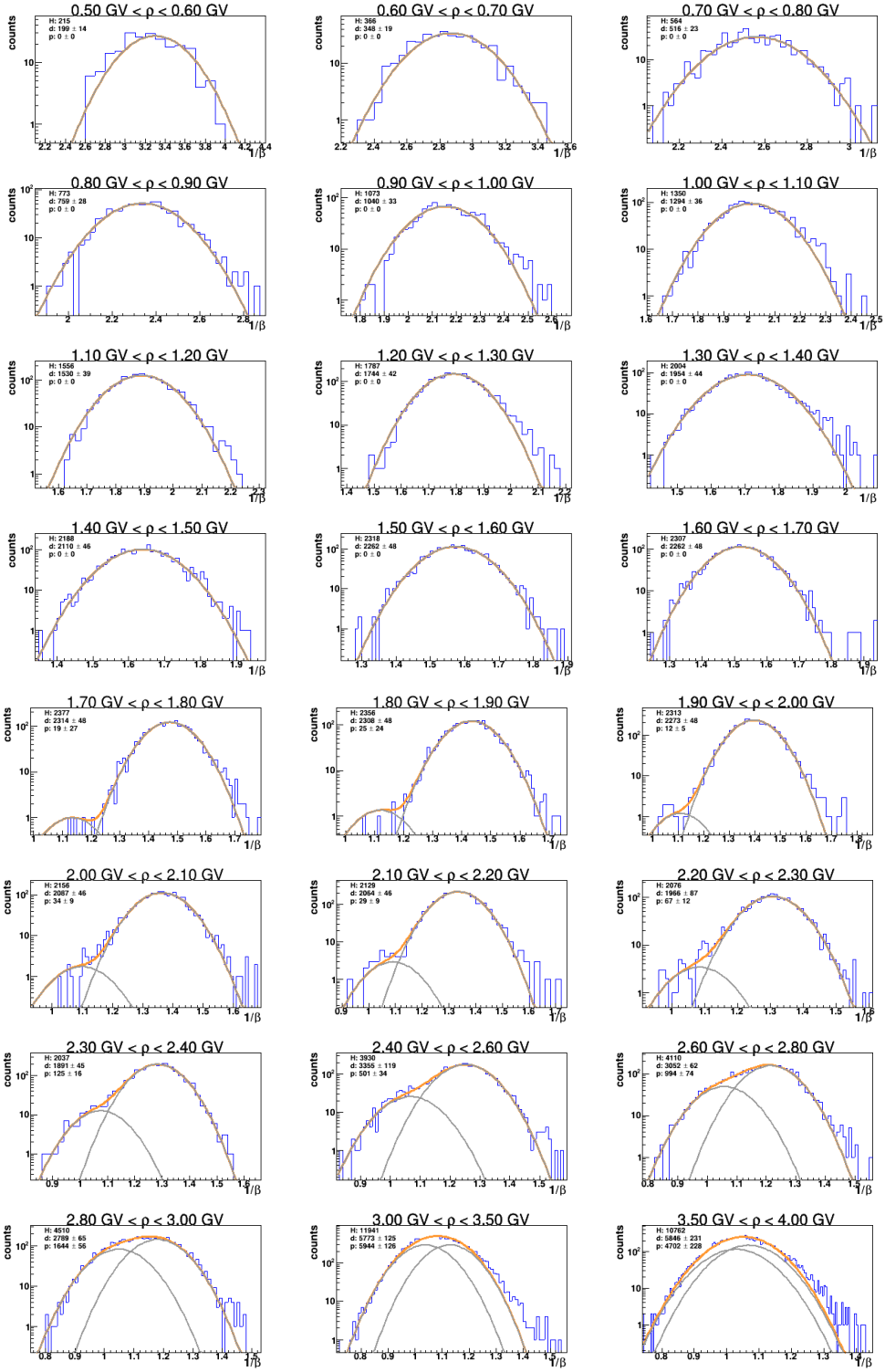

Figure 4.22: Double Gaussian fit of the $1/\beta$ distributions for all the rigidity bins.

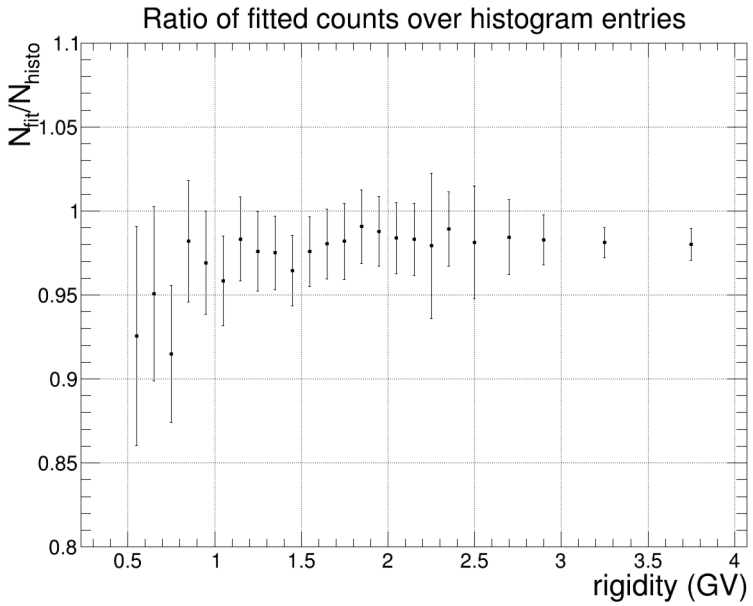

Figure 4.23: Ratio of the total number of events obtained from the fit over the number of events in the $1/\beta$ distributions calculated for 2006.

the following way: the area subtended by each Gaussian function was calculated and then divided by the bin width of the considered $1/\beta$ histogram, giving as a result the number of the events. The standard deviation on these numbers was then obtained from the error on the subtended area caused by the parameter uncertainties. This was implemented through the IntegralError method in Root [115], which requires in input the covariance matrix for the parameters of the fitting function to use the estimated variance and covariance values for the calculation of the error on the integrated area. This was then divided by the bin width of the $1/\beta$ histogram to obtain the error on the counts given by the fit. This was done for the number of total events of protons and deuterons.
The number of total events evaluated by the fits was then compared with the total counts of the $1/\beta$ histograms for each rigidity bin. A systematic underestimation of event numbers by the double Gaussian fit, at the level of a few percent, was observed as it can be seen in Figure 4.23 for the year 2006. This was considered a systematic error.

The ratio of proton counts over deuteron counts was then calculated for each rigidity bin for each year to evaluate the amount of residual protons as a function of the rigidity. Figure 4.24 shows these ratios for the year 2006, when the proton counts were under 10% of the deuterons ones up to 2.3 GV

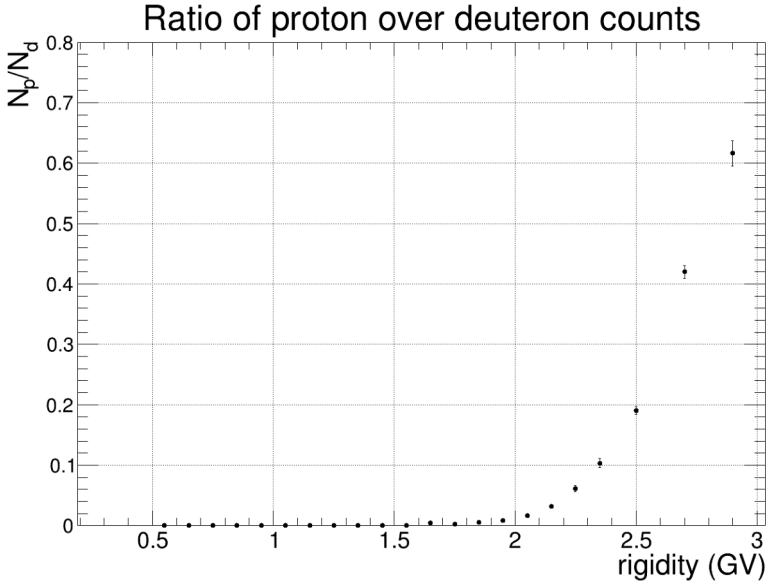

Figure 4.24: Ratio of the total number of events obtained from the fit over the number of events in the $1/\beta$ distributions calculated for 2006.

and then grew fast at higher values reaching a level higher than 60% at 2.9 GV. Since up to the bin $[2.4, 2.6]$ GV the proton counts were lower than the 20% of the deuteron counts for all the years and the distance between the two Gaussian peaks was larger than the FWHM of both the two Gaussians, this bin was arbitrarily considered the upper limit up to which deuteron counts could be estimated with negligible contamination. In the following rigidity bins, the deuteron counts were not used to calculate final deuteron fluxes at those rigidities, but they were only included in the unfolding procedure (see Section 5.4).
The fractions of events identified as deuterons $f_d = \frac{N_d}{N_{tot}}$ and as protons $f_p = \frac{N_p}{N_{tot}}$ over total number of events found by the fit were also calculated together with the corresponding standard deviations calculated using the variance propagation equation. These values were then used for the next step, when the events collected in the geomagnetic cut-off slices were retrieved.
For each geomagnetic cut-off slice, the number of events in each rigidity bin was multiplied by the fractions of protons and deuterons achieved before for that bin and that year. The resulting numbers were taken as the evaluated proton and deuteron counts for the considered bin, in the considered geomagnetic cut-off of the considered year. In the bins where the proton fraction

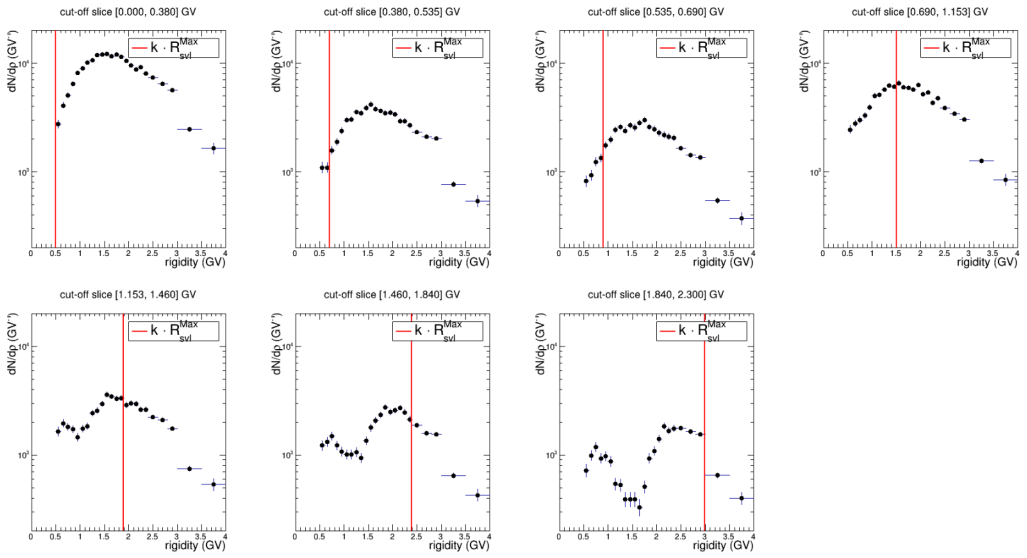

Figure 4.25: Counts of deuterons divided by the rigidity bin widths as a function of the rigidity for each of the seven geomagnetic cut-off slices.

was zero, the standard deviation was the Poissonian one $\sigma_d = \sqrt{n_{events}}$ where n_{events} is the total number of events in the $1/\beta$ distribution. In the bins with residual contamination of protons present, the variance propagation equation was used to calculate the standard deviation on the deuterons counts estimated by the fit procedure:

$$\sigma_d = \sqrt{n_{event}^2 \cdot \sigma_{f_d}^2 + \sigma_n^2 \cdot f_d} \tag{4.12}$$

where n_{event} is the number of total events in the considered $1/\beta$ distribution, the σ_{f_d} is the sigma on the estimated fraction of deuterons f_d, $\sigma_n = \sqrt{n_{events}}$ is the Poissonian standard deviation on the number of events in the $1/\beta$ distribution.
At this point, the deuteron counts as a function of the rigidity for each cut-off slice and for each year were obtained. In Figure 4.25 these results are shown for the year 2006 after having divided the number of events for the rigidity bin widths. These count distributions still consisted of two deuteron components, one of re-entrant albedo particles and one of galactic cosmic rays. Later in the analysis, only deuterons with rigidities higher than the maximum geomagnetic cut-off rigidity of the corresponding slice multiplied by a factor k (red lines in Figure 4.25) were selected to contribute to the fluxes of the galactic deuterons.

Chapter 5

The flux calculation

At the end of chapter 4, yearly proton and deuteron counts were obtained for each geomagnetic cut-off slice for the period from 2006 to 2014. As it will be described in this chapter, these counts were used to calculate the yearly fluxes. For this purpose, the efficiency of each selection criterium, the contamination from re-entrant albedo particles and from the products of fragmentation of heavier nuclei in the aluminium dome, the geometrical factor and the live time of the instrument were calculated. The particle flux is calculated as:

$$\phi(\rho) = \frac{n(\rho)}{\Delta\rho \; G_N(\rho) \, T(\rho) \, \varepsilon(\rho)} \quad . \tag{5.1}$$

where $\phi(\rho)$ is the flux as a function of the measured rigidity ρ, the other quantities are:

- $n(\rho)$ the number of events after the background subtraction,
- $\Delta\rho$ is the width of the considered rigidity bin,
- $G_N(\rho)$ is the nominal geometrical factor as a function of the rigidity,
- $\varepsilon(\rho)$ is the overall efficiency derived from the products of the efficiency values of each selection,
- $T(\rho)$ is the instrumental live time for the considered rigidity bin.

The fluxes were then reconstructed as a function of p_0, i.e. the momentum of the particles before any interaction with the PAMELA apparatus, by means of an unfolding procedure applied on the count distributions for each geomagnetic cut-off slice. Moreover, since protons and deuterons have charge $Z = 1$, assuming natural units ($c = 1$, $e = 1$), the Equation 1.2 entails that p_0 also corresponds to the actual rigidity R of the particle as at the top of

the payload before any interaction with the instrument.
In the following sections, the procedure of flux calculation is discussed step by step.

5.1 Efficiency calculation

The efficiency of any selection is defined as the fraction of events which satisfy the required criterion. This can be expressed as follows:

$$\varepsilon = \frac{n_{passed}}{n_{sample}} \quad , \tag{5.2}$$

where ε is the efficiency value, n_{sample} is the number of events of the starting sample, called efficiency sample, and n_{passed} is the number of events that passed the selection.
An accurate evaluation of the efficiency values is a fundamental step to get reliable fluxes. The efficiency can be calculated using efficiency samples from flight data or relying on a Monte Carlo simulation of the experimental apparatus. Generally, the flight data are preferred because avoids introducing systematics induced by any time variation of the detector response, which in space experiments like PAMELA, are difficult to control.
A Monte Carlo simulation of the PAMELA apparatus based on the GEANT4 software was developed to reproduce as best as possible the detectors. However, the validation of the simulated results is always needed to not introduce any systematics in the flux calculation.
The redundancy of the PAMELA detectors enabled to define a set of selection criteria, already illustrated in chapter 4, to select efficiency samples uncorrelated from the studied selections. These samples allow to evaluate the flight efficiency at least in a part of the rigidity range and cross-check the simulated efficiency. This allows to validate the simulation and use it to calculate the efficiency in those rigidity intervals where the flight efficiency samples are affected by residual contamination.
The efficiencies had to be measured for each year in order to monitor the detector performance over time. In the next sections, the time-dependent efficiency of the selection criteria used for the proton and deuteron analysis is calculated as a function of the rigidity.

5.2 Tracking efficiency

Criteria 1-6 are selections on the quality of the reconstructed track. To estimate the rigidity-dependent efficiency of these selection criteria, the sim-

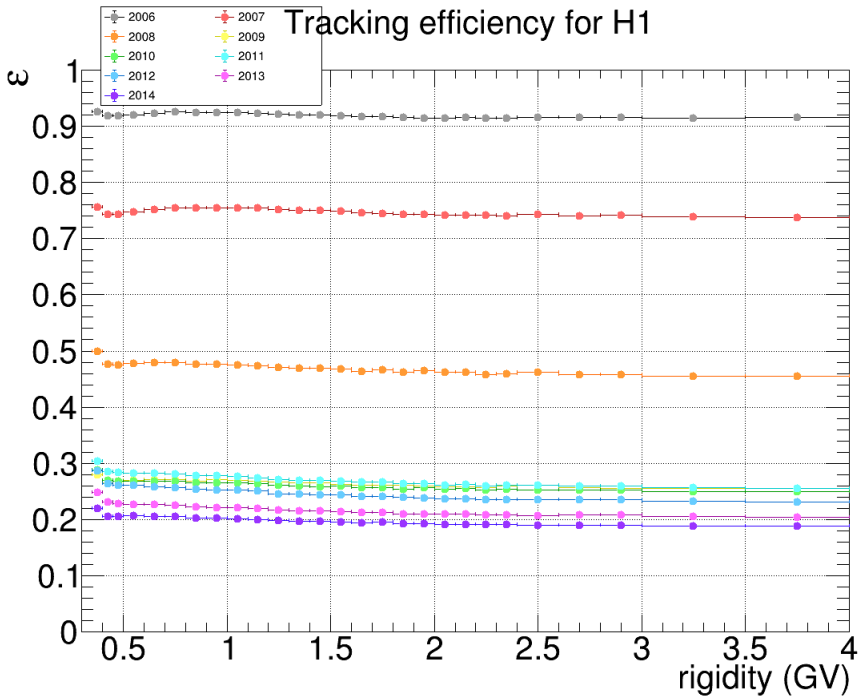

Figure 5.1: Tracking efficiency values calculated as a function of the actual rigidity R (which corresponds to p_0) over time in simulation for protons.

ulation had to be used, since no rigidity measurement independent from the tracker was provided by PAMELA.
Samples of simulated protons and deuterons were generated to evaluate the efficiency of the selection criteria 1-6, which is referred to as tracking efficiency for simplicity. Events were generated between 0.01 GeV/n and 3.5 GeV/n according to the spectral shapes of protons and deuterons found in [30]. The simulations included the degradation in the tracker performance, due to the progressively random failure of some readout electronic chips connected to the microstrip detectors, which created dead areas over the silicon planes and consequently a decrease in the tracking performance. This effect was implemented in the simulation with a time-dependent map of the dead chips, as described in more detail in [117].

Since the simulation provides the values of the initial momentum p_0 of the generated particles, the tracking efficiency was studied as a function of p_0. Figure 5.1 and Figure 5.2 shows the yearly averaged simulated tracking efficiency for protons and deuterons respectively measured between 2006 and

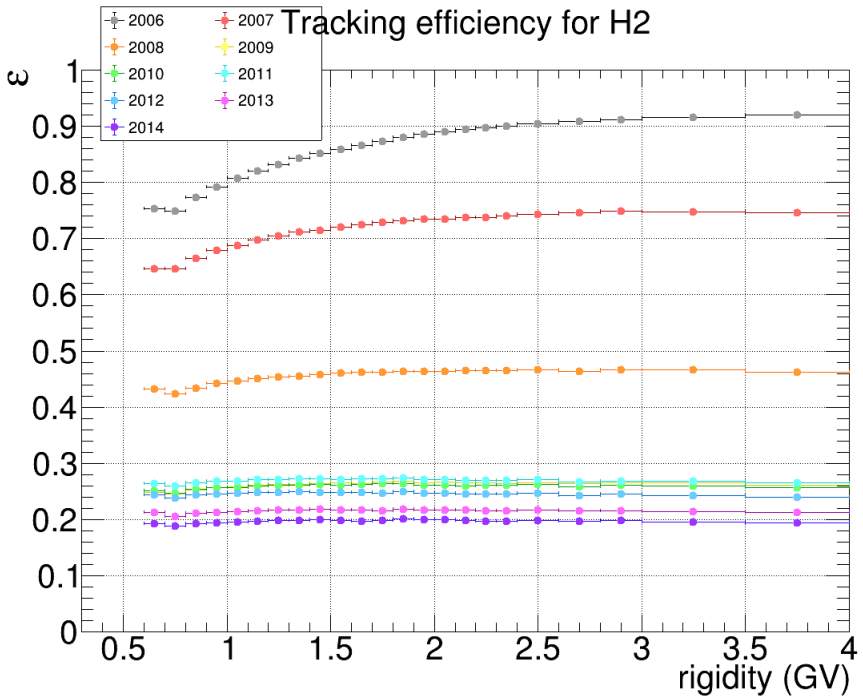

Figure 5.2: Tracking efficiency values calculated as a function of the actual rigidity R (which corresponds to p_0) over time in simulation for protons at the top and deuterons.

2014 as a function of p_0. The efficiency was obtained as:

$$\epsilon_{track} = \frac{n_{trace}}{n_{all}} \quad , \tag{5.3}$$

where n_{all} is the efficiency sample of protons or deuterons and n_{track} is the number of events that survive the selection criteria 1-6. As it can be seen in two figures, the tracking efficiency considerably changes over time, decreasing from around 90% during 2006 down to 20% in 2014 as an effect of the increasing dead area on the tracker silicon planes.
It can also be observed a different trend at lower rigidities below 1.5 GV between protons and deuterons. The efficiency values of deuterons decrease more than those of protons at low rigidities, because of the higher ionisation energy losses and multiple scatterings experienced by deuterons at the same rigidities of protons.
The tracking efficiencies were used in the flux calculation by dividing the counts of the selected protons and deuterons as the function of p_0 after an unfolding procedure, which is described in Section 5.4.

5.3 Estimation of the selection efficiency in simulation

The efficiency of the criteria 8, 9, 10p, 10d and 11d were calculated with proton and deuteron simulated data and flight data. With simulated data, the efficiencies were measured with the following procedure: initial efficiency samples were selected with criteria 1-7 for both protons and deuterons, called respectively n^p_{eff} and n^d_{eff}. Then, applying in cascade the criteria 8, 9, 10p for protons or 8, 9,10d, 11d for deuterons, the efficiency samples for each criterion were obtained. These are referred to as $n^{p,d}_{AC}$, $n^{p,d}_{Z=1}$, $n^{p,d}_{dEdx_{trk}}$, $n^{d}_{dEdx_{ToF}}$, with the indices p and d referring to protons and deuterons respectively. The efficiencies were then measured as follows:

$$\epsilon_{AC} = \frac{n_{AC}}{n_{eff}} \tag{5.4}$$

$$\epsilon_{Z=1} = \frac{n_{Z=1}}{n_{AC}} \tag{5.5}$$

$$\epsilon_{dEdx_{trk}} = \frac{n_{dEdx_{trk}}}{n_{Z=1}} \tag{5.6}$$

$$\epsilon_{dEdx_{ToF}} = \frac{n_{dEdx_{ToF}}}{n_{dEdx_{tracker}}} \tag{5.7}$$

where ϵ_{AC}, $\epsilon_{Z=1}$, $\epsilon_{dEdx_{trk}}$ and $\epsilon_{dEdx_{ToF}}$ are respectively the efficiency of selection criteria 8, 9, 10p or 10d, and 11d. The efficiency values obtained in this way were then compared with those obtained from flight data. This was done to check the reliability of the efficiency values obtained in simulation. Simulated and flight efficiency of each criterion are described in the next subsections.

5.3.1 Efficiency of the AC selection (criterion 8)

A clean efficiency sample of deuterons was selected from flight data with criteria 1-7,9,10d,11d,12d in order to reject interacting events. For this purpose, an additional criterion, referred to as ToF pattern cut, was also used. This required that:

- there were no more than one paddle hit (both TDC signals) on S11, S12, S21, S22;
- on S1 and S2, if there is a hit paddle, it must be associated to the extrapolated track from the spectrometer.

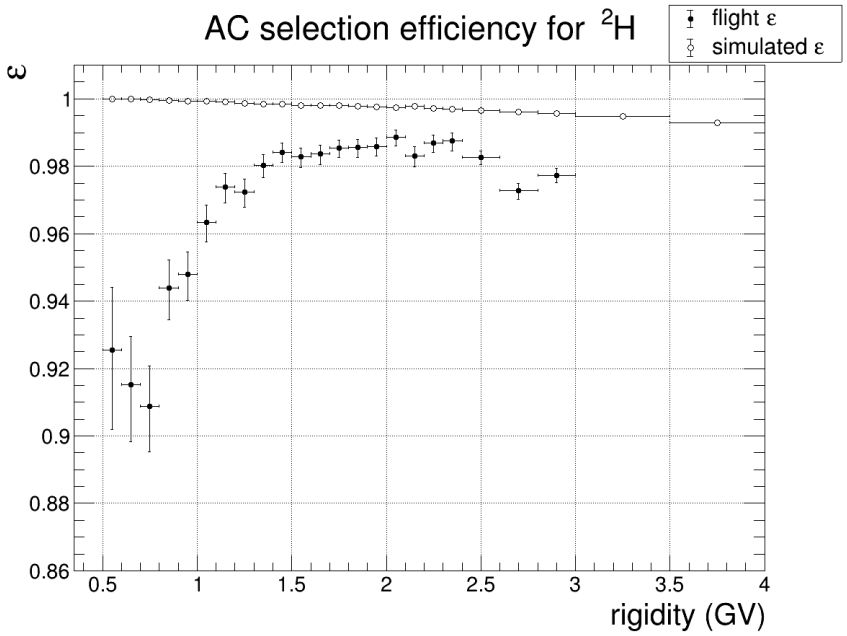

Figure 5.3: Efficiency values calculated for criterion 8 (AC selection) as a function of the rigidity with flight (black points) and simulated deuterons (open points).

On this sample of events, the efficiency for criterion 8 was calculated. This efficiency was calculated for all the years, but no significant time variations were observed. The efficiency for year 2006 is shown in Figure 5.3 (black points) and compared with the simulated values (open points). The simulated efficiency is almost constant as a function of the rigidity, whereas the flight efficiency below 1.5 GV presents a decrease. Since the amount of this decrease in flight efficiency was observed to vary relaxing a few selections rejecting multitrack events, like the ToF pattern cut, it can be concluded that this decrease is due to the presence of residual contamination from products of fragmentations and other multitrack events. Between 1.5 and 2.5 GV, the flight efficiency has a flat trend, which then starts to decrease for rigidities higher than 2.6 GV. Because of the residual contamination in the flight sample, for the deuteron flux calculation it was decided to use the simulated efficiency normalized on the flight values in the range [1.4, 2.5] GV.
The same procedure was followed also for protons, selecting the flight efficiency samples with criteria 1-7,9,10p,11p,$\overline{12d}$ and the TofPattern cut. The efficiency values are shown in Figure 5.4 (black points) compared with the simulated ones (open points). Above 0.8 GV a good agreement is found between the shapes of simulated and flight efficiency, although a discrepancy

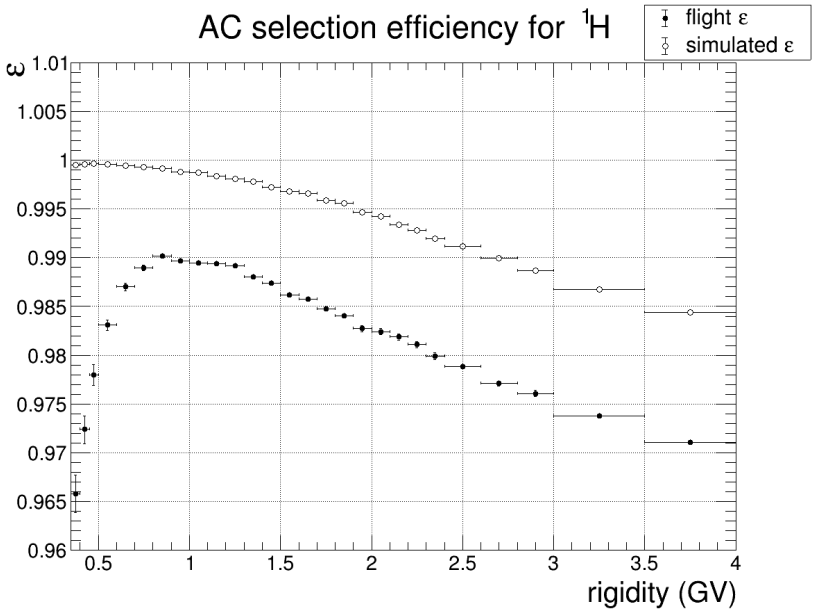

Figure 5.4: Efficiency values calculated for criterion 8 (AC selection) as a function of the rigidity with flight (black points) and simulated protons (open points).

of about 1% is present between the two sets of values. At rigidities lower than 0.8 GV, a decreasing trend is observed in flight values due to residual contamination of multitrack events present in the efficiency sample. Also for protons, it was decided to use the simulated efficiency values normalized to those of the flight ones for the flux calculation.

5.3.2 Efficiency of the charge-one selection (criterion 9)

Efficiency samples were selected from flight data through criteria 1-8, 10d,12d for deuterons. On these samples the four cuts defined in criteria 9 for the

layers S11, S12, S21, S22 were applied to calculate the related efficiencies:

$$\varepsilon_{S11} = \frac{n_{S12+S21+S22+S11}}{n_{S12+S21+S22}} \tag{5.8}$$

$$\varepsilon_{S12} = \frac{n_{S11+S21+S22+S12}}{n_{S11+S21+S22}} \tag{5.9}$$

$$\varepsilon_{S21} = \frac{n_{S11+S12+S21}}{n_{S11+S12}} \tag{5.10}$$

$$\varepsilon_{S22} = \frac{n_{S11+S12+S21+S22}}{n_{S11+S12+S21}} \tag{5.11}$$

where ε_{S11}, ε_{S12}, ε_{S21}, ε_{S22} are the efficiencies for each ToF layers. The subscripts of each sample n indicate the layers on which the cuts of criteria 9 were required to build the cleanest possible efficiency samples. To build efficiency samples for S11 and S12, the cuts of all the other three ToF layers were applied. This was done to reject those events reconstructed as deuteron, but originated from the fragmentation of heavier nuclei in the ToF material. The efficiency values for the four selection cuts are shown in Figure 5.5 for deuterons. For the four layers, the selection cuts are very high, $\geq 99\%$, and have a flat trend for S21 and S22, for the rigidity range $[1.5, 3.0]$ GV for S11 and S12. These efficiencies were also calculated for the other years but no significant time variations were observed. The flight efficiencies were also compared with the corresponding simulated data efficiencies (open points in Figure 5.5). For the first two layers in $[1.5, 3.0]$ GV the simulated efficiency reproduces the shapes of the flight efficiency, although with higher values of a factor 1% and 0.5% for S11 and S12 respectively. Below 1.5 GV, the flight efficiencies diverge from the simulated because of the falling trend not present in simulated data. Also in this case, the amount of this decrease was observed to vary relaxing a few selections, in particular those on S21 and S22, indicating the presence of residual contamination of the products of heavier nuclei fragmentation occurring in the ToF material and in the aluminum dome. For the next layers, S21 and S22, a good agreement is observed between simulated and flight efficiencies, they present the same shapes although they differ in values of a factor of about 0.2%.
For protons the same procedure was followed, starting from an initial flight sample selected with criteria 1-8, 10p and then applying the four cuts of criterion 9 as was made for deuterons. The resulting efficiency values are shown in Figure 5.6 as black points for the four ToF layers. The efficiencies present high values, $\geq 0.99\%$ following a flat trend, except for the range $[0.35, 0.7]$ GV in S11 and S12. Also in this case, the observed falling trend is caused by residual contamination of products of fragmentation. These efficiencies were calculated for all the years also for protons but no time

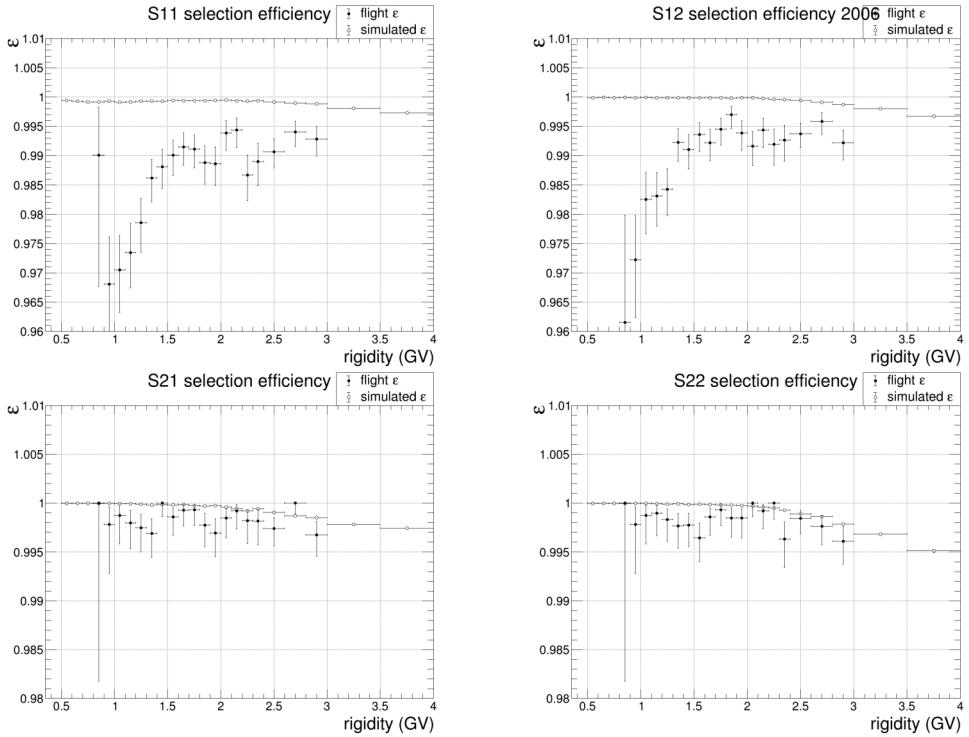

Figure 5.5: Efficiency values calculated for charge-one selection defined in S11 (top left), S12(top right), S21 (bottom left) and S22 (bottom right) in criterion 9 as a function of the rigidity with flight (black points) and simulated deuterons (open points).

variation was observed. In Figure 5.6 the flight efficiency values are also compared with those obtained with simulated data (open points). Also for protons, the simulated efficiency values are systematically higher of about 1% and flat for all the rigidities.
From all these observations, for both protons and deuterons, it was decided to normalize the simulated efficiency values to those obtained with flight data in the rigidity ranges $[1.5, 3.0]$ GV and use these new values for the deuteron flux calculation.

5.3.3 Efficiency of the tracker dE/dX selection (criteria 10d, 10p)

Clean deuteron efficiency samples were selected with criteria 1-9, 11d, 12d and 13d to calculate the efficiency of criterion 10d in the rigidity range $[0.8, 3.0]$. This was done for each year to evaluate the time evolution of

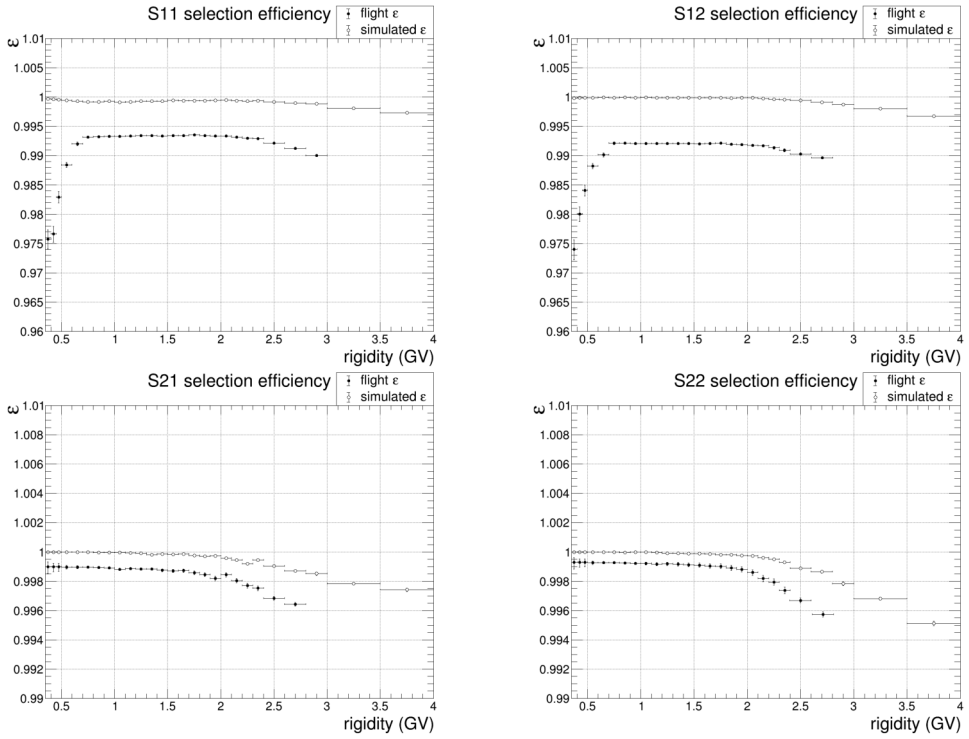

Figure 5.6: Efficiency values calculated for charge-one selection defined in S11 (top left), S12(top right), S21 (bottom left) and S22 (bottom right) in criterion 9 as a function of the rigidity with flight (black points) and simulated protons (open points).

the efficiency over the years. The resulting efficiency values are displayed in Figure 5.7 as a function of the rigidity and for each of the nine years with different colours. For each year, the efficiency decreases at higher rigidities. This depends on the shape of the selection, which is defined to reject more protons and consequently cut more deuterons. Time dependence is also observed, the efficiency values change from about 0.68 in 2006 at 2.7 GV up to around 0.82 GV in the last 4 years. This is caused by the lower number of energy deposits detected inside the tracker on average per event as an effect of the dead areas over the silicon planes. Indeed, a lower number of hits leads to the truncated mean algorithm used for the dE/dX in the tracker to select higher dE/dX values, making consequently the dE/dX distributions rise at higher values. This leads to an increment of the efficiency values over time for criterion 10d, but at the same time also to more protons surviving the selections. This is not a relevant issue, because the surviving protons are discarded through the fitting procedure of the $1/\beta$ distributions. Because of

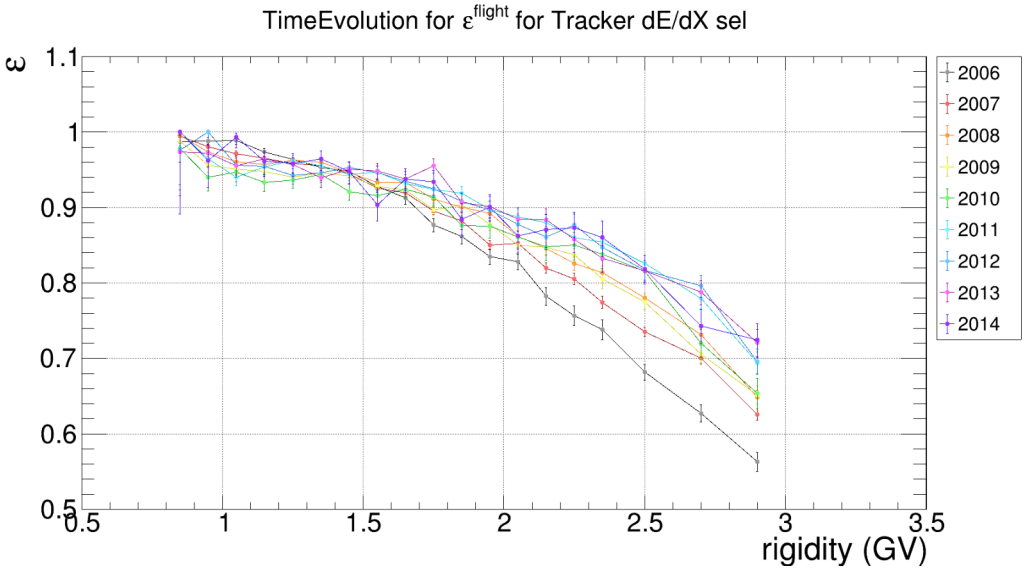

Figure 5.7: Time evolution of efficiency values calculated for criterion 10d (tracker dE/dX selection of deuterons) as a function of the rigidity with yearly flight deuteron efficiency samples.

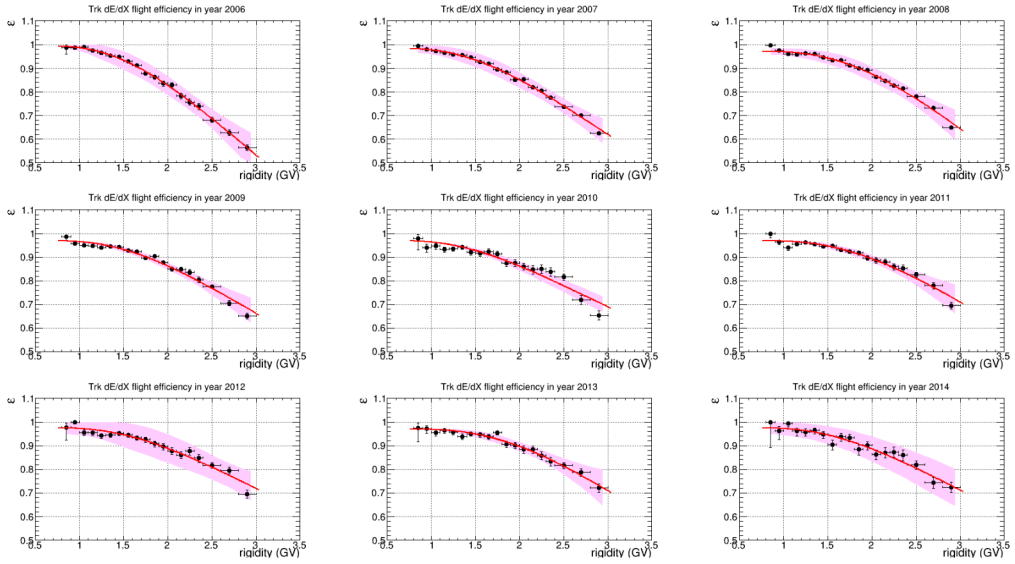

Figure 5.8: Flight efficiency values for criterion 10d (black points) calculated for each year from 2006 (top left) to 2014 (bottom right) and fitted with Equation 5.12. The fitting curves and the associated confidence intervals are shown as red lines and magenta shaded areas respectively.

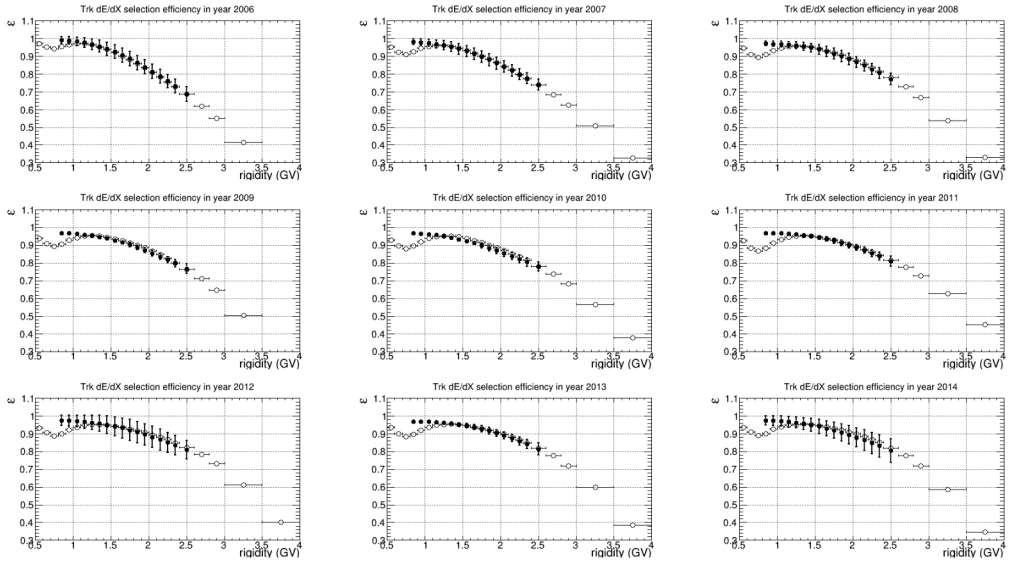

Figure 5.9: Flight fitted efficiency values with the associated confidence intervals (black points) for criterion 10d are compared with the corresponding simulated efficiency values (open points) for each year from 2006 (top left) to 2014 (bottom right).

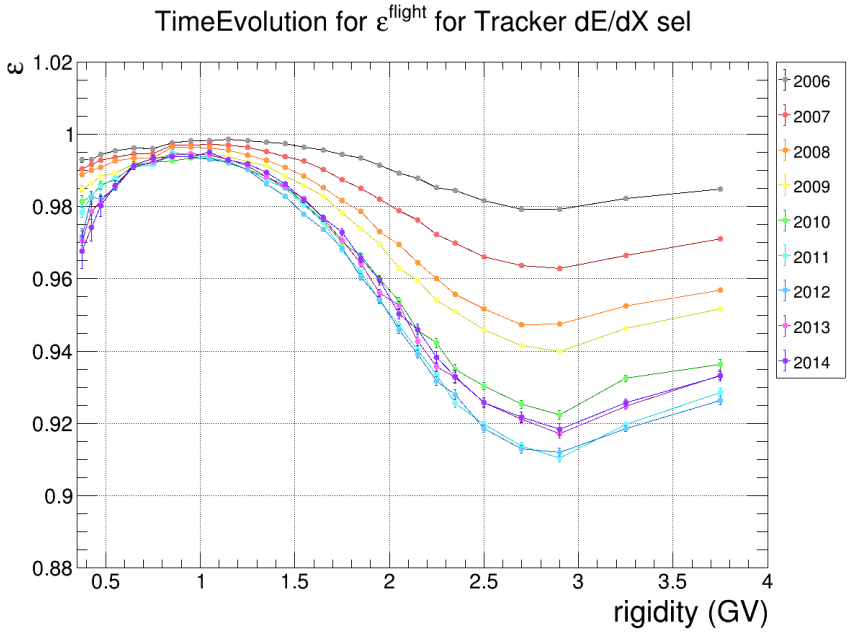

Figure 5.10: Time evolution of efficiency values calculated for criterion 10p (tracker dE/dX selection of protons) as a function of the rigidity with yearly flight proton efficiency samples.

the relevant fluctuations of the efficiency, these were fitted with the following function:

$$a \cdot \left(1 - \left(b \cdot \exp\left(-\frac{c}{x}\right)\right)\right) \quad , \tag{5.12}$$

arbitrarily chosen to reproduce the observed trends. The resulting fitting curves are shown as red lines in Figure 5.8 along with the confidence intervals estimated by the fit with the ROOT software as magenta shaded areas. The fitting trends with the associated confidence intervals (black points in Figure 5.8) were then compared with the efficiency values obtained from simulated data (open points in Figure 5.9). For the flux calculation, it was decided to use the simulated efficiency values taking the confidence intervals estimated in flight data as systematic errors. At low rigidities in [0.8,1.2], the difference between flight and simulated values were treated as systematic errors.

The same procedure was followed also for criterion 10p. Clean proton samples were selected with criteria 1-9, 12p, $\overline{12d}$ to calculate the efficiency in the rigidity range $[0.35, 3.0]$ GV. The resulting efficiency values are displayed in Figure 5.10 as a function of the rigidity and for each of the nine years. Also in this case, the efficiency values are observed to vary over time in particu-

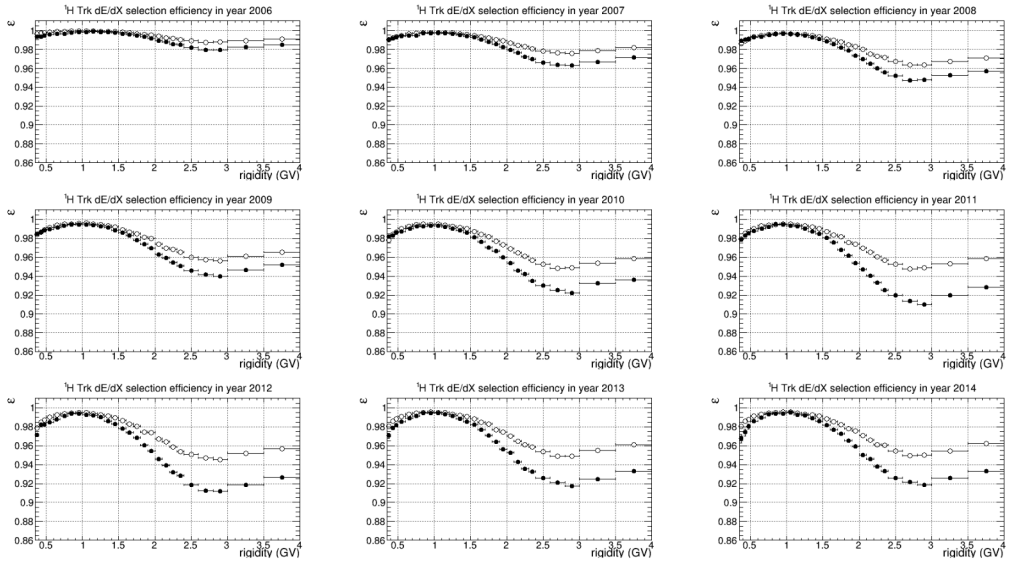

Figure 5.11: Flight efficiency values (black points) for criterion 10p are compared with the corresponding simulated efficiency values (open points) for each year from 2006 (top left) to 2014 (bottom right).

lar at the higher rigidities. The decrease over time is opposite to what was observed for criterion 10d: the minor number of hits available on average per event in the last year makes the dE/dX distributions rise with the effect of a gradually increasing small fraction of protons which are not selected by criterion 10p. The calculated efficiency samples were then compared with the simulated values shown in Figure 5.11. It can be noted that for each year the simulated values reproduce qualitatively well the shapes of the flight, although a small discrepancy is observed growing as a function of the rigidity at 3.0 GV. This discrepancy increases also as a function of time, from a level of 0.8% in 2006 at 3.0 GV to a 3% in 2014. The source of this discrepancy is still under study and it was treated as a systematic uncertainty in the proton flux calculation.

5.3.4 Efficiency of the ToF dE/dX selection (criterion 11d)

Also for criterion 11d, clean efficiency samples were selected for each year. Similarly to what was done for criterion 10d, deuteron events were selected with criteria 1-9,10d,12d,13d and the efficiency for criterion 11d was calcu-

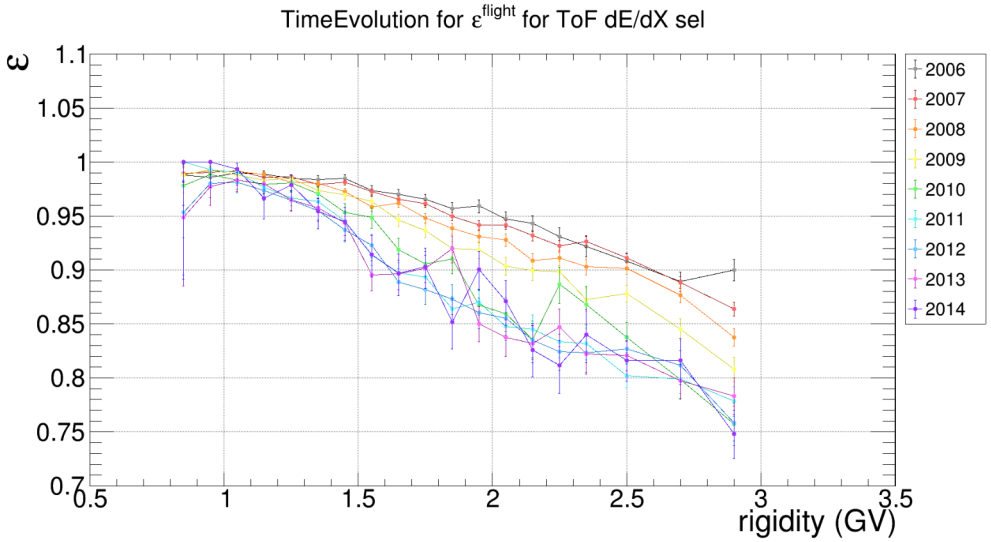

Figure 5.12: Time evolution of efficiency values calculated for criterion 11d (ToF dE/dX selection of deuterons) as a function of the rigidity with yearly flight deuteron efficiency samples.

lated from fight data. These are shown in Figure 5.12. Time evolution is observed, with flight efficiency values decreasing from about 0.91 for the first two years down to 0.82 for the last three years. The observed decrease is an effect of the aging of the ToF system. Also in this case, to reduce the statistical fluctuations, the efficiency values were fitted with the function 5.12. The fits are shown in Figure 5.13 (res lines) together with the estimated confidence intervals (magenta shaded areas). The fitted values were then compared with the simulated efficiency values in Figure 5.14. A good agreement was observed for the first three years along all the range $[0.8, 3.0]$ GV, but a small discrepancy is observed growing as a function of the rigidity and over time. This could be due to increasing proton contamination in the flight efficiency samples over time due to the time effects observed in criterium 10d. For this reason, it was decided to use the simulated efficiency values for the deuteron flux calculation and take the gap with the lower border of the confidence intervals of flight efficiency values as a systematic uncertainty.

5.4 Unfolding method

The rigidity ρ measured by the magnetic spectrometer does not coincide with the value of p_0. This is due to two physical effects:

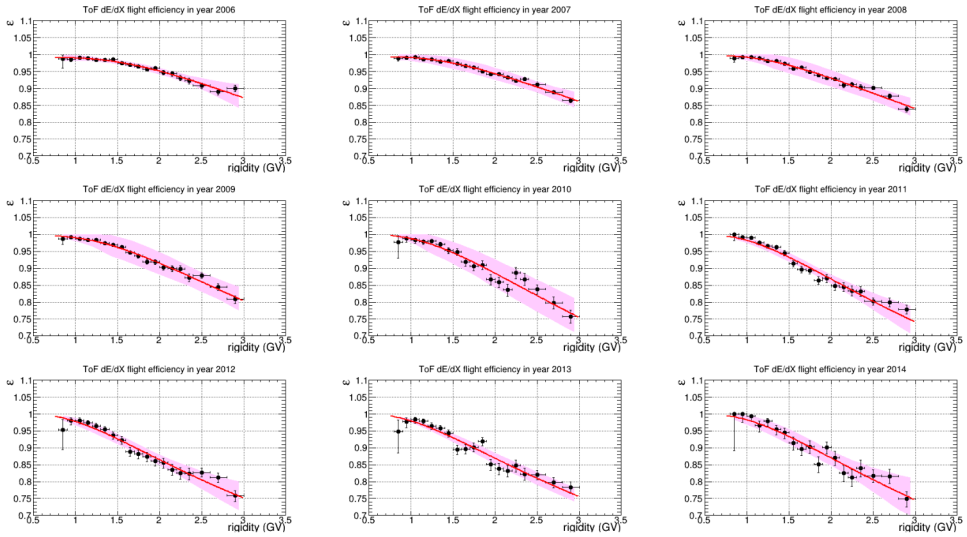

Figure 5.13: Flight efficiency values for criterion 11d (black points) calculated for each year from 2006 (top left) to 2014 (bottom right) and fitted with Equation 5.12. The fitting curves and the associated confidence intervals are shown as red lines and magenta shaded areas respectively.

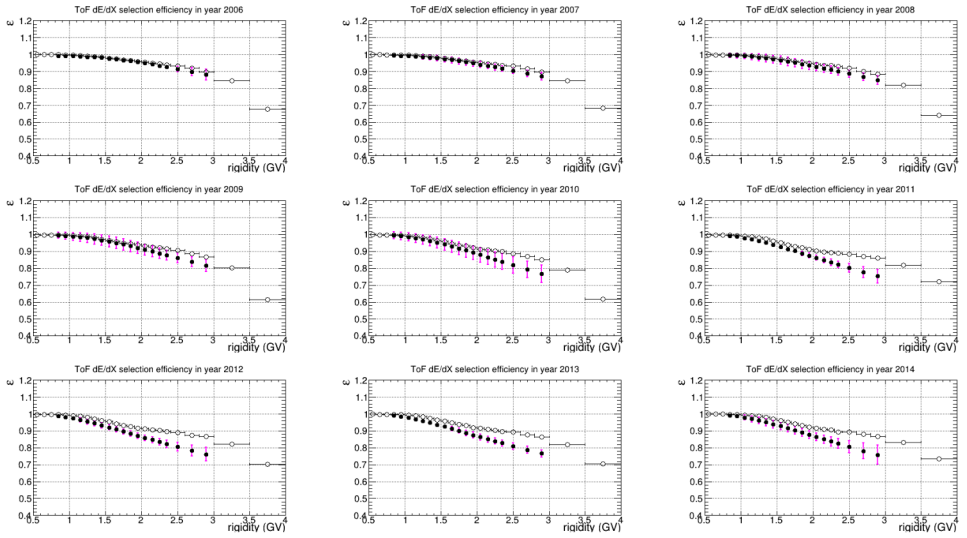

Figure 5.14: Flight fitted efficiency values with the associated confidence intervals (black points) for criterion 11d are compared with the corresponding simulated efficiency values (open points) for each year from 2006 (top left) to 2014 (bottom right).

- The energy lost by the particles crossing the aluminium dome and the first two layers of the ToF system above the tracker.
- The finite resolution of the spectrometer in the rigidity measurement.

These two effects produce a distortion of the spectrum measured as a function of p_0. To fix this problem, an iterative unfolding method based on Bayes' theorem and proposed by G. D'Agostini [116] was used.
Two histograms of selected events with the same binning are considered, one as a function of the reconstructed rigidity (histogram A) and the other as a function of p_0 (histogram B). To reproduce histogram B starting from histogram A, the Bayes theorem can be applied as follows:

$$P\left(p_{0_i}|\rho_j\right) = \frac{P\left(\rho_j|p_{0_i}\right) P_0\left(p_{0_i}\right)}{\sum_{k=1}^{n_{p_0}} P\left(\rho_j|p_{0_k}\right) P_0\left(p_{0_k}\right)} \tag{5.13}$$

where:

- $P\left(p_{0_i}|\rho_j\right)$ is the conditional probability that p_0 falls in the i-th bin of the histogram B given the measured rigidity falling in the j-th bin of the histogram A.
- $P\left(\rho_j|p_{0_i}\right)$ is the conditional probability that the measured rigidity of the event falls in the j-th bin of the histogram A given a p_0 located in the j-th bin of the histogram B.
- $P_0\left(p_{0_i}\right)$ is the a priori probability of p_0.

Given n_ρ the number of rigidity bins and $n\left(\rho_j\right)$ the number of events measured with a rigidity value falling in any j-th bin of histogram A, the best estimate of the number of particles with actual rigidity p_{0_i} falling in the i-th bin of histogram B is:

$$\hat{n}\left(p_{0_i}\right) = \frac{1}{\epsilon - i} \sum_{j=1}^{n_\rho} n\left(\rho_j\right) P\left(p_{0_i}|\rho_j\right) \quad , \tag{5.14}$$

where ϵ_i is the efficiency of detecting a p_0 value given any measured rigidity ρ_j and it is defined as follows:

$$\epsilon_i = \sum_{j=1}^{n_\rho} P\left(\rho_j|p_{0_i}\right) \tag{5.15}$$

The a priori probability $P\left(p_{0_i}\right)$ required an assumption. A constant probability was assumed considering all the bins of the histogram B equally likely,

which corresponds to a flat spectrum. Then to reach a more precise approximation an iterative procedure was employed. At each iteration the $P(p_{0_i})$ was calculated as follows:

$$P(p_{0_i}) = \frac{\hat{n}(p_{0_i})}{\sum_{j=1}^{n_\rho} \hat{n}\left(p_{0_j}\right)} \quad , \tag{5.16}$$

where $\hat{n}(p_{0_i})$ is the estimate calculated in the previous iteration. Empirically two or three iterations are sufficient to recover accurately the true spectrum. The probabilities $P(\rho_j|p_{0_i})$ form the elements S_{ij} of the so-called smearing matrix and they must be estimated as well. One method to calculate the S_{ij} elements needs the use of a reliable Monte Carlo simulation reproducing with great accuracy the instrumental response. Following this approach, the smearing matrix elements were calculated using a simulated set of events both for protons and deuterons for each year of the analysis as follows:

$$S_{ij} = P(\rho_j|p_{0_i}) = \frac{n(\rho_j)}{n(p_{0_i})} \quad , \tag{5.17}$$

where p_0 is provided by the Monte Carlo information.

Figure 5.15 shows the smearing matrix calculated using a simulated deuteron sample for the year 2006. It can be noticed that particles simulated with p_0 can be reconstructed with a measured rigidity falling in a wide range. The diagonal elements contain events for which the measured rigidity ρ and p_0 fall in the same rigidity bin. Events that populate off-diagonal bins were reconstructed with a higher measured rigidity (upper matrix sector) or lower measured rigidity (lower matrix sector) with respect to p_0. From 4 GV down to 1 GV, the highest probability corresponds to diagonal elements while below this rigidity value the lower off-diagonal elements become dominant. This means that most of the selected events below 1 GV were reconstructed with a lower rigidity since a no-negligible fraction of their energy was lost by ionisation in the dome and in the S1 and S2 planes. Since the smearing matrix does not account for the migration of events beyond the edges of the considered rigidity range, the counts at the extreme rigidity bins provided by the unfolding procedure can not be reliable.

The systematics associated with the unfolding procedure was estimated with simulated data. In particular, starting from a deuteron spectrum as a function of p_0 (provided by the Monte Carlo information), for the same events the spectrum as a function of the measured rigidity was obtained in simulation, which is referred to as folded spectrum from now on. Using the unfolding procedure on this folded spectrum, an unfolded spectrum as a function of the actual rigidity was reconstructed statistically.

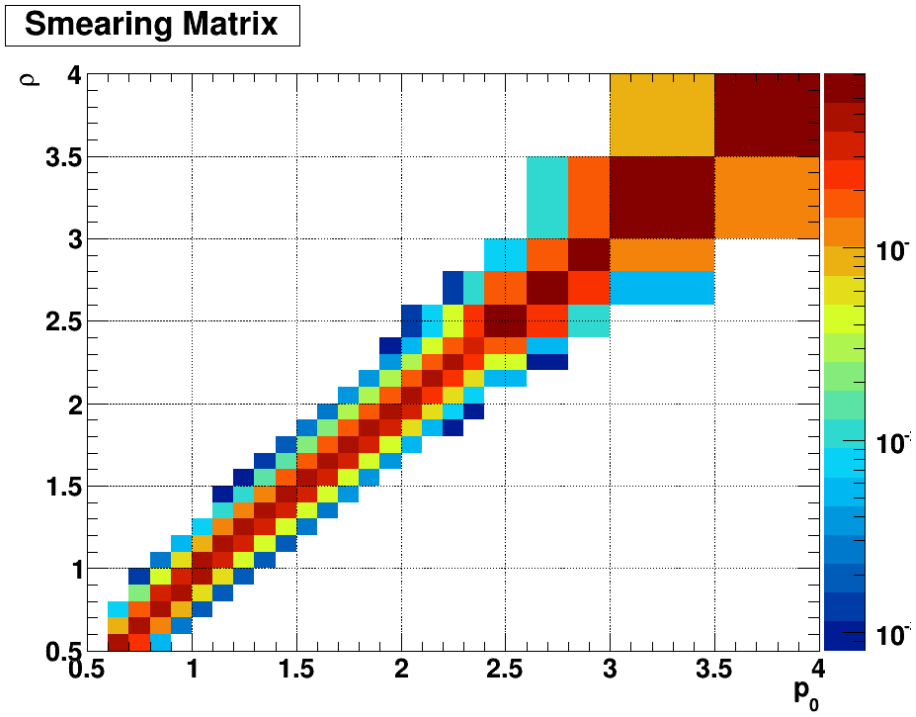

Figure 5.15: Smearing matrix for the simulated deuteron sample in 2006.

In Figure 5.16 upper panel, the reconstructed folded (magenta lines) and unfolded (green lines) spectra are compared with the initial simulated spectrum (black lines). For a more quantitative insight, the ratio of the folded-over-simulated counts (magenta points) and of the unfolded-over-simulated counts (green points) were calculated for each rigidity bin and shown in the lower panel of Figure 5.16. Looking at the folded spectrum, this deviates significantly from the simulated spectrum at the lowest rigidities up to about 1.6 GV as an effect of the ionisation energy losses. Moreover, the folded spectrum has counts close to 0.5 GV, where no counts are present there in the simulated spectrum.
The unfolding spectrum is in better agreement with the simulated spectrum, the count difference between them is less than 5% along all the studied rigidity range, except for the last bin [3.5,4.0] GV, where it is around 13%. A part of this last bin, the more evident deviations from the simulated counts are observed below 0.9 GV because the unfolding procedure can not reconstruct the event migration at the edges of the measured spectrum. However, the disagreement in these bins remains small and all the events in the first bin [0.5,0.6] GV of the folded spectrum were shifted at higher rigidities leaving it empty as in the simulated spectrum.

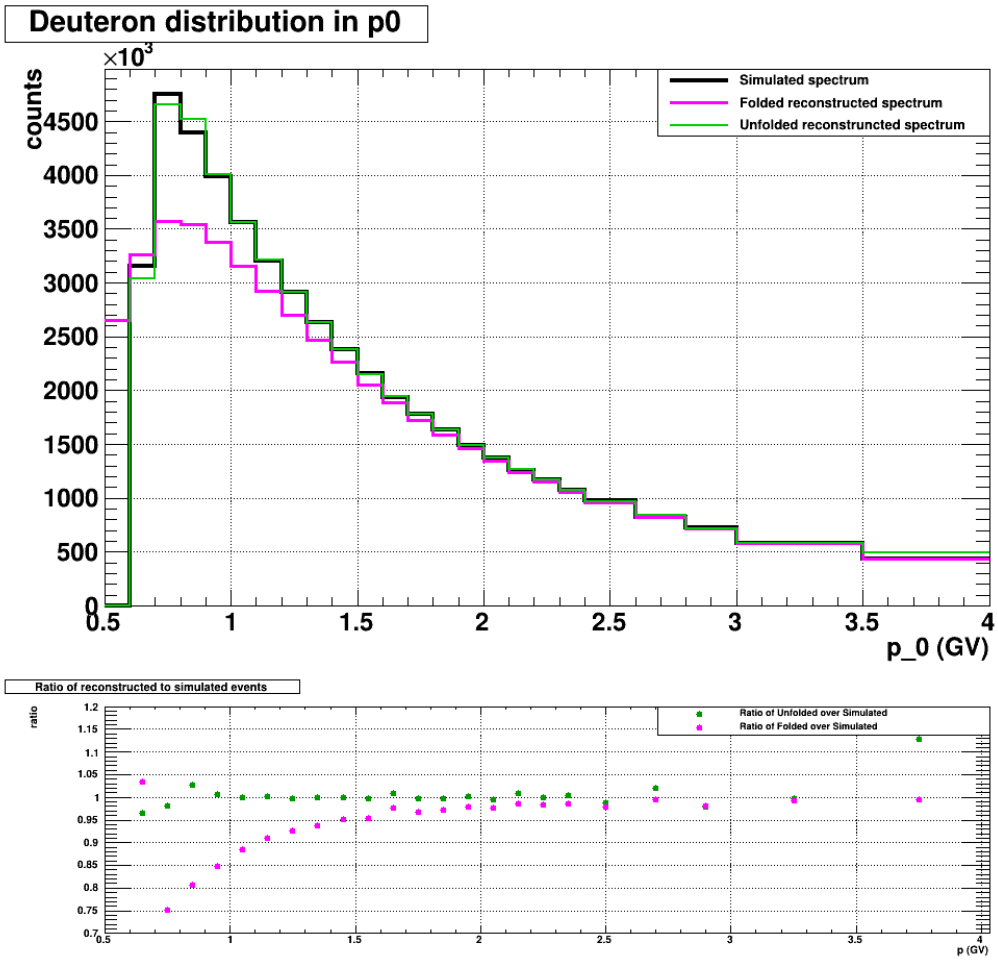

Figure 5.16: Upper panel: comparison between simulated spectrum in black, folded reconstructed spectrum in magenta and unfolded reconstructed spectrum in green as a function of the rigidity. Lower panel: ratios of folded- over simulated counts in magenta and of unfolded- over simulated counts in green as a function of the rigidity. The related standard deviations were calculated according to the variance propagation law.

The same work was done also for protons with results in agreement with those obtained for deuterons. For both protons and deuterons, the obtained ratios of unfolded- over simulated counts were used later in the analysis to account for the systematic uncertainty introduced in the flux calculation by the unfolding procedure.
After its validation in simulation, the unfolding procedure was applied to the event counts already divided for the efficiency values of the selection crite-

ria 7, 9, 10p for protons and 7, 9, 10d, 11d for deuterons since these were calculated as a function of the measured rigidities. This enabled to reconstruct statistically for each geomagnetic cut-off slice the proton and deuteron counts as a function of p_0, before proceeding to discard the re-entrant albedo particles.

5.5 Galactic particle selection

At this point of the analysis, the re-entrant albedo particles were still present in the selected proton and deuteron samples. These events can be rejected with a selection of this type:

$$\rho_l > k \cdot R_{svl} \tag{5.18}$$

This criterion requires that the lowest edge of a rigidity bin (ρ_l) must be a factor k higher than the Störmer vertical cut-off to contribute with its events to the final flux. The factor $k = 1.3$ is a constant that makes the selection efficient in rejecting all the trapped particles. This k value was obtained in [114] by comparing the proton fluxes measured by PAMELA at the magnetic poles, where the rigidity cut-off was of the order of tens of MV and the fluxes measured by PAMELA could be safely assumed as unaffected by Earth magnetosphere, with the fluxes measured by PAMELA at the other geomagnetic locations using this k value. The resulting fluxes were found to be compatible.
As already discussed in Section 4.7, the selected events for both protons and deuterons were divided into different geomagnetic cut-off intervals (see Table 4.2). This was done to apply the unfolding procedure before this galactic selection. In fact, an event may have an actual rigidity R (i.e. p_0) higher than its associated geomagnetic cut-off (i.e. a galactic particle) but it could be reconstructed with a measured rigidity ρ significantly lower than the geomagnetic cut-off (i.e. like a trapped particle). If the galactic selection was applied to the folded distribution, a fraction of galactic events would be rejected. Thus, to consider the event migration, the galactic selection was performed on the unfolded spectra.
The galactic selection was applied to each cut-off slice selecting the rigidity bins of the count distributions with the lower edge greater than 1.3 times the upper edge of the cut-off interval (see Figure 4.9 and Figure 4.25). After this selection, the galactic distribution for each cut-off interval was summed up weighted by the instrumental live time and divided by the geometrical acceptance as explained in the next sections.

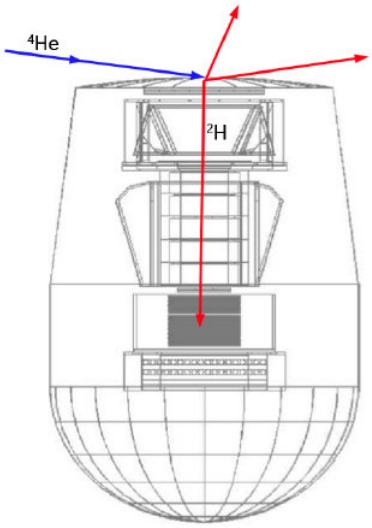

Figure 5.17: Pictorial representation of the fragmentation of a ^{4}He nucleus producing a secondary deuteron inside the instrumental acceptance and passing all the selections.

5.6 Contamination from fragmentation products

As discussed in Chapter 4, criterion 9 enabled to discard events with $Z = 1$ produced by interactions of heavier nuclei with the ToF layer above the magnetic spectrometer. However, these interactions could still occur in the 2 mm aluminium dome covering the PAMELA apparatus, producing secondary particles, which can cross the PAMELA apparatus and be triggered. Among these secondary particles, there are also protons and deuterons. This phenomenon is depicted in a pictorial representation in Figure 5.17 Because of their smaller abundance in cosmic rays with respect to that of protons and helium nuclei, deuterons are more affected by this type of contamination. In Figure 1.4 in Chapter 1 it was shown that according to the abundance of the main nuclides in cosmic rays and their inelastic cross section values evaluated in [29], the interaction of the galactic ^{4}He nuclei with the ISM generates the largest amount of deuterons in the kinetic energy range considered in this analysis, $[0.1; 1]$ GeV/n. This conclusion can also be extended for the case of inelastic interactions with the aluminium dome.
This contamination can not be evaluated directly with flight data, but it has to be derived by simulating helium nuclei hitting isotropically the PAMELA apparatus. For this purpose, a simulated sample of ^{4}He was generated using

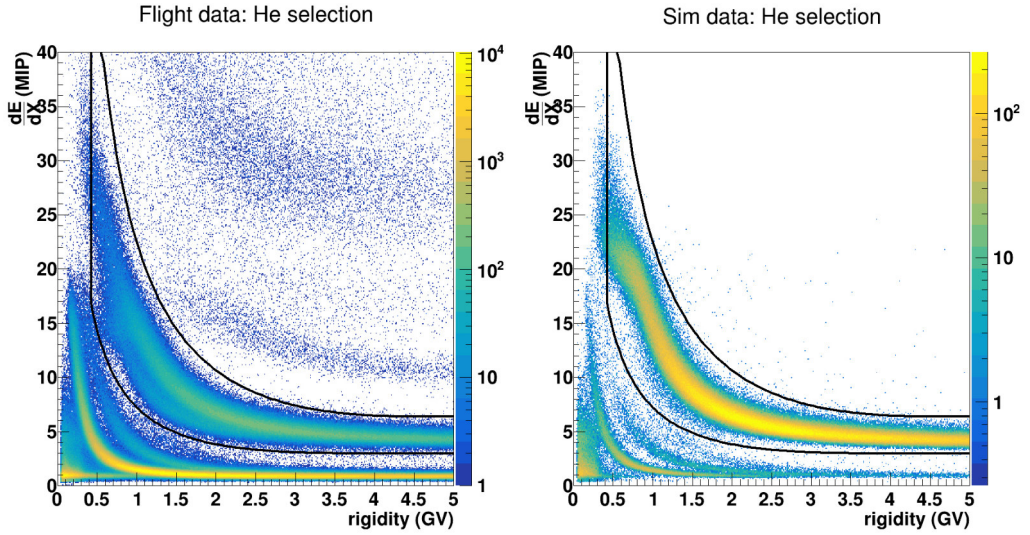

Figure 5.18: Left panel: truncated mean dE/dX distribution measured in the tracker as a function of the rigidity for flight events selected with criteria 1-8 and belonging to the first geomagnetic cut-off slice. Right panel: truncated mean dE/dX distribution measured in the tracker as a function of the rigidity for simulated ^4He nuclei selected with criteria 1-8. In both the two panels the cuts selecting He nuclei are depicted as black curves.

the FTFP_BERT Geant4 physics list. To calculate the number of the locally produced deuterons, the selected sample of the simulated ^4He were normalized to the counts measured in flight data. A set of criteria was defined to select ^4He and then applied on both flight and simulated events. The flight events were required to belong to the first geomagnetic cut-off slice to obtain a sample free of re-entrant albedo particles. Finally, new cuts were defined according to Equation 4.6 to select He nuclei in the truncated mean dE/dX distribution measured in the tracker as a function of the rigidity. Figure 5.18 left panel shows these cuts depicted as black curves on the truncated mean dE/dX distribution measured in the tracker for flight events selected with criteria 1-8 in 2006. Figure 5.18 right panel depicts the same cuts on truncated mean dE/dX distribution measured in the tracker for simulated ^4He data. Here, the cuts acted selecting the galactic ^4He nuclei generated in simulation, rejecting those events which fragmented producing secondary particles with Z=1, visible in Figure 5.18 right panel below the lower cut.
While almost no ^3He events are present in the selected simulated events, ^3He are still present in a significant number, at the level of 10%, among the selected flight events. To exclude this component and obtain ^4He counts

from flight data, a double Gaussian fit was used on the $1/\beta$ distributions of each rigidity bin. In this case, the mean and sigma parameters were left free but initialised with reasonable values, in particular the Gaussian means were initialised to the $1/\beta$ values predicted by Equation 4.4.
At this point, the ^4He counts as a function of the rigidity from both flight and simulated data were converted as a function of the kinetic energy over nucleon E_{kin}/A . This was done because an energy-dependent scaling factor obtained from the ratios of flight over simulated ^4He counts can also be applied on the number of secondary particles produced from ^4He fragmentation in simulation because of the E_{kin}/A conservation in this process. The conversion from rigidity ρ to kinetic energy over nucleon E_{kin}/A is expressed as follows:

$$E_{kin}/A = \frac{\sqrt{Z^2\rho^2 - m^2c^4} - mc^2}{A} \tag{5.19}$$

where Z and A are the atomic and mass numbers respectively, m the mass of the considered nuclide. This $\rho - E_{kin}/A$ relation enabled to convert the edge values of ach rigidity bin into the corresponding E_{kin}/A values and obtain the ^4He counts as a function of E_{kin}/A for both simulated and flight data. Later, the numbers of simulated and flight ^4He events were divided by the energy bin width and then compared, as shown in the top panel Figure 5.19. In the bottom panel of the same figure, the related ratios of flight-over-simulated events are depicted for the same energetic range. These ratios, at the level of 32%, had a not significantly energy dependence and therefore were fitted with a constant value (red horizontal line in Figure 5.19 bottom panel) to obtain a scaling factor to normalize the number of simulated ^4He events to those measured in flight data. Because of the approximated lack of energy dependence, this scaling factor could be applied later to the counts of the secondary particles produced in simulation directly as a function of the rigidity.
At this point, the secondary particles produced by ^4He fragmentation in the simulation were analysed starting from the tritons. This was done because as already discussed, galactic tritons can not survive the propagation in the Galaxy because of their short half-life time. For this reason, every triton detected in the flight data had to be generated from the local fragmentation of heavier nuclei, mainly of ^4He. This gives the chance to check the reliability of the modelling of the processes of ^4He fragmentation and secondary particle production in simulation by comparing the triton counts found in ^4He simulations and in flight data. A set of selections was defined to select tritons: criteria 1-8 were required and the dE/dX band shown in Figure 5.20 for flight events at left and simulated events at right was selected. The selected sample included deuterons, tritons and in minimal part protons. For

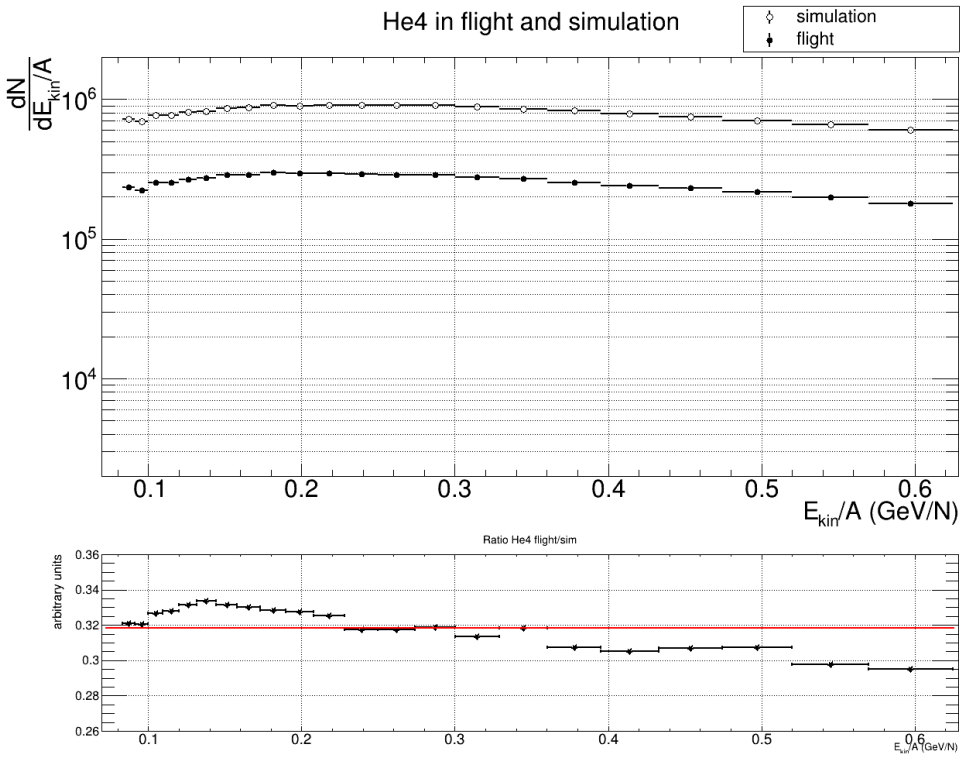

Figure 5.19: Top panel: Simulated and flight ^4He counts compared as a function of the E_{kin}/A. Bottom panel: related ratios of flight- over simulated ^4He counts.

this reason, a triple Gaussian fit was applied on the $1/\beta$ distributions of each rigidity bin to measure the triton counts for both simulated and flight samples. The simulated triton counts were then divided by the scaling factor obtained for the ^4He simulations. Finally, both simulated and flight triton counts were divided by the rigidity bin width. The results were compared in Figure 5.21 top panel. The simulated triton numbers appear significantly lower than those observed in flight data. The ratios of the simulated over flight triton numbers were calculated and shown in Figure 5.21 bottom panel. Fitting the ratios with a constant, this gives a value of 0.25, showing that the triton measured in flight data is underestimated by a factor of four in simulation. This could be due to not accurate modelling of the physical processes involved in the ^4He fragmentation in the Monte Carlo simulation. Other simulations with different physics lists were also generated and analysed but results in agreement with those from FTFP_BERT were obtained. Simulated ^3He nuclei and protons were also generated and analysed looking for a possibly significant contribution from their fragmentation to the triton

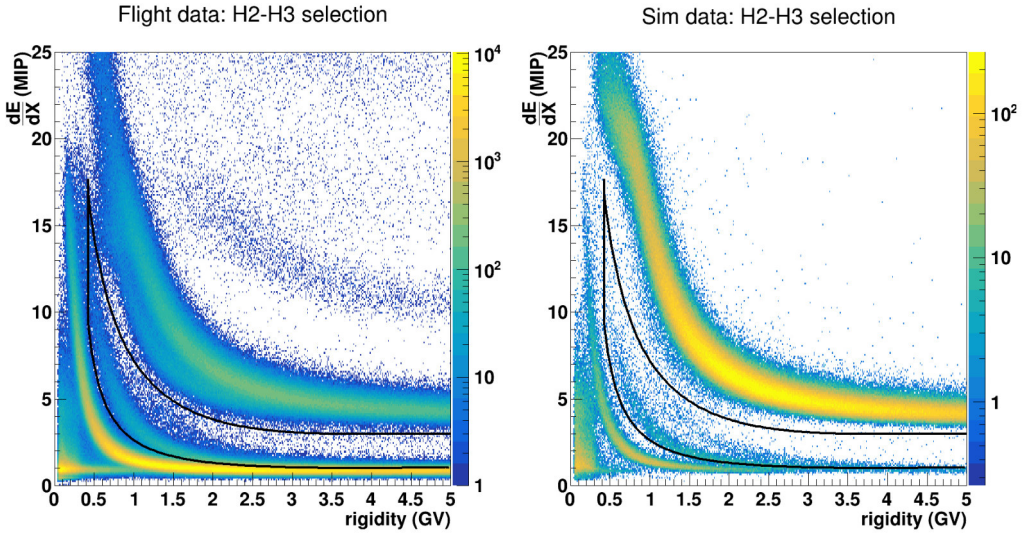

Figure 5.20: Left panel: truncated mean dE/dX distribution measured in the tracker as a function of the rigidity for flight events selected with criteria 1-8 and belonging to the first geomagnetic cut-off slice. Right panel: truncated mean dE/dX distribution measured in the tracker as a function of the rigidity for simulated ^4He nuclei selected with criteria 1-8. In both the two panel the cuts selecting ^2H and ^3H nuclei are depicted as black curves.

component, but a negligible amount of tritons was found. For this reason, the disagreement found between flight and simulated tritons was considered an upper systematic uncertainty affecting the secondary particle production from ^4He fragmentation in the simulation.
Finally, the deuteron produced by the fragmentation of ^4He was studied. The $1/\beta$ distributions of the ^4He simulated events surviving criteria 1-9, 10d, 11d were fitted with a double Gaussian in order to estimate the number of secondary deuterons. The use of criterion 9 entails that the secondary deuterons observed in simulation were produced by fragmentation of He4 only in the aluminium dome covering the PAMELA apparatus. The counts of the selected simulated deuterons were divided by the scaling factor obtained for ^4He simulated spectrum and by the rigidity bin width and then compared with the counts of the deuterons selected in flight data in the first geomagnetic cut-off slice. This comparison is shown in Figure 5.22, whereas the related ratios of simulated over flight deuteron counts are shown in Figure 5.23. These ratio values are below 1% along the whole rigidity range. These values were then fitted with a second-order polynomial as shown Figure 5.23, where the pale blue shaded area depicts the confidence intervals es-

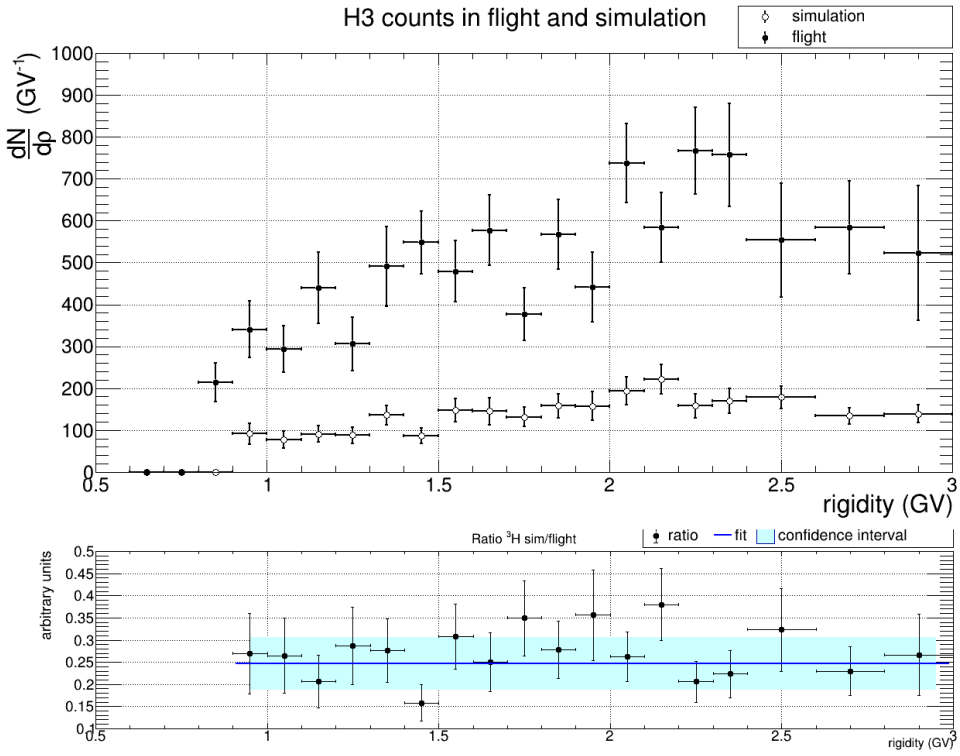

Figure 5.21: Top panel: Simulated and flight ^3H counts compared as a function of the rigidity. Bottom panel: related ratios of flight- over simulated ^3H counts.

timated by the fit. Because of the disagreement found between triton events in flight and simulated data, the upper uncertainty band was obtained multiplying the fitted curve by a factor of four. This is depicted in Figure 5.22 as a blue band. This systematics could be overestimated since the deuteron coalescence is an easier process to model than the triton coalescence.
The obtained values of fraction of deuterons generated from ^4He fragmentation were used in the flux calculation, to subtract this contamination from the deuteron counts of each year.

5.7 Geometrical factor

The geometrical acceptance was estimated with the simulation by defining a set of planes, called acceptance planes, that model the geometrical properties of the apparatus. A particle is inside the geometrical acceptance if it satisfies the trigger condition and crosses all the acceptance planes. The acceptance

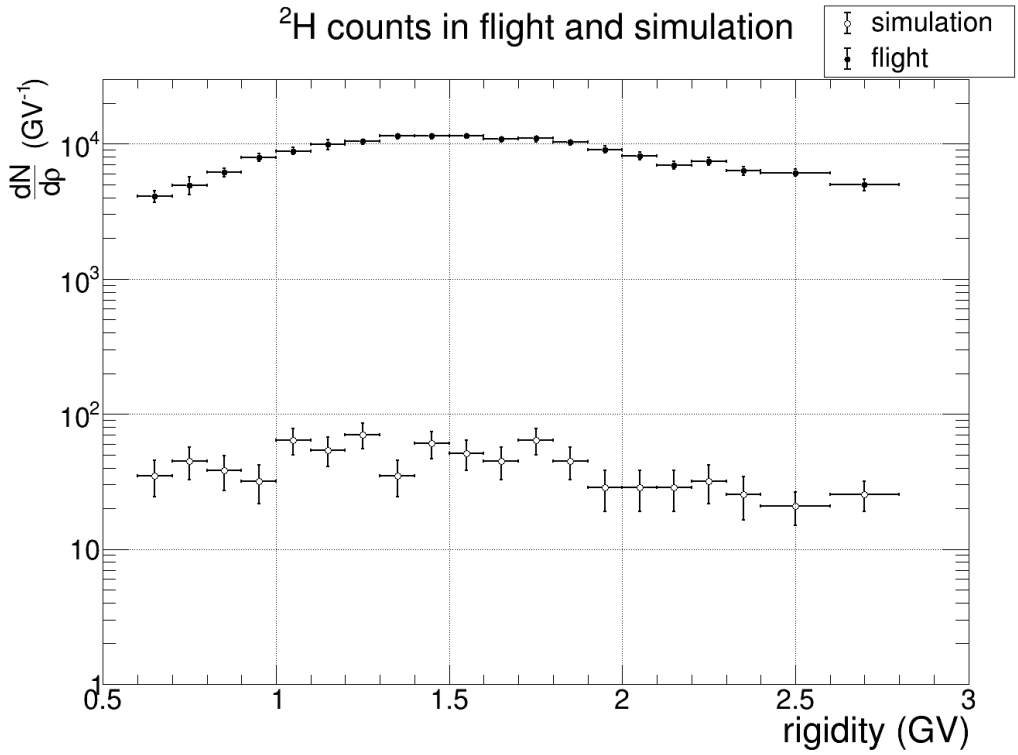

Figure 5.22: Simulated and flight ^2H counts compared as a function of the rigidity.

planes are:

- all ToF planes, which are needed for a trigger,
- all tracker planes.

The fiducial cut (criterium 5), selecting tracks at least 1.5 mm away from the magnet walls, was also required. The definition of the geometrical factor developed in [118] can be applied to define the PAMELA geometrical factor:

$$G_N = \int_\Omega d\omega \int_\Sigma d\vec{\sigma} \cdot \hat{r} \quad , \tag{5.20}$$

where $d\vec{\omega}$ is the solid angle element, $\hat{r}$ is the versor relative to the direction defined by the zenithal θ and azimuthal ϕ angles, $d\vec{\sigma} \cdot \hat{r}$ is the effective area element under the solid angle $d\omega$. The integration boundaries are the detector surface and the whole solid angle. However, the curvature of the particle track

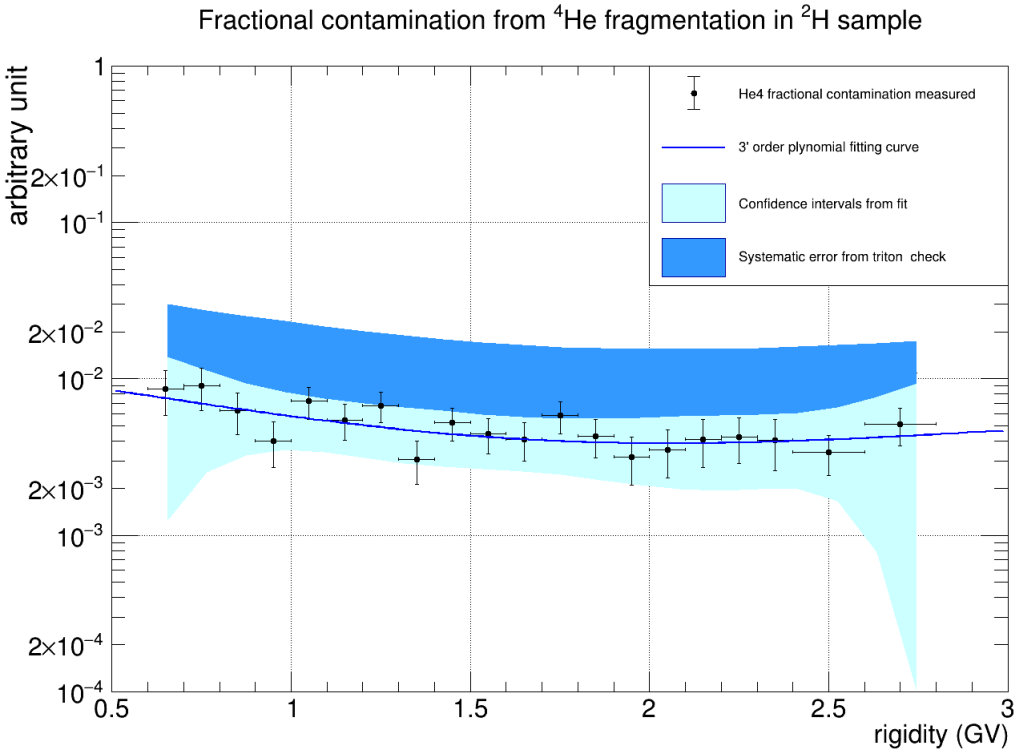

Figure 5.23: Ratios of flight- over simulated ^2H counts as a function of the rigidity.

had to be taken into account. Thus, an additional term was introduced to consider the presence of the magnetic field in the spectrometer:

$$G_N(\rho) = \int_\Omega d\omega \int_\Sigma f(x, y, \theta, \phi, \rho)\, d\vec{\sigma} \cdot \hat{r} \tag{5.21}$$

where $G_N(\rho)$ is the nominal geometrical factor, $f(x, y, \theta, \phi, \rho)$ is a function of the spatial (x, y) and angular coordinates (θ, ϕ) and of the measured rigidity ρ and it assumes the values 1 and 0 if the particle was or was not in the defined acceptance considering its curved trajectory inside the magnetic field. It was not possible to solve Equation 5.21 analytically because of the complex geometry, therefore $G_N(\rho)$ was calculated with a Monte Carlo simulation. Figure 5.24 shows the $G_N(\rho)$ values which are approximately constant with the rigidity at a value of 19.9 cm^2 sr. The decrease below 400 MV was caused by the increasing deflection of particles.

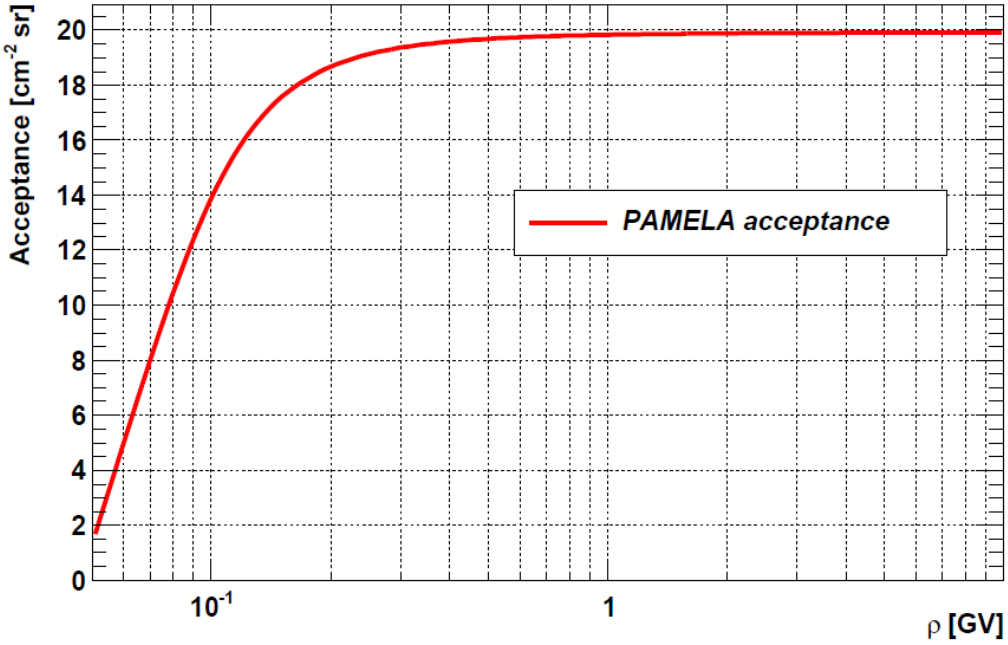

Figure 5.24: Geometrical acceptance of the PAMELA experiment as derived by simulation.

5.8 Live time

The live time was provided by an on-board clock, that measured the time during which the apparatus was waiting for a trigger. To account for the different geomagnetic regions crossed by PAMELA, the live time was separately measured for each geomagnetic cut-off slice listed in Table 4.2. Figure 5.25 shows the histogram of the live time evaluated in 2006 as a function of the geomagnetic cut-off for deuterons. The binning of the histogram corresponds to the geomagnetic cut-off slices used for the deuteron analysis, whereas the bin contents correspond to the time spent by the satellite within that geomagnetic latitude interval. For protons, this was done accordingly to the geomagnetic cut-off slices defined for that analysis.

Then, a cumulative distribution was built for each rigidity bin summing the live times t_i measured in the geomagnetic cut-off intervals with an upper edge lower than the lower edge of the considered bin:

$$T(\rho_i) = \sum_{k=0}^{i-1} t_k \tag{5.22}$$

In this way, the $T(\rho_i)$ represented the live time spent by the apparatus in

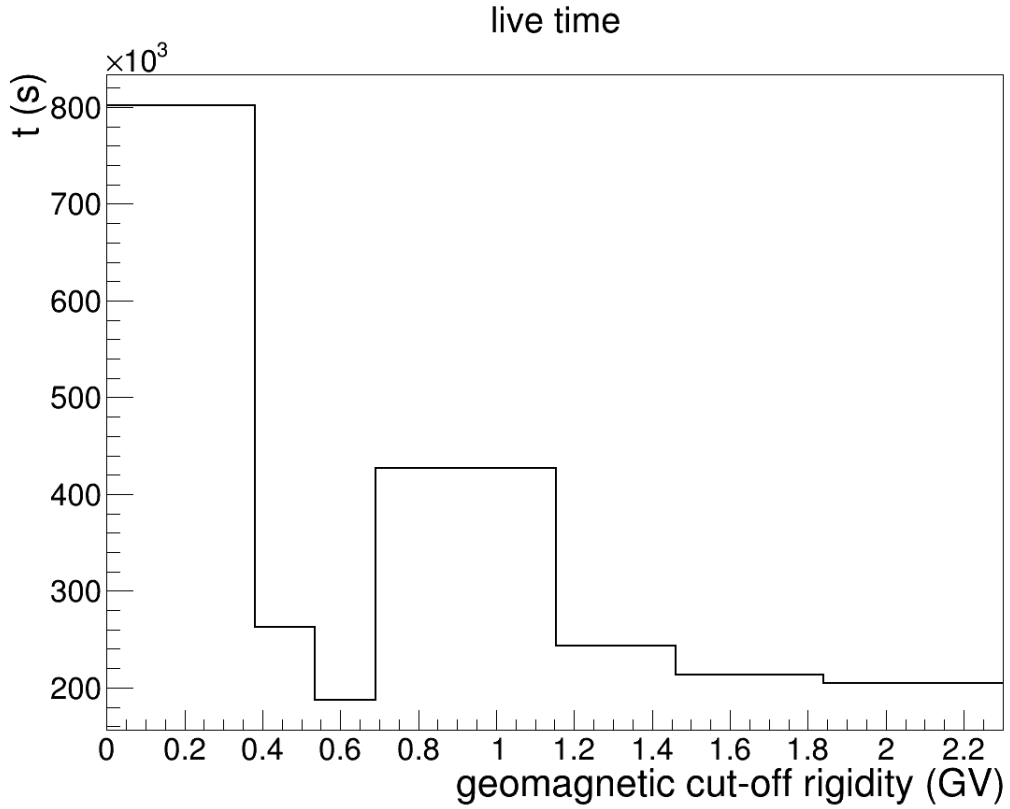

Figure 5.25: Histogram of the live time as a function of the geomagnetic cut-off rigidity.

the orbital positions where $k \cdot R_{svl}$ was lower than the rigidity ρ_i. Figure 5.26 shows the histogram of the cumulative live time obtained from the 2006 data as a function of the rigidity. As it can be seen, the distribution for the live time is increasing as a function of the rigidity.

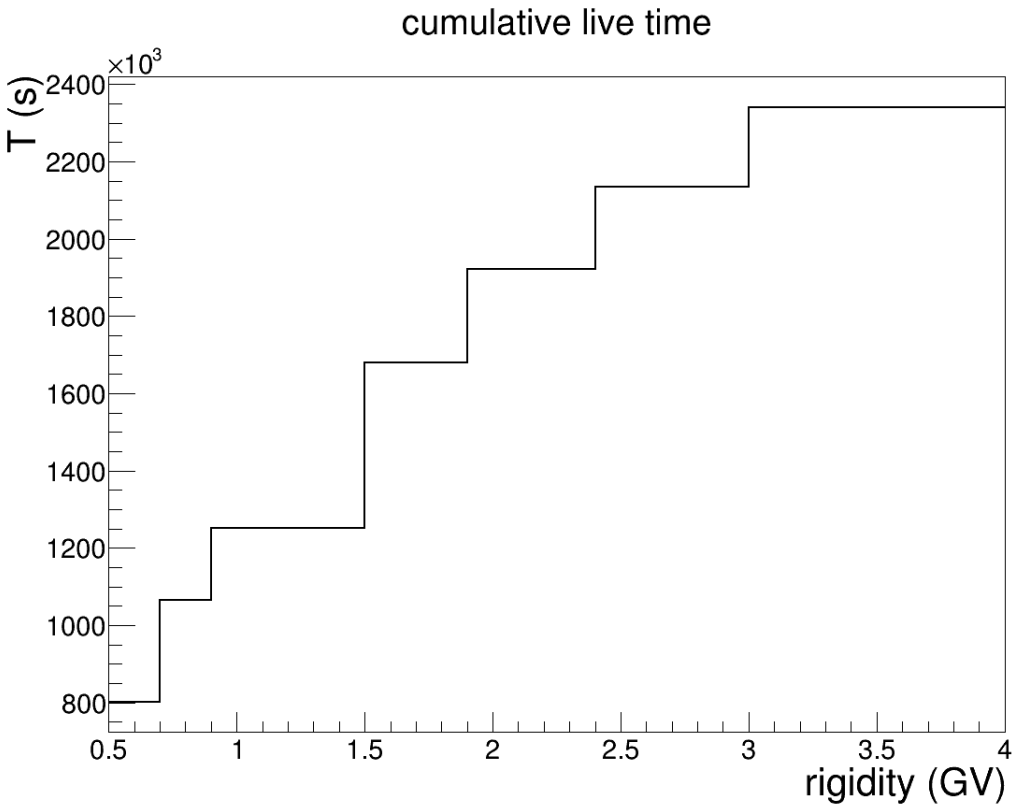

Figure 5.26: Histogram of the cumulative live time as a function of the rigidity.

Chapter 6

Proton and Deuteron fluxes

In this chapter the galactic proton and deuteron fluxes obtained in this analysis work for the period 2006-2014 are discussed. The time dependence observed in the fluxes of both the two isotopes as well as in the deuteron-to-proton flux ratios is analysed in detail. Subsequently, the deuteron solar modulation is studied also comparing the experimental spectra with numerical models. Finally, a study of the time evolution of the deuteron fluxes was performed using the Force-Field approximation and analysing the deviations of the measured fluxes from the expected values computed through the Force Field approach from an ad-hoc computed LIS.

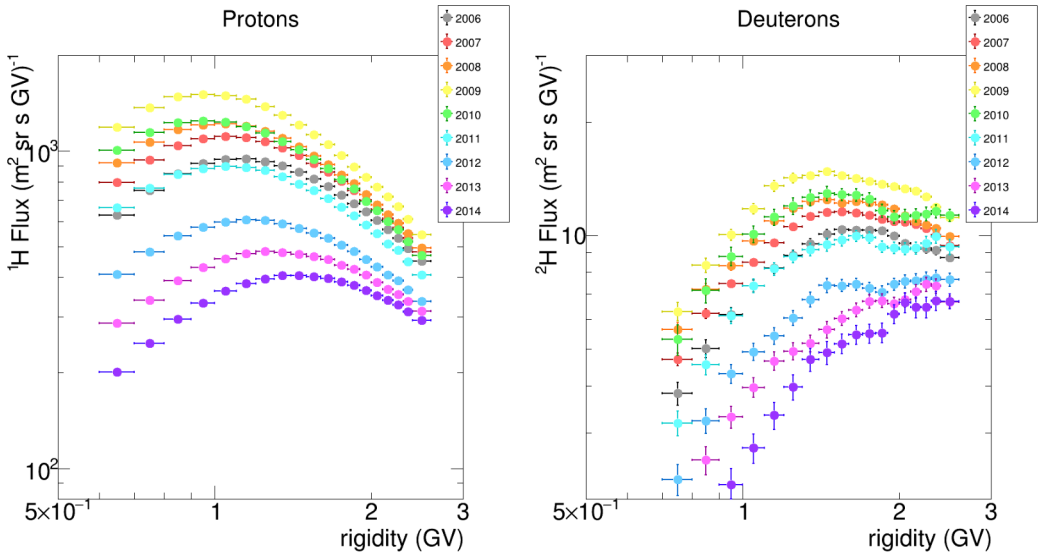

Figure 6.1: Proton (left) and deuteron (right) yearly fluxes as a function of the rigidity measured for the period between July 2006 and September 2014 included.

6.1 Yearly Fluxes proton and deuteron fluxes

Yearly fluxes of galactic protons and deuterons were obtained for the period between July 2006 and September 2014 included, with the analysis procedure described in the previous chapters. The resulting fluxes are shown in Figure 6.1 as a function of the rigidity, for protons (left panel) and for deuterons (right panel). Different colours were adopted to depict the fluxes of different years as pointed in the legends. The vertical error bars represent the statistical uncertainties affecting the flux measurements. Looking at the yearly fluxes of the two nuclides, an evident time dependence induced by solar modulation effects can be seen. Starting from 2006, the fluxes gradually increase over time during the minimum of the 23^{rd} solar cycle reaching their maximum values in 2009. In the following years, they progressively decrease approaching the next solar maximum, reaching their minimum values in 2014. In the proton spectra, the flux is observed to increase at 0.75 GV by a factor of 1.8 from 2006 to 2009 and then decrease from 2009 to 2014 by a factor of 6, at 2.05 GV the increase and decrease factors are 1.2 and 2.2 respectively. For the deuteron spectra, the flux is observed to increase at 0.75 GV by a factor of 1.7 from 2006 to 2009 and then decrease from 2009 to 2014 by a factor of 5.3, at 2.05 GV the increase and decrease factors are 1.4 and 2 respectively. Moreover, not only the intensity but also the spectral shape is observed

to change over time as an effect of the solar modulation: the proton and deuteron spectra become progressively softer from 2006 to 2009 as more low-energy particles could reach the Earth during the solar minimum phase. Consequently, the spectral peak (i.e. the turning point in the value of the maximum flux of each spectrum) moves from higher to lower rigidities: in 2006 the proton and deuteron spectral peaks are located at 1.15 GV and 1.65 GV respectively and gradually move at lower rigidities approaching the year 2009, for which they are positioned at 0.95 GV and 1.45 GV respectively. In the following years, this trend is reversed because fewer low-energy protons and deuterons could reach the Earth as an effect of the increasing solar activity and consequently the observed spectra become progressively harder: from 2010 to 2014 the proton spectral peak moves from 0.95 GV to 1.45 GV. This effect is also present in the deuteron spectra, however a precise determination of the spectral peak is complicated by significant systematic effects present in the deuteron fluxes at higher rigidities (> 1.8 GV) after 2009. In fact, at the highest rigidities, a strange hardening is observed in the deuteron spectra from 2010, particularly evident in 2014, and not accounted for by the estimated systematic uncertainties. Similar smaller distorting effects are also observed in the deuteron spectra for the solar minimum. These distortions are consistent with the estimated statistical and systematic uncertainties but nonetheless they could be related to the same source of systematics affecting the solar maximum. The source of this time-dependent systematic effect has not been identified yet and is currently under study.
Finally, from the time variations observed in Figure 6.1 at the lowest rigidities on galactic proton and deuteron fluxes, some considerations can also be done on the solar modulations effects expected on the low-energy galactic antiproton and antideuteron fluxes within the GAPS sensitivity. In first approximation, neglecting the charge-sign effect induced by the drift motions in the Heliosphere, the solar modulation effects observed at rigidities below 0.73 GV for protons and 1.46 GV for deuterons are the same for antiprotons and antideuterons respectively, for energies below 0.25 GeV/n.

6.2 Systematic uncertainties

The contributions to the systematic uncertainties in the proton and deuteron measurements are the following:

- Uncertainty on the selection efficiency: this is introduced by the statistical error due to the final size of the efficiency sample. This error was considered and propagated as a systematic uncertainty. However, in the rigidity ranges where flight and simulated efficiencies were found not in

agreement within the statistical errors, the difference of the flight and simulated values was treated as a systematic error with a uniform probability density. Since the difference is only in one direction, this introduced only a lower or a higher systematic uncertainty. For deuterons, the efficiency of AC selection (criterion 8) and the charge-one selection (criterion 9) on S11 and S12 were affected by a lower systematic uncertainty of 1.15%, 0.65% and 0.87% respectively below 1 GV. For protons, the efficiencies of criteria 8 and 9 (on both S11 and S12) are affected by a lower systematic uncertainty of 0.58% and 0.5% respectively below 0.5 GV. Since the discrepancies found in flight and simulated efficiencies of ToF dE/dX selection of deuterons (criterion 11d) and tracker dE/dX selection of protons (criterion 10p) change with time, time-dependent systematic uncertainty was introduced. The uncertainty for criterion 11d was 0.87% in 2006 at 2.05 GV and increases up to 3.2% in 2014, for criterion 10p it was of 0.17% at 2.35 GV and increased up to 0.83% for 2014.

- Subtraction of contamination of fragmentation products: the disagreement found between flight and simulated triton counts was considered an upper systematic uncertainty affecting the secondary particle production from ^4He fragmentation in the simulation. For this reason, the estimation of the fraction of deuterons generated by fragmentation of ^4He nuclei in the aluminium dome was affected by this uniformed-distributed systematic uncertainty. This uncertainty is about 0.9% at 0.6 GV and decreases down to 0.5% for rigidities greater than 1.5 GV.

- Intrinsic accuracy of the unfolding procedure: this was estimated in simulation by reconstructing a known spectral shape as a function of p_0 with the unfolding procedure from the corresponding measured spectrum as a function of the measured rigidity in simulation as explained in Section 5.4. The uncertainty resulting from the ratio of unfolded-to-simulated fluxes are more significant at rigidities below 1 GV, where it provides a maximum uncertainty of about 1.3% at 0.65 GV.

- The underestimation of the total number of events in the $1/\beta$ distributions by the double-Gaussian fit procedure: this discrepancy is constant, at a level of about 2% (see Figure 4.23), and was introduced as a systematic error for the only rigidity bins where proton contamination was identified by the fit procedure.

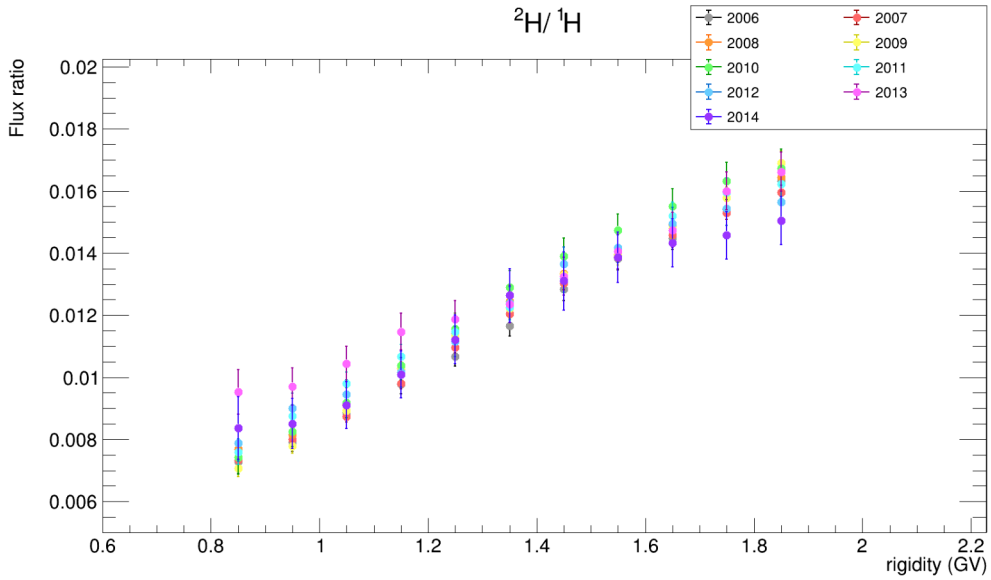

Figure 6.2: Deuteron-to-proton flux ratios calculated as a function of the rigidity for each year between 2006 and 2014.

6.3 The deuteron-to-proton flux ratio

The deuteron-over-the proton flux ratios were also evaluated in the rigidity range [0.8,1.9] GV, where 1.9 GV was chosen to exclude the systematic effects just discussed. These ratio values are shown in Figure 6.2 as a function of the rigidity for each year considered in the analysis. In this rigidity range, the ratios increase by about a factor 2 as the rigidity increases. This trend can be ascribed to the difference in the LIS shapes of protons and deuterons. No obvious time dependence is visible in Figure 6.2, except for the year 2013 for which the ratios, at rigidities lower than 1.2 GV, are higher by a factor of 1.3 with respect to those measured in 2009. All the others agree within a sigma along all the analysed range.

6.4 Comparison of the deuteron fluxes with numerically modulated spectra

The deuteron spectra measured for 2006 and 2009, converted as a function of the kinetic energy over nucleon, are shown in Figure 6.3 as blue and red points respectively. These fluxes were compared with the computed spectra obtained from the numerical 3D model developed in [38] [39] [40] (blue and

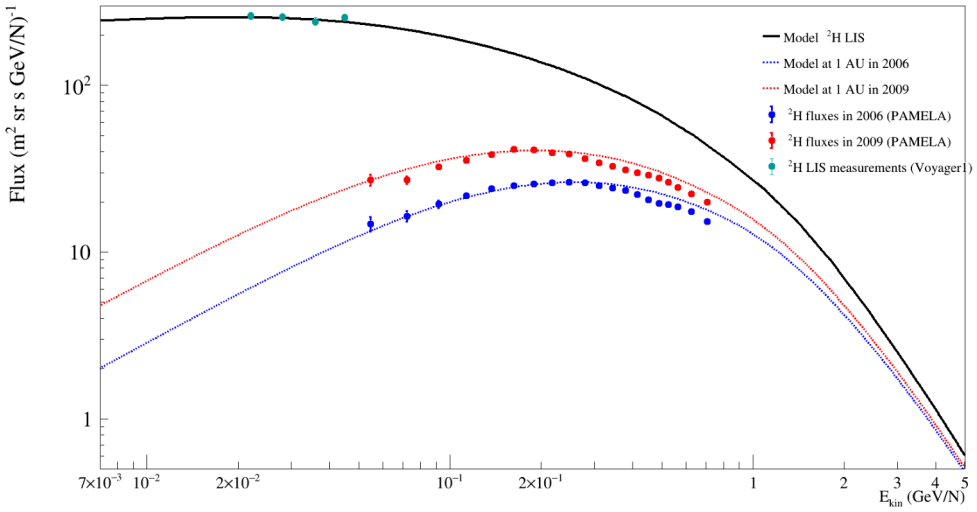

Figure 6.3: Deuteron spectra measured for years 2006 (blue points) and 2009 (red points) as a function of the kinetic energy over nucleon and scaled by a factor of 0.8 to overlay the numerically modulated spectra (blue and red dotted lines). The latter were computed by the 3D numerical model of solar modulation developed in [38], [39] and [40] from a LIS obtained with GALPROP and modified at the lowest energies to agree with the deuteron fluxes measured by Voyager 1 outside the Heliosphere [120] (teal points).

red dotted lines) from an input deuteron LIS (black solid curve) obtained with GALPROP [1] and modified at the lowest energies to agree with the deuteron fluxes measured by Voyager 1 outside the Heliosphere [120] (teal points). The diffusion coefficients and their rigidity and time dependences used to modulate the deuteron LIS were those obtained for the galactic protons in [121]. This is choice is motivated by the fact that the two hydrogen nuclides should be similarly affected by the propagation mechanisms in the Heliosphere. In order to allow a proper overlap in Figure 6.3 between numerically computed spectra and measured fluxes, the latter were multiplied by a factor of 0.8. The shape of the two modulated curves follows in relatively good agreement the trends of the two measured spectra until 0.3 MeV/n, whereas from this value the curves decrease less quickly than the measured spectra. The discrepancies observed in the intensities and the shapes between the modelled curves and the measured spectra seem to be more probably due to the use of a not fully reliable LIS more than a solar-modulation modelling issue. This claim is also supported by the further analysis discussed in the

next section.

6.5 Test on time evolution of the deuteron fluxes

The time evolution of the deuteron spectra was also studied with a comparison with the predictions of the force-field approximation, a simpler model of cosmic-ray solar modulation. This was done to analyse the time variation for all the nine years, including also those during the solar maximum phase for which the more advanced solar-modulation modelling used in Figure 6.3 becomes significantly more complex. Since the force field model requires several assumptions which work for rigidities higher than about 1 GV, only deuteron fluxes above this value were considered for this study. The deuteron spectra were converted as a function of the kinetic energy and from them, spectra unfolded for the solar modulation were obtained using the Equations 1.37 and 1.38 and the set of yearly values listed in Table 6.1. These values were the arithmetic means of the Φ values obtained in [122] for each Carrington rotation in the period between July 2006 and September 2014. The resulting

Yearly values for the Φ parameter

Year	Φ
2006	0.483 MV
2007	0.440 MV
2008	0.396 MV
2009	0.343 MV
2010	0.374 MV
2011	0.487 MV
2012	0.606 MV
2013	0.707 MV
2014	0.755 MV

Table 6.1: Force field parameter values obtained as arithmetic means of the Φ values calculated in [122] for each Carrington rotation in the period between July 2006 and September 2014.

local interstellar fluxes are shown in Figure 6.4 (coloured connected points) as a function of the kinetic energy over nucleon. Differences can be noticed between the fluxes of the nine spectra; to obtain an estimation of the LIS, the local interstellar fluxes were merged in the following way: the kinetic energy range in Figure 6.4 was divided into an array of kinetic-energy bins

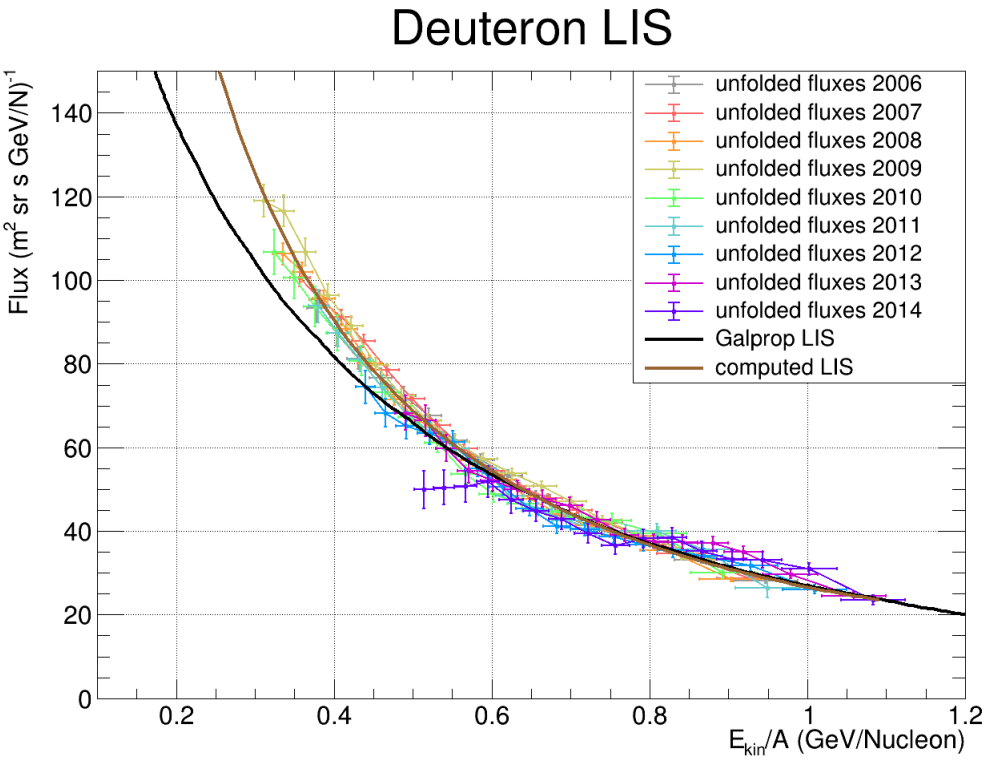

Figure 6.4: Unfolded fluxes as outside the Heliosphere boundaries calculated according to the force field approximation (coulored connected points) as a function of the kinetic energies over nucleon. The deuteron LIS obtained from the fit of the weighted mean values obtained from the unfolded fluxes is also shown as a brown curve. This obtained LIS can be compared to the one obtained from GALPROP and modified to agree with the Voyager measurements at low energies, shown as a black curve in the picture.

with suitable widths to include no more than one flux for each spectrum. Then, for each bin, weighted means of the included kinetic energy values and local interstellar fluxes were performed using the related uncertainties as weights. The weighted-mean fluxes were then fitted with the following power-law function:

$$f(x) = a \cdot x^{-b} + c \cdot x + d \tag{6.1}$$

where x represents the kinetic energy over nucleon. This allowed obtaining a smooth LIS, which is shown in Figure 6.4 as a brown line. In the same picture, the LIS computed by GALPROP and modified to agree with the Voyager measurements at low energies is also shown as a black curve. A disagreement between the two LIS for kinetic energies over nucleon values lower

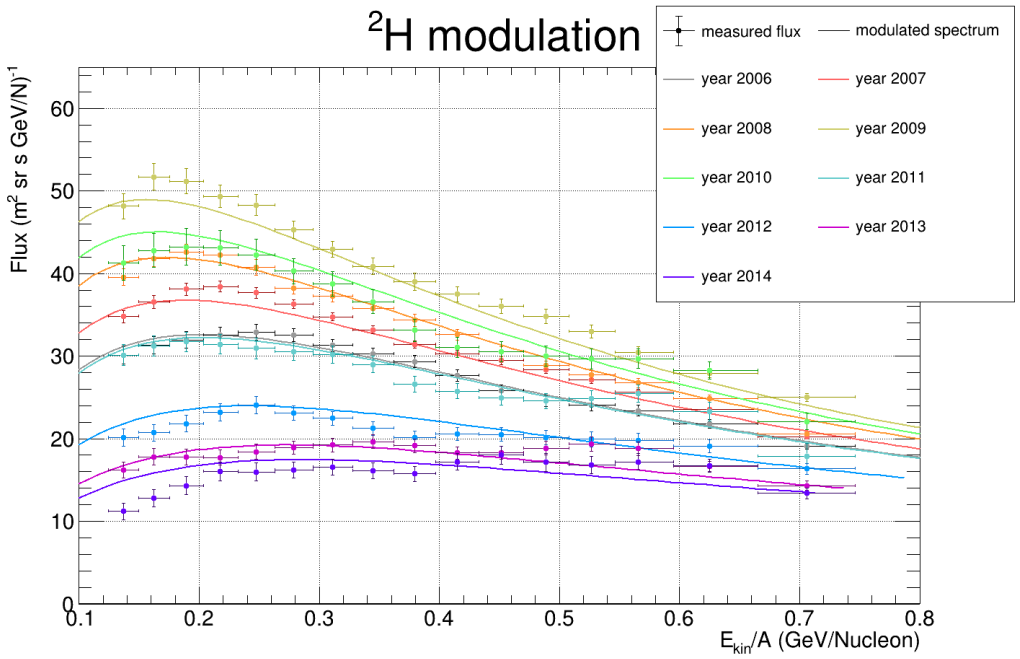

Figure 6.5: Folded spectra calculated for deuterons with the force-field approximation as inside the Heliosphere (coloured curves) as a function of the kinetic energy over nucleon. These modulated curves are compared with the measured deuteron fluxes (coloured points).

than 0.6 GeV/n can be noticed, in particular the obtained LIS results are about 21% higher than the GALPROP one at 0.3 GeV/nucleon. This result suggests that the disagreement in intensity and partially in shape observed in Figure 6.3 between the measured and numerically-modulated spectra come from the too low values assumed below 0.6 GeV/n by the GALPROP LIS, which is used as input by the 3D numerical model.
The obtained LIS was then used to verify if the measured time variation was in agreement within one standard deviation with the time evolution predicted by the force field approximation. For this purpose, spectra at 1 AU were obtained from this LIS using Equations 1.37 and 1.38 and the set of yearly values of the force-field parameter listed in Table 6.1. The resulting spectra are shown in Figure 6.5 (coloured curves) along with the measured deuteron fluxes as a function of the kinetic energy over nucleon (coloured points). It can be observed that the computed modulated spectra follow qualitatively the trend of the measured fluxes. To perform a quantitative comparison, for each kinetic-energy-over-nucleon bin of the measured fluxes a pull value was

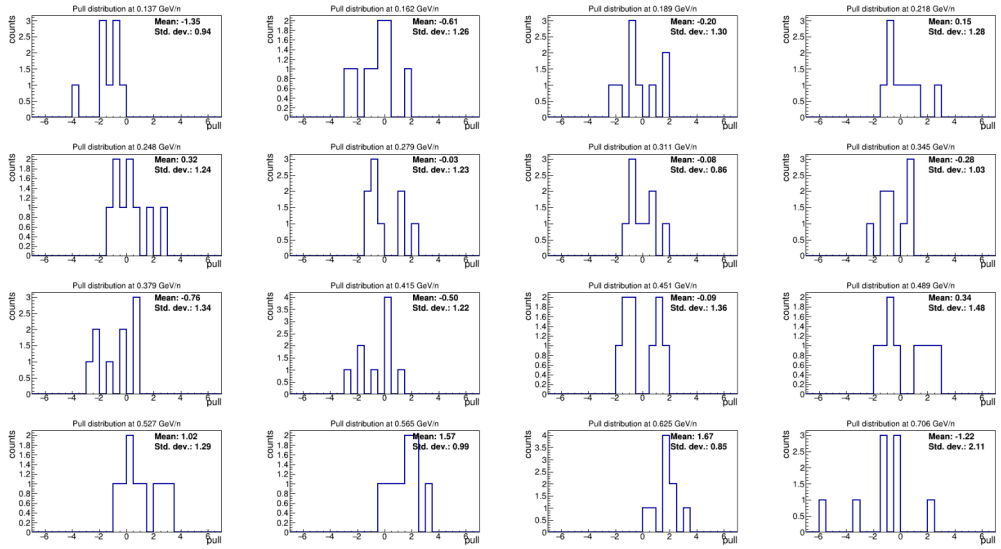

Figure 6.6: Distributions of the nine computed pull values, one for each year, for the kinetic energy over nucleon bins considered in the test.

calculated. Generally, the pull value is defined as:

$$g_{pull} = \frac{x - \mu}{\sigma} \quad , \tag{6.2}$$

where x is a measured value that distributes around a mean μ and with width σ. According to the central limit theorem, the pull values g_{pull} distribute according to a standard Gaussian distribution with mean zero and unit width. This property allows to have some indications on the quality of the measurements x: a pull distribution with a non-zero mean is a hint of a bias in the measured values x, whereas if the pull distribution has a standard deviation higher (lower) than one, it suggests that the error associated to the measurements x are too small (large). In the specific case of this analysis, the pull value was calculated as:

$$g_{pull} = \frac{f_{meas} - f_{fold}}{\sigma_{meas}} \quad , \tag{6.3}$$

where f_{meas} is the measured flux, f_{fold} is the intensity of the obtained folded spectrum and σ is the statistical error associated to the measured fluxes. The pull values were calculated according to Equation 6.3 for each year, obtaining a distribution of nine pull values for each kinetic-energy-over-nucleon bin, as shown in Figure 6.6. Mean and standard deviations were calculated for each pull distribution. Although nine values are too few to have a clear

distribution, some considerations can be drawn. Except for the lowest energy bin, up to 0.345 GeV/n the distributions have a mean value close to zero and standard deviations $\leq$1.30. This suggests that in this kinetic- energy-over-nucleon range the measurements and the associated uncertainty are reasonably good. However, this is no longer true at 0.137 GeV/nucleon and for the highest energies, from 0.379 GeV/n, where the pull distributions appear more distorted. Especially from 0.527 GeV/nucleon, the pull distributions present means in absolute values higher than 1.5, indicating the presence of a bias in the fluxes in these energy bins. This bias is due to the systematic hardening observed in the fluxes above 2.0 GV from 2010 to 2014.

Chapter 7

Identification of cosmic-ray deuterons with the GAPS experiment

In this chapter, there is described a first study of the capability of measuring cosmic-ray deuterons rejecting as much as possible the large background of cosmic-ray protons with the information provided by the GAPS detectors.
The antinucleus component of cosmic radiation at low energy is the main scientific goal of the GAPS mission and the primary trigger of the experiment (trigger level 2) is designed to select cosmic-ray antinuclei rejecting the huge background of standard galactic particles. However, there is interest to measure low-energy cosmic-ray nuclei with GAPS as well, by using the unbiased trigger (trigger level 1) for a fraction of the collected events, approximately one out of one hundred triggers. The interest in these measurements is various. Measurements of well-studied cosmic-ray components while worthwhile studied by themselves, will provide insight into systematic uncertainties of the GAPS experiment. Additionally, measurements of the cosmic-ray nuclei performed by GAPS during its flights will deliver crucial information about the solar modulation effects. In particular, a study of the proton and deuteron fluxes measured by GAPS with a numerical model of cosmic-ray propagation in the Heliosphere will provide an accurate estimation of the solar-modulation effects on the contemporary antiproton and antideuteron fluxes.
Although the novel detection technique developed for GAPS is based on an antinucleus capture and the subsequent formation and de-excitation of a short-lived exotic atom, it is still possible to exploit the information provided by the GAPS detectors to measure the counterpart of cosmic-ray nuclei at low energy. Using the velocity information provided by the ToF system and

the ionization energy deposits of the crossing particle in the active materials of the apparatus, it is straightforward to distinguish particles of different absolute values of electrical charge. Differently from PAMELA, GAPS lacks a magnetic spectrometer and therefore rigidity measurements are not available, making the isotopic separation more complex to perform. The analysis work performed on GAPS simulated data had the purpose to explore the potential techniques useful to separate deuterons from the large background of protons at low energy, below 0.25 GeV/n. These data were generated by a state-of-the-art GEANT4-based simulation software developed to reproduce accurately the GAPS apparatus and the radiation-matter interactions occurring inside it. Based on these data, a custom detection technique was developed exploiting the fact that protons and deuterons with the same velocity have different kinetic energies and consequently they stop at a different depth inside the GAPS tracker.
For this identification technique, the corresponding rejection power of proton contamination and the achieved acceptance for a deuteron measurement with GAPS were calculated and presented here as a function of the β quantity.

7.1 Selection criteria for the incoming particles

Simulated data of protons and deuterons crossing the GAPS apparatus were generated for this analysis. In particular, the simulated particles were ejected downward from a generation surface with a flat spectrum in the β range $[0.1; 1]$. The adopted generation surface was a cube with an area of 116.16 m^2 encapsulating the whole GAPS apparatus.
The raw information from the GAPS detectors in the simulation was then digitized and processed by a custom advanced reconstruction algorithm developed by the GAPS collaboration. This reconstruction algorithm extrapolates the values of the quantities useful for the (anti)particle identification. A detailed description of this reconstruction algorithm and its performances are reported in [110].
In the analysis, in addition to the reconstructed quantities, the β information coming from the Monte Carlo truth was also used. This will be referred to as simulated β (β_{sim}) in contraposition to the reconstructed β (β_{rec}), whose value is obtained from the reconstruction algorithm.
As a first step, a set of criteria on the reconstructed information was defined to select an initial sample of particles crossing the GAPS apparatus from the

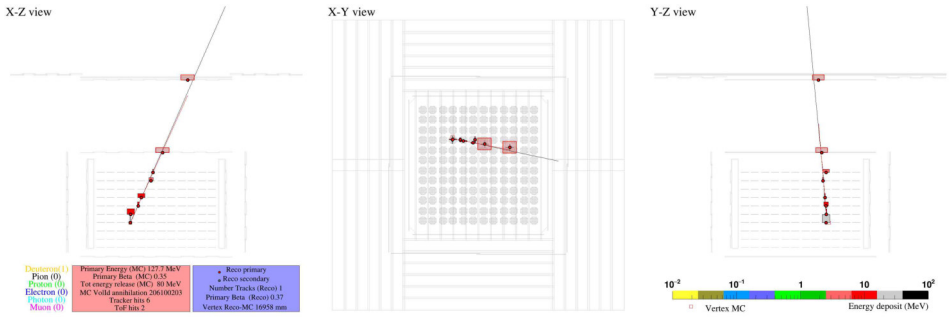

Figure 7.1: A simulated event corresponding to a deuteron with $\beta_{sim} = 0.35$ crossing the GAPS apparatus displayed in the X-Z, X-Y and Y-Z views.

top. This choice is supported by two considerations: particles crossing the apparatus from the top have a longer flight path, which improves the resolution of the track length evaluation and therefore of the velocity measurement as well. Moreover, in a real situation, the oblique events correspond to cosmic rays crossing a path in the atmosphere and therefore more affected by energy losses and fragmentation. These used criteria to selected particles crossing GAPS from the top are listed hereinafter:

(A) only events recorded with a trigger of level 1 were selected.

(B) events with a single primary track reconstructed in the apparatus were required.

(C) The trajectory of the reconstructed track was required to cross downward the ToF Umbrella and the first tracker plane. Since the particle can cross the first tracker plane through the passive aluminium material, this requirement does not imply a hit in that layer. This selection rejects the most oblique events entering the tracker from the sides.

(D) At least a hit in the tracker is required. This ensures that for any event some information is provided by the tracker.

(E) Events with a value of the reconstructed velocity beta greater than 0.55 were rejected because the vast majority do not stop in the apparatus.

Using these requirements samples of simulated protons and deuterons were extracted for further analysis. A graphical view of an event crossing the GAPS apparatus and satisfying all the A-E criteria is shown in Figure 7.1.

In the next section, a first deuteron identification technique developed in this work is detailed.

7.2 Deuteron identification with Bragg peaks in the tracker layers

In lack of a rigidity measurement in the GAPS data, isotopic separation techniques different from that used in the deuteron analysis of the PAMELA data were looked for. In agreement with the Bethe-Bloch formula, all particles with the same charge value Z, as protons and deuterons, distribute in the same dE/dX band as a function of β, preventing from separating particles with different masses.
The developed deuteron identification technique is based on a consideration: deuterons have a mass approximately twice higher than that of protons and therefore at the same β they have larger kinetic energy which enables them to travel deeper. The kinetic energy of a particle is given by:

$$E_{kin} = (\gamma - 1)\, mc^2, \tag{7.1}$$

where γ is the Lorentz $\gamma = \frac{1}{\sqrt{1-\beta^2}}$, m is the mass of the particle and c is the speed of light in the vacuum. It follows Equation 7.1 that particles with the same β but different masses have different values of kinetic energy, in particular, the more massive particle is the more energetic.

In Figure 7.2 the dE/dX distributions measured in each tracker layer for proton in red and deuteron in black are shown together as a function of the reconstructed velocity (β_{rec}). In each of these distributions, regions dominated by deuteron dE/dX values are visible at low β values. In these regions, deuteron-selecting areas (blue closed broken lines in Figure 7.2) almost free of proton energy deposits were defined. These deuteron-dominated regions are explainable in the following way: moving along the x-axis towards lower β_{rec} values in the distributions of Figure 7.2, the kinetic energy of the particles decreases and their ionisation energy deposits grow proportionally to $1/\beta_{rec}^2$ up to reach a dE/dX peak, called Bragg peak [113], just before to come to rest. Because of the kinetic-energy difference at the same β_{rec}, protons reach their Bragg peak at higher β_{rec} than deuterons. The deuteron-dominated regions are thus $\beta_{rec} - dE/dX$ areas populated by low-energy deuterons approaching their Bragg peaks, while almost no protons are present since most of them did not have sufficient energy to reach the layer under study. Since higher kinetic energy is needed to travel deeper in the tracker, going down into the lower layers, the proton and deuteron Bragg peaks (and therefore the deuteron dominated regions) move towards higher β_{rec} values. In this way, each of the deuteron-selecting areas in Figure 7.2 worked in a restricted β_{rec} range, which moves gradually to higher values going from the highest- to the deepest tracker layers. Requiring that an event satisfied any of the

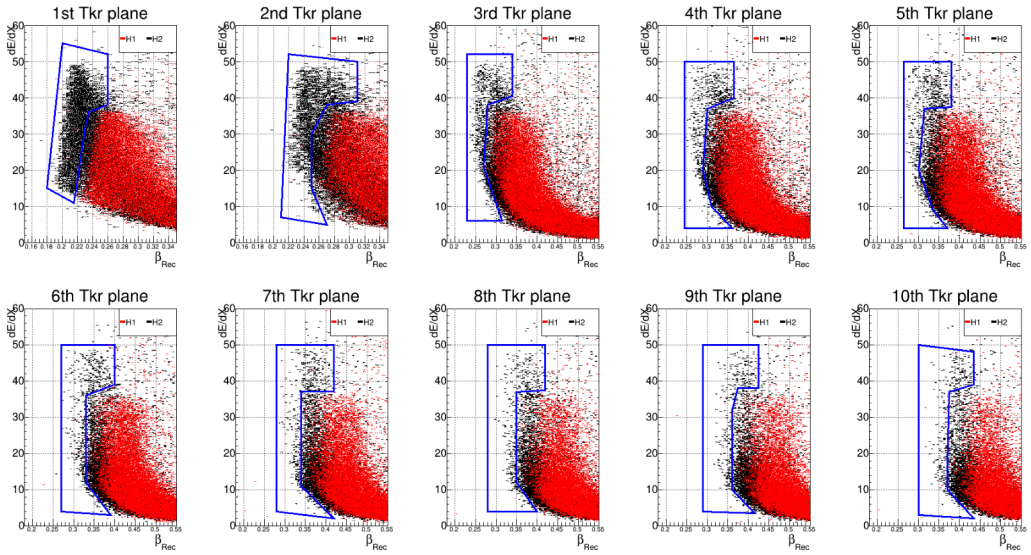

Figure 7.2: dE/dX distributions as a function of the reconstructed β (β_{rec}) in each of the ten tracker layers for simulated samples of protons in red and deuteron in black satisfying selection criteria A-E. The blue closed broken lines were calibrated to enclose the areas dominated by deuteron dE/dX values and almost free of proton energy deposits.

deuteron-selecting areas, allowed to perform the deuteron identification in the overall β_{rec} range $[0.18, 0.44]$.
From now on, this identification technique will be referred to as the Bragg peak method.

7.3 Selection efficiency

The efficiency of the Bragg peak method was studied. Since the deuterons-selecting areas require hits in the tracker layers where they are defined, first the efficiency of the presence of a hit in any layer was calculated as follows:

$$\varepsilon_{hit} = \frac{n_{hit}}{n_{crit_{A-E}}} \quad , \tag{7.2}$$

where $n_{crit_{A-E}}$ is the number of events selected with criteria A-E and n_{hit} are the selected events having also a hit in the considered i-th layer. This efficiency was calculated for each layer and shown in Figure 7.3. In the first layer, the efficiency is equal to one for β_{sim} values up to 0.28, since criterion D requires at least a hit in the tracker. At this low energy range, deuterons

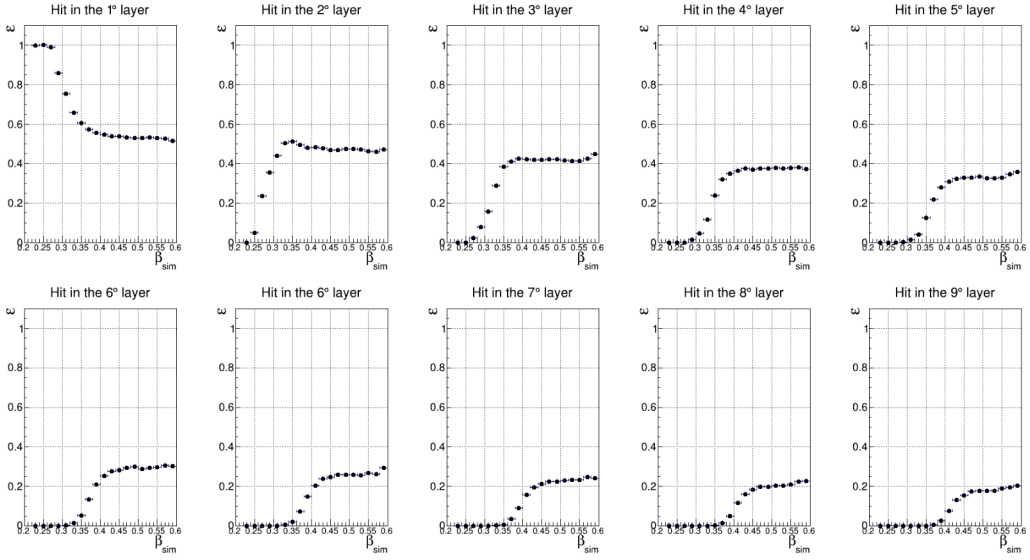

Figure 7.3: Fraction of events selected with criteria A-E and with a hit in a considered tracker layer. This is calculated and shown for each of the ten layers as a function of the β_{sim}.

can not reach the second layer in the tracker but stop in the first one. For the next layers, the efficiency starts to rise from zero up to reach a plateau as the events gain enough energy to reach the layer. Moreover, moving down from the upper into the deepest layers, the efficiency decreases from about 0.5 to lower than 0.2 in its plateau region. These numbers are the results of two main causes of inefficiency inside the GAPS tracker. The first one is the presence of passive material for each tracker layer, this means that a deuteron may cross the layers useful for its identification through the no-detecting material. This leads to discard this event, because it has no dE/dX measurement inside the deuteron-selecting areas probing a β_{rec} range containing the β_{rec} value measured for it. The other possibility is that a deuteron exits the tracker through the sides before reaching the layers useful for its identification. Also in this case, this event is rejected because no dE/dX measurement is inside the deuteron-selecting areas in those layers. This occurs more often for the deepest layers, since the crossing of the whole tracker was not required to preserve enough high acceptance and thus the particles following their trajectory can go out through the sides before reaching the tracker bottom.
At this point, the efficiency of each deuteron-selecting area in presence of a hit in the considered layer was calculated as a function of the β. The efficiency sample of deuterons was selected with criteria A-E and requiring a hit

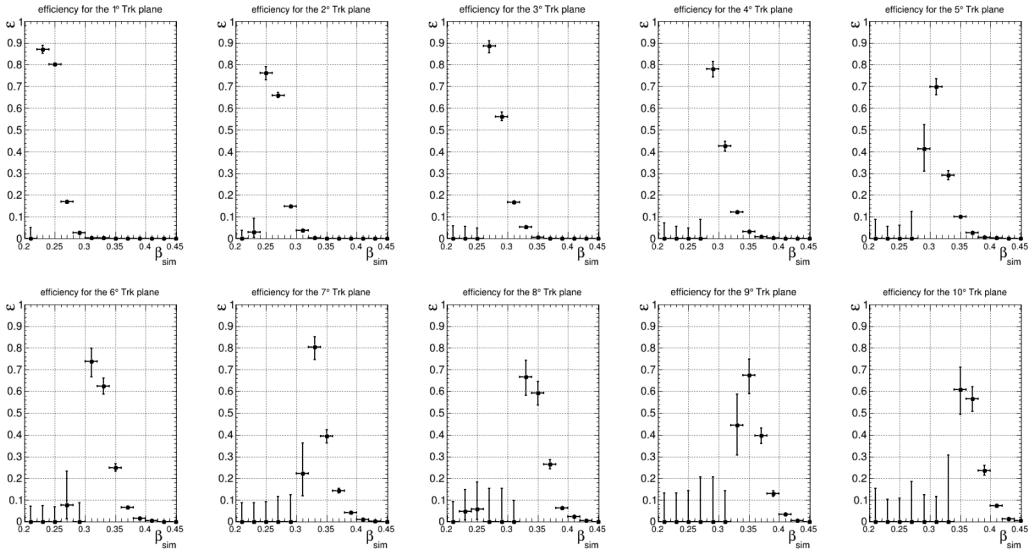

Figure 7.4: Efficiency values calculated as a function of the β_{sim} for each deuteron-selecting area in presence of a hit in the specific layer.

in a specific tracker layer, then the events lying inside the deuteron-selecting area were selected to obtain the final sample of events. The efficiency was finally calculated in the following way:

$$\varepsilon_{sel} = \frac{n_{sel}}{n_{hit}} \quad , \tag{7.3}$$

where n_{sel} is the number of selected events in a β bin, whereas n_{hit} is the number of events of the efficiency sample in that β bin. The results are shown in Figure 7.4 for each of the ten layers of the tracker. As expected, the deuteron-selecting areas have high efficiency only within a thin β slice. It is possible to observe that this efficiency does not reach the same values in each layer, especially the first planes it presents higher values, for instance, the first and third tracker layers have maximum efficiency around 0.87 and 0.885 respectively, whereas the three deeper planes have lower efficiency values, around 0.62 in the last layer. This efficiency drop is due to the fact that in the first layers there is a clearer separation between the Bragg peaks of protons and deuterons and consequently the deuteron-selecting areas can select a larger number of events. Instead, in the layers deeper in the tracker the proton and deuteron distributions overlap more and the deuteron-selecting areas can select fewer deuteron events while keeping a high rejection power for protons. This progressive resolution loss in the β-dE/dX distributions of the bottom layers is intrinsic to the process of ionisation energy loss and can

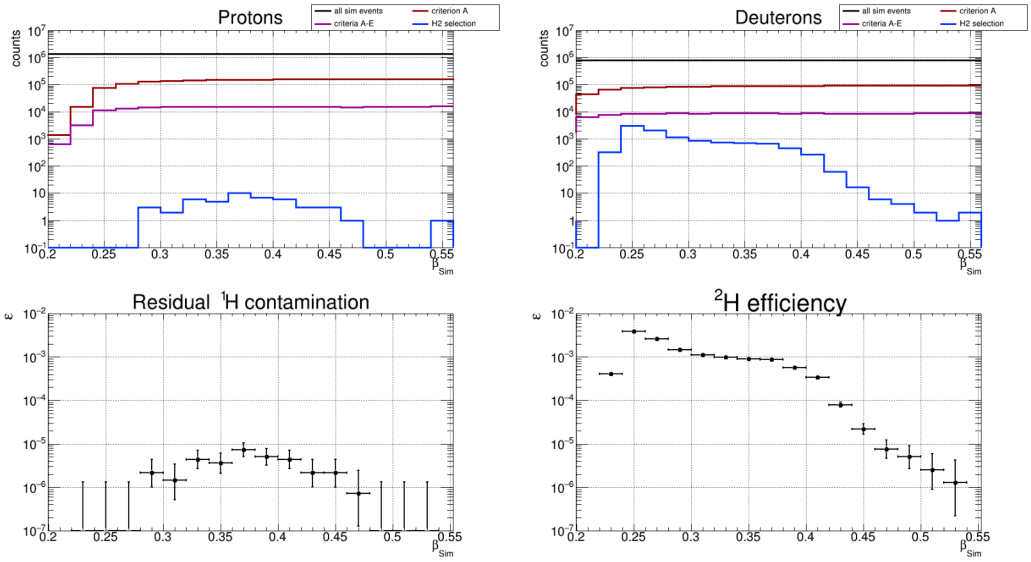

Figure 7.5: Top panels: histograms for protons, left, deuterons, right, satisfying criterion A in black, criteria A-E in purple, criteria A-E and selected as deuterons by the Bragg peak method in blue. Bottom panel: the fraction of protons surviving the deuteron selection, left, and the overall selection efficiency for deuterons, right.

be explained based on the following considerations. The ionisation energy losses released by a particle interacting with the matter distribute according to a Landau probability distribution with a mean value predicted by the Bethe-Bloch formula and a long tail on the higher dE/dX values, therefore particles with the same velocity and the same traversed mass thickness (dX) can experience slightly different energy losses. Furthermore, particles crossing the tracker with different direction angles interact with different amounts of matter, this means they also experience a different energy loss. Since the energy-loss fluctuations due to the ionisation process and the different track slopes become more relevant with the amount of crossed materials, the resolution of the dE/dX distributions is more affected in the bottom layers.
Finally, the overall selection efficiency as well as the fraction of surviving protons were calculated for the developed deuteron-identification technique (criteria A-E plus Bragg peak method) as a function of the simulated β. Each selection step was performed on the simulated samples of protons and deuterons obtaining the selected events for both the two isotopes, which went filling the corresponding histograms as a function of the β_{sim}. In Figure 7.5, the top panels show the number of protons, left, and deuterons, right, surviving the various selection criteria as a function of the β_{sim}. In particular,

the black histograms show the events generated, the brown histograms the events triggered by the ToF system (criteria A), the purple histograms the events satisfying the criteria A-E and finally the blue histograms the events which are selected as deuterons. The bottom panels show the fraction of protons surviving the deuteron selection, left, and the overall selection efficiency for deuterons, right. The efficiency values are the results of the ratio of the events of the black and blue histograms for each β_{sim} bin. In the whole β_{sim} range, the fraction of protons surviving the deuteron selection is less than 10^{-5}. Below $\beta_{sim} = 0.26$, no protons were selected and therefore only lower limits are available. On the other side, the overall selection efficiency for deuterons peaks at $\beta = 0.25$ with an efficiency of of about 0.004, then the efficiency decreases reaching a plateau of about 0.001 in the β_{sim} range $[0.3; 0.38]$. For $\beta_{sim} > 0.38$ the efficiency decreases steeply because of the high edge of the overall β_{rec} range where the deuteron-selecting areas work is approached and crossed.

7.4 Estimation of the residual proton contamination

With the obtained results about the overall efficiency of the deuteron selection (ε_{H2}) and the fraction of surviving protons (ε_{H1}), the relevance of the residual proton contamination in the selected deuteron sample was estimated by calculating a rejection power defined as:

$$RP = \frac{\varepsilon_{H2}}{\varepsilon_{H1}} \quad , \tag{7.4}$$

The resulting rejection power is presented as a function of the simulated velocity β_{sim} in Figure 7.6. The red and orange dashed horizontal lines represent the two arbitrary values of 130 and 1950, used as benchmarks for the rejection power. According to the deuteron to proton flux ratio obtained with the PAMELA experiment in chapter 6 (which is about 0.032 at β equal 0.5), 130 and 1950 correspond to about 25% and 1.5% respectively of proton contamination in the deuteron sample. The 25% was chosen as the maximal acceptable contamination in this analysis, whereas the 1.5% is about the minimum contamination value obtained in the limited β_{sim} range $[0.24, 0.24]$. Generally, up to $\beta_{sim} = 0.36$, the rejection power is higher than the benchmark value of 130, whereas above 0.36 up to 0.4 the values agree within one sigma with that benchmark. Finally, beyond 0.4, the power rejection decreases below 130.
The Bragg peak method ensures negligible or small contamination up to

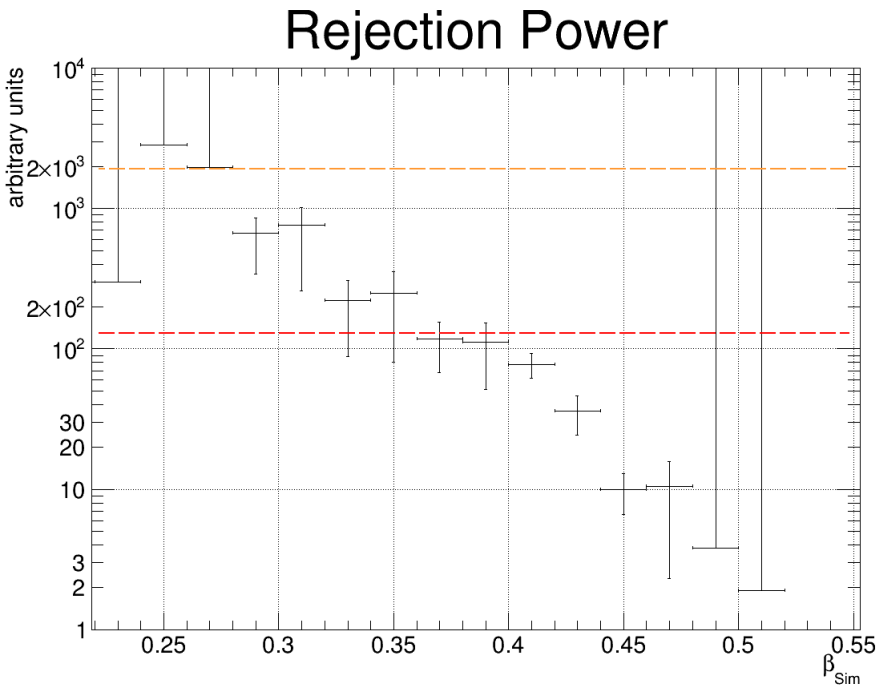

Figure 7.6: Proton rejection power calculated as in Equation 7.4 as a function of the β_{sim} for the deuteron identification implemented through the Bragg peak method.

$\beta_{sim} = 0.36$. At higher β_{sim} values, the fraction of surviving protons become more significant, exceeding 25% of the selected sample above $\beta_{sim} = 0.4$, where this method is unable to provide sufficient proton rejection.

7.5 The acceptance

The final step of this analysis was the acceptance calculation. The experimental acceptance for a specific CR component constitutes the figure of merit of the sensitivity of the experiment to the detection of this cosmic particle. The deuteron acceptance was calculated with the simulated data using the overall efficiency of the deuteron selection shown in Figure 7.5. The efficiency ε_{H2} value must be multiplied by the area of the generation surface A used in the simulation and the geometrical factor $\Theta = \pi/2$ for down-going particles ejected from a plane surface. Thus, the acceptance was calculated as:

$$G = \varepsilon_{H2} \cdot A \cdot \Theta \quad , \tag{7.5}$$

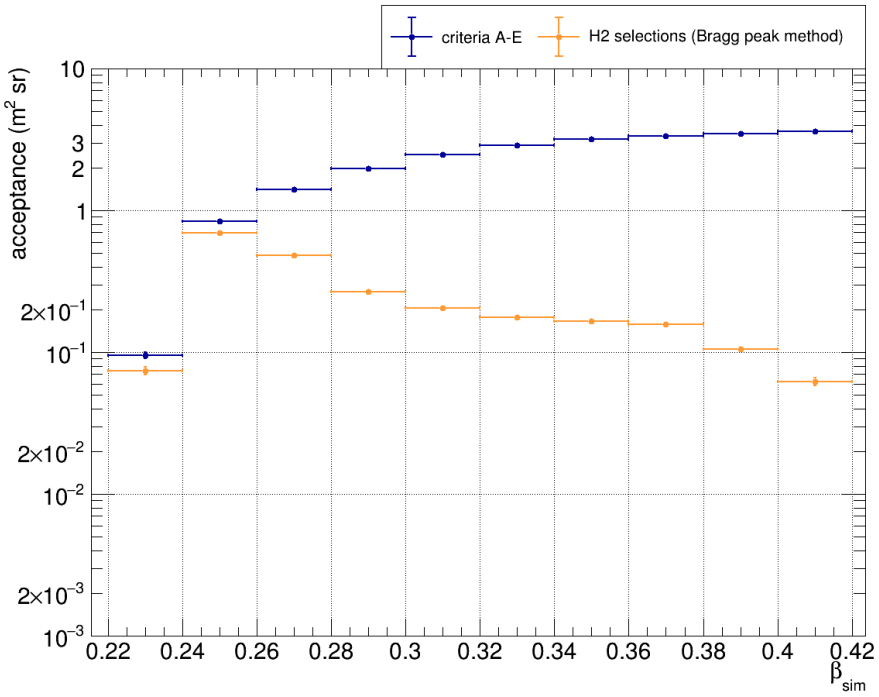

Figure 7.7: Acceptance values calculated as a function of the simulated β requiring criteria A-E (blue points) and additionally the deuteron identification with the Bragg peak method (orange points).

In Figure 7.7 the acceptance results for the deuteron selection are drawn with orange points in comparison with the dark blue points which represent the ideal maximum acceptance values for deuterons, which account for only the initial criteria A-E. These results agree with what was already noted in the overall deuteron selection efficiency in Figure 7.5 and in the rejection power in Figure 7.6. The deuteron identification technique developed with the Bragg peak method works well in the β_{sim} range $[0.22; 0.28]$, where it ensures acceptance values close to ideal maximum values together with a high proton rejection. Above 0.28 the deuteron acceptance decreases gradually reaching a plateau up to a β_{sim} value of 0.38 at $\sim$ 0.2 m^2 sr, significantly lower than the ideal maximum acceptance and with increasingly significant proton contamination.
In Figure 7.8 the acceptance values were converted into numbers of deuteron events detected per hour as a function of the kinetic energy. The conversion from β_{sim} to kinetic energy was performed using the Equation 7.1. The number of events shown in Figure 7.8 was obtained by multiplying the acceptance values by 3600 seconds, the kinetic energy bin width and the deuteron flux

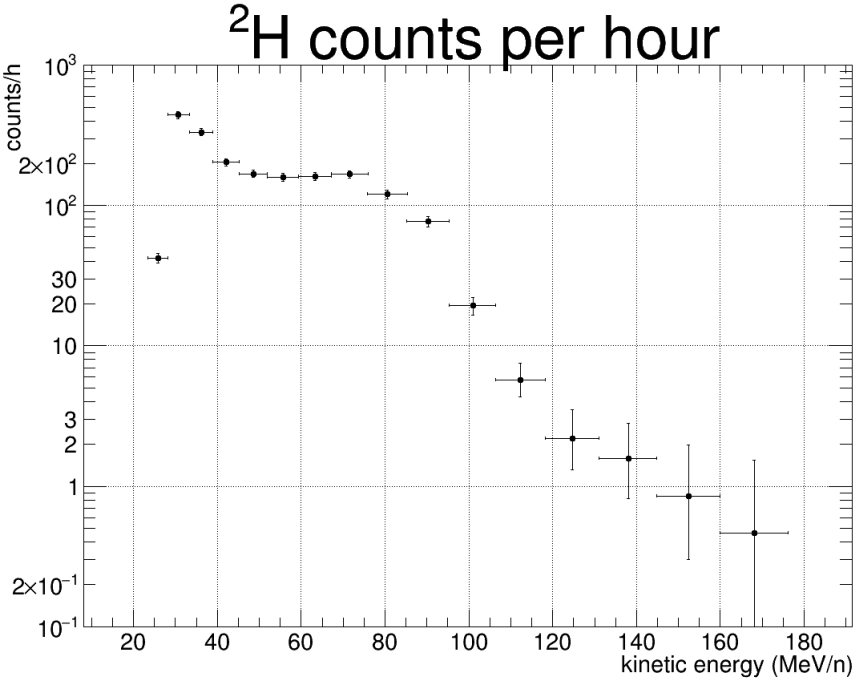

Figure 7.8: Predicted deuteron counts measured by GAPS during an overall hour of live time with the trigger level 1. These counts must be scaled for the trigger 1 use rate, still not completely defined but approximately of one over 100 events.

obtained in chapter 6 for the year 2009 at $E_{kin}/A = 0.8$ MeV/N. These numbers should then be divided by a scale factor of the order of 100, to consider the live-time fraction defined by the rate of use of the trigger Level 1, which has not been completely defined by the GAPS collaboration yet.
In conclusion, the Bragg peak method turned out to be an efficient deuteron selection technique with minimal proton contamination in the very low kinetic energy range ($\leq$ 40 MeV/n). At kinetic energies between 40 MeV/n and about 80 MeV/n, this technique can be still used but the geometrical acceptance and therefore the number of recorded events decreases and the residual proton contamination increases up to about 25%. More efficient identification techniques are required to extend the energy range and increase the acceptance and they will be the topic of a future analysis.

Chapter 8

Conclusions

In this thesis, a new measurement of the time-dependent galactic cosmic-ray proton and deuteron fluxes was discussed. The analysis was conducted on the data collected by the PAMELA experiment from July 2006 to September 2014. This period is particularly relevant for solar-modulation studies because it covers almost a whole solar cycle and includes a change of solar magnetic polarity in 2013 as well.
As a result, nine yearly rigidity spectra from 2006 to 2014 for both galactic protons and deuterons and the related deuteron-to-proton flux ratios were measured between 0.6 and 2.6 GV. These results constitute the most accurate cosmic-ray proton and deuteron fluxes ever measured at low rigidities, below 1 GV, as a function of time for almost a whole solar cycle.
The time evolution of the proton and deuteron fluxes was observed to be anticorrelated with the solar activity: from 2006 the fluxes progressively increase over time during the minimum of the 23rd solar cycle reaching their maximum values in 2009. In the following years, the fluxes begin to gradually decrease approaching the next solar maximum, reaching their minimum values in 2014. Moreover, not only the intensity but also the spectral shape was observed to change over time as an effect of the solar modulation: the proton and deuteron spectra become progressively softer from 2006 to 2009 with their spectral peaks moving gradually towards lower rigidities. This trend is reversed with the increase of the solar activity, from 2010 to 2014 the observed spectra become progressively harder and their spectral peak moves towards higher rigidities.
The deuteron-over-proton flux ratios were also calculated for the rigidity range $[0.8, 1.9]$ GV. These ratios present an increasing trend as a function of the rigidity, which is ascribed to the difference in the LIS shapes of protons and deuterons. No obvious time dependence was observed, except for the year 2013, whose ratios, at rigidities lower than 1.2 GV, are higher by a

factor of 1.3 with respect to those measured in 2009.
The deuteron fluxes were also compared with the output of a 3D numerical model for cosmic-ray propagation in the Heliosphere for the years 2006 and 2009. Starting from a deuteron LIS calculated with the software GALPROP and modified at the lower energies to agree with the Voyager I measurements outside the Heliosphere, this model provided numerically modulated deuteron spectra. These are in good agreement with the spectral shape of the measured spectra up to about 0.3 MeV/n, but they present an intensity systematically lower of about 20% than the measured fluxes. Since the parameters used in this model can reproduce very accurately the proton spectra observed by PAMELA in 2006 and 2009, this systematics is most likely due to the deuteron LIS, which needs to be modified to reproduce the observed spectra.
To analyse the time evolution of all the nine measured deuteron spectra, a simpler model, which is the force-field approximation, was also used. A new deuteron LIS was obtained with this approach, and it turned out to be higher in intensity at the low energies with respect to the GALPROP LIS. This has suggested the necessity to modify below 0.6 GeV/n the input deuteron LIS used in the 3D numerical model to obtain a better agreement in intensity between numerical and measured deuteron spectra.
Moreover, taking into account the charge-sign effect induced by the drift motions in the Heliosphere, accurate modelling of the measured deuteron fluxes will also allow reproducing accurately the solar modulation of the energy spectra of antideuterons. In fact, there is great interest in the component of antideuterons in cosmic rays, because, at energies below 1 GeV/n, they could constitute a background-free channel for indirect dark-matter search. The antideuterons, as well as the other antinuclei, will be the object of research of the future GAPS experiment.
A preliminary study of the deuteron acceptance achievable with the GAPS experiment was also presented. The analysis was performed with simulated data provided by the GEANT-4 based GAPS simulation software. Indeed, although GAPS will use a novel detection technique based on the formation and decay of an exotic atom to measure antinuclei, proton and deuteron detection will be possible at low energy using a classical identification technique. The deuteron measurements with GAPS during its flight operation will allow calibrating with more accuracy the solar-modulation model in order to better estimate the antiparticle fluxes. The deuteron identification technique developed in this work resulted efficient and affected by minimal proton contamination in a very low kinetic energy range ($\leq$ 40 MeV/n) providing acceptance values up to 0.7 m^2sr. Beyond this value up to about 80 MeV/n, this identification technique can be still used but the geometrical

acceptance decreases down to less than 0.2 m^2sr and the residual proton contamination increases up to about 25%. To improve the obtained acceptance values in this energy range reducing at the same time the residual contamination and to extend the range to higher energies, complementary identification techniques are currently object of study.

Bibliography

[1] https://galprop.stanford.edu/

[2] M. S. Longair, *High energy Astrophics – Volume 1 particles, photons and their detection*, Cambrige University Press (1997).

[3] T. K. Gaisser, *Cosmic Rays and Particle Physics*, Cambrige University Press (1990).

[4] S. P. Wakely et al., Particle Data Group, Chinese Phys. C. 38/9 (2014) 378.

[5] M. Boezio, E. Mocchiutti, Astrop. Phys. 39-40 (2012) 95-108.

[6] E. Mocchiutti, Nucl. Phys. B 256-257 (2014) 161-172.

[7] M. Boezio, R. Munini, P. Picozza, Progress in Particle and Nuclear Physics Volume 112, May 2020, 103765

[8] A. Strong, I.G. Moskalenko, V. S. Ptuskin, Annual Review of Nuclear and Particle Science, vol. 57, Issue 1, p.285-327

[9] M. S. Potgieter, Living Rev. Solar Phys. 10 (2013) 3.

[10] Usoskin, I. G., *A history of solar activity over millennia*, Living Rev Sol Phys 14 (2017) 3.

[11] Heber B., Space Sci. Rev. 2013, 176, 265-278

[12] A. Panoz et al., Bull. Russ. Acad. Sci. Phys. 71 (2007) 494.

[13] Y. Ajima et al., Nucl. Instr. Meth. 433 (2000) 71.

[14] S. Barwick et al., Astrophys. J. Lett. 482 (1997) 191.

[15] M. L. Ambriola et al., Nucl. Phys. B-Proc.Suppl. 78 (1999) 32.

[16] P. Picozza et al., Astropart. Phys. 27 (2007) 296.

[17] A. A. Abdo et al., Phy. Rev. Lett. 102 (2009) 181101.

[18] J. Chang et al., Astrop. Phys. 95 (2017) 6-24.

[19] M. Aguilar et al., Phys. Rev. Lett. 110 (2013) 141102.

[20] S. Torii, P. S. Marrocchesi et al., Advances in Space Research 64 (2019) 2531-2537

[21] https://www.physics.utah.edu/ whanlon/spectrum.html

[22] N. Chiba et al., Nucl. Instr. Meth. A 311 (1992) 338.

[23] H. Kawai et al., Nucl. Phys. B 175-176 (2008) 221-226.

[24] J. Abraham et al., Nucl. Instrum. Meth. A523 (2004) 50.

[25] D. J. Bird et al., ICRC 3 (1995) 504.

[26] C. Baixera et al., Nucl. Phys. 114 (2003) 247-252.

[27] F. Krennrich, New Astron. Rev. vol. 48 (2004) 345-349.

[28] W. Hofmann et al., ICRC 2001, 2785.

[29] B. Coste et al., A&A 539 (2012) A88.

[30] O. Adriani et al., ApJ 818 (2016) 68.

[31] I. V. Moskalenko, Nuovo Cim. C034N3 (2011) 149-156.

[32] M. Waldmeier, Solar Phys. 73 (1981) 207.

[33] A. J. Hundhausen, Coronal Expansion and Solar Wind XII, Springer-Verlag (1977).

[34] O. Adriani et al., Phys. Rev. Lett. 102 (2009) 051101.

[35] O. Adriani et al., Phys. Rev. Lett. 116 (2016) 241105.

[36] L. J. Gleeson and W. I. Axford, Astrophys. J. (1968), 154, 1011.

[37] R. A. Caballero-Lopez and H. Moraal, J. of Geophys. Res. (2004) 109, A01101.

[38] M. S. Potgieter, *The modulation of galactic cosmic rays as described by a three-dimensional drift model*, PhD thesis, Potchefstroom University for CHE, South Africa, 1984.

[39] M. Hattingh, *The modulation of galactic cosmic rays in a three-dimensional heliosphere*, PhD thesis, Potchefstroom University for CHE, South Africa, 1998.

[40] E. E. Vos, *Modelling charge-sign dependent modulation of cosmic rays in the heliosphere*, PhD thesis, North-West University, South Africa, 2016.

[41] C. J. Mertens et al., Current Topics in Ionizing Radiation Research, IntechOpen 2012, Chapter 31.

[42] M. Klasen et al., Progress in Particle and Nuclear Physics Volume 85, November 2015, Pages 1-32.

[43] D. Gaggero and M. Valli, Advances in High Energy Physics 2018(1).

[44] J. Conrad and O. Reimer, Nature Physics volume 13, pages 224-231 (2017).

[45] T. Aramaki e al., Physics Reports 618 (2016) 1-37.

[46] P. von Doetinchem et al., JCAP 08(2020) 035.

[47] M. Nolta et al., Astrophys. J. Suppl. 180 (2009), 296-305.

[48] M. Tegmark et al., Astrophys.J. 606 (2004), 702-740.

[49] C. Alcock et al., ApJ 471 (1996), 774.

[50] P. Tisserand et al., A&A 469 (2007), 387-404.

[51] L. Wyrzykowski et al., MNRAS 416 (2011), 2949-2961.

[52] B. J. Carr et al., Phys. Rev. D 81 (10) (2010), 104019.

[53] C. J. Copi et al., Science 267 (1995), 192-199.

[54] D. S. Akerib et al., Phys. Rev. Lett. 112 (2014) 091303.

[55] Z. Ahmed et al., Phys. Rev. Lett. 102 (2009) 011301.

[56] R. Bernabei, P. Belli, F. Cappella, et al., Eur. Phys. J. C 73 (2013) 12, 2648.

[57] C. E. Aalseth et al., Phys. Rev. Lett. 101 (2008) 251301.

[58] L. Evans, P. Bryant, JINST 3 (2008) S08001.

[59] G. Giesen et al., JCAP 09 (2015), 023.

[60] A. Cuoco et al., Physical Review Letters (2016) 118(19).

[61] Gammaldi, V. (2016) EPJ Web Conf. 121:06003.

[62] J. Silk and M. Sredniki, Physical Rev. Lett. 53 (1984), 624

[63] F. W. Stecker, S. Rudaz amd T.F. Walsh, Physical Rev. Lett. 55 (1985), 2622

[64] M. Ackermann et al., ApJ 840 (2017) 43

[65] Adriani et al., Nature 458 (2009) 607

[66] Aguilar et al., PRL 113 (2014) 121102

[67] Ackermann et al., PRL 115 (2015) 231301

[68] H. Abdallah et al. Phys. Rev. Lett. 117 (2016), 111301

[69] A. Yamamoto et al., Advances in Space Research 51 (2013) 227

[70] K. Abe et al., Physical Review Letters 108 (2012) 051102

[71] D. Bergstroem et al., Astrophysical Journal Letters 534, (2000) L177

[72] O. Adriani et al., Physical Review Letters 102, 051101 (2009)

[73] O. Adriani et al., Physical Review Letters 105, 121101 (2010), 1007.0821.

[74] M. Cirelli et al., JCAP 12, 045 (2014), 1407.2173.

[75] M. Aguilar et al., Phys. Rev. Lett. 117, 091103 (2016),

[76] C. Evoli, D. Gaggero, and D. Grasso, JCAP 12, 039 (2015), 1504.05175.

[77] X.-J. Huang et al., Physical Review D 95, 063021 (2017), 1611.01983.

[78] H. Fuke et al., Phys. Rev. Lett. 65 (2005) 081101

[79] H. Baer, S. Profumo, J. Cosmol. Astropart, Phys. 0512 (2005) 008

[80] F. Donato et al., Phys. Rev. D 78 (2008) 043506

[81] A. Ibarra, S Wild, Phys. Rev. D 88 (2013) 023014

[82] L. Dal, A. Raklev, Phys. Rev. D 89 (2014) 103504

[83] V. Chuotko, F. Giovacchini, PoS ICRC2008 (2008) 765-768

[84] C. J. Hailey, New J. Phys. 11 (2009) 105022+

[85] T. Aramaki et al., Astropart. Phys. 74 (2016) 6-13

[86] O.P.M. Aslam et al., Astrophys. J. 909 (2021) 215.

[87] O.P.M. Aslam, D. Bisschoff and M.S. Potgieter, PoS ICRC2019 (2020) 1054

[88] P. Picozza et al., Astropart. Phys. 27 (2007) 296.

[89] PAMELA official webpage. http://pamela.roma2.infn.it.

[90] G. Petrie, GeoInformatics 13/3 (2010) 30.

[91] O. Adriani et al., Phys. Rep. 544 (2014) 323-370.

[92] G. Osteria et al., Nucl. Instrum. Meth. A535 (2004) 152.

[93] D. Campana et al., Nucl. Instr. Met. A598 (2009) 696-701.

[94] S. Orsi et al., Proc. 29th Int. Cosmic Ray Conf. (Pune) vol. 3 (2005) 369.

[95] O. Adriani et al. Nucl. Instrum. Meth. A511 (2003) 72.

[96] M. Bongi, *Sviluppo dell'algoritmo di allineamento per lo spettrometro magnetico di PAMELA*, Master's thesis, Università degli Studi di Firenze (2001).

[97] M. Boezio et al. Nucl. Instrum. Meth. A487 (2002) 407.

[98] Y. Stozhkov et al., Internat. J. Modern Phys. A20 (2005) 6745.

[99] C. J. Hailey et al., New J. Phys. 11 (2009) 105022.

[100] C. J. Haley et al., Adv. Space Res. 51 (2013) 290-296.

[101] T. Aramaki et al., Rhys. Rep. 618 (2016) 1-37.

[102] F. Rogers et al., PoS (ICRC2021) 136

[103] N. Saffold et al., Astropart. Phys. 130 (2021) 102580

[104] T. Aramaki et al., Astropart. Phys. 74 (2016) 6-13.

[105] K. Perez et al., 33rd ICRC, Rio de Janeiro 2013.

[106] S. Quinn et al., PoS(ICRC2021)079

[107] http://gaps1.astro.ucla.edu/gaps/

[108] T. Aramaki et al., Astropart. Phys. 49 (2013) 52-62.

[109] P. von Doentinchem et al., PoS ICRC 2015 1219.

[110] R. Munini et al., Astropart. Phys. 133 (2021) 102640

[111] T. von Doentichem, Astropart.Phys. 54 (2013) 93-109.

[112] ApJ 742 (2011) 102

[113] W. R. Leo, *Techniques for Nuclear and Particle Physics Experiments* Springer-Verlag (1994).

[114] V. Formato, *Measurement of the nuclear and isotopic composition of galactic cosmic rays with the PAMELA experiment*, PhD Thesis, Università degli Studi di Trieste (2013).

[115] https://root.cern/

[116] G. D'Agostini. Nucl. Instr. Met. A 362 (1995) 487-498.

[117] O. Adriani et al. Astrophys. Journal vol. 765 (2013) pag 91.

[118] J. D. Sullivan Nuclear Instruments and Methods, (1971) 95:5.

[119] R. Munini et al., Astroparticle Physics (2021) Vol 133, 102640

[120] W. Webber et al., arXiv:1802.08273 [physics.space-ph]

[121] M.S Potgieter et al., Solar Phys. (2014) 289, 391-406.

[122] N. Marcelli et al., *Helium fluxes measured by the PAMELA experiment from the minimum to the maximum solar activity for solar cycle 24* ApJL in press (2021).